

DISSERTATION

SYNTHESIS AND CHARACTERIZATION OF STERICALLY AND ELECTRONICALLY
TUNED LIGANDS TOWARD MAGNETIC CONTROL OF IRON AND COBALT
COMPLEXES

Submitted by

Christina M. Klug

Department of Chemistry

In partial fulfillment of the requirements

For the Degree of Doctor of Philosophy

Colorado State University

Fort Collins, Colorado

Spring 2015

Doctoral Committee:

Advisor: Matthew P. Shores

Anthony K. Rappé

Christopher J. Ackerson

Nancy E. Levinger

Mingzhong Wu

Copyright by Christina Marie Klug 2015

All Rights Reserved

ABSTRACT

SYNTHESIS AND CHARACTERIZATION OF STERICALLY AND ELECTRONICALLY TUNED LIGANDS TOWARD MAGNETIC CONTROL OF IRON AND COBALT COMPLEXES

Presented within this dissertation are the syntheses and characterizations of iron and cobalt complexes featuring ligands designed to tune the magnetic properties. Two key magnetic phenomena are of interest: spin crossover and single-molecule magnetism. Both of these topics are known to be significantly influenced by subtle changes in coordination and inter- and intramolecular interactions. The overarching goal is to understand how the magnetic properties of the metal center can be controlled via electronic and steric modifications.

In Chapter 1, I offer a brief introduction into the background and motivation of the works presented in this dissertation in the realm of spin crossover and single-molecule magnetism. The first section of this chapter is focused on spin crossover and how host:guest interactions can be exploited to alter the magnetic behavior of first-row transition metals. Examples of Fe(II) complexes that display anion-dependent spin state behaviors in both the solid-state and in solution are discussed. Functionalized tripodal Schiff-base ligands are placed into context as an extension of previous research into tripodal ligands for use as metal-based anion-receptors and tripodal spin crossover complexes. The second section of Chapter 1 gives a brief introduction into single-molecule magnetism. An examination of mononuclear Co(II) complexes displaying slow magnetic relaxation and application of acetylide-bridged metal centers to enhance magnetic communication are also given.

In Chapter 2, I discuss the preparation and characterizations of a Fe(II) complex coordinated by the alcohol functionalized hexadentate tripodal iminopyridine L^{6-OH} with varying anions. Solid-state magnetic susceptibility measurements of $[FeL^{6-OH}]X_2$ ($X = OTf, Br^-, I^-,$ or BPh_4^-) reveal an anion-dependence on the magnetic behavior. Magnetostructural correlations indicate that stronger hydrogen-bonding interactions are achieved with larger anions, which are better able to undergo bifurcated interactions with the hydroxyl groups from two of the arms. Removal of the tether between the ligand arms leads to the formation of $[Fe(L^2)_2](OTf)_2$, a bis(tridentate) complex that remains high spin at all temperatures. Variable temperature magnetic measurements in d_3 -methanol reveal that the high spin state of $[FeL^{6-OH}]^{2+}$ persists regardless of the anion down to 183 K.

In Chapter 3, attempts towards synthesizing the heteroarmed tris(imine) $[FeL^{556}]^{2+}$ and analogous bis(imine)-mono(amine) $[FeL^{556-NH}]^{2+}$ complexes are discussed. Several routes are attempted to synthesize the tris-iminopyridine species including selective deprotonation of tris(2-aminoethyl)amine·3 HCl, *in situ* complex formation *via* metal-templated self-assembly, and use of presynthesized ligands. Analyses of the reaction mixtures by mass spectrometry suggest that mixtures of products are formed regardless of the method. An anion and solvent dependence leads to preferential formation of the low-spin species $[FeL^{5-ONHtBu}]^{2+}$, while using solvents such as acetonitrile and ethanol lead to increased production of the desired $[FeL^{556}]^{2+}$. To test if anion-dependent magnetic behavior can be observed with this ligand type, the comparable complex $[FeL^{556-NH}]^{2+}$ was synthesized and characterized. Variable temperature solution measurements in d_3 -acetonitrile suggest that host:guest interactions in solution induce a stabilization of the low-spin state for $[FeL^{556-NH}]^{2+}$ as indicated by a decrease in susceptibility at lower temperatures for the Cl^- salt.

In Chapter 4, the preparation, structural, and magnetic characterizations for a family of Fe(II) complexes of tripodal ligands based on $L^{5-ONHtBu}$ are presented. The series of ligands aim to tune the

ligand field by selectively reducing imines to amines, producing the ligands $L^{5-(NH)_x}$ ($x = 1 - 3$, number of amines). In the solid state, the three Fe(II) complexes formed are high spin, but significant differences in the structural distortion of both the coordination environment of the Fe(II) center as well as the anion-binding pocket of the amides are noted. In solution, the complexes $[FeL^{5-(NH)_3}]^{2+}$ and $[FeL^{5-NH}]^{2+}$ are high spin between 183 and 308 K in d_6 -acetone but interestingly, $[FeL^{5-(NH)_2}]^{2+}$ undergoes a spin-state change with decreasing temperature. Variable temperature studies in d_6 -acetone and anion titrations in d_3 -acetonitrile at room temperature monitored by Evans' method of $[FeL^{5-(NH)_2}]^{2+}$ show host:guest interactions stabilize the high spin state. These studies suggest a viable method of ligand tuning for spin-state control by host:guest interactions.

In Chapter 5, I discuss the structural and magnetic properties of $[Co^{5-ONHtBu}]X_2$ ($X = Cl^-$, Br^- , I^- , and ClO_4^-). These hexadentate Co(II) complexes vary only in the charge-balancing anion, but marked differences in their magnetic properties are observed. Investigation of the magnetic anisotropy of the various salts reveal that the chloride salt possesses the most axial anisotropy, which manifests as an exhibition of slow magnetic relaxation under application of an external field. To my knowledge this is the first example of anion-binding influencing the magnetic anisotropy and 'turning on' single-molecule magnet-like behavior.

Lastly, Chapter 6 describes the syntheses and magnetic properties of a series of mono- and dinuclear Fe(III) complexes bridged by ethynylmesitylene ligands. Inclusion of steric bulk onto the bridging-aryl ligand is predicted to increase orbital overlap between the singly-occupied molecular orbital of the metal center and the π -system of the aryl linker. The addition of methyl groups to the aryl ring cements the desired equatorial ligand orientation with respect to the π -system. This leads to an increase in ferromagnetic coupling between the metal centers.

ACKNOWLEDGMENTS

The first person I need to thank is my advisor, Prof. Matt Shores. I don't know where to begin to thank you. The last several years have been some of the hardest, yet some of the most fulfilling years of my life. You have pushed me harder than anyone ever has before. Without that though, I *never* would be where I am today. I know my stubbornness is not always my greatest asset, but I am incredibly thankful that you allowed me to pursue some of my wild ideas, which hopefully have enticed some interest from you. Additionally, my undergraduate advisor Cynthia Strong and physical chemistry professor Craig Teague. You *really* opened my eyes to how amazing and challenging research and chemistry can be. My first summer of research was probably one of the best experiences of my life which you both had a hand in. Without those experiences, none of this would have been possible.

To the past and present Shores group members, I owe you infinite thanks. Dr. Ashley McDaniel and Dr. Stephanie Fiedler-Gleich, with whom I spent most of my formative years in graduate school. You were invaluable to my development into the chemist I am today and I will forever be in your debt. To Doctors Wes Hoffert and Brian Newell: while our time together in the Shores lab was rather short, your advice and knowledge, especially for the last few years with crystallography, magnetism, or just commiserating has been incredibly helpful. Dr. Indrani Bhowmick has been a vital resource to my understanding of magnetism and it has been truly a pleasure to get to know you. Tarik Ozumerzifon and Robert Higgins: you two have made my last few years of graduate school interesting and very enjoyable. Your knowledge and passion for organic chemistry has actually excited interest and understanding in me, something I never thought possible. To Dr. David Boston, Michael Nguyen, and Romeo Portillo: while the overlap of our research has been rather limited, I hope the knowledge you have learned from me is at least

proportional to what I have learned from you. I wish you the best of luck in the future. And lastly, to all of the undergraduate students I have had the pleasure to work with: Ethan Hill, Andrew Stephen, David Daley, and Kelsey Schulte. It was a pleasure to work with you and I wish you the absolute best in all of your future endeavors.

Without my grandmother, Shirley Klug, none of this would have been possible. Since the first time I mentioned going to graduate school, she never let me forget the passion and excitement I had for chemistry and research. She pushed me further than I ever expected and I hope that I am making her proud. My parents, Chris and Nancy Klug, have always stood behind and supported me no matter what, and the last several years have been no exception. You never pushed me towards something I didn't want to do, but you never let me back down from what I have wanted. Your continued support of all of my endeavors has helped me through some dark days. Lastly, I would love to thank my boyfriend, Scott Menke. Without your patience and support, I would have never made it as far as I did. While 'the future freaks me out', I know that you'll always stand beside me and encourage me. There is no one else I want to be here with than you. I love you more than I can ever express and I am really excited to start our next adventure.

AUTOBIOGRAPHY

Christina Marie Klug was born on March 29th, 1985 in Cedar Rapids, IA to Chris and Nancy Klug. She attended John F. Kennedy High School in Cedar Rapids, IA, graduating in 2003. In the fall of 2003, she attended Cornell College in Mount Vernon, IA, earning B.A. degrees in Chemistry and Biochemistry and a minor in German in 2007. While at Cornell, she worked with Cynthia Strong investigating metal binding and activity of mutated forms of copper-zinc superoxide dismutase (CuZnSOD) that have been linked to genetic forms of ALS. After graduation, Christina began work at Integrated DNA Technologies Inc. in Coralville, IA as a raw materials quality control chemist. In 2009, she began her Ph.D. work at Colorado State University, studying inorganic chemistry under the direction of Prof. Matthew P. Shores. In her spare time, she enjoys gardening, playing with her dog Ferris, and drinking beer with her boyfriend Scott.

DEDICATION

I dedicate these works to the most important people in my life, my parents Chris and Nancy Klug and my *most* significant other Scott Menke. Without your emotional support and patience, none of this work would have been possible.

TABLE OF CONTENTS

ABSTRACT.....	ii
ACKNOWLEDGMENTS	v
AUTOBIOGRAPHY	vii
DEDICATION.....	viii
Chapter 1. Controlling magnetic properties via exploitation of anion binding and steric hindrance	1
1.1 Introduction.....	1
1.2 Spin-state control via anion-cation interactions	1
1.2.1 Spin crossover.....	1
1.2.2 Anion-dependent spin-state switching.....	3
1.2.3 Tripodal Schiff base ligands and spin crossover.	6
1.2.4 Podands for Anion Recognition.....	7
1.3 Single molecule magnetism	10
1.3.1 Slow magnetic relaxation.....	10
1.3.2 Mononuclear Co(II) species.....	12
1.3.3 Coupling metal centers through acetylide linkages.	15
1.4 Outline of Dissertation Chapters.	17
References.....	19
Chapter 2. Anion Dependence in the Spin-Crossover Properties of a Fe(II) Podand Complex...	24
2.1 Introduction.	24
2.2 Division of Labor	26
2.3 Experimental Details	26
2.3.1 General Considerations.....	26
Tris{4-[(6-methanol)-2-pyridyl]-3-aza-3-butenyl} amine (L^{6-OH}).	27
$[FeL^{6-OH}](CF_3SO_3)_2 \cdot 0.25 EtOH$ (2.1).....	27
$[FeL^{6-OH}]Br_2$ (2.2).	28
$[FeL^{6-OH}]Br_2 \cdot 0.5 MeOH$ (2.3).	28
$[FeL^{6-OH}]I_2$ (2.4).	28
$[FeL^{6-OH}](BPh_4)_2 \cdot 2 MeCN$ (2.5).	29

4-[(6-methanol)-2-pyridyl]-3-aza-3-butenyl (L^2).....	29
$[\text{Fe}(L^2)_2](\text{OTf})_2$ (2.6).....	30
2.3.2. Crystallographic data collection and refinement.....	30
2.3.3 Magnetic susceptibility measurements.....	31
2.3.4. Other physical measurements.....	31
2.4 Results and discussion.....	35
2.4.1 Syntheses.....	35
2.4.2 Anion dependence in solid state magnetic properties.....	36
2.4.3 Structural studies.....	39
2.4.4 Solution (magnetic) properties.....	52
2.5 Conclusions.....	56
2.6 Acknowledgments.....	57
References.....	58
Chapter 3. Efforts Toward synthesizing The Asymmetric tripodal complex $[\text{FeL}^{556}]^{2+}$	60
3.1 Introduction.....	60
3.2 Division of Labor.....	61
3.3 Experimental Section.....	62
3.3.1 General Considerations.....	62
Synthesis of $[\text{FeL}^{556}]$ via Selective Deprotonation.....	62
Nominal synthesis of <i>N,N</i> -Bis[2-(5- <i>tert</i> -butylamide-2-pyridyl)-3-aza-butenyl]- <i>N</i> -[2-(6-methyl-2-pyridyl)-3-aza-3-butenyl]amine (L^{556}).....	62
General Reaction Procedure of $[\text{FeL}^{556}]^{2+}$ Using Presynthesized Ligand.....	63
General Reaction Procedure for <i>In Situ</i> Self-Assembly.....	63
<i>N,N</i> -bis[(2-aminoethyl)- <i>N</i> -(6-methylpyridyl)methylamino)ethyl]amine (tren(6-Me)(NH_2) ₂).....	64
$[\text{Fe}(\text{tren}(6\text{-Me})(\text{NH}_2)_2)\text{Cl}]\text{Cl}$ (3.1).....	64
<i>N,N</i> -bis[(5- <i>tert</i> -butylamide-pyridyl)-3-aza-3-butenyl]- <i>N</i> -(6-methyl-2-pyridyl)methylamino)ethyl]amine ($L^{556\text{-NH}}$).....	65
$[\text{FeL}^{556\text{-NH}}]\text{Cl}_2$ (Route 1) (3.2).....	65
$[\text{FeL}^{556\text{-NH}}]\text{Cl}_2$ (Route 2).....	65
$[\text{FeL}^{556\text{-NH}}](\text{BF}_4)_2$ (3.3).....	66
3.3.2 Mass spectral analysis.....	66

3.3.3 X-ray Structural Determination.	67
3.3.4 Other Physical Measurements.	67
3.4 Results and Discussion.....	69
3.4.1 Syntheses via Self-assembly.....	69
3.4.2 Anion Dependence.....	72
3.4.3 Solvent Dependence.....	74
3.4.4 Production Distribution Dependence on Stoichiometry and Order of Addition.	74
3.4.5 Synthesis of $[\text{FeL}^{556\text{-NH}}]^{2+}$	76
3.5 Conclusions and Future Work.....	81
3.6 Acknowledgments.....	82
References.....	83
Chapter 4. Effect of imine reduction on the spin state properties of Fe(II) complexes using amide-functionalized tripodal pyridine-based ligands.....	84
4.1 Introduction.	84
4.2 Division of Labor.	85
4.3 Experimental Section	85
4.3.1 General considerations.....	85
Tris{4-[(5- <i>tert</i> -butylamide-2-pyridyl)-3-amino-3-butenyl]amine ($\text{L}^{5(\text{NH})_3}$).	86
<i>N,N</i> -bis[2-(5- <i>tert</i> -butylamidepyridine-methylamino)ethyl]- <i>N</i> -[2-aminoethyl]amine (di-5- <i>tert</i> -butylamide-tren).	86
<i>N,N</i> -bis[2-(5- <i>tert</i> -butylamidepyridine-methylamino)ethyl]- <i>N</i> -[2-(5- <i>tert</i> -butylamidepyridine)-3-aza-3-butyenyl]amine ($\text{L}^{5\text{-(NH)}_2}$).	87
<i>N,N</i> -bis[2-(4-nitro(phenylsulfonamido))ethyl]- <i>N</i> -[2-(<i>tert</i> -butylcarbamoylethyl)ethyl]amine (dinosyl-monoBoc-tren).	87
<i>N,N</i> -bis[2-(4-nitro(phenylsulfonamido))ethyl]- <i>N</i> -[2-(amino)ethyl]amine (dinosyl-tren).	88
<i>N,N</i> -bis[2-(4-nitro(phenylsulfonamido))ethyl]- <i>N</i> -[2-(5- <i>tert</i> -butylamidepyridine-methylamino)ethyl]amine (dinosyl-5- <i>tert</i> -butylamide-tren).	88
<i>N,N</i> -bis[2-(amino)ethyl]- <i>N</i> -[2-(5- <i>tert</i> -butylamidepyridine-methylamino)ethyl]amine (5- <i>tert</i> -butylamide-tren) (Route 1).	89
<i>N,N</i> -bis[2-(<i>tert</i> -butylcarbamoylethyl)- <i>N</i> -[2-(5- <i>tert</i> -butylamidepyridine-methylamino)ethyl]amine (5- <i>tert</i> -butylamide-diboc-tren).	90

<i>N,N</i> -bis[2-(amino)ethyl]- <i>N</i> -[2-(5- <i>tert</i> -butylamidepyridine-methylamino)ethyl]amine (5- <i>tert</i> -butylamide-tren) (Route 2).....	90
<i>N,N</i> -bis[2-(5- <i>tert</i> -butylamidepyridine)-3-aza-3-butyenyl]- <i>N</i> -[2-(5- <i>tert</i> -butylamidepyridine-methylamino)ethyl]amine (L ^{5-NH}).....	90
[FeL ^{5-(NH)} ₃](BF ₄) ₂ (4.1).....	91
[FeL ^{5-(NH)} ₂](BF ₄) ₂ (4.2).....	91
[FeL ^{5-NH}](BF ₄) ₂ (4.3).....	92
[FeL ^{5-NH}](BPh ₄) ₂ ·3 MeCN (4.4).....	92
4.3.2 X-ray Structure Determination.....	92
4.3.3 Magnetic Measurements.....	93
4.3.4 Other Physical Methods.....	94
4.4 Results and Discussion.....	96
4.4.1 Synthesis and Characterization.....	96
4.4.2 X-ray Structural Analyses.....	103
4.4.3 Magnetic Properties.....	109
4.4.4 Anion-dependent Spin-state Behavior.....	110
4.5 Conclusions and Future Work.....	115
4.6 Acknowledgments.....	116
References.....	117
Chapter 5. Tuning the Magnetic Relaxation via Out-of-sphere Hydrogen-bonding Interactions in Co(II) Tripodal Iminopyridine Complexes.....	118
5.1 Introduction.....	118
5.2 Division of Labor.....	119
5.3 Experimental Section.....	119
5.3.1 General Considerations.....	119
[CoL ^{5-ONH^tBu}]Cl ₂ (5.1).....	119
[CoL ^{5-ONH^tBu}]Br ₂ (5.2).....	120
[CoL ^{5-ONH^tBu}]I ₂ (5.3).....	120
[CoL ^{5-ONH^tBu}](ClO ₄) ₂ (5.4).....	121
5.3.2 Magnetic Measurements.....	121
5.3.3 X-ray Structure Determinations.....	122

5.3.4 Other Physical Methods.....	123
5.4 Results.....	125
5.4.1 Synthesis and Characterization.....	125
5.4.2 X-ray Structural Analyses.....	129
5.4.3 Magnetic Susceptibility Measurements.....	133
5.4.4 Dynamic Magnetic Properties.....	140
5.6 Discussion.....	142
5.7. Conclusions and Future Work.....	146
5.8 Acknowledgements.....	147
References.....	148
Chapter 6: Mesitylene-based molecules towards topological control of Fe(III)-alkynyl complexes.....	151
6.1 Introduction.....	151
6.2 Division of Labor.....	153
6.3 Experimental Section.....	153
6.3.1 Preparation of Compounds.....	153
[(dmpe) ₂ FeCl(CCTMS)](OTf) (6.1).....	153
[(dmpe) ₂ FeCl(MEM)] (6.2).....	154
[(dmpe) ₂ FeCl(MEM)](OTf) (6.3).....	154
[(dmpe) _{2x} Fe _x Cl _x (μ - <i>m</i> -H _{3-x} TEM)] (X = 1, 2) (6.4).....	155
[(dmpe) _{2x} Fe _x Cl _x (μ - <i>m</i> -H _{3-x} TEM)](OTf) _x (X = 1, 2) (6.5).....	155
[(dmpe) ₄ Fe ₂ Cl ₂ (μ ₂ - <i>m</i> -DEM)] (6.6).....	156
[(dmpe) ₄ Fe ₂ Cl ₂ (μ ₂ - <i>m</i> -DEM)](OTf) ₂ (6.7).....	156
6.3.2 X-Ray Structure Determinations.....	157
6.3.3 Magnetic Susceptibility Measurements.....	158
6.3.4 Other Physical Measurements.....	159
6.4 Results and Discussion.....	161
6.4.1 Syntheses and Characterizations.....	161
6.4.2 X-ray Structures.....	166
6.4.3 Magnetic Properties.....	171
6.5.3 Fitting of Magnetic Data.....	176

6.6 Conclusions.....	183
6.7 Acknowledgements.....	183
References.....	184
Appendix 1. Supporting Information for Chapter 2.....	186
$[\text{FeL}^{6\text{-OH}}](\text{BPh}_4)_{1.75}\text{Br}_{0.25}\cdot\text{MeCN}$ (A.1.1).....	187
Appendix 2. Supporting Information for Chapter 3.....	196
Appendix 3. Supporting Information for Chapter 4.....	199
Appendix 4. Supporting Information for Chapter 5.....	206
A.4.1 Preparation of Compounds.....	206
(<i>E</i>)- <i>N</i> -(<i>tert</i> -butyl)-6-((ethylimino)methyl)nicotinamide ($\text{L}^{\text{ethyl-5-OH}t\text{Bu}}$).....	206
$[\text{Co}(\text{L}^{\text{ethyl-5-OH}t\text{Bu}})_3]\text{Cl}_2$ (A.4.1).....	206
$[\text{Co}(\text{L}^{\text{ethyl-5-OH}t\text{Bu}})_3](\text{ClO}_4)_2$ (A.4.2).....	207
References.....	209
Appendix 5. Notebook cross-references and crystal structure data sets for relevant compounds. Notebook IDs from notebooks belonging to Kelsey Schulte (KAS) and Christina Klug (CMK).	210

LIST OF TABLES

Table 2.1. Crystallographic data for 2.1–2.6	33
Table 2.2. Selected bond distances (Å) and distortion parameters (°).....	43
Table 2.3. Shortest intermolecular hydrogen-bond interactions.....	44
Table 3.1. Crystallographic data for compound 3.1	68
Table 3.2. Relative percentages of the sum of 1+ and 2+ species of complexes observed in mass spectra obtained on reaction mixtures.....	74
Table 3.2. Percentages of the sum of 1+ and 2+ species of complexes observed in mass spectra obtained of reaction mixtures in various solvents.....	75
Table 4.1. Crystallographic data for compounds [FeL ^{5-(NH)3}](BF ₄) ₂ (4.1), [FeL ^{5-(NH)2}](BF ₄) ₂ (4.2), and [FeL ^{5-NH}](BPh ₄) ₂ ·3 MeCN (4.4)	95
Table 4.2. Selected bond lengths and angles for 4.1, 4.2, 4.4 , and [FeL ^{5-ONHtBu}] ²⁺	105
Table 5.1. Crystallographic and structural refinement data for [CoL ^{5-ONHtBu}] ₂ Cl ₂ (5.1), [CoL ^{5-ONHtBu}] ₂ Br ₂ (5.2), [CoL ^{5-ONHtBu}] ₂ I ₂ (5.3), [CoL ^{5-ONHtBu}] ₂ (ClO ₄) ₂ (5.4).	124
Table 5.2. Selected bond lengths and angles for 5.1–5.4	131
Table 5.3. Comparison of <i>D</i> and <i> E /D</i> parameters obtained from fitting of susceptibility data using julX and magnetization data using ANISOFIT 2.0.	137
Table 5.4. Attempted fits using ANISOFIT 2.0 for 5.1	139
Table 5.5. Attempted fits using ANISOFIT 2.0 for 5.2	139
Table 5.6. Attempted fits using ANISOFIT 2.0 for 5.3	139
Table 5.7. Attempted fits using ANISOFIT 2.0 for 5.4	139
Table 6.1. Crystallographic data for compounds [(dmpe) ₂ FeCl(CCTMS)](OTf) (6.1), [(dmpe) ₂ FeCl(MEM)](OTf) (6.3), and [(dmpe) ₄ Fe ₂ Cl ₂ (μ ₂ - <i>m</i> -DEM)](OTf) ₂ (6.7·1.5 MeOH)	160
Table 6.2. Comparison of structural components of [(dmpe) ₂ FeCl(MEM)](OTf) (6.3), [(dmpe) ₂ FeCl(CCPh)](OTf), [(dmpe) ₄ Fe ₂ Cl ₂ (μ ₂ - <i>m</i> -DEM)](OTf) ₂ (6.7) and [(dmpe) ₄ Fe ₂ Cl ₂ (μ ₂ - <i>m</i> -DEB)](BAr ^F) ₂	170
Table 6.3. Attempted fitting scenarios for 6.7 . “TW temp” is a mean-field correction for weak intermolecular magnetic exchange. “ <i>f</i> _{sum} ” value is the sum of the point-by-point squared errors.	179
Table A.4.1. Crystallographic data for [Co(L ^{ethyl-5-ONHtBu}) ₃](ClO ₄) ₂ (A.4.2)	208

LIST OF FIGURES

Figure 1.1. Spin-state dependent electronic configurations for a high spin and low spin Fe(II) center in an octahedral ligand field.....	2
Figure 1.2. Left: Solid-state variable temperature magnetic susceptibility for [Fe(H ₂ bip) ₃](BPh ₄) ₂ and [Fe(H ₂ bip) ₃]Br ₂ . Left inset: Variable temperature solution magnetic susceptibility in CD ₂ Cl ₂ . Right: Crystal structure of the cation of [Fe(H ₂ bip) ₃] ²⁺	5
Figure 1.3. Assorted tripodal Schiff base ligands.....	8
Figure 1.5. Schematic representing the magnetization and relaxation processes of a single-molecule magnet.....	11
Figure 1.6. Left: In-phase (χ') and out-of-phase (χ'') of the ac magnetic susceptibility for ((Me ₃ Si) ₂ N) ₂ (THF)Tb) ₂ (μ - η^2 : η^2 -N ₂) ⁻ under zero applied dc field. Top, right: Magnetization (M) versus dc magnetic field (H) from 11 to 15 K at a sweep rate of 0.9 mT/s. Bottom, right: Crystal structure of ((Me ₃ Si) ₂ N) ₂ (THF)Tb) ₂ (μ - η^2 : η^2 -N ₂) ⁻	12
Figure 1.7. Cobalt(II) complexes that display slow magnetic relaxation.....	14
Figure 2.1. Depiction of the complex cation [FeL ^{6-OH}] ²⁺	26
Figure 2.2. Temperature dependence of $\chi_M T$ for 2.1–2.5	37
Figure 2.3. Temperature dependence of $\chi_M T$ for 2.2 and 2.3	38
Figure 2.4. Crystal structure of 2.1·RT at 296 K and 2.1·LT at 120 K.....	40
Figure 2.5. Crystal structure of 2.2 at 120 K.....	41
Figure 2.6. Crystal structure of 2.3 at 120 K.....	41
Figure 2.7. Crystal structure of 2.4·RT at 296 K and 2.4·LT at 120 K.....	42
Figure 2.8. Crystal structure of 2.5 at 120 K.....	42
Figure 2.9. Crystal structure of 2.6 at 120 K.....	43
Figure 2.10. Overlay of room temperature and low temperature structures for the cations in 2.1 and 2.4	44
Figure 2.11. Packing plot of 2.2 down the a axis.....	47
Figure 2.12. Packing plot of 2.2 down the b axis.....	48
Figure 2.13. Packing plot of 2.3 down the b axis.....	48
Figure 2.14. Intermolecular interactions for the structures of compound 2.4·LT	49
Figure 2.15. Anion-cation interactions of 2.1·RT	49
Figure 2.16. Anion-cation and cation-cation interactions of 2.1·LT	50

Figure 2.17. Intermolecular interactions of 2.5	50
Figure 2.18. Comparison of key intermolecular interactions in 2.1·RT and 2.1·LT	51
Figure 2.19. Cation-anion interactions for 2.6	52
Figure 2.20. ¹ H NMR spectra obtained at 295 K of 2.2 at t=10 min., t=24 hr, and t=3 days.....	54
Figure 2.21. ¹ H NMR spectra of 2.1 at 295 K and 213 K.....	55
Figures 2.22. Variable temperature solution magnetic susceptibility of 2.1 , 2.2 , 2.4 , and 2.6	55
Figure 3.1. Depiction of the complex cation [FeL ⁵⁵⁶] ²⁺ highlighting the desired hydrogen bonding interactions and steric tuning	61
Figure 3.2. ESI-MS of [FeL ⁵⁵⁶](PF ₆) ₂ in positive mode.	73
Figure 3.3. X-ray crystal structure of the cationic complex in compound 3.1	78
Figure 3.4. Qualitative UV-visible spectral comparison of 3.2 and 3.3 in acetonitrile between 325 and 800 nm.....	80
Figure 3.5. Variable temperature solution magnetic susceptibility measurement of 3.2 and 3.3 in <i>d</i> ₃ -acetonitrile.....	81
Figure 4.2. Electronic absorption spectra of 4.1 , 4.2 , 4.4 , and [FeL ^{5-OH<i>t</i>Bu}](BF ₄) ₂ collected in acetonitrile from 230 to 800 nm. Inset: Visible range from 330 to 800 nm.	99
Figure 4.3. Paramagnetic ¹ H NMR spectra of 4.1 , 4.2 , and 4.4 at 298 K.....	100
Figure 4.4a. FT-IR comparison of complexes 4.1 , 4.2 , 4.4 and [FeL ^{5-OH<i>t</i>Bu}](BF ₄) ₂	101
Figure 4.4b. FT-IR comparison of complexes 4.1 , 4.2 , 4.4 and [FeL ^{5-OH<i>t</i>Bu}](BF ₄) ₂ from 1750 to 1250 cm ⁻¹	102
Figure 4.5. X-ray crystal structures of the complex cations of 4.1 , 4.2 , and 4.4	104
Figure 4.6. Cation-anion interactions for 4.1	106
Figure 4.7. Cation-anion interactions for 4.2	106
Figure 4.8. Cation-anion interactions for 4.4	107
Figure 4.9. Trigonal pocket distortions as defined by 6'-position carbon atoms for 4.1 , 4.2 , 4.4 , and {[FeL ^{5-OH<i>t</i>Bu}]-Cl} ⁺	108
Figure 4.10. Solid-state magnetic susceptibility measurements of 4.1 , 4.2 , and 4.4	111
Figure 4.11. Solution variable temperature magnetic susceptibility for 4.1 , 4.2 , and 4.4 between 308 and 183 K in <i>d</i> ₆ -acetone.....	111
Figure 4.12. Changes in the solution room temperature χ_{MT} values upon addition of Bu ₄ NCl to 4.2 and 4.4 in CD ₃ CN	113
Figure 4.13. Proposed anion binding for 4.2 in the presence of a strongly interacting anion (X)	113

Figure 4.14 Variable temperature solution magnetic susceptibility measurements of 4.1 and plus one equivalent of Bu ₄ NCl collected between 294 and 232 K in CD ₃ CN.	114
Figure 4.15. Variable temperature solution magnetic susceptibility measurements of 4.2 and plus two equivalents of Bu ₄ NCl collected between 308 and 183 K in <i>d</i> ₆ -acetone.	114
Figure 5.1. Paramagnetic NMR spectra of 5.1 , 5.2 , 5.3 , and 5.4 obtained in CD ₃ CN at 294 K	126
Figure 5.2. FT-IR comparison of complexes 5.1–5.4	127
Figure 5.2b. FT-IR comparison of complexes 5.1–5.4 from 1740 cm ⁻¹ to 650 cm ⁻¹	128
Figure 5.3. X-ray crystal structures of 5.1 , 5.2 , 5.3 , and 5.4	130
Figure 5.4. Comparison of the iminopyridine bond lengths (Å) for 5.1–5.4	133
Figure 5.5. Packing plot of 5.1 down <i>c</i> axis.....	134
Figure 5.6. Packing plot of 5.4 down <i>c</i> axis.....	134
Figure 5.7. Intermolecular interactions for the structure of complex 5.4	135
Figure 5.8. Variable temperature magnetic susceptibility measurements of 5.1–5.4	136
Figure 5.9. M vs H/T curves for 5.1 , 5.2 , 5.3 , and 5.4	138
Figure 5.10. Variable-field in-phase and out-of-phase susceptibility data for 5.1 , 5.2 , 5.3 , and 5.4	141
Figure 5.11. Frequency vs. field plot for 5.1	142
Figure 5.12. Dependence of temperature on the in-phase and out-of-phase susceptibility for complex 5.1 at various temperatures	143
Figure 5.13. Temperature dependence on the in-phase and out-of-phase magnetic susceptibility of 5.1 at various frequencies	143
Figure 5.14. Arrhenius plot of 5.1 constructed from data collected under a dc field of 2500 Oe	144
Figure 5.15. Depictions of [(tpa ^R)Fe] ⁻ and [Co(Me ₆ tren)X] ⁺	145
Figure 6.1. ¹ H NMR of 6.2 in C ₆ D ₆	164
Figure 6.2. ¹ H NMR of 6.4 in C ₆ D ₆	164
Figure 6.2. ¹ H NMR of 6.7 in CD ₂ Cl ₂	165
Figure 6.3. Cyclic voltammograms of 6.2 and 6.3 in 0.1 M (Bu ₄ N)PF ₆ in CH ₂ Cl ₂ at a scan rate of 100 mV/s.....	165
Figure 6.4. Cyclic voltammograms of 6.6 and 6.7 in 0.1 M (Bu ₄ N)PF ₆ in CH ₂ Cl ₂ at a scan rate of 100 mV/s.....	166
Figure 6.5. X-ray crystal structures of the complex cations of 6.1 , 6.3 , and 6.7	168

Figure 6.6. Packing diagrams for 6.7 viewed down the <i>c</i> axis and <i>b</i> axis.....	169
Figure 6.7. X-ray structure of the complex cation of 6.7 viewed down the Cl–Fe2–C axis and down the Cl–Fe1–C axis.....	170
Figure 6.8. Temperature dependent magnetic susceptibility data for 6.1 collected at 5000 Oe. Inset: Magnetization data for 6.1 collected at 100 K.....	172
Figures 6.9. Temperature dependent magnetic susceptibility data for 6.3 collected at 5000 Oe. Inset: Magnetization data for 6.3 collected at 100 K.....	173
Figure 6.10. Temperature dependent magnetic susceptibility data for 6.7 collected at 1000 Oe. Inset: Magnetization data for 6.7 collected at 100 K.....	173
Figure 6.11. X-band EPR spectrum of 6.1 in a dichloromethane:dichloroethane glass at 100 K.....	174
Figure 6.12. X-band EPR spectrum of 6.3 in a dichloromethane:dichloroethane glass at 100 K.....	175
Figure 6.13. X-band EPR spectrum of 6.7 in a dichloromethane:dichloroethane glass at 100 K.....	175
Figure 6.14. X-band EPR spectrum of [(dmpe) ₆ Fe ₃ Cl ₃ (μ ₃ -TEM)](OTf) ₃ in a dichloromethane:dichloroethane glass at 100 K.....	176
Figure 6.15. Raw and TIP-corrected magnetic susceptibility data for 6.1	177
Figure 6.16. Raw and TIP-corrected magnetic susceptibility data for 6.3	177
Figure 6.17. Raw and TIP-corrected magnetic susceptibility data for 6.7 with best fit from <i>J</i> model (model 1).....	180
Figure 6.18. Raw and subtracted magnetic susceptibility data for 6.7 with best fit from <i>J</i> model (model 2).....	180
Figure 6.19. Weiss plot of 6.7	181
Figure 6.20. Magnetization versus reduced field data for 6.7	182
Figure 6.21. Magnetization versus reduced field data for [(dmpe) ₆ Fe ₃ Cl ₃ (μ ₃ -TEM)](OTf) ₃	182
Figure A.1.1. ¹ H NMR spectrum of L^{6-OH} in CD ₃ OD.....	186
Figure A.1.2. ¹³ C NMR spectrum of L^{6-OH} in CD ₃ OD.....	186
Figure A.1.3. FT-IR spectrum of L^{6-OH}	187
Figure A.1.4. Temperature dependence of χ _M T for A.1.1	188
Figure A.1.5. ¹ H NMR spectrum of L² in CDCl ₃	189
Figure A.1.6. ¹³ C NMR spectrum of L² in CDCl ₃	189
Figure A.1.7. FT-IR spectrum of L²	190

Figure A.1.8. ^1H NMR spectra obtained at 295 K of 2.6 in CD_3OD at $t=10$ min., $t=1$ day, and $t=3$ days.	191
Figure A.1.9. ^1H NMR spectra of 2.2 before and after addition of 3 equivalents of 2,2'-bipyridine	192
Figure A.1.10. ^1H NMR spectra of 2.2 before and after addition of 3 equivalents of 2,2'-bipyridine	192
Figure A.1.12. ^1H NMR spectra of 2.6 before and after addition of 3 equivalents of 2,2'-bipyridine	194
Figure A.1.13. ^1H NMR spectra of 2.6 at 298 K and 193 K.....	195
Figure A.2.1. ^1H NMR spectrum of L⁵⁵⁶ in CD_3OD . Inset: Zoomed in on aromatic region.	196
Figure A.2.2. ^1H NMR spectrum of tren(6-Mepy)(NH₂)₂ in CD_3OD	196
Figure A.2.3. ^{13}C NMR spectrum of tren(6-Mepy)(NH₂)₂ in CD_3OD	197
Figure A.2.4. FT-IR spectrum of 3.1	197
Figure A.2.5. ^1H NMR spectrum of L^{556-NH} in CD_3CN	198
Figure A.3.2. ^{13}C NMR spectrum of L^{5-(NH)₃} obtained in CDCl_3	200
Figure A.3.3. ^1H NMR spectrum of di-5-tert-butylamide-tren obtained in CDCl_3	200
Figure A.3.4. ^{13}C NMR spectrum of di-5-tert-butylamide-tren obtained in CDCl_3	201
Figure A.3.5. ^1H NMR spectrum of L^{5-(NH)₂} obtained in CD_3CN . Inset: Zoomed in on the aromatic region.	201
Figure A.3.6. ^1H NMR spectrum of dinosyl-monoboc-tren obtained in d_6 -DMSO	202
Figure A.3.7. ^{13}C NMR spectrum of dinosyl-monoboc-tren obtained in d_6 -DMSO.	202
Figure A.3.8. ^1H NMR spectrum of dinosyl-5-tert-butylamide-tren obtained in CDCl_3	203
Figure A.3.9. ^{13}C NMR spectrum of dinosyl-5-tert-butylamide-tren obtained in CDCl_3	203
Figure A.3.10. ^1H NMR spectrum of 5-tert-butylamide-tren obtained in CDCl_3	204
Figure A.3.11. ^1H NMR spectrum of L^{5-NH} obtained in CD_3CN	204
Figure A.4.1. X-ray crystal structure of A.4.2	208

LIST OF SCHEMES

Scheme 1.1. (a) Tripodal ligands of interest highlighting metal-binding (red) and host:guest interactions (blue). (b) Idealized spin state and binding behavior for $[\text{FeL}^{5\text{-ONHtBu}}]^{2+}$ (top) and $[\text{FeL}^{6\text{-OH}}]^{2+}$ (bottom).	9
Scheme 2.1. Reaction sequence for preparing $[\text{FeL}^{6\text{-OH}}]^{2+}$ and $[\text{Fe}(\text{L}^2)_2]^{2+}$ complex salts.	36
Scheme 3.1. Synthetic scheme employed for synthesis of $[\text{FeL}^{660}]^{2+}$ (top) and potential products formed from reactions of tren, 2-pyridinecarboxaldehyde, 6-methyl-2-pyridinecarboxaldehyde, and Fe(II) (bottom).	71
Scheme 3.2. General reaction scheme and potential products isolated with expected distribution based on stoichiometry.	73
Scheme 3.3. Reaction schemes controlling (a) order of addition and (b) stoichiometry by addition of excess 6-methyl-2-pyridinecarboxaldehyde.	76
Scheme 3.4. Reaction scheme employed for the syntheses of tren(6-Me)(NH₂)₂ , L^{556-NH} , 3.1 , 3.2 (Route 1 and 2), and 3.3	78
Scheme 3.5. Proposed binding modes possible for $[\text{FeL}^{556\text{-NH}}]^{2+}$	80
Scheme 4.1. Synthetic scheme employed for the syntheses of L^{5-(NH)₃} and L^{5-(NH)₂}	97
Scheme 4.2. Synthetic scheme employed for the synthesis of L^{5-NH}	98
Scheme 6.1. Syntheses of complexes 6.1–6.7	163

CHAPTER 1. CONTROLLING MAGNETIC PROPERTIES VIA EXPLOITATION OF ANION BINDING AND STERIC HINDRANCE

1.1 Introduction

The intent of this chapter is to offer a brief introduction into the background and motivation of the works presented in this dissertation in the realm of spin crossover and single-molecule magnetism. The first section of this chapter will be focused on spin crossover and how hydrogen bonding and anion–cation interactions can be exploited to alter the magnetic behavior of first-row transition metals. The second section will give a brief introduction into single-molecule magnetism. An examination of Co(II) complexes displaying slow magnetic relaxation and application of acetylide-bridged metal centers to enhance magnetic communication will be given. Lastly, an outline of the work presented in this dissertation.

1.2 Spin-state control via anion-cation interactions

1.2.1 Spin crossover. Spin crossover (SCO) or spin state switching is a phenomenon that is possible for first-row transition metals with $d^4 - d^7$ electrons in response to an external perturbation of the system. Initially, this was first observed in an Fe(III) complex of dithiocarbamate in 1931,¹ but is mostly commonly studied in complexes of Fe(II). During the spin crossover event, there is a change in the spin multiplicity of the metal center, going from a state that maximizes the spin multiplicity, which is the high spin (HS) state, to a state that minimizes the spin multiplicity, or the low spin (LS) state. This is usually observed with changing temperature, but examples implementing light²⁻⁴ and pressure^{5,6} are also common. While this is mostly frequently studied and detected in octahedral Fe(II) complexes, there are abundant examples of Cr(II),⁷ Mn(III),⁸⁻¹⁰ Fe(III),¹¹ Co(II),^{12,13} Co(III),^{14,15} and Ni(II)^{16,17} complexes that undergo spin state changes in response to external stimuli.

Specifically, for octahedral complexes of Fe(II), a d^6 ion, the spin-state change involves a transformation from a paramagnetic $S = 2$ species in the HS state to a diamagnetic $S = 0$ species in the LS state. In such cases, a delicate balance between the spin pairing energy (Π) and the ligand field splitting (Δ_o) (Figure 1.1) is required. If the spin pairing energy is greater than the ligand field splitting, the species will obey Hund's rule and be HS. Inversely, if the ligand field splitting is greater than the spin pairing energy, the electrons will pair up to fill the t_{2g} orbitals and the species will be LS. In order for spin crossover to occur, the difference in energy between the two spin states must be thermally accessible ($\Delta E \approx k_B T$).¹⁸ To observe SCO in Fe(II) complexes, the ligand field splitting should range from 11,200–12,400 cm^{-1} for the corresponding Ni(II) complexes, which act as model of the HS state.¹⁹

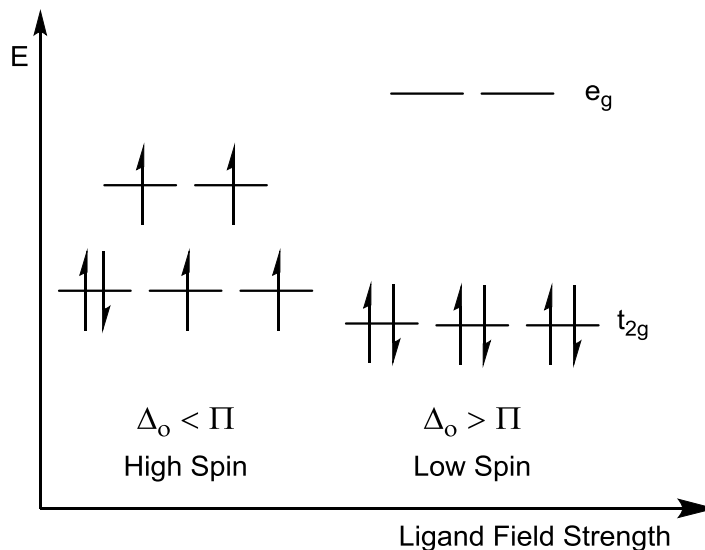


Figure 1.1. Spin-state dependent electronic configurations for a high spin (left) and low spin (right) Fe(II) center in an octahedral ligand field.

Manifestations of a spin state change include: (a) change in magnetic susceptibility (χ_{MT}), (b) color change, (c) changes in IR and/or Raman spectra, and (d) changes in metal-to-ligand bond lengths. Changes in magnetic susceptibility can be measured in solution or in the solid state. Most commonly, solution measurements are performed using Evans' method via ^1H NMR

spectroscopy.²⁰⁻²² This allows for binary monitoring of the spin-state change by narrowing of the ¹H NMR spectral window as the LS state becomes populated and peak differences between a reference solvent in the sample and an internal standard. This peak separation between the standard and the solution containing the paramagnetic species is proportional to the magnetic susceptibility of the solution. In the solid state, the change in the magnetic susceptibility is most commonly monitored by SQUID magnetometry, but Mössbauer spectroscopy and calorimetry are also used.²³ By altering the temperature of the sample and measuring the magnetic moment at the given temperature, the transition type (complete, incomplete, gradual, abrupt, bistable) and the spin crossover temperature ($T_{1/2}$ = temperature at which 50:50 mixture of HS:LS components) can be determined. The colorimetric change that occurs due to changes in the electronic transitions undertaken by the complex after the spin-state change is the most visually obvious. This behavior makes the complexes potentially useful for sensing temperature, pressure, or anions (*vida infra*). With the spin-state change, additional changes in the metal-to-ligand bond lengths and vibrational spectra are observed. As electrons move from the antibonding e_g orbitals to the nonbonding t_{2g} subset, shortening of the metal-ligand bond lengths occur, which also manifests in the vibrational transitions of the ligand. These changes are monitored by X-ray techniques such as single-crystal or powder diffraction and by vibrational spectroscopies such as IR or Raman.

1.2.2 Anion-dependent spin-state switching. One method to modulate the spin crossover temperature and behavior is by varying the outer-sphere charge-balancing anions or cocrystallizing solvent. The energy of hydrogen bonding (3–15 kcal/mol) as well as other non-covalent interactions are sufficient to perturb if not completely alter the spin state as the energy required for the HS–LS transition (6.3–8.3 kcal/mol) is within the regime of the energies of these interactions.²⁴

Recent examples have actively sought to exploit the influence non-covalent interactions have on the spin-state properties of first-row transition metals.²⁵⁻²⁸ These complexes incorporate functional groups that are able to undergo hydrogen-bonding interactions with anions or solvent to manipulate the spin crossover temperature or even expose or quench the behavior. One such example from Tuchagues is $[\text{Fe}(\text{trim})]\text{X}_2 \cdot \text{Y MeOH}$ (trim = 4-(4-imidazolylmethyl)-2-(2-imidazolylmethyl)imidazole; X = F⁻, Cl⁻, Br⁻, I⁻; Y = 0 or 1).²⁹ Secondary amines in the ligand allow for non-covalent, hydrogen-bonding interactions to occur with the hope of modulating the SCO temperature of the Fe(II) center. The $\chi_{\text{M}}T$ versus T plot for the four salts shows the magnetic behavior of the cation is dependent on the charge-balancing anion and the solvation; the F⁻ salt remains HS at all temperatures and SCO is observed for the Cl⁻, Br⁻, and I⁻ salts with increasing spin crossover temperatures ($T_{1/2}$) as the anion size increases. Nitschke and coworkers have synthesized a tetranuclear Fe(II) capsule through subcomponent self-assembly.³⁰ This cage-like structure possess a cavity able to accommodate guest molecules. Variable-temperature magnetic susceptibility measurements in solution and the solid state indicate the parent OTf⁻ salt undergoes spin crossover. Additionally, they studied the influence of encapsulating guests into the cage in CD₃NO₂, which depending on the size of the guest, the spin crossover temperature in solution was affected.

Previous work in our group has attempted to couple spin-state switching and anion sensing. Much of this work has focused on using the ditopic bidentate ligand H₂bip (H₂bip = 2,2'-bi-1,4,5,6-tetrahydropyrimidine). The formation of a homoleptic complex with Fe(II) forms $[\text{Fe}(\text{H}_2\text{bip})_3]\text{X}_2$ (X = Br⁻ or BPh₄⁻).³¹ Solid-state magnetic susceptibility measurements of either salt display marked differences in the spin-state behavior depending on the counter anion used: the BPh₄⁻ salt remains HS at all temperatures, while the Br⁻ salt is low spin at all temperatures. In solution, as

monitored by Evans' method in d_2 -dichloromethane, both species undergo a temperature-dependent spin transition. Like the solid state data, the HS state of the Fe(II) center is stabilized when BPh_4^- is the anion and undergoes a spin transition at lower temperature compared to the Br^- salt. The difference in these behaviors is attributed to the interaction that occurs between the amines of the ligand and the bromide in solution which is not possible when the weakly interacting BPh_4^- anion is used as the counter ion.

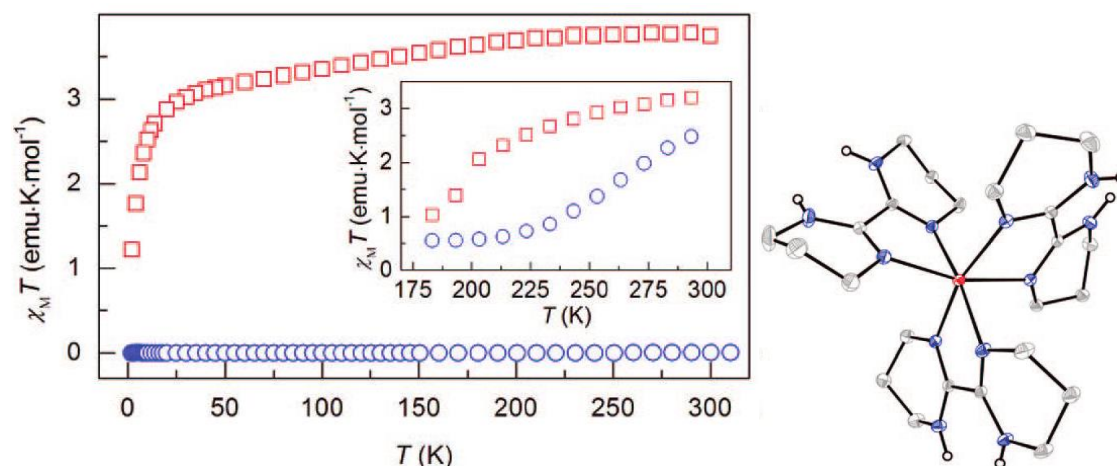


Figure 1.2. Left: Solid-state variable temperature magnetic susceptibility for $[\text{Fe}(\text{H}_2\text{bip})_3](\text{BPh}_4)_2$ (red squares) and $[\text{Fe}(\text{H}_2\text{bip})_3]\text{Br}_2$ (blue circles). Left inset: Variable temperature solution magnetic susceptibility in CD_2Cl_2 . Right: Crystal structure of the cation of $[\text{Fe}(\text{H}_2\text{bip})_3]^{2+}$ Reproduced from ref. 31.

Attempts to tune the spin state properties by using ligands with stronger and weaker ligand fields than H_2bip have also been undertaken.³²⁻³⁴ These species utilize two H_2bip ligands to maintain hydrogen-bonding capabilities with the two charge-balancing anions and the third bidentate ligand tunes the ligand field. Unfortunately, these heteroleptic complexes tend to be labile in polar solvents, leading to 'ligand scrambling' in solution when solvents more polar than dichloromethane are used.

An additional example of anion-dependent behavior in solution examined the spin-state properties of $[\text{Fe}(\text{3-bpp})_2]\text{X}_2$ (3-bpp = 2,6-di(pyrazol-3-yl)pyridine; $\text{X} = \text{BPh}_4^-, \text{BF}_4^-, \text{OTf}^-$,

NCS⁻, NO₃⁻, Br⁻).³⁵ Variable-temperature magnetic susceptibility measurements in solution (9:1 *d*₆-acetone:D₂O or pure *d*₆-acetone) were monitored by Evans' method with the various anions. Depending on the counter anion used, the $T_{1/2}$ decreased with weaker interacting anions. While the differences in magnetic behavior between the various salts was not as drastic as with [Fe(H₂bip)₃]²⁺, the incorporation of D₂O into the solvent promotes competition between the anions and solvent for hydrogen-bonding interactions. This finding is promising for altering the spin-state by host:guest interactions in the presence of polar/protic solvents. Additionally, this complex also displays solvent dependent behavior on the variable-temperature solution state properties; more polar solvents stabilize the LS state in much the same fashion as strongly interacting anions thus increasing $T_{1/2}$.³⁶

1.2.3 Tripodal Schiff base ligands and spin crossover. Due to the similar nature of Schiff bases to bipyridines and other diimines, ligands of this type can be easily adapted to display spin crossover in Fe(II) species. An advantage of using hexadentate tripodal ligands over bidentate heteroleptic complexes is the inherent stability imparted by the chelate effect. In most cases, these tripodal ligands are hexadentate in nature, thus saturating the coordination environment of the metal center. The first example of applying tripodal Schiff base ligands to spin crossover was done in the 1970s.³⁷ This seminal study showed that various amounts of steric bulk added adjacent to the coordinating nitrogen of a pyridine can change the fully low-spin complex [Fe(py)₃tren]²⁺ (L¹, Figure 1.3) into a species that undergoes spin crossover. The SCO temperature changes depending on the number of arms containing the methyl group adjacent to the nitrogen; the Fe(II) complex with three methyl groups, [Fe(6-Mepy)₃tren]²⁺ (L⁴, Figure 1.3), undergoes SCO in the solid state centered at 200 K, two methyl groups in [Fe(6-Mepy)₂(py)tren]²⁺ (L³, Figure 1.3) around 250 K, and one methyl group in [Fe(6-Mepy)(py)₂tren]²⁺ (L², Figure 1.3) at approximately 375 K. Studies

of the Ni(II) complexes showed that the ligand field strength is decreased with increasing steric bulk imparted on the coordination environment, thus leading to destabilization of the LS state and lower spin crossover temperatures.³⁸

Since this initial example, countless examples of spin crossover using tripodal Schiff-base derived ligands using Fe(II) and Fe(III) are known. These efforts tune the ligand field by altering heterocycle size,^{40,41} protonation of the ligand,⁴²⁻⁴⁵ or imine reduction.⁴⁶ One example of a tripodal Schiff-base complex displaying anion-dependent spin-state properties is $[\text{FeL}^7]\text{X}_2$ ($\text{L}^7 = \text{tris}(4\text{-pyrazol-3-yl-3-aza-3-butenyl)amine}$; $\text{X} = \text{NO}_3^-$, OTf^- , ClO_4^- , or BF_4^-) (L^7 , Figure 1.3).³⁹ At room temperature in the solid state, all four salts are HS. With cooling, the BF_4^- and ClO_4^- salts remain high spin to 5 K. An incomplete gradual spin transition is observed for the OTf^- salt (“ $T_{1/2}$ ” = 139 K) and a gradual complete transition is displayed by the NO_3^- salt ($T_{1/2} = 144$ K). In solution, the OTf^- displays spin crossover ($T_{1/2} = 200$ K), but the other salts were not tested, so the anion dependence in solution is not known.

1.2.4 Podands for Anion Recognition. Many architectures of tripodal organic molecules have been devised for anion sensing and binding and have been reviewed extensively.⁴⁷⁻⁴⁹ Including a metal center into the complex architecture has added benefits of increased rigidity and charge to promote electrostatic interactions.⁵⁰⁻⁵³ Additionally, the metal center can act as a multifaceted reporter, displaying changes in luminescent, potentiometric, or colorimetric properties.⁵⁴⁻⁵⁶

One example of utilizing a Fe(II) metal center to maintain the desired scaffold is from Fabbrizzi and coworkers.⁵⁷ A tris(imidazolium) cage synthesized was capped with an aromatic ring and appended bipyridines to the ligand allowing for coordination to Fe(II). While the species

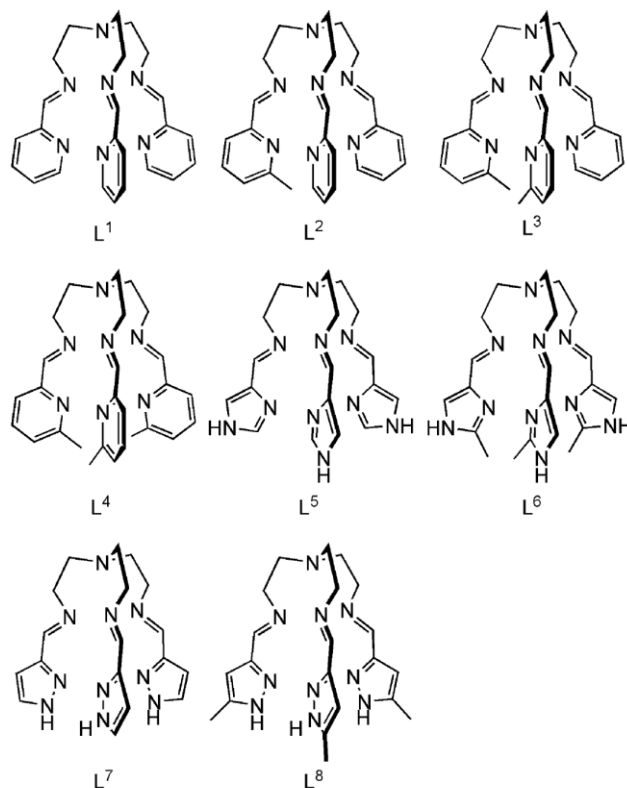


Figure 1.3. Assorted tripodal Schiff base ligands. Adapted from ref. 39.

is low spin, the addition of Br^- to the complex in a 4:1 $\text{CD}_3\text{CN}:\text{D}_2\text{O}$ solution, significant shifts of the protons adjacent to the binding imidazolium were observed.

Bridging the idea of using tripodal Schiff-base ligands to chelate $\text{Fe}(\text{II})$ and promote anion binding, the novel tripodal iminopyridine ligand $\text{L}^{5-\text{ONH}t\text{Bu}}$ has been devised and synthesized. This ligand is functionalized with *tert*-butylamides *meta* to the pyridyl nitrogen atom.⁵⁸ Interestingly, while the $\text{Fe}(\text{II})$ complex remains low spin at all temperatures, in the presence of chloride, significant downfield shifts for the NH proton of the amide are observed *via* ^1H NMR spectroscopy consistent with anion binding (Figure 1.4).

With these ideas in mind, we intend devise a set of ligands that either sterically or electronically tune the ligand field strength to entice anion-dependent spin-state switching. As shown in Scheme 1.1, the iminopyridine is involved in coordination while incorporation of

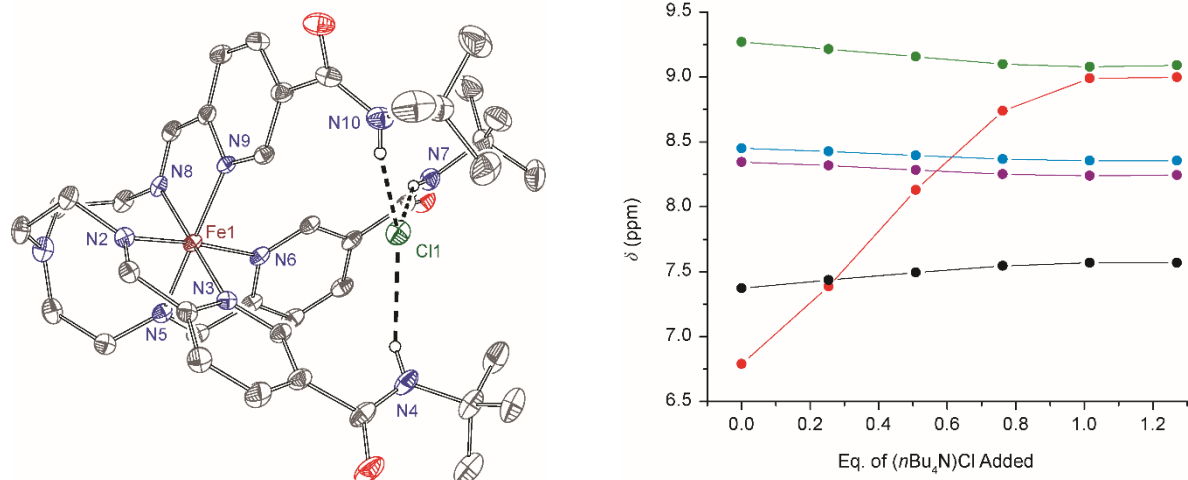
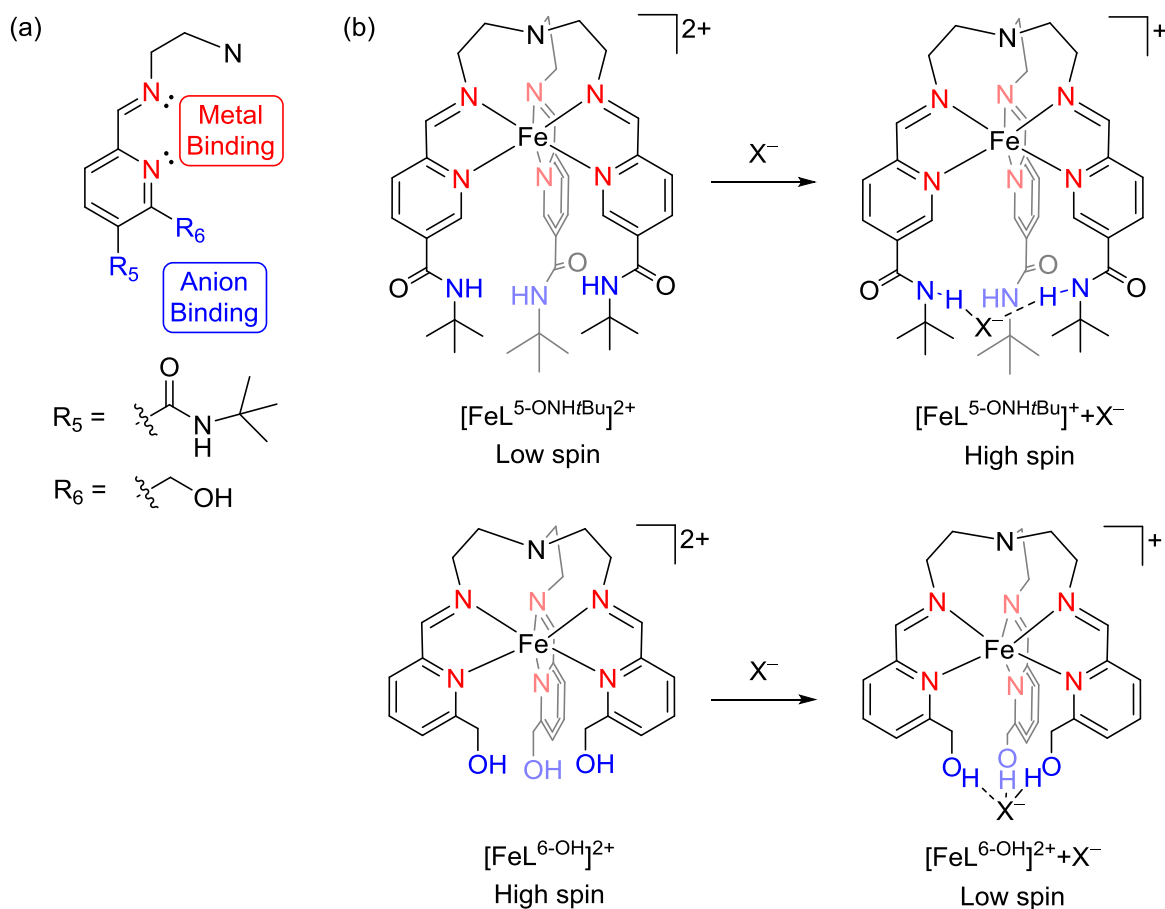


Figure 1.4. Left: Crystal structure of $[\text{FeL}^{5\text{-OHtBu}}\text{Cl}]^+$, highlighting the hydrogen-bonding interactions between the amide and the chloride. Right: Chemical shift changes of the aromatic protons for $[\text{FeL}^{5\text{-OHtBu}}](\text{BF}_4)_2$ with the addition of Cl^- in CD_3CN . Reproduced from ref. 58.

Scheme 1.1. (a) Tripodal ligands of interest highlighting metal-binding (red) and host:guest interactions (blue). (b) Idealized spin state and binding behavior for $[\text{FeL}^{5\text{-OHtBu}}]^{2+}$ (top) and $[\text{FeL}^{6\text{-OH}}]^{2+}$ (bottom).



hydrogen-bonding functionalities at the 5'- and 6'-positions of the pyridine allow for host:guest interactions. Guest binding into the trigonal pocket formed by the hydrogen-bonding groups is hypothesized to either (a) cause a low spin species to become high spin, or (b) induce a high spin species to become low spin, as exemplified by $[\text{FeL}^{5\text{-ONHtBu}}]^{2+}$.

1.3 Single molecule magnetism

1.3.1 Slow magnetic relaxation. The hallmark of single-molecule magnetism is the ability for the species to retain its magnetization once the polarizing field is removed. This occurs due to the existence of a potential energy barrier between two states possessing positive ($M_s = +S$) and negative ($M_s = -S$) magnetic moments. The height of the barrier to spin reorientation (U) is proportional to the magnetic anisotropy or zero-field splitting parameter (D) and the spin (S). The sign of D is pivotal: a positive sign implies that $M_s = 0$ for integer spin systems or $M_s = \pm 1/2$ for half-integer systems is the lowest energy, and slow magnetic relaxation should not be observed, while a negative D value puts the $M_s = \pm S$ states at the lowest energy, thus maximizing the magnetization.⁶⁰ Under zero applied field, the $\pm M_s$ states are at equilibrium. With the application of an external magnetic field, the $-M_s$ state becomes stabilized and thus becomes lower in energy than the $+M_s$ state. In response, this state becomes preferentially occupied and upon saturation of the magnetization, only the $M_s = -S$ will be populated. Removal of the field will cause the system to return to equilibrium. There are two mechanisms through which this can occur: thermal relaxation or quantum tunneling (Figure 1.5). For thermal relaxation, the barrier needs to be large to maximize the relaxation time and thus maintenance of the magnetization.⁶¹

One of the first examples of a single molecule displaying slow relaxation of magnetization was $[\text{Mn}_{12}\text{O}_{12}(\text{CH}_3\text{COO})_{16}(\text{H}_2\text{O})_4]$ or 'Mn₁₂ac'.⁶² Since then, an explosion in the field has occurred

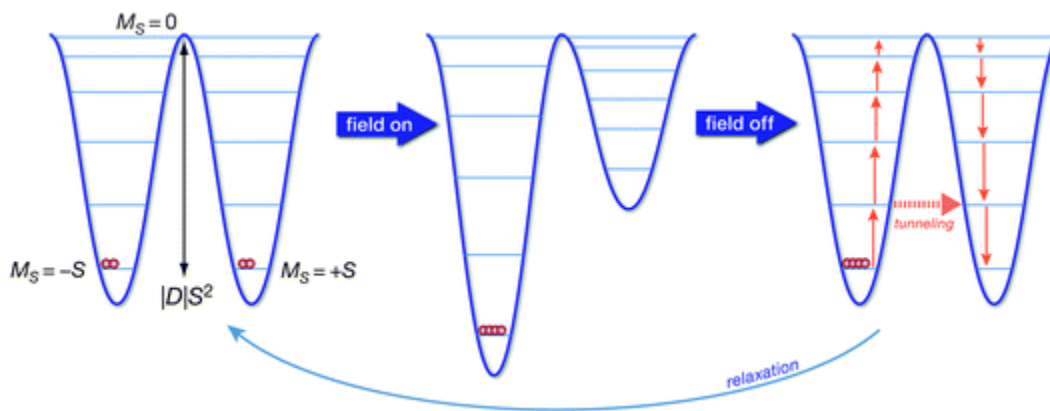


Figure 1.5. Schematic representing the magnetization and relaxation processes of a single-molecule magnet. Reproduced from ref. 61.

leading to the synthesis of a variety of species ranging from large clusters to mononuclear complexes. To date, the highest working temperature for any single molecule magnet is 13.9 K for $[(\text{Me}_3\text{Si})_2\text{N}]_2(\text{THF})\text{Tb}_2(\mu-\eta^2: \eta^2-\text{N}_2)^-$.⁶³ This dinuclear Tb(III) N_2^{3-} radical-bridged complex displays slow magnetic relaxation up to 34 K under zero applied field as measured by ac susceptibility (Left, Figure 1.6) and opening of the magnetic hysteresis loop up until 14 K (Top right, Figure 1.6).

Two techniques are generally used for measuring SMM properties, which are exemplified by $[(\text{Me}_3\text{Si})_2\text{N}]_2(\text{THF})\text{Tb}_2(\mu-\eta^2: \eta^2-\text{N}_2)^-$: ac susceptibility and magnetic hysteresis. During the dynamic ac susceptibility experiment, a small oscillating ac magnetic field is applied to the sample. The magnetic moment oscillates in response to the ac field. Appearance of a non-zero out-of-phase (χ'') susceptibility value implies that the sample's magnetization is not aligned to the field as the internal magnetization of the complex is relaxing slower than the oscillation of the magnetic field. This concomitantly leads to a decrease to the 'real' in-phase susceptibility (χ') as the out-of-phase component increases.⁶⁰ Another method commonly implemented is measuring magnetic hysteresis under variable dc fields. Magnetization of the sample and sweeping of the field at variable rates and/or temperatures will result in opening of the hysteresis loop when magnetization is maintained

due to the sufficiently slow magnetic relaxation of the sample. Additionally, the behavior is highly dependent on the sweep rate, similar to the frequency dependence in the ac susceptibility measurements. Faster sweep rates decrease equilibration of the complex's magnetization to the sweeping field, which could produce a falsely widened hysteresis loop.⁶⁰

1.3.2 Mononuclear Co(II) species. With the discovery of mononuclear lanthanide and actinide species able to display slow relaxation of the magnetization, focus has been also placed on mononuclear first-row transition metals. Recently, several novel mononuclear high-spin Co(II) complexes have been synthesized and characterized. These complexes display slow relaxation of

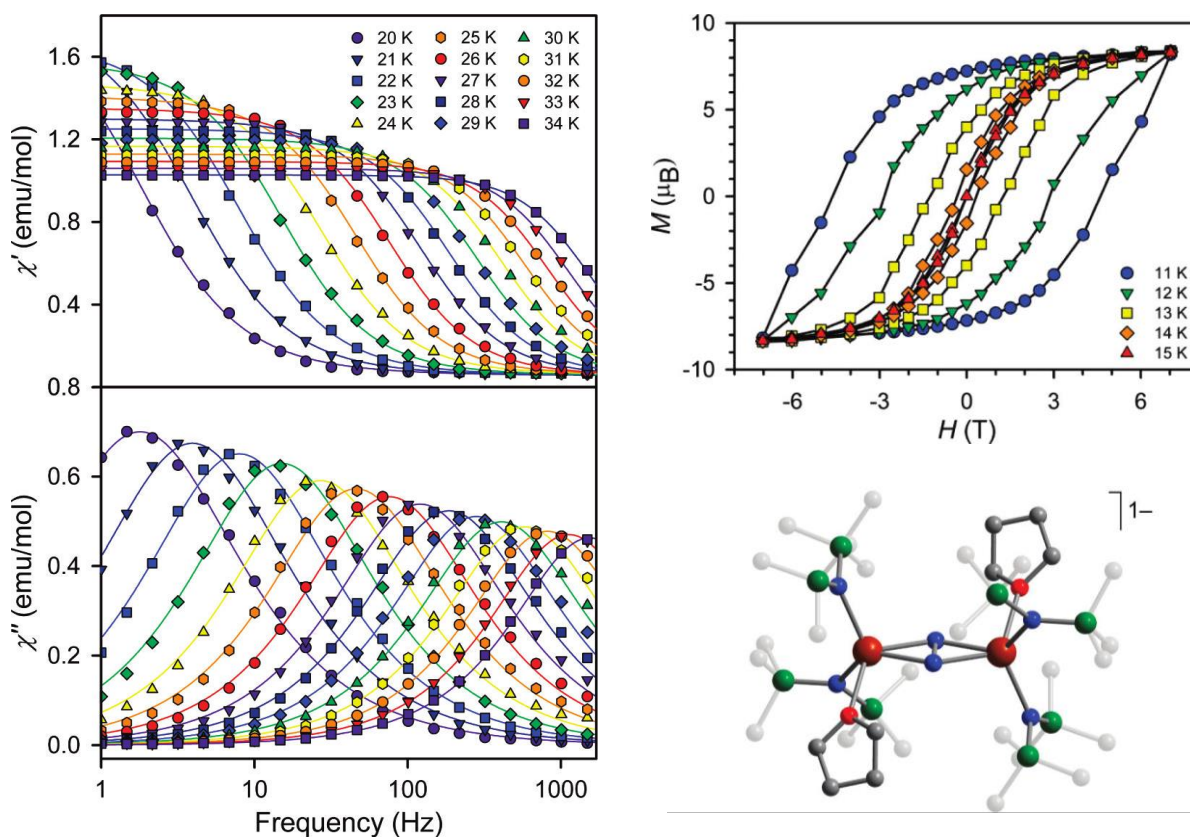


Figure 1.6. Left: In-phase (χ' , top) and out-of-phase (χ'' , bottom) of the ac magnetic susceptibility for $[(\text{Me}_3\text{Si})_2\text{N}]_2(\text{THF})\text{Tb}_2(\mu-\eta^2: \eta^2-\text{N}_2)^-$ under zero applied dc field. Top, right: Magnetization (M) versus dc magnetic field (H) from 11 to 15 K at a sweep rate of 0.9 mT/s. Bottom, right: Crystal structure of $[(\text{Me}_3\text{Si})_2\text{N}]_2(\text{THF})\text{Tb}_2(\mu-\eta^2: \eta^2-\text{N}_2)^-$. Reproduced from ref. 63.

the magnetization as an artifact of the intrinsic magnetic anisotropy of the metal center. In most cases, the ligands employed in these complexes further increase the magnetic anisotropy by lowering the symmetry of the Co(II) coordination. This has been achieved by three-,⁶⁴ four-,⁶⁵⁻⁷⁴ five-,⁷⁵⁻⁷⁷ six-,⁷⁸⁻⁸⁰ seven-,⁸¹ and eight-coordinate⁸² complexes. Additionally, since these first-row transition metal ions are more susceptible to ligand field effects, the proper ligand field must be employed so the orbitals are close in energy.⁸³

Manipulation of the coordination environment of the metal center has been known to drastically affect the magnetic properties. One such example of this is observed in the bis(imino)pyridine pincer ligand modified with methyls or phenyls on the imine carbon from Murugesu and coworkers. The resulting pentacoordinate Co(II) centers $[(\text{ArN}=\text{CR})_2(\text{NPh})\text{Co}(\text{NCS})_2]$ ($\text{R} = \text{Me}$ or Ph), after coordination of two isothiocyanate ligands, have similar coordination environments aside from a 0.13 Å difference in the distortion of the metal center from the plane of the pincer ligand. This difference manifests as a difference in the spin-orbit coupling of the metal center and the more distorted complex displays a larger anisotropic barrier.⁷⁵ Similarly, when terpyridine (terpy) is used as the ligand, the complexes $[\text{Co}(\text{terpy})\text{Cl}_2]$ and $[\text{Co}(\text{terpy})(\text{NCS})_2]$ display similar structural distortions. When chloride ions are coordinated to the cobalt center, the metal is raised above the plane of the terpy ligand. In comparison, if NCS^- anions are coordinated, the metal center resides within the plane of the terpy. Again, these minor differences in coordination environment lead to differences in the anisotropy barrier; more structural distortion leads to a larger barrier to spin reorientation heights.⁷⁶

There are several examples of mononuclear C_3 -symmetric Co(II) complexes that display slow relaxation of the magnetization. One of these examples is $[(3\text{G})\text{CoCl}](\text{OTf})$ ($3\text{G} = 1,1,1$ -tris-[2*N*-(1,1,3,3-tetramethylguanidino)methyl]ethane) from the Long group.⁸⁴ This complex has a

positive D value of 12.7 cm^{-1} , confirmed by high field EPR experiments. Under zero applied dc field, no out-of-phase ac response was observed, but when an external dc field is applied, slow magnetic relaxation is observed. These results were unexpected, as traditionally, complexes with positive D values are not expected to undergo slow magnetic relaxation even under the application of an external field. It is postulated that the direct relaxation between the $M_S = \pm 1/2$ is slow and allows for an equilibrium to be established between the higher energy $M_S = \pm 3/2$ levels, leading to the appearance of slow magnetic relaxation.

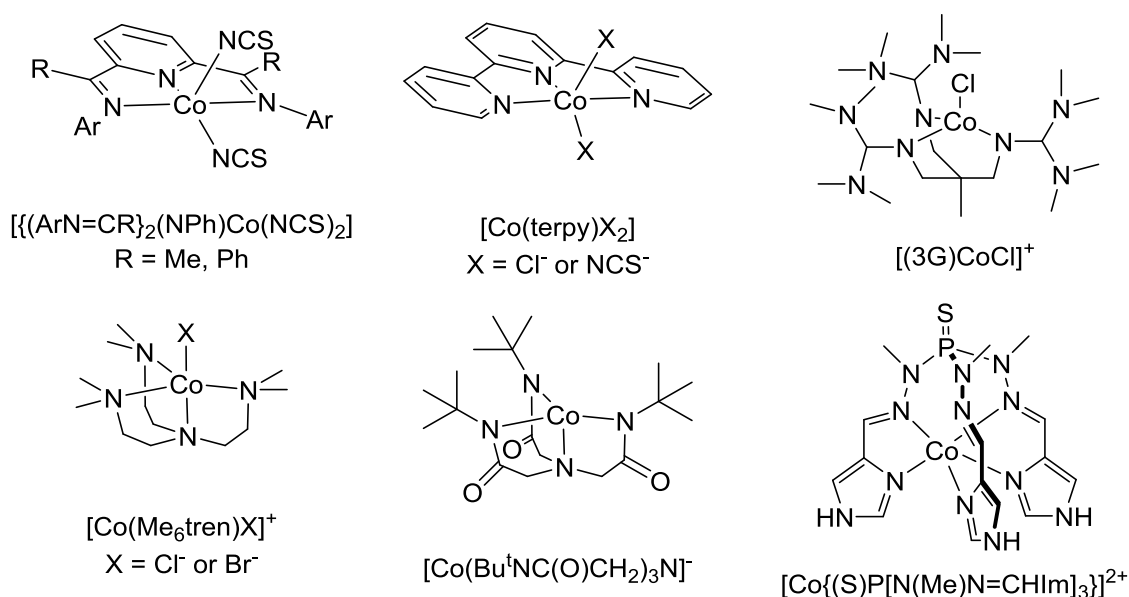


Figure 1.7. Cobalt(II) complexes that display slow magnetic relaxation.

A Co(II) trigonal pyramidal complex with Me₆tren was synthesized by Guih ry *et al.*, based on the Ni(II) complex, [Ni(Me₆tren)Cl](ClO₄), which had been shown to exhibit substantial axial anisotropy.⁸⁵ Two Co(II) complexes with varied axial ligands were synthesized using either Cl⁻ or Br⁻, which was shown to have an effect on the magnitude of the magnetic anisotropy.⁷⁷ For both anions, the value of D is negative. The differences in the magnitude are attributed to the differences in the π -donating ability of the axially coordinated ligand; the more π -donating chloride anion induces more axial anisotropy ($D = -8 \text{ cm}^{-1}$) than the bromide anion ($D = -2.4 \text{ cm}^{-1}$).

An example from Ruiz and coworkers used DFT calculations to determine the best coordination environments to use for first-row transition metals in various oxidation state to tune magnetic anisotropy.⁸⁶ In this work, the validity of the calculation were tested by measuring the magnetic properties of two trigonal Co(II) complexes: the four-coordinate complex $[\text{Co}(\text{Bu}^t\text{NC}(\text{O})\text{CH}_2)_3\text{N}]^-$ originally synthesized by Borovik and coworkers,⁸⁷ and the six-coordinate complex $[\text{Co}\{(\text{S})\text{P}[\text{N}(\text{Me})\text{N}=\text{CHIm}]_3\}](\text{NO}_3)_2$ originally synthesized by Steiner and coworkers.⁸⁸ Based on the calculations, the four-coordinate complex should display a large positive D value while the six-coordinate complex should show a large negative D value. Both species ultimately displayed SMM-like properties and the magnitude of the extracted D values were in good agreement with the prediction.⁸⁶

1.3.3 Coupling metal centers through acetylide linkages. In tune with trying to control magnetic properties via steric interactions, connecting diamagnetic metal centers through acetylide linkages is well-established in the context of applications to nonlinear optics and molecular wires.^{89,90} Recently, these linkages have been used to connect paramagnetic metal centers to promote exchange coupling through the π -system. These multinuclear complexes need to have substantial magnetic coupling (J) to isolate any low-lying excited states from the ground state. Theoretical considerations have indicated that significant magnetic coupling can be achieved through these extended π -networks.^{91,92} Orthogonal arrangements of paramagnetic centers with hard axes of magnetic anisotropy ($D_{\text{ion}} > 0$) are predicted to produce polynuclear complexes with large, negative D values overall.

Work with these systems has been undertaken using triethynylbenzene (H_3TEB) and diethylbenzenes (both *meta* and *para* substituted) as bridging ligands between paramagnetic metal centers. Various equatorial ligands have been coupled to form complexes of $[(\text{dppe})\text{FeCp}^*]^+$ end

groups (dppe = 1,2-bis(diphenylphosphino)ethane and Cp* = pentamethylcyclopentadiene)⁹³⁻⁹⁶ and $[(\text{dmpe})_2\text{FeCl}]^+$ (dmpe = 1,2-bis(dimethylphosphino)ethane).^{97,98} In these examples, when the alkynyl linkages are placed *meta* to one another on an aromatic ring, ferromagnetic coupling between the metal centers is expected, while *para* substitution drives antiferromagnetic coupling between the metal centers.⁹⁵ As expected, bridging multiple $[(\text{dmpe})_2\text{FeCl}]^+$ centers through TEB produced a complex that displays ferromagnetic coupling.⁹⁷ Since the dmpe moieties are free to rotate around each Fe(III) center, intermolecular interactions between triflate anions and the ethylene bridge of dmpe appears to influence the orientation of the dmpe ligands. The subtle differences in the torsion angles of the dmpe ligands prevents the optimum orbital overlap to occur between the singly-occupied molecular orbital (SOMO) of the metal in the solid state. This leads to a decrease in the intramolecular ferromagnetic coupling the complex demonstrates ($J = 37, 5, 5 \text{ cm}^{-1}$ for a two J fit) in comparison to what is expected from TD-DFT calculations with the proper orbital overlap between the SOMO and the π -system ($J = 49, 47, 47 \text{ cm}^{-1}$ for a two J fit).

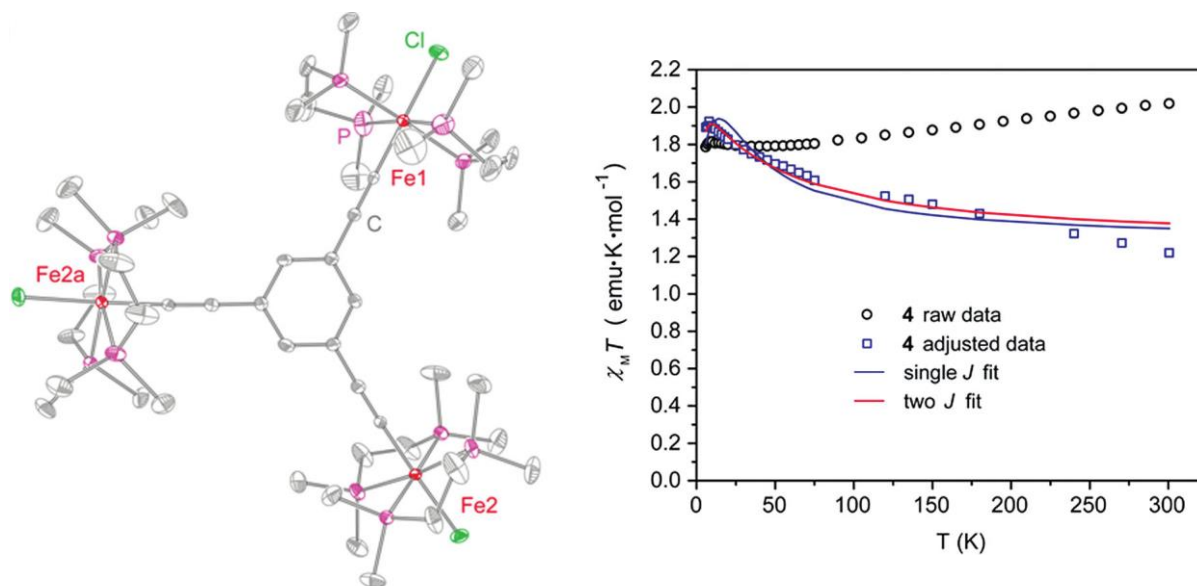


Figure 1.7. Left: Crystal structure of the complex cation $[(\text{dmpe})_6\text{Fe}_3\text{Cl}_3(\mu_3\text{-TEB})]^{3+}$. Right: Variable temperature magnetic susceptibility of $[(\text{dmpe})_6\text{Fe}_3\text{Cl}_3(\mu_3\text{-TEB})]^{3+}$ with (blue squares) and without subtraction (black circles). Solid lines are lines of best fit for a single J value (blue) and two J values (red) for the subtracted data. Reproduced from ref. 97.

1.4 Outline of Dissertation Chapters.

In our attempts to expand and diversify the application of tripodal iminopyridine-based ligands on spin crossover research, a series of functionalized ligands and their corresponding Fe(II) complexes have been synthesized. Through anion binding, spin-state switching can be achieved using the tripodal ligand architecture. The work presented in Chapter 2 is a continuation of work initially began by Dr. Ashley McDaniel of synthesizing and characterizing a series of Fe(II) salts using a tripodal iminopyridine-based ligand functionalized with a hydroxymethyl group adjacent to the pyridine nitrogen. This work has been published in *Dalton Transactions*.⁵⁹ Chapter 3 will detail the attempts at synthesizing ‘heteroarmed’ tripodal iminopyridine ligands *via* self-assembly and presynthesized ligands. In order to tune the ligand field by incorporating steric bulk adjacent to the Fe(II) coordination site while adding in functionalization able to undergo hydrogen-bonding interactions *meta* to the coordinating nitrogen. The works detailed in Chapter 4 focus on alternative methods of tuning the ligand field by varying the number of imines and replacing with secondary amines.

In chapter 5, the efforts to merge the ideas of manipulating magnetic properties by host-guest interactions and single-molecule magnetism will be discussed. Coordination of various Co(II) salts with $L^{5-ONHtBu}$ forms a C_3 -symmetric complex. Depending on the anion, the magnetic anisotropy exhibited by the metal center is maximized with chloride. This manifests as slow magnetic relaxation under an applied dc field for the chloride salt, while little to no relaxation is observed for the bromide, iodide, or perchlorate salts. This appears to be the first examples of non-covalent outer-sphere hydrogen bonding interactions ‘turning on’ single-molecule magnet-like properties for a Co(II) salt. Chapter 6 will detail the work attempting to impart steric hindrance to lock in the ligand conformation of a novel Fe(III) arylalkynyl system. These results suggest that

installing steric bulk on the aryl ring increases the ferromagnetic coupling between the two Fe(III) centers as a consequence of improved orbital overlap between the SOMO of the metal center and the π -system of the aryl-bridge.

REFERENCES

- (1) Cambi, L.; Cagnasso, A. *Atti. Accad. Naz. Lincei*. **1931**, *13*, 809.
- (2) Hauser, A. *Top. Curr. Chem.* **2004**, *234*, 155.
- (3) Letard, J.-F. *J. Mater. Chem.* **2006**, *16*, 2550.
- (4) Boillot, M.-L.; Zarembowitch, J.; Sour, A. *Top. Curr. Chem.* **2004**, *234*, 261.
- (5) Craig, G. A.; Costa, J. S.; Roubeau, O.; Teat, S. J.; Shepherd, H. J.; Lopes, M.; Molnar, G.; Bousseksou, A.; Aromi, G. *Dalton Trans.* **2014**, *43*, 729.
- (6) Ksenofontov, V.; Gaspar, A.; Gütllich, P. *Spin Crossover in Transition Metal Compounds III*; Springer Berlin Heidelberg: 2004; Vol. 235, p 23.
- (7) Halepoto, D. M.; Holt, D. G. L.; Larkworthy, L. F.; Leigh, G. J.; Povey, D. C.; Smith, G. *W. J. Chem. Soc., Chem. Commun.* **1989**, 1322.
- (8) Morgan, G. G.; Murnaghan, K. D.; Müller-Bunz, H.; McKee, V.; Harding, C. J. *Angew. Chem. Int. Ed.* **2006**, *118*, 7350.
- (9) Liu, Z.; Liang, S.; Di, X.; Zhang, J. *Inorg. Chem. Commun.* **2008**, *11*, 783.
- (10) Shongwe, M. S.; Al-Barhi, K. S.; Mikuriya, M.; Adams, H.; Morris, M. J.; Bill, E.; Molloy, K. C. *Chem. Eur. J.* **2014**, *20*, 9693.
- (11) Koningsbruggen, P.; Maeda, Y.; Oshio, H. *Spin Crossover in Transition Metal Compounds I*; Gütllich, P., Goodwin, H. A., Eds.; Springer Berlin Heidelberg: 2004; Vol. 233, p 259.
- (12) Goodwin, H. A. *Spin Crossover in Transition Metal Compounds II*; Springer Berlin Heidelberg: 2004; Vol. 234, p 23.
- (13) Krivokapic, I.; Zerara, M.; Daku, M. L.; Vargas, A.; Enachescu, C.; Ambrus, C.; Tregenna-Piggott, P.; Amstutz, N.; Krausz, E.; Hauser, A. *Coord. Chem. Rev.* **2007**, *251*, 364.
- (14) Kläui, W.; Eberspach, W.; Gütllich, P. *Inorg. Chem.* **1987**, *26*, 3977.
- (15) Garcia, Y.; Gütllich, P. *Spin Crossover in Transition Metal Compounds II*; Springer Berlin Heidelberg: 2004; Vol. 234, p 49.
- (16) Thies, S.; Sell, H.; Schuett, C.; Bornholdt, C.; Naether, C.; Tuczek, F.; Herges, R. *J. Am. Chem. Soc.* **2011**, *133*, 16243.
- (17) Thies, S.; Sell, H.; Bornholdt, C.; Schuett, C.; Koehler, F.; Tuczek, F.; Herges, R. *Chem. Eur. J.* **2012**, *18*, 16358.
- (18) Gütllich, P.; Goodwin, H. A. *Top. Curr. Chem.* **2004**, *233*, 1.
- (19) Gütllich, P.; Garcia, Y.; Goodwin, H. A. *Chem. Soc. Rev.* **2000**, *29*, 419.
- (20) Evans, D. F. *J. Chem. Soc.* **1959**, 2003.
- (21) Ostfeld, D.; Cohen, I. A. *J. Chem. Educ.* **1972**, *49*, 829.
- (22) Shores, M. P.; Klug, C. M.; Fiedler, S. R. *Spin-Crossover Materials*; John Wiley & Sons Ltd: 2013, p 281.

- (23) Guetlich, P.; Gaspar, A. B.; Garcia, Y. *Beilstein J. Org. Chem.* **2013**, *9*, 342.
- (24) König, E. *Complex Chemistry*; Springer Berlin Heidelberg: 1991; Vol. 76, p 51.
- (25) Quesada, M.; Prins, F.; Bill, E.; Kooijman, H.; Gamez, P.; Roubeau, O.; Spek, A. L.; Haasnoot, J. G.; Reedijk, J. *Chem. Eur. J.* **2008**, *14*, 8486.
- (26) Fujinami, T.; Nishi, K.; Matsumoto, N.; Iijima, S.; Halcrow, M. A.; Sunatsuki, Y.; Kojima, M. *Dalton Trans.* **2011**, *40*, 12301.
- (27) Jameson, G. N. L.; Werner, F.; Bartel, M.; Absmeier, A.; Reissner, M.; Kitchen, J. A.; Brooker, S.; Caneschi, A.; Carbonera, C.; Letard, J.-F.; Linert, W. *Eur. J. Inorg. Chem.* **2009**, 3948.
- (28) Leita, B. A.; Neville, S. M.; Halder, G. J.; Moubaraki, B.; Kepert, C. J.; Letard, J.-F.; Murray, K. S. *Inorg. Chem.* **2007**, *46*, 8784.
- (29) Lemerrier, G.; Bréfuel, N.; Shova, S.; Wolny, J. A.; Dahan, F.; Verelst, M.; Paulsen, H.; Trautwein, A. X.; Tuchagues, J.-P. *Chem. Eur. J.* **2006**, *12*, 7421.
- (30) Bilbeisi, R. A.; Zarra, S.; Feltham, H. L. C.; Jameson, G. N. L.; Clegg, J. K.; Brooker, S.; Nitschke, J. R. *Chem. Eur. J.* **2013**, *19*, 8058.
- (31) Ni, Z.; Shores, M. P. *J. Am. Chem. Soc.* **2008**, *131*, 32.
- (32) Ni, Z.; Shores, M. P. *Inorg. Chem.* **2010**, *49*, 10727.
- (33) Ni, Z.; Fiedler, S. R.; Shores, M. P. *Dalton Trans.* **2011**, *40*, 944.
- (34) Ni, Z.; McDaniel, A. M.; Shores, M. P. *Chem. Sci.* **2010**, *1*, 615.
- (35) Barrett, S. A.; Halcrow, M. A. *RSC Adv.* **2014**, *4*, 11240.
- (36) Barrett, S. A.; Kilner, C. A.; Halcrow, M. A. *Dalton Trans.* **2011**, *40*, 12021.
- (37) Hoselton, M. A.; Wilson, L. J.; Drago, R. S. *J. Am. Chem. Soc.* **1975**, *97*, 1722.
- (38) Wilson, L. J.; Georges, D.; Hoselton, M. A. *Inorg. Chem.* **1975**, *14*, 2968.
- (39) Lazar, H. Z.; Forestier, T.; Barrett, S. A.; Kilner, C. A.; Letard, J. F.; Halcrow, M. A. *Dalton Trans.* **2007**, 4276.
- (40) Sunatsuki, Y.; Sakata, M.; Matsuzaki, S.; Matsumoto, N.; Kojima, M. *Chem. Lett.* **2001**, 1254.
- (41) Yamada, M.; Ooidemizu, M.; Ikuta, Y.; Osa, S.; Matsumoto, N.; Iijima, S.; Kojima, M.; Dahan, F.; Tuchagues, J.-P. *Inorg. Chem.* **2003**, *42*, 8406.
- (42) Brewer, C.; Brewer, G.; Luckett, C.; Marbury, G. S.; Viragh, C.; Beatty, A. M.; Scheidt, W. R. *Inorg. Chem.* **2004**, *43*, 2402.
- (43) Brewer, C.; Brewer, G.; Butcher, R. J.; Carpenter, E. E.; Cuenca, L.; Noll, B. C.; Scheidt, W. R.; Viragh, C.; Zavalij, P. Y.; Zielaski, D. *Dalton Trans.* **2006**, 1009.
- (44) Brewer, C. T.; Brewer, G.; Butcher, R. J.; Carpenter, E. E.; Schmiedekamp, A. M.; Viragh, C. *Dalton Trans.* **2007**, 295.
- (45) Sunatsuki, Y.; Ohta, H.; Kojima, M.; Ikuta, Y.; Goto, Y.; Matsumoto, N.; Iijima, S.; Akashi, H.; Kaizaki, S.; Dahan, F.; Tuchagues, J.-P. *Inorg. Chem.* **2004**, *43*, 4154.

- (46) Morgenstern-Badarau, I.; Lambert, F.; Philippe Renault, J.; Cesario, M.; Maréchal, J.-D.; Maseras, F. *Inorg. Chim. Acta* **2000**, 297, 338.
- (47) Steed, J. W. *Chem. Commun.* **2006**, 2637.
- (48) Bowman-James, K. *Acc. Chem. Res.* **2005**, 38, 671.
- (49) Beer, P. D.; Gale, P. A. *Angew. Chem. Int. Ed.* **2001**, 40, 486.
- (50) Amendola, V.; Fabbrizzi, L. *Chem. Commun.* **2009**, 513.
- (51) Steed, J. W. *Chem. Soc. Rev.* **2009**, 38, 506.
- (52) Vilar, R. *Eur. J. Inorg. Chem.* **2008**, 2008, 357.
- (53) Mercer, D. J.; Loeb, S. J. *Chem. Soc. Rev.* **2010**, 39, 3612.
- (54) Beer, P. D.; Bayly, S. R. *Anion Sensing*; Stibor, I., Ed.; Springer Berlin / Heidelberg: 2005; Vol. 255, p 373.
- (55) Beer, P. D. *Acc. Chem. Res.* **1998**, 31, 71.
- (56) Suksai, C.; Tuntulani, T. *Chem. Soc. Rev.* **2003**, 32, 192.
- (57) Amendola, V.; Boiocchi, M.; Colasson, B.; Fabbrizzi, L.; Rodriguez Douton, M.-J.; Ugozzoli, F. *Angew. Chem. Int. Ed.* **2006**, 45, 6920.
- (58) McDaniel, A. M.; Klug, C. M.; Shores, M. P. *Eur. J. Inorg. Chem.* **2013**, 2013, 943.
- (59) Klug, C. M.; McDaniel, A. M.; Fiedler, S. R.; Schulte, K. A.; Newell, B. S.; Shores, M. P. *Dalton Trans.* **2012**, 41, 12577.
- (60) Gatteschi, D. *Molecular nanomagnets*; Oxford University Press: Oxford, 2006.
- (61) Neese, F.; Pantazis, D. A. *Faraday Discuss.* **2011**, 148, 229.
- (62) Sessoli, R.; Gatteschi, D.; Caneschi, A.; Novak, M. A. *Nature* **1993**, 365, 141.
- (63) Rinehart, J. D.; Fang, M.; Evans, W. J.; Long, J. R. *J. Am. Chem. Soc.* **2011**, 133, 14236.
- (64) Eichhoefer, A.; Lan, Y.; Mereacre, V.; Bodenstern, T.; Weigend, F. *Inorg. Chem.* **2014**, 53, 1962.
- (65) Zadrozny, J. M.; Long, J. R. *J. Am. Chem. Soc.* **2011**, 133, 20732.
- (66) Buchholz, A.; Eseola, A. O.; Plass, W. C. R. *Chim.* **2012**, 15, 929.
- (67) Zadrozny, J. M.; Liu, J.; Piro, N. A.; Chang, C. J.; Hill, S.; Long, J. R. *Chem. Commun.* **2012**, 48, 3927.
- (68) Cao, D.-K.; Feng, J.-Q.; Ren, M.; Gu, Y.-W.; Song, Y.; Ward, M. D. *Chem. Commun.* **2013**, 49, 8863.
- (69) Huang, W.; Liu, T.; Wu, D.; Cheng, J.; Ouyang, Z. W.; Duan, C. *Dalton Trans.* **2013**, 42, 15326.
- (70) Yang, F.; Zhou, Q.; Zhang, Y.; Zeng, G.; Li, G.; Shi, Z.; Wang, B.; Feng, S. *Chem. Commun.* **2013**, 49, 5289.
- (71) Boca, R.; Miklovic, J.; Titis, J. *Inorg. Chem.* **2014**, 53, 2367.

- (72) Zadrozny, J. M.; Telser, J.; Long, J. R. *Polyhedron* **2013**, *64*, 209.
- (73) Saber, M. R.; Dunbar, K. R. *Chem. Commun.* **2014**, *50*, 12266.
- (74) Fataftah, M. S.; Zadrozny, J. M.; Rogers, D. M.; Freedman, D. E. *Inorg. Chem.* **2014**, *53*, 10716.
- (75) Jurca, T.; Farghal, A.; Lin, P.-H.; Korobkov, I.; Murugesu, M.; Richeson, D. S. *J. Am. Chem. Soc.* **2011**, *133*, 15814.
- (76) Habib, F.; Luca, O. R.; Vieru, V.; Shiddiq, M.; Korobkov, I.; Gorelsky, S. I.; Takase, M. K.; Chibotaru, L. F.; Hill, S.; Crabtree, R. H.; Murugesu, M. *Angew. Chem. Int. Ed.* **2013**, *52*, 11290.
- (77) Ruamps, R.; Batchelor, L. J.; Guillot, R.; Zakhia, G.; Barra, A.-L.; Wernsdorfer, W.; Guihery, N.; Mallah, T. *Chem. Sci.* **2014**, *5*, 3418.
- (78) Herchel, R.; Vahovska, L.; Potocnak, I.; Travnicek, Z. *Inorg Chem* **2014**, *53*, 5896.
- (79) Vallejo, J.; Castro, I.; Ruiz-Garcia, R.; Cano, J.; Julve, M.; Lloret, F.; De Munno, G.; Wernsdorfer, W.; Pardo, E. *J Am Chem Soc* **2012**, *134*, 15704.
- (80) Plenk, C.; Krause, J.; Rentschler, E. *Eur. J. Inorg. Chem.* **2015**, *2015*, 370.
- (81) Huang, X.-C.; Zhou, C.; Shao, D.; Wang, X.-Y. *Inorg. Chem.* **2014**.
- (82) Chen, L.; Wang, J.; Wei, J.-M.; Wernsdorfer, W.; Chen, X.-T.; Zhang, Y.-Q.; Song, Y.; Xue, Z.-L. *J. Am. Chem. Soc.* **2014**, *136*, 12213.
- (83) Dey, M.; Gogoi, N. *Angew. Chem. Int. Ed.* **2013**, *52*, 12780.
- (84) Zadrozny, J. M.; Liu, J.; Piro, N. A.; Chang, C. J.; Hill, S.; Long, J. R. *Chem. Commun.* **2012**, *48*, 3927.
- (85) Ruamps, R.; Maurice, R.; Batchelor, L.; Boggio-Pasqua, M.; Guillot, R.; Barra, A. L.; Liu, J.; Bendeif, E.-E.; Pillet, S.; Hill, S.; Mallah, T.; Guihery, N. *J. Am. Chem. Soc.* **2013**, *135*, 3017.
- (86) Gomez-Coca, S.; Cremades, E.; Aliaga-Alcalde, N.; Ruiz, E. *J. Am. Chem. Soc.* **2013**, *135*, 7010.
- (87) Ray, M.; Hammes, B. S.; Yap, G. P. A.; Rheingold, A. L.; Borovik, A. S. *Inorg. Chem.* **1998**, *37*, 1527.
- (88) Chandrasekhar, V.; Azhakar, R.; Pandian, B. M.; Boomishankar, R.; Steiner, A. *Dalton Trans.* **2008**, 5962.
- (89) Long, N. J.; Williams, C. K. *Angew. Chem. Int. Ed.* **2003**, *42*, 2586.
- (90) Ren, T. *Organometallics* **2005**, *24*, 4854.
- (91) Ruiz, E.; Rodríguez-Forteza, A.; Alvarez, S. *Inorg. Chem.* **2003**, *42*, 4881.
- (92) Oshio, H.; Nakano, M. *Chem. - Eur. J.* **2005**, *11*, 5178.
- (93) Le Narvor, N.; Lapinte, C. *Organometallics* **1995**, *14*, 634.
- (94) Weyland, T.; Lapinte, C.; Frapper, G.; Calhorda, M. J.; Halet, J.-F.; Toupetc, L. *Organometallics* **1997**, *16*, 2024.

- (95) Weyland, T.; Costuas, K.; Mari, A.; Halet, J.-F.; Lapinte, C. *Organometallics* **1998**, *17*, 5569.
- (96) Costuas, K.; Cador, O.; Justaud, F.; Le Stang, S.; Paul, F.; Monari, A.; Evangelisti, S.; Toupet, L.; Lapinte, C.; Halet, J.-F. *Inorg. Chem.* **2011**, *50*, 12601.
- (97) Hoffert, W. A.; Rappé, A. K.; Shores, M. P. *J. Am. Chem. Soc.* **2011**, *133*, 20823.
- (98) Berben, L. A. Toward acetylide- and N-heterocycle-bridged materials with strong electronic and magnetic coupling. Ph.D. University of California, Berkeley, CA, 2005.

CHAPTER 2. ANION DEPENDENCE IN THE SPIN-CROSSOVER PROPERTIES OF A FE(II) PODAND COMPLEX*

2.1 Introduction.

Octahedral coordination of $d^4 - d^7$ transition metal centres combined with a properly tuned ligand field can facilitate switching between high- and low-spin states (HS and LS, respectively).¹⁻

⁵ This spin-crossover (SCO) phenomenon can be triggered by small environmental forcing ($E \sim k_B T$), and exploitation of this molecular effect in materials is a major synthetic goal. SCO materials have been widely investigated for use in data storage and display devices due to the dramatic magnetic and color changes that can accompany spin-state switching.^{3,5,6}

Recent inquiries have focused on combining host-guest interactions with the SCO phenomenon, both to probe non-covalent interactions as well as to develop new signalling pathways for chemosensing.⁷⁻¹⁴ In the solid state, inclusion of guest molecules into metal-organic frameworks such as $[\text{Fe}(\text{bpbd})_2(\text{NCS})_2]$ and $[\text{Fe}_2(\text{azpy})_4(\text{NCS})_4]$ have been shown to induce SCO.^{7,8} The presence and identity of counter anions have also been shown to have an impact on the spin transition temperature in both the solid state and in solution.^{3,9} Investigation of a series of Fe(II) triimidazole-halide complexes have shown SCO in the solid state: large anions with low charge density induce SCO at higher temperatures than their smaller, more charge dense counterparts.¹⁰ Our previous studies, using 2,2'-bi-1,4,5,6-tetrahydropyrimidine (H_2bip) in homo-^{11,12} and heteroleptic¹³⁻¹⁵ complexes with Fe(II), have also shown anion-dependent spin-state switching both in solution and in the solid state.

* Klug, C. M.; McDaniel, A. M.; Fiedler, S. R.; Schulte, K. A.; Newell, B. S.; Shores, M. P. *Dalton Trans.* 2012, 41, 12577. Reproduced with permission of The Royal Society of Chemistry. <http://pubs.rsc.org/en/content/articlelanding/2012/dt/c2dt31213a>

In order to exploit the color change induced by SCO for use in anion sensors, more robust ligand sets must be procured to overcome the lability associated with HS Fe(II) complexes featuring bidentate ligands.¹⁶ Thus, we have become interested in tripodal Schiff base ligands based on tris{4-[(6-R)-2-pyridyl]-3-aza-3-butenyl}amine ($H_{3-x}(6-R-py)_x$ tren (R = H, Me, X = 1–3)).^{17,18} The parent Fe(II) complexes have been shown to undergo SCO in solution and the solid state, with the SCO temperature dependent on the R substituent at the 6-position of the pyridine: steric hindrance associated with substitution at the carbon adjacent (α) to the pyridyl N donor stabilizes the HS state, lowering the SCO temperature in the solid state and in solution with each additional substitution.¹⁷

More recent work on Fe(II) complexes with pyrazole-containing tripodal ligands has shown anion dependence in the solid state SCO temperatures and completeness; SCO in solution has also been observed.¹⁹ Related, hydrogen-bonding interactions in mixed anion-cation salts of Fe(II) complexes with analogous imidazole-containing ligands have been shown to affect the percentage of HS moieties at room temperature.²⁰

As part of our efforts to combine spin-state changes with anion binding in environmentally relevant media, we have investigated the preparations and magnetic properties of salts of the Fe(II) complex with tris{4-[(6-methanol)-2-pyridyl]-3-aza-3-butenyl}amine (\mathbf{L}^{6-OH} , Figure 2.1) and the non-tethered derivative 4-[(6-methanol)-2-pyridyl]-3-aza-3-butenyl (\mathbf{L}^2 , Scheme 2.1). The tripodal complex was chosen for several reasons. First, hexadentate coordination should increase complex solution stability, especially in protic solvents.¹⁶ Second, electrostatic attractions of anions to the cationic complex trigonal pocket would be enhanced by incorporation of hydrogen-bonding methanol groups at the 6(α) position. The trigonal pocket formed by chelation of Fe(II) may allow for stronger binding and better selectivity for C_3 symmetric and/or larger spherical

anions compared to bidentate chelation. Combining these factors, tridentate anion interactions could force the Fe(II) ion to adopt a LS state due to the contraction of the trigonal pocket. Meanwhile, structural and physical influences of the bridgehead nitrogen could be investigated by removal of the tether, via study of Fe(II) complexes with L^2 .

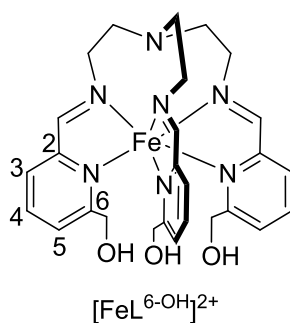


Figure 2.1. Depiction of the complex cation: hexadentate chelation aims to increase stability, while positioning of hydroxyl groups tunes SCOs properties and entices anion-cation hydrogen-bonding interactions.

2.2 Division of Labor

Synthesis of L^{6-OH} , X-ray crystals structure of **2.3**, and preliminary magnetic results were obtained by Dr. Ashley McDaniel. X-ray crystal structure of **2.2** was collected and solved by Dr. Stephanie Fielder-Gleich. Synthesis and characterization of L^2 and **2.6** were performed by Kelsey Schulte. All other syntheses and characterizations were performed by Christina Klug.

2.3 Experimental Details

2.3.1 General Considerations. The ligand L^{6-OH} was prepared under anaerobic conditions and L^2 was prepared under aerobic conditions; compound manipulations involving Fe(II) ions were performed inside a dinitrogen-filled glovebox (MBRAUN Labmaster 130). Pentane was distilled over sodium metal and subjected to three freeze–pump–thaw cycles. Acetonitrile (MeCN) and diethyl ether (Et_2O) were sparged with dinitrogen, passed over molecular sieves, and subjected to three freeze–pump–thaw cycles. All other reagents were obtained from commercial sources and

were used without further purification; 2-pyridinecarboxaldehyde-6-methanol²¹ and $[\text{Fe}(\text{MeCN})_2(\text{CF}_3\text{SO}_3)_2]$ ²² were synthesized using previously described procedures.

Tris[4-[(6-methanol)-2-pyridyl]-3-aza-3-butenyl]amine ($\text{L}^{6\text{-OH}}$). A 25 mL flask was charged with one equivalent of tris(2-aminoethyl)amine (tren, 0.248 g, 1.70 mmol), 3.1 equivalents of 2-pyridinecarboxaldehyde-6-methanol (0.785 g, 5.25 mmol), 8 mL of methanol and 1 g of molecular sieves (3Å). The mixture was stirred until the alcohol precursor dissolved. The resulting brown–yellow oil was triturated with 10 mL of Et_2O . The oil was mixed with NaSO_4 in methanol to remove residual water. The solution was filtered, the solvent was removed from the filtrate and the product was dried under vacuum for 8 hours to afford 0.629 g of yellow oil (80%). The product was used as isolated without any additional purification. IR (ATR) ν_{OH} 3273 cm^{-1} , ν_{CH} 2845 cm^{-1} , $\nu_{\text{C=N}}$ 1647 cm^{-1} . ^1H NMR (400 MHz; CD_3OD ; Me_4Si): 8.3 (3H, s), 7.8 (3H, t, $J = 7.715, 7.696$ Hz), 7.72 (3 H, d, $J = 7.628$ Hz), 7.53 (3 H, d, $J = 7.567$ Hz), 4.68 (6 H, s), 3.77 (6H, t, $J = 6.157, 6.003$ Hz), 2.98 (6H, t, $J = 6.207, 6.291$ Hz) ppm. ^{13}C NMR (CD_3OD) δ 161.4 (s), 159.4 (s), 151.4 (s), 135.9 (s), 120.1 (s), 118.2 (s), 62.5 (s), 57.6 (s), 53.2 (s) ppm. Anal. MS (CH_3OH): m/z 526.253 $[\text{L}^{6\text{-OH}} + \text{Na}]^+$, 504.271 $[\text{L}^{6\text{-OH}} + \text{H}]^+$

$[\text{FeL}^{6\text{-OH}}](\text{CF}_3\text{SO}_3)_2 \cdot 0.25 \text{ EtOH}$ (2.1). A solution of $\text{L}^{6\text{-OH}}$ (0.250 g, 0.49 mmol) in 6 mL of methanol was added to a colourless solution of $[\text{Fe}(\text{MeCN})_2(\text{CF}_3\text{SO}_3)_2]$ (0.255 g, 0.49 mmol) in 4 mL of methanol. The instantly–formed red solution was stirred for 30 minutes. The solvent was removed in vacuo and the crude product was triturated with 20 mL of Et_2O to produce a brick red free flowing powder. The solid was isolated by filtration and X–ray quality crystals were obtained by Et_2O diffusion into an ethanolic solution of the compound (0.38 g, 91% yield). IR (ATR) ν_{OH} 3434, 3238 cm^{-1} . λ_{max} (CH_3OH)/nm 500 (1160 $\text{M}^{-1}\cdot\text{cm}^{-1}$); (MeCN)/nm 490 (1300 $\text{M}^{-1}\cdot\text{cm}^{-1}$). ^1H NMR (300 MHz; CD_3OD ; Me_4Si): 66.1, 59.6, 48.6, 33.9, 26.4, 18.5, –9.4 ppm. χ_{MT}

(SQUID, 295 K) = $3.63 \text{ cm}^3 \cdot \text{K} \cdot \text{mol}^{-1}$ ($\mu_{\text{eff}} = 5.39 \mu_{\text{B}}$). Anal. Calcd for $\text{C}_{29.5}\text{H}_{34.5}\text{N}_7\text{O}_{9.25}\text{FeS}_2\text{F}_6$: C, 40.8; H, 4.0; N, 11.3. Found: C, 40.7; H, 3.8; N, 11.3.

[FeL^{6-OH}]Br₂ (2.2). A solution of **L^{6-OH}** (0.189 g, 0.88 mmol) in 6 mL of methanol was added to a stirring, light brown-coloured solution of FeBr₂ (0.447 g, 0.88 mmol) in 8 mL of methanol. The instantly formed dark red-coloured solution was stirred for 30 minutes. A dark red powder was isolated by removing the solvent under vacuum; the product was triturated with 5 mL of Et₂O. X-ray quality crystals of **2** were obtained by slow diffusion of Et₂O into a methanolic solution of the compound (0.561 g, 95.2% yield). IR (ATR) ν_{OH} 3357, 3232 cm^{-1} . λ_{max} (CH₃OH)/nm 502 ($1140 \text{ M}^{-1} \cdot \text{cm}^{-1}$). ¹H NMR (300 MHz; CD₃OD; Me₄Si): 64.8, 57.3, 48.3, 33.9, 28.2, 18.0, 10.4, -7.5 ppm. χ_{MT} (SQUID, 295 K) = $3.45 \text{ cm}^3 \cdot \text{K} \cdot \text{mol}^{-1}$ ($\mu_{\text{eff}} = 5.25 \mu_{\text{B}}$). Anal. Calcd for $\text{C}_{27}\text{H}_{33}\text{N}_7\text{O}_3\text{FeBr}_2$: C, 45.1; H, 4.6; N, 13.6. Found: C, 45.0; H, 4.4; N, 13.5.

[FeL^{6-OH}]Br₂·0.5 MeOH (2.3). X-ray quality crystals of the solvated compound were obtained by slow diffusion of Et₂O into a 50:50 methanol:ethanol solution of **2.2**. χ_{MT} (SQUID, 295 K) = $3.50 \text{ cm}^3 \cdot \text{K} \cdot \text{mol}^{-1}$ ($\mu_{\text{eff}} = 5.32 \mu_{\text{B}}$). Anal. Calcd for $\text{C}_{27.50}\text{H}_{35}\text{N}_7\text{O}_{3.50}\text{FeBr}_2$: C, 44.9; H, 4.8; N, 13.3. Found: C, 44.6; H, 4.6; N, 13.3.

[FeL^{6-OH}]I₂ (2.4). A solution of **2.1** (0.033 g, 0.38 mmol) was added to a solution of *n*-Bu₄NI (0.057 g, 0.15 mmol) in 2 mL of acetonitrile to form immediately a red precipitate; the mixture was stirred for one additional hour. The light red solid was isolated by filtration and washed with 10 mL of acetone and 5 mL of pentane. The product was purified by recrystallization via diffusion of Et₂O into a methanolic solution of the compound (0.024 g, 77 % yield); X-ray quality crystals were selected from the product. IR (KBr) ν_{OH} 3339, 3202 cm^{-1} . λ_{max} (CH₃OH)/nm 502 ($1180 \text{ M}^{-1} \cdot \text{cm}^{-1}$). ¹H NMR (300 MHz; CD₃OD; Me₄Si): 65.6, 58.5, 48.8, 34.0, 28.4, 17.7,

-8.9 ppm. χ_{MT} (SQUID, 296 K) = 3.52 cm³·K·mol⁻¹ (μ_{eff} = 5.31 μ_{B}). Anal. Calcd for C₂₇H₃₃N₇O₃FeI₂: C, 39.9; H, 4.1; N, 12.1. Found: C, 39.7; H, 3.9; N, 11.9.

[FeL^{6-OH}](BPh₄)₂·2 MeCN (2.5). Carried out in a manner similar to the preparation of **2.4**, anion exchange of **2.2** (0.103 g, 0.144 mmol) into 6 mL of methanol with NaBPh₄ (0.205 g, 0.599 mmol) produced a light pink precipitate. The mixture was stirred for 30 minutes, and then the solid was isolated by filtration. The resulting solid was triturated with methanol (6 mL) and stirred for 16 hours. The solid was isolated by filtration and washed with 6 mL of Et₂O to produce a brick red, free flowing powder. X-ray quality crystals were obtained by Et₂O diffusion into a concentrated acetonitrile solution (0.120 g, 66 % yield); IR (ATR) ν_{OH} 3509 cm⁻¹. λ_{max} (MeCN)/nm 489 (1340 M⁻¹·cm⁻¹). ¹H NMR (300 MHz; CD₃CN; Me₄Si): 75.3, 56.9, 47.9, 40.7, 32.3, 10.4, 8.9 ppm. χ_{MT} (SQUID, 296 K) = 3.62 cm³·K·mol⁻¹ (μ_{eff} = 5.38 μ_{B}). Anal. Calcd for C₇H₇NO₃FeB₂: C, 74.1; H, 6.2, N, 9.9. Found: C, 74.1; H, 5.9; N, 9.5.

4-[(6-methanol)-2-pyridyl]-3-aza-3-butenyl (L²). In a similar synthetic procedure as used for **L^{6-OH}**, 2-pyridinecarboxaldehyde-6-methanol (0.208 g, 1.518 mmol) and ethyl amine (0.103 g, 2.277 mmol) were combined, resulting in a pale yellow oil (0.170 g, 68% yield). The product was used as isolated without any additional purification. IR (KBr) ν_{OH} 3282 cm⁻¹, ν_{CH} 2972, 2952, 2869 cm⁻¹, $\nu_{\text{C=N}}$ 1650 cm⁻¹. ¹H NMR (400 MHz; CDCl₃): 8.39 (1H, s), 7.87 (1H, d, J = 7.79 Hz), 7.73 (1 H, t, J = 7.71, 7.72 Hz), 7.28 (1 H, d, J = 7.68 Hz), 4.80 (2H, s), 3.92 (1H, s), 3.70 (2H, q, J = 14.57, 7.28, 7.30 Hz), 1.32 (3H, t, J = 7.28, 7.28 Hz) ppm. ¹³C NMR (CDCl₃): 16.4 (s), 56.0 (s), 64.4(s), 120.1 (s), 121.8 (s), 137.6 (s), 153.8 (s), 159.4 (s), 161.5 (s) ppm. Anal Calcd for C_{9.075}H_{12.15}N₂OCl_{0.15} (L²·0.075 CH₂Cl₂): C, 63.9; H, 7.2; N, 16.4. Found: C, 63.8; H, 7.2; N, 16.5; the compound was dissolved in CH₂Cl₂ for preparation of the elemental analysis sample.

[Fe(L²)₂](OTf)₂ (2.6). Similarly to **2.1**, **L²** (0.100 g, 0.609 mmol) in 4 mL of methanol was added to a stirring solution of [Fe(CH₃CN)₂(OTf)₂] (0.132 g, 0.305 mmol) in 4 mL of methanol. The immediately dark red coloured solution was stirred for an additional 30 min. The solvent was removed in vacuo and the resulting red oil was triturated in ether (15 mL) for 2 hours. The resulting red free-flowing powder was isolated by vacuum filtration. X-ray quality crystals were obtained by slow diffusion of ether into an ethanolic solution of the compound (0.140 g, 55% yield). IR (KBr) ν_{OH} 3137 cm⁻¹. λ_{max} (MeOH)/nm 496 (1570 M⁻¹·cm⁻¹). ¹H NMR (400 MHz; CD₃OD; Me₄Si): 188.6, 162.7, 131.4, 128.9, 73.4, 53.4, 8.33, -2.48 ppm. Anal Calcd for C₂₀H₂₄F₆FeN₄O₈S₂: C, 35.2; H, 3.5; N, 8.2. Found: C, 35.2; H, 3.4; N, 8.2.

2.3.2. Crystallographic data collection and refinement. All single crystals were coated in Paratone–N oil prior to removal from the glovebox. For structures obtained at 100–120 K, the crystals were supported on Cryoloops and mounted under a stream of cold dinitrogen. For data collection at higher temperatures, the crystal was encased in epoxy resin and mounted to a glass fibre. Data were collected using a Bruker Kappa Apex II CCD diffractometer with Mo K_α radiation and a graphite monochromator. Data were integrated and corrected for absorption effects with the Apex II software package.²³ The SHELXTL software package was used for solving the structures by direct methods and for subsequent refinements.²⁴ Unless otherwise noted, thermal parameters for all non-hydrogen atoms were refined anisotropically. Hydrogen atoms were added at the ideal positions and refined using a riding model where the thermal parameters were set at 1.2 times those of the attached carbon atom. Crystallographic information is collected in Table 2.1.

In the structure of **2.1·LT**, one triflate anion was disordered over 2 positions. These components were modelled with partial occupancies and refined anisotropically. The structure for **2.1·RT** was found to contain several disordered components. Disorder of the triflate anion and O1

were modelled with partial occupancies and refined anisotropically. The position of O3 was disordered over three sites; the thermal parameters of each part were refined isotropically. One bromide in the structure of **2.2** was disordered over two positions; the disordered components were restrained to maintain spherical atoms. Free refinement of disordered solvent for **2.3** resulted in 52% methanol, 45% ethanol, and 3% void; for simplicity, the occupation was constrained to 50% and atoms were refined isotropically due to the large amount of disorder. One hydroxyl group in the structure of **2.5** was disordered over two positions; thermal parameters for each part were refined anisotropically.

2.3.3 Magnetic susceptibility measurements. All samples were prepared under a dinitrogen atmosphere. Crystals of compounds **2.1-2.3** and **2.6** were ground into fine powders, loaded into gelatin capsules, encased in six drops of Eicosane, and inserted into straws for analysis; crystals were not ground for **2.5**. Measurements were performed using a Quantum Design model MPMS–XL superconducting quantum interference device (SQUID) magnetometer in the temperature range of 5 to 300 K under a measuring field of 1000 Oe. The data were corrected by subtracting the measured susceptibility of an empty sample holder and six drops of Eicosane. Diamagnetic corrections were calculated by using Pascal's constants.²⁵

2.3.4. Other physical measurements. Infrared spectra were measured with a Nicolet 380 FT–IR under a dinitrogen flow using an ATR attachment. Visible absorption spectra were obtained using an Agilent 8453 UV-visible spectrometer under air-free conditions using a glass cuvette. ¹H NMR spectra were recorded using Varian INOVA instruments operating at 300 or 400 MHz. Solution magnetic susceptibility measurements were obtained by Evans' method using TMS as the reference at 300 MHz.²⁶⁻²⁸ Elemental analysis was performed by Robertson Microlit

Laboratories in Ledgewood, NJ. High-resolution mass spectra were obtained on an Agilent Technologies 6220 Time-of-flight LC/MS.

Table 2.1. Crystallographic data for **2.1–2.6**.

	2.1·LT	2.1·RT	2.2	2.3
Formula	C ₂₉ H ₃₃ Fe N ₇ O ₉ S ₂ F ₆	C ₂₉ H ₃₃ Fe N ₇ O ₉ S ₂ F ₆	C ₂₇ H ₃₃ Fe N ₇ O ₃ Br ₂	C _{28.50} H ₃₈ Fe N ₇ O ₄ Br ₂
Form wt/ g mol ⁻¹	857.59	857.59	719.27	757.32
Color	Red	Red	Red	Red
Habit	Block	Block	Plate	Plate
T/K	120	296	120	120
Crystal system	Monoclinic	Monoclinic	Monoclinic	Monoclinic
Space group	<i>P2₁/c</i>	<i>P2₁/c</i>	<i>P2₁/c</i>	<i>P2₁/c</i>
Z	4	4	4	4
a/Å	10.2032(2)	10.3855(4)	10.2839(5)	10.0980(2)
b/Å	19.557(3)	20.1767(8)	14.5320(7)	14.0077(3)
c/Å	17.283(2)	17.4647(8)	19.9842(9)	22.0804(5)
α/°	90	90	90	90
β/°	96.879(8)	93.046(1)	96.513(2)	94.7740(10)
γ/°	90	90	90	90
V/Å ³	3423.8(9)	3654.5(3)	2967.3(2)	3112.43(12)
d _{calc} /g cm ⁻³	1.664	1.559	1.610	1.616
Meas. ref	39875	42446	45940	40279
Ind. ref	6490	6008	6790	9462
<i>R</i> _{int}	0.0373	0.0333	0.0793	0.0270
GOF	1.026	1.046	1.010	1.044
<i>R</i> ₁ / % ^a	4.26	4.70	4.20	3.38
<i>wR</i> ₂ / % ^b	10.79	12.51	9.93	8.33

$$^a R_1 = \sum ||F_o| - |F_c|| / \sum |F_o|; \quad ^b wR_2 = \{ \sum [w(F_o^2 - F_c^2)^2] / \sum [w(F_o^2)^2] \}^{1/2}$$

Table 2.1 continued. Crystallographic data

	2.4-LT	2.4-RT	2.5	2.6
Formula	C ₂₇ H ₃₃ Fe N ₇ O ₃ I ₂	C ₂₇ H ₃₃ Fe N ₇ O ₃ I ₂	C ₇₉ H ₇₉ Fe N ₉ O ₃ B ₂	C ₂₀ H ₂₄ Fe N ₄ O ₈ S ₂ F ₆
Form wt/ g·mol ⁻¹	813.25	813.25	1197.88	682.40
Color	Red	Red	Red	Red
Habit	Block	Block	Block	Plate
T/K	120	296	120	100
Crystal system	Ortho	Ortho	Triclinic	Monoclinic
Space group	<i>Pbca</i>	<i>Pbca</i>	<i>P</i> $\bar{1}$	<i>P</i> ₂ / <i>c</i>
Z	8	8	2	4
a/Å	11.0878(4)	11.3371(4)	13.850(3)	13.3173(8)
b/Å	18.8979(6)	19.1168(6)	13.890(3)	15.4235(10)
c/Å	28.2307(9)	28.6754(9)	17.930(4)	14.8826(8)
α /°	90	90	94.41(3)	90
β /°	90	90	103.10(3)	112.692(3)
γ /°	90	90	100.01(3)	90
V/Å ³	5915.4(3)	6214.8(4)	3283.9(11)	2820.2(3)
d _{calc} / g cm ⁻³	1.826	1.738	1.211	1.607
Meas. ref	116396	104197	65015	38061
Ind. ref	6271	7402	16647	10522
<i>R</i> _{int}	0.0525	0.0445	0.0570	0.0387
GOF	1.032	1.034	1.019	1.042
<i>R</i> ₁ / % ^a	2.34	3.18	4.72	3.59
<i>wR</i> ₂ / % ^b	4.99	6.45	11.24	7.96

$$^a R_1 = \sum ||F_o| - |F_c|| / \sum |F_o|; \quad ^b wR_2 = \{ \sum [w(F_o^2 - F_c^2)^2] / \sum [w(F_o^2)^2] \}^{1/2}$$

2.4 Results and discussion.

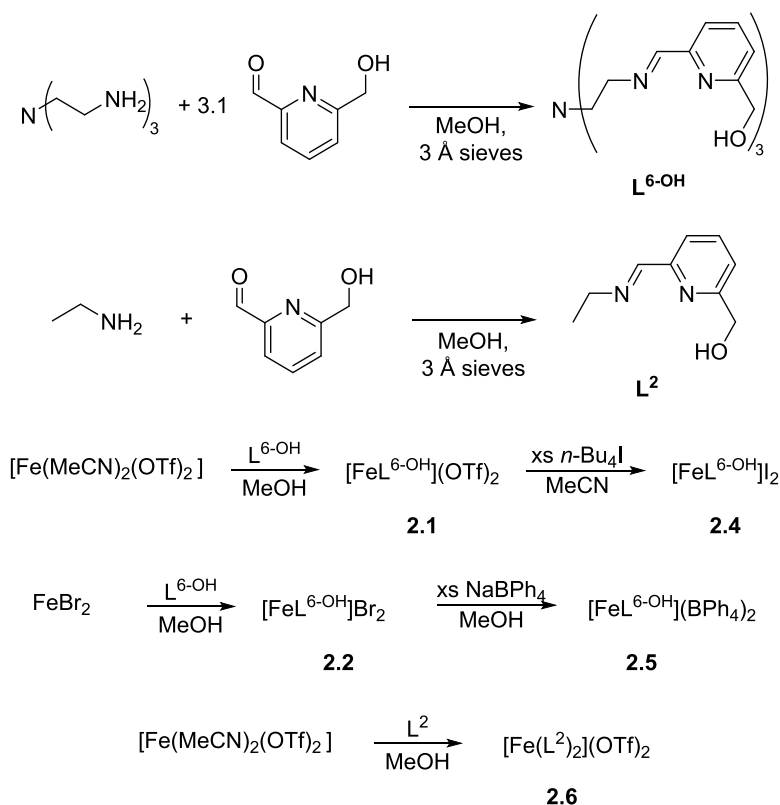
2.4.1 Syntheses. The ligand $\mathbf{L}^{6\text{-OH}}$ is obtained by a condensation reaction of 2-pyridinecarboxaldehyde-6-methanol²¹ with tris(2-amino-ethyl)amine (tren) in methanol at room temperature. The oily ligand is used with minimal purification, and pure metal-containing products are obtained via crystallization. As shown in Scheme 2.1, the ligand is combined with $[\text{Fe}(\text{MeCN})_2(\text{OTf})_2]$ ²² or FeBr_2 in methanol to produce the triflate (**2.1**) or bromide (**2.2** and **2.3**) salts, respectively; subsequent anion exchanges and crystallizations produce analytically pure samples of the iodide (**2.4**) and tetraphenylborate (**2.5**) salts. The triflate anion was chosen because of its C_3 symmetry, potentially enabling greater interaction with the trigonal pocket formed by the ligand. Meanwhile, the halides bromide and iodide allow us to explore the effect of anion size and packing interactions on SCO temperature. The use of tetraphenylborate aims to demonstrate the complex cation's solid-state properties in the absence of significant hydrogen-bonding interactions.

X-ray quality crystals of **2.1**, **2.2**, and **2.4** are obtained by diethyl ether diffusion into saturated alcohol solutions of the compounds; crystals of **2.3** are formed by diethyl ether diffusion into a 50:50 ethanol:methanol solution of **2.2**. Based on elemental analysis and ^1H NMR spectroscopy, a small amount of ethanol co-crystallises with the triflate salt to produce **2.1**, but it is not evident in the crystal structure (vide infra). X-ray quality crystals of **2.5** are produced by ether diffusion into acetonitrile. Elemental analyses and crystallography data for compound **2.5** indicate that approximately two acetonitrile molecules co-crystallise with the salt.

The non-tethered derivative of the $\mathbf{L}^{6\text{-OH}}$ ligand is synthesised by condensation of ethylamine and 2-pyridinecarboxaldehyde-6-methanol to produce \mathbf{L}^2 . This combines with $[\text{Fe}(\text{MeCN})_2(\text{OTf})_2]$ to produce the bis(tridentate) complex **2.6**. X-ray quality crystals are

obtained by diethyl ether diffusion into an ethanolic solution of the complex. Regardless of reactant stoichiometry (2:1 or 3:1 ligand:metal), crystals of $[\text{Fe}(\text{L}^2)_2](\text{OTf})_2$ are isolated.

Scheme 2.1. Reaction sequence for preparing $[\text{FeL}^{6\text{-OH}}]^{2+}$ and $[\text{Fe}(\text{L}^2)]^{2+}$ complex salts.



2.4.2 Anion dependence in solid state magnetic properties. The variable temperature solid-state magnetic susceptibilities for ground crystals of **2.1–2.5** are shown in Figure 2.2. At room temperature, all salts are HS, with $\chi_{\text{M}}T$ values typical for high-spin octahedral Fe(II) complexes ($S = 2$). For the triflate salt **2.1**, $\chi_{\text{M}}T$ is $3.63 \text{ cm}^3 \cdot \text{K} \cdot \text{mol}^{-1}$ at 295 K. Upon cooling, a sharp decrease in $\chi_{\text{M}}T$ begins at 178 K and is virtually complete by 150 K ($T_{1/2} = 173 \text{ K}$), ultimately giving a fully LS sample with $\chi_{\text{M}}T$ equal to $0.06 \text{ cm}^3 \cdot \text{K} \cdot \text{mol}^{-1}$ at 4 K. This salt undergoes the highest and sharpest spin transition observed for all the salts studied in this work. Note that this occurs at 40 K *less* than the parent $[\text{Fe}(\text{6-Me-py})_3\text{tren}](\text{PF}_6)_2$ complex reported by Drago and coworkers.¹⁷

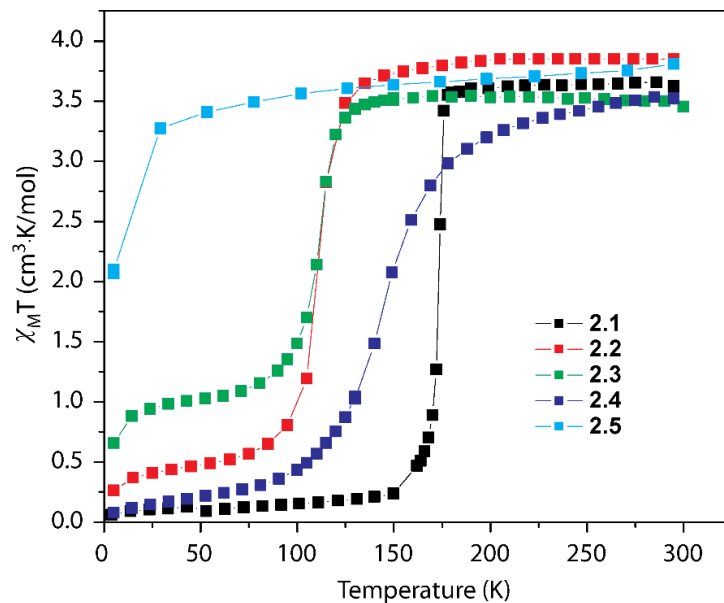


Figure 2.2. Temperature dependence of $\chi_{\text{M}}T$ for **2.1–2.5**. Lines connecting data points are guides to the eye. $H_{\text{dc}} = 1000$ Oe.

Similar to **2.1**, the bromide salts **2.2** and **2.3** show SCO, albeit at a lower temperature. The anion appears to be the major contributor to spin-state properties since both **2.2** and **2.3** show SCO at approximately the same temperature (“ $T_{1/2}$ ” = 113 and 111 K, respectively[‡]). However, the presence of solvate molecules influences the completeness of SCO behavior. In the absence of solvate molecules, the SCO is more complete for **2.2** as $\chi_{\text{M}}T$ decreases to $0.65 \text{ cm}^3 \cdot \text{K} \cdot \text{mol}^{-1}$ at 85 K and $0.26 \text{ cm}^3 \cdot \text{K} \cdot \text{mol}^{-1}$ at 5 K. In contrast, the partially solvated compound **2.3** shows incomplete SCO: $\chi_{\text{M}}T$ is $1.20 \text{ cm}^3 \cdot \text{K} \cdot \text{mol}^{-1}$ at 85 K, and drops to $0.66 \text{ cm}^3 \cdot \text{K} \cdot \text{mol}^{-1}$ at 5 K. The interplay is complex, since we also find for **2.2** that varying sample grinding conditions changes SCO completeness (Figure 2.3). Such impacts on Fe(II) SCO properties have been observed elsewhere.^{29,30} Regardless of the origins, a comparison of the data for both compounds indicates significant intermolecular effects are operative.

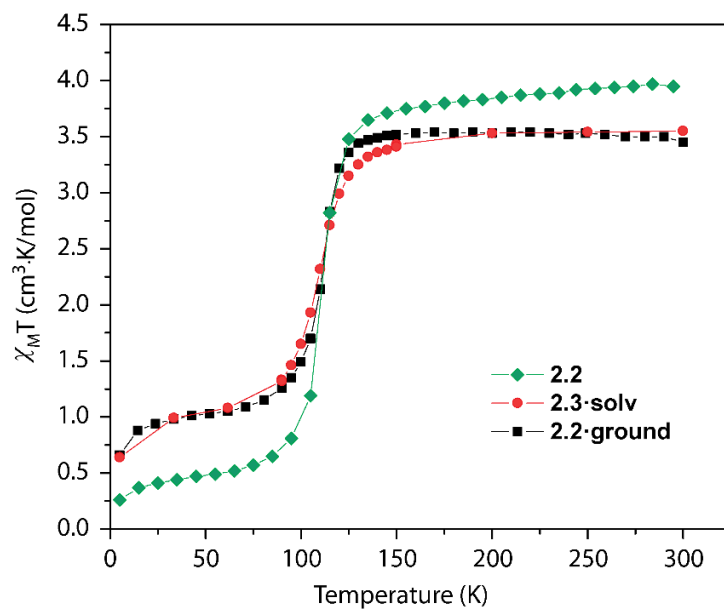


Figure 2.3. Temperature dependence of $\chi_{\text{M}}T$ for **2.2** and **2.3**. Samples **2.2** and **2.2·ground** differ only in the amount of grinding applied to the crystals (**2.2·ground** was ground more vigorously than **2.2**). $H_{\text{dc}} = 1000$ Oe.

Meanwhile, the iodide salt **2.4** undergoes complete SCO ($T_{1/2} = 145$ K), albeit more gradually than **2.1**. The $\chi_{\text{M}}T$ value at 295 K of $3.52 \text{ cm}^3 \cdot \text{K} \cdot \text{mol}^{-1}$ gradually decreases to $3.20 \text{ cm}^3 \cdot \text{K} \cdot \text{mol}^{-1}$ at 198 K, then decreases more sharply to $0.44 \text{ cm}^3 \cdot \text{K} \cdot \text{mol}^{-1}$ at 100 K, and levels out to $0.08 \text{ cm}^3 \cdot \text{K} \cdot \text{mol}^{-1}$ at 5 K.

The tetraphenylborate salt **2.5** remains HS throughout the temperature range probed. A $\chi_{\text{M}}T$ value of $3.81 \text{ cm}^3 \cdot \text{K} \cdot \text{mol}^{-1}$ at 295 K decreases slightly to $3.27 \text{ cm}^3 \cdot \text{K} \cdot \text{mol}^{-1}$ by 29 K; a downturn in $\chi_{\text{M}}T$ to $2.07 \text{ cm}^3 \cdot \text{K} \cdot \text{mol}^{-1}$ at 5 K is ascribed to zero-field splitting of the HS complex.

Similarly, magnetic susceptibility data acquired at 120 K and 5 K (3.38 and $2.50 \text{ cm}^3 \cdot \text{K} \cdot \text{mol}^{-1}$, respectively) indicate that the complex **2.6** remains HS. The slight decrease in $\chi_{\text{M}}T$ is attributed to zero-field splitting of the HS compound.

Irrespective of structural considerations, a few trends can be gleaned from the magnetic susceptibility data. The largest counteranions capable of hydrogen bonding (OTf^- , Γ^-) favour higher SCO temperatures as well as more complete transitions. Decreasing the size of the anion

appears to stabilise the high spin state, as indicated by lower $T_{1/2}$ values and incomplete conversion in the case of **2.2**. For the same anion, solvate molecules appear to affect the degree of completion of SCO. Disruption of hydrogen-bonding interactions also appears to stabilize HS states as seen with **2.5**. Whereas the magnetic behavior of the iodide salt **2.4** can be considered spin equilibrium, those of **2.1** and **2.2** show stronger cooperativities. Finally, iminopyridine groups do not offer sufficient ligand field strength to overcome the weak field generated by direct coordination of hydroxyl groups, as exemplified in the magnetic behavior of **2.6**.

2.4.3 Structural studies. To better understand the subtle differences in magnetic properties, single-crystal X-ray diffraction analyses were performed on compounds **2.1–2.6**. Relevant bond lengths, angles, and distortion parameters are provided in Table 2.1. All cationic complexes (except **2.6**) show the same basic features. The first coordination sphere of the Fe-podand complexes comprises six nitrogen atoms, from three bridgehead nitrogen (N7) does not coordinate to the iron centre; the closest contact observed in all of the structures presented here is 3.167(1) Å for **2.4·RT**. The structural distortion parameters Σ^{31-33} and $\Theta^{33,34}$ for **2.1·RT**, **2.2**, **2.3**, **2.4·RT**, **2.5**, and **2.6** are indicative of large distortion away from perfect octahedral coordination, similar to HS Fe(II) complexes containing bidentate ligands. Structures **2.1·LT** and **2.4·LT** show smaller octahedral and trigonal distortion values, consistent with conversion to LS configurations.

Comparing high- and low-temperature structures for **2.1** and **2.4**, no crystallographic phase transitions are observed upon cooling, as indicated by retention of the same space group at 296 K and 120 K; unit cell volumes contract by approximately 6% and 5% for **2.1** and **2.4**, respectively, as expected. Characteristic of this ligand type,^{18,19,35} the Fe-N7 distance shows strong dependence on the spin state (Figure 2.10): in the LS state, the bridgehead nitrogen adopts a quasi-planar conformation, pointing slightly *away* from the Fe(II) centre; upon warming

it assumes a more pyramidal geometry, pointing *towards* the metal. The conformation change is a consequence of the Fe–N bonds expanding upon the LS→HS conversion. The change is less pronounced for the iodide salt **2.4**, as conversion to the fully LS state is not complete at 120 K.

Variations on the anion chelation are seen between **2.1·RT** and **2.1·LT**: at room temperature, the two chelating arms bind with two oxygen atoms of the triflate; while at 120 K, the two arms interact with only one oxygen atom. In the structures of **2.4**, we note that the two arms of the iodide-containing structures do not interact with the anion equally, as denoted by significantly different O···I distances.

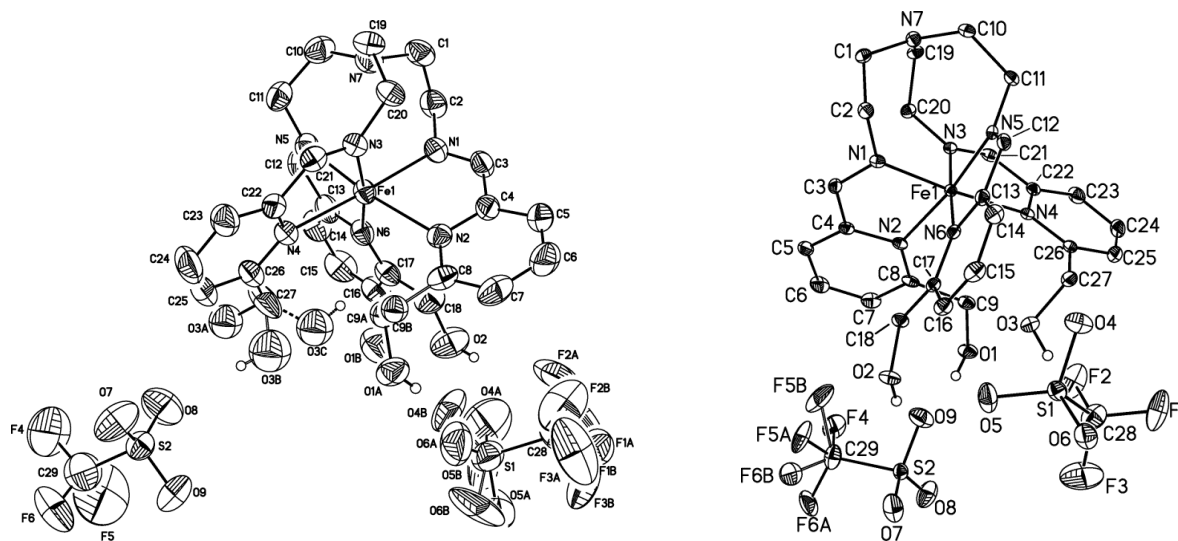


Figure 2.4. Crystal structure of **2.1·RT** (left) at 296 K and **2.1·LT** (right) at 120 K. Atoms rendered with 40% thermal ellipsoids. Hydrogen atoms except those of the hydroxyls have been omitted for clarity.

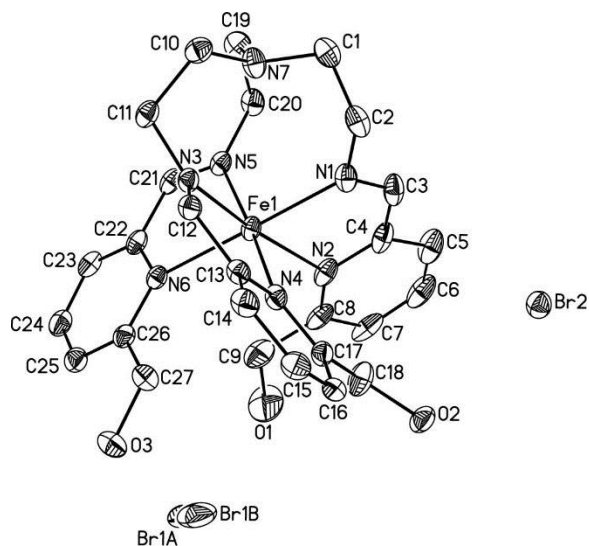


Figure 2.5. Crystal structure of **2.2** at 120 K. Atoms rendered with 40% thermal ellipsoids. Hydrogen atoms have been omitted for clarity.

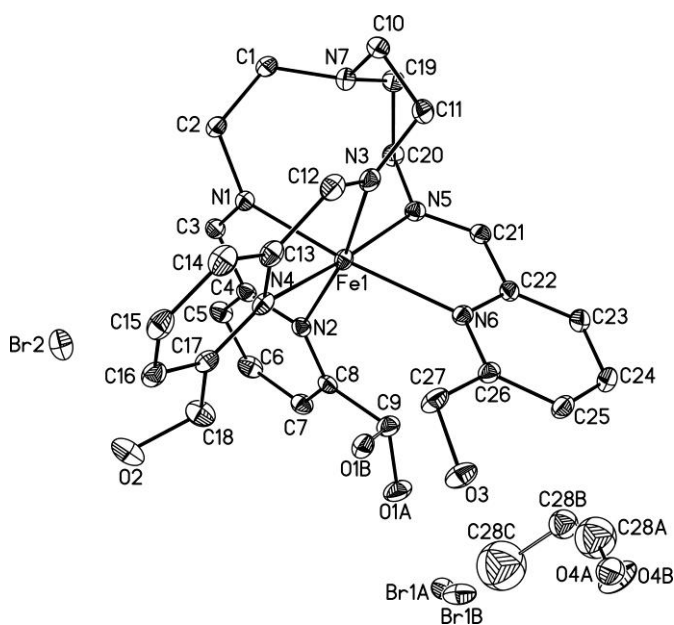


Figure 2.6. Crystal structure of **2.3** at 120 K. Hydrogen atoms have been removed for clarity. Atoms rendered with 40% thermal ellipsoids. Solvent molecules (C28a, C28b, C28c, O4a and O4b) were refined isotropically due to high level of disorder.

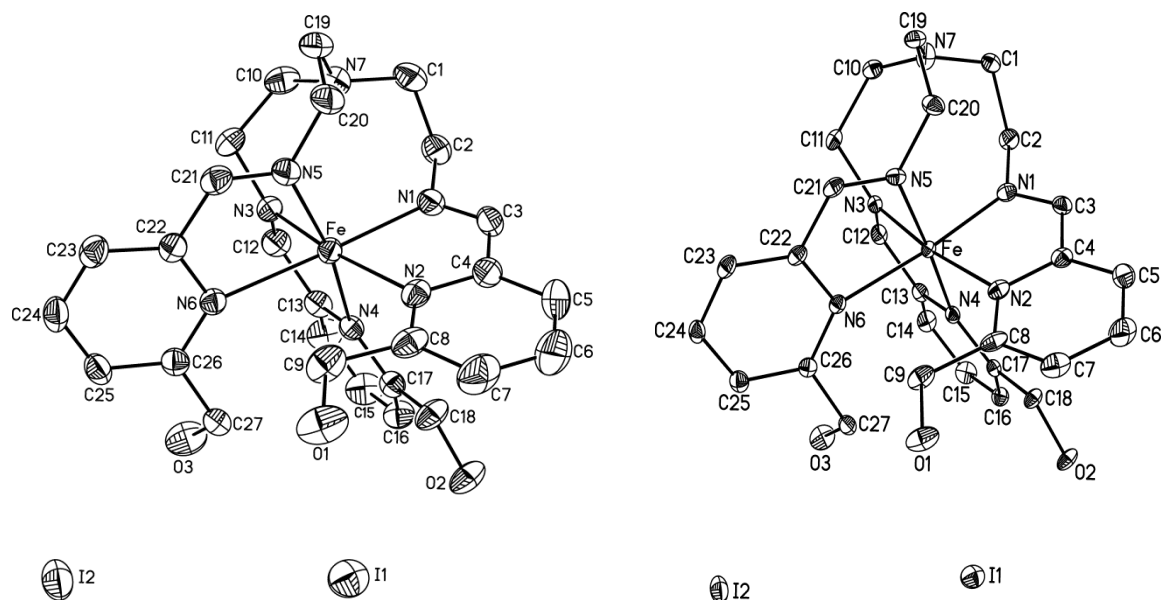


Figure 2.7. Crystal structure of **2.4-RT** at 296 K (left) and **2.4-LT** (right) at 120 K. Atoms rendered with 40% thermal ellipsoids. Hydrogen atoms have been omitted for clarity.

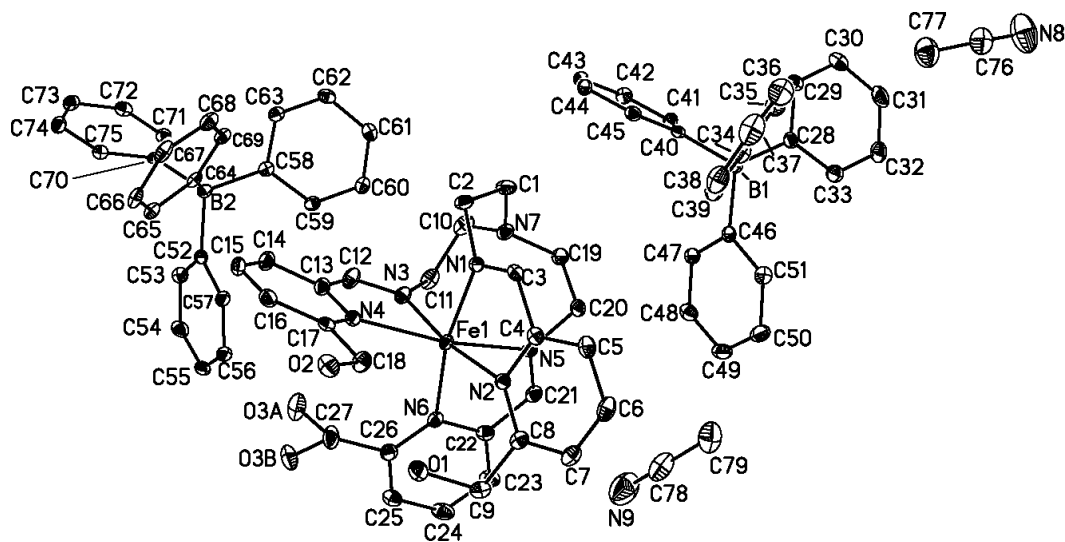


Figure 2.8. Crystal structure of **2.5** at 120 K. Atoms rendered with 40% thermal ellipsoids. Hydrogen atoms have been omitted for clarity.

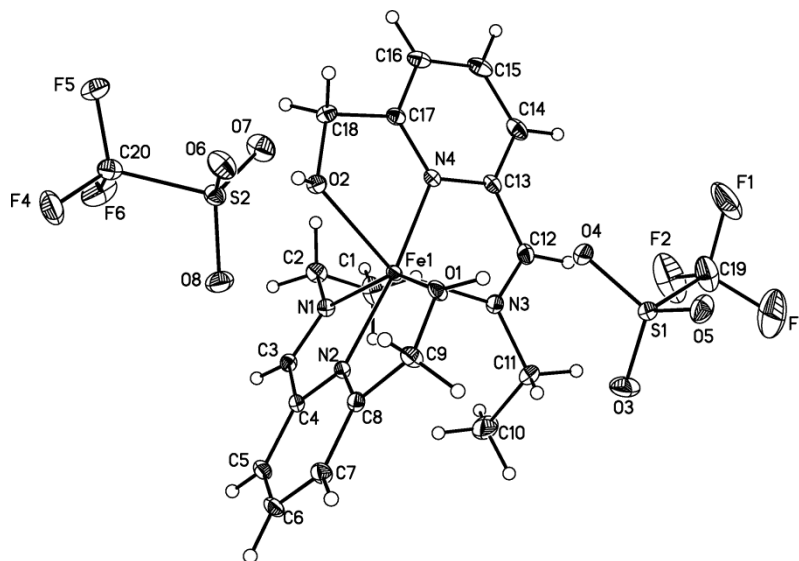


Figure 2.9. Crystal structure of **2.6** at 120 K. Atoms rendered with 40% thermal ellipsoids.

Table 2.2. Selected bond distances (Å) and distortion parameters (°)

	Fe–N _{im}	Fe–N _{py}	Fe–N _{bridge}	Fe···Fe ^a	Σ	θ
2.1·LT	1.948(2)	2.098(2)	3.723(2)	10.937(1)	80.5(3)	119.5
2.1·RT	2.147(4)	2.331(4)	3.187(3)	11.323(4)	115.5(3)	196.6
2.2	2.128(3)	2.319(7)	3.192(4)	9.0074(3)	107.8(2)	195.3
2.3	2.151(3)	2.322(3)	3.241(1)	8.8440(1)	114.7(2)	196.6
2.4·LT	1.967(4)	2.112(4)	3.537(1)	8.8845(5)	85.0(3)	129.5
2.4·RT	2.134(4)	2.325(4)	3.167(1)	9.1254(5)	112.9(3)	195.4
2.5	2.159(3)	2.277(3)	3.244(2)	9.327(4)	125.4(2)	196.6
2.6	2.184(2)	2.093(2)	^b	8.0556(5)	140.1(1)	441.7

^a shortest contact in structure; ^b d_{Fe–OH} = 2.174(1) Å

Table 2.3. Shortest intermolecular hydrogen-bond interactions.^a

	2.1·RT	2.1·LT	2.2	2.3	2.4·RT	2.4·LT	2.5	2.6
O1···X1 ^b	2.58(1) ^c	2.813(3) ^d	3.354(8)	3.22(4)	3.410(2)	3.360(2)	–	2.636(1)
O2···X1	2.68(1) ^c	2.964(3) ^d	3.203(7)	3.277(6)	4.037(2)	3.888(2)	3.154(7) ^e	2.610(1)
O3···X2	2.83(2)	–	3.224(3)	3.213(2)	3.599(2)	3.596(2)	3.326(13) ^e	–
O3···N7	4.40(9)	2.827(3)	–	–	–	–	–	–
O1···O2a	–	–	–	–	2.743(3)	2.705(3)	2.742(2)	–

^a Interaction defined as distance less than the sum of the van der Waals radii: (O···O = 3.04 Å, O···Br = 3.37 Å, O···I = 3.50 Å, O···N = 3.02 Å; taken from "Atomic Radii of the Elements," in CRC Handbook of Chemistry and Physics, 92nd Edition (Internet Version 2012), W. M. Haynes, ed., CRC Press/Taylor and Francis, Boca Raton, FL.)

^b X1 is defined as 'anion 1' (lies closest to the trigonal pocket), X2 is defined as 'anion 2' (See renderings/packing plots).

^c Interact with two different oxygen atoms of triflate

^d Interact with same oxygen atom of triflate

^e Defined as the distance between the centroid of the phenyl and the oxygen

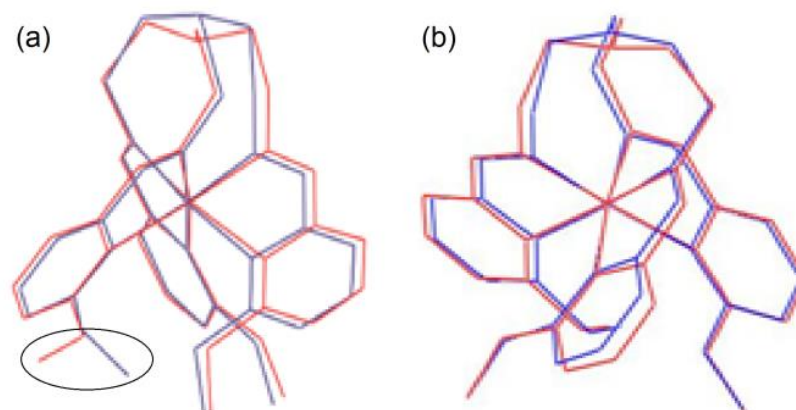


Figure 2.10. Overlay of room temperature (red) and low temperature (blue) structures for the cations in **2.1** (a) and **2.4** (b). All hydrogen atoms and the disordered components of **2.1·RT** have been omitted for clarity. The circle emphasizes the orientation of O3 in the HS and LS states for **2.1**.

For the structures of **2.1–2.4**, the immediate anion-cation interactions of each salt are not identical, but comparable: two hydroxyl groups on the same complex (containing O1 and O2) chelate one of the anions, while the third hydroxyl (O3) contorts out of the plane of the pyridine. This facilitates better interaction either with the second anion (**2.1•RT**, **2.2** and **2.4**) or the bridgehead nitrogen of an adjacent cation (**2.1•LT**). Details of anion-cation interactions are provided in Table 2.3.

Since the local interactions are comparable for **2.1, 2.2, 2.4**, yet the magnetic properties are quite distinct, more detailed investigations of packing and other subtle intermolecular interactions are warranted. We note a trend between increasing (shortest) Fe²⁺–Fe distances (**2.3** \approx **2.2** < **2.4•RT** < **2.1•RT**, Table 2.2) and increasing SCO $T_{1/2}$ and cooperativity. This is consistent with the general notion that anion-cation interactions are critical, and suggests that larger anions may provide more lattice flexibility for Fe–ligand bond contraction upon SCO.

Comparing the structures of the bromide salts, small differences in interactions may give some insight into differences in the completeness of SCO, with the caveat that the magnetic properties have already been shown to be affected by grinding (i.e. bulk interactions may be more important than local interactions). Although the average Br[–]–O distances are shorter in **2.3** than **2.2** (3.22 versus 3.27 Å respectively⁸), additional hydrogen-bonding interactions occur between the anions and the solvent in **2.3**. Also, complex packing in **2.3** prevents hydrogen-bonding interactions between cations, with a column of solvent molecules parallel to the *c* axis in **2.3** (Figure 2.13). Similar to what was observed with the spin-state properties of partially solvated [(H₂bip)₂Fe(pic)]Br₂ salts,¹³ we propose that additional solvent-anion interactions reduce the strength of anion-cation interactions, effectively separating metal centres from each other and resulting in incomplete SCO. The effect would be similar to that of exhaustive grinding: smaller

particles with more surface-site Fe(II) ions are less connected to neighbouring Fe(II) ions and have higher barriers to SCO, stabilizing the HS state.²⁹

Comparing the two salts that unambiguously undergo complete SCO (**2.1** and **2.4**), the packing of cations in **2.4** (Figure 2.14) generates unique intermolecular interactions: adjacent cations show hydrogen bonding through the hydroxyl groups containing O1 and O2. This interaction lengthens the O2...F contact (Table 2.3), making the distance between those atoms greater than the sum of their van der Waals radii. Through this contact, it is plausible that if one Fe(II) centre switches from HS to LS, an adjacent cation may be compelled to remain HS to maintain the hydrogen bond. The combination of weaker anion chelation and cation-cation hydrogen-bonding may inhibit productive cooperativity between metal centres, resulting in a more gradual SCO process.

Meanwhile, cation-cation interactions are also observed in the structures of **2.1**, as mentioned earlier, but in this case they appear to *enhance* SCO cooperativity. The cations of **2.1·RT** pack in a head-to-toe fashion, with the hydroxyl groups all interacting with triflate anions. Upon cooling, the hydroxyl group (O3) does not interact with a triflate, but shifts so that it has a significant interaction with the bridgehead nitrogen of a neighbouring complex (Figure 2.18, right; also Figure 2.16). Combined with spin-state induced Fe-N distance changes in the podand ligand, the temperature-dependent changes in packing evoke a “push-pull” type mechanism: the SCO experienced by the Fe(II) centre pushes the bridgehead amine out while the hydroxyl orientation change and subsequent acid-base interaction pulls on the amine. Although the observed interactions may be an artefact of the molecular packing arrangement, they highlight a potentially critical spin-state directing role for the unbound (to Fe) bridgehead amine group, one that should be considered when seeking to control spin-state changes in solution with this family of complexes.

Note that a previous study has demonstrated that pyramidalization of the tren backbone via alkylation converts a Fe(II) SCO complex to a LS species.³⁶

In comparison, strong anion-cation interactions are not observed in the structure of **2.5**. The large size of tetraphenylborate prevents the anion from packing within the trigonal pocket, allowing cation-cation hydrogen bonding between O1 and O2 of adjacent complexes, and the cations pack in a toe-to-toe fashion (Figure 2.17). Some subtle OH \cdots BPh $_4^-$ - π interactions are apparent (Figure 2.17, Table 2.3); however, unlike the other podand structures with pocket-packing anions, the anion does not pull ligand hydroxyl groups and their associated arms towards one another. The lack of significant anion-cation interactions and the presence of cation-cation interactions similar to those seen for **2.4** apparently contribute to the lack of SCO observed in this salt.

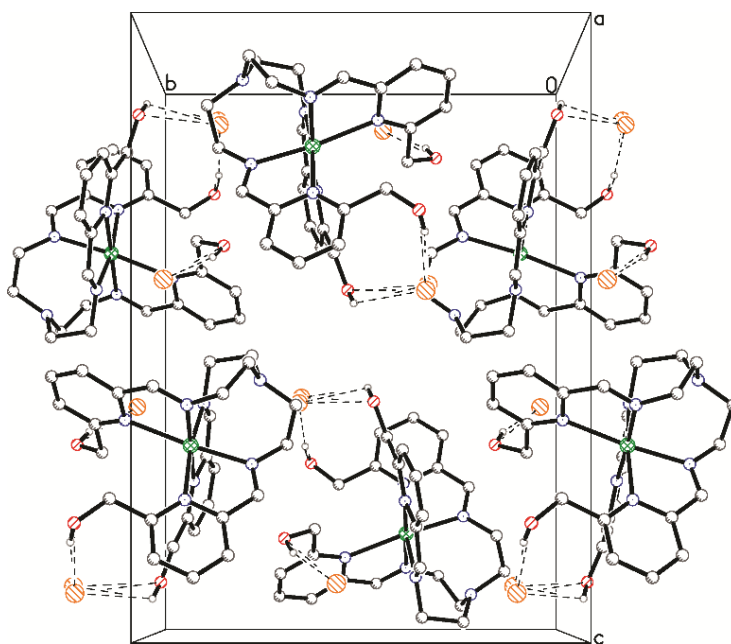


Figure 2.11. Packing plot of **2.2** down the *a* axis. Fe, C, N, O, H and Br atoms are colored green, dark gray, blue, red, light gray and orange respectively. Dashed bonds are to emphasize hydrogen bonding interactions.

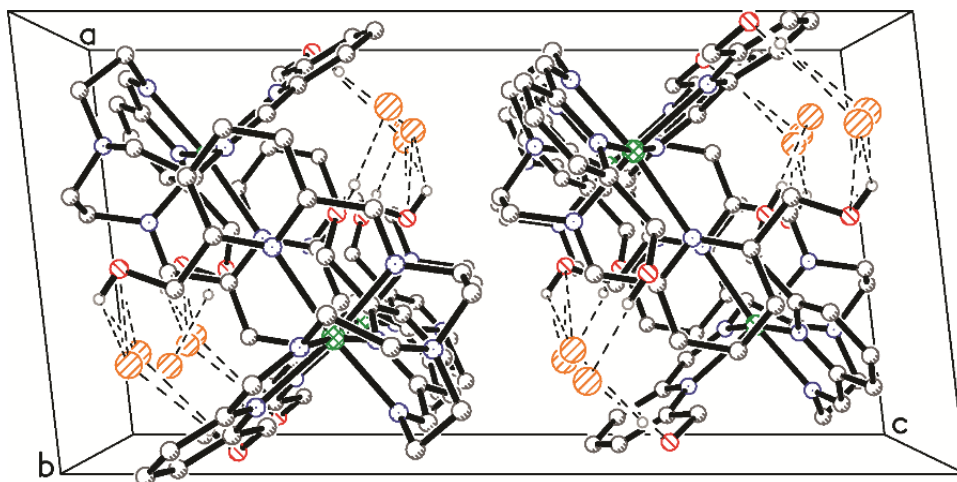


Figure 2.12. Packing plot of **2.2** down the *b* axis. Fe, C, N, O, H and Br atoms are colored green, dark gray, blue, red, light gray and orange respectively. Dashed bonds are to emphasize hydrogen bonding interactions.

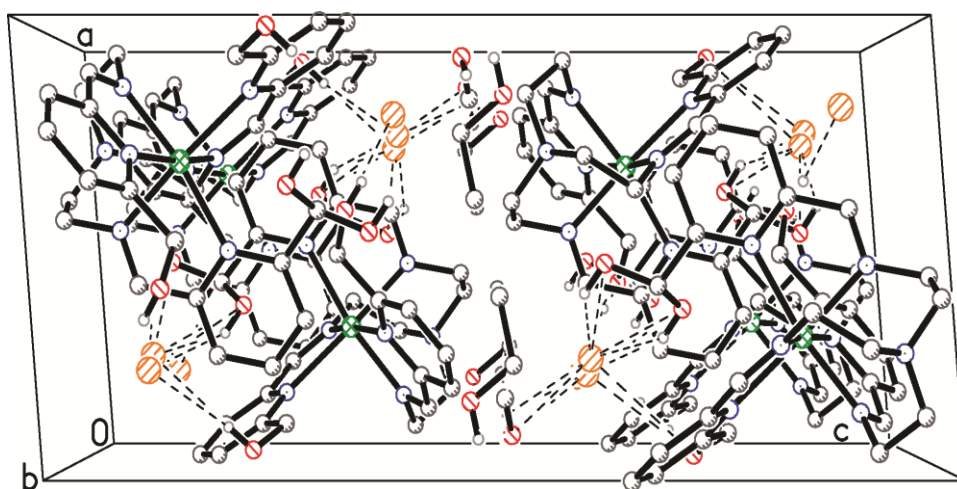


Figure 2.13. Packing plot of **2.3** down the *b* axis. Fe, C, N, O, H and Br atoms are colored green, dark gray, blue, red, light gray and orange respectively. Dashed bonds are to emphasize hydrogen bonding interactions.

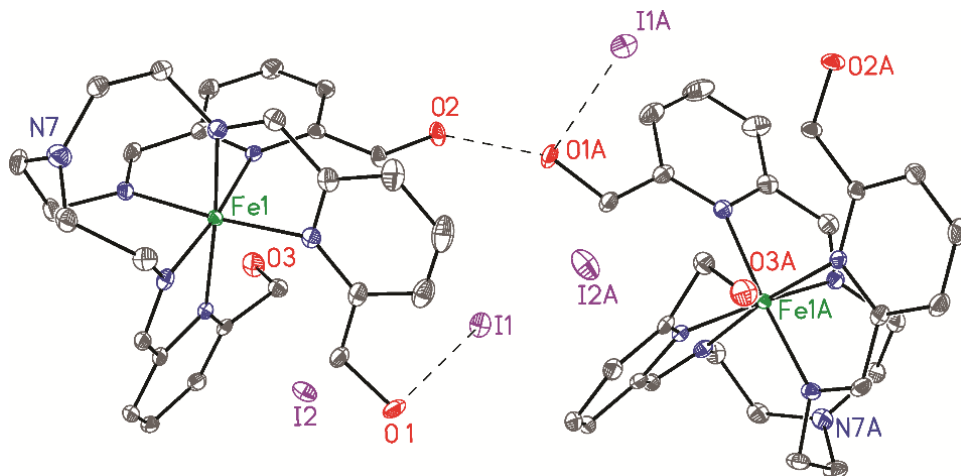


Figure 2.14. Intermolecular interactions for the structures of compound **2.4-LT**. Analogous interactions are seen at 296 and 120 K. Atoms rendered with 40% thermal ellipsoids. Fe, C, N, O and I atoms are colored green, dark gray, blue, red and purple respectively. Hydrogen atoms have been omitted for clarity.

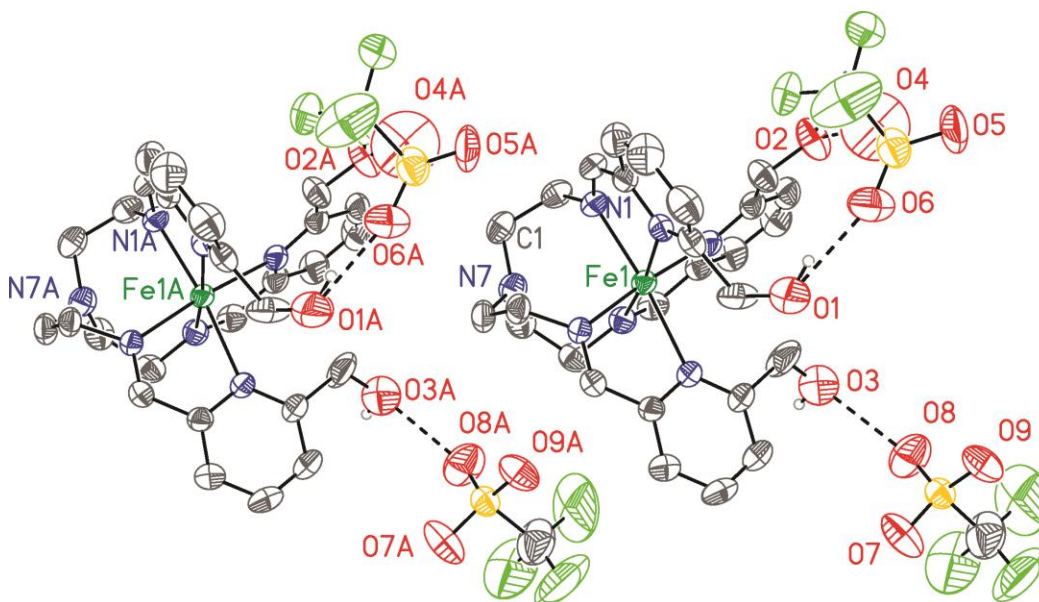


Figure 2.15. Anion-cation interactions of **2.1-RT**. Atoms rendered with 40% thermal ellipsoids. Fe, C, N, O, S and F atoms are colored dark green, dark gray, blue, red, yellow and light green respectively. Hydrogen atoms except those of the hydroxyls have been omitted for clarity.

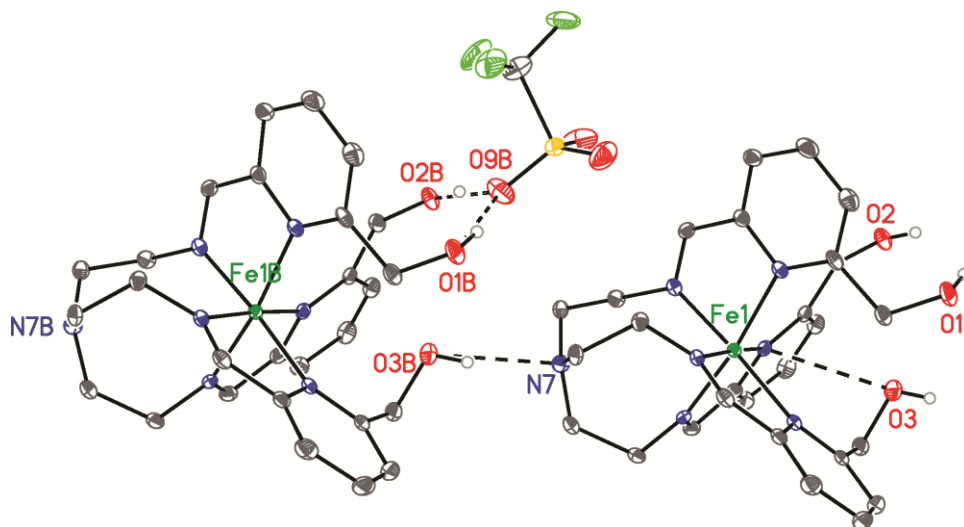


Figure 2.16. Anion-cation and cation-cation interactions of **2.1·LT**. Fe, C, N, O, S and F atoms are colored dark green, dark gray, blue, red, yellow and light green respectively. Hydrogen atoms except those of the hydroxyls have been omitted for clarity.

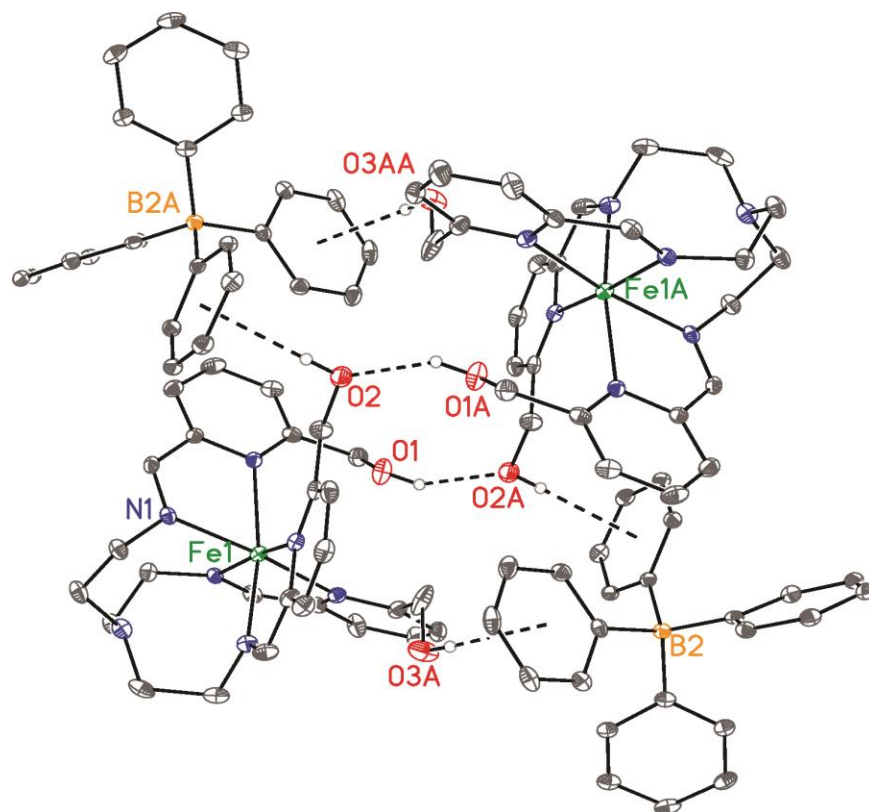


Figure 2.17. Intermolecular interactions of **2.5**. Fe, C, N, O, and B atoms are colored dark green, dark gray, blue, red, and yellow respectively. Hydrogen atoms except those of the hydroxyls and disorder of O3 have been omitted for clarity.

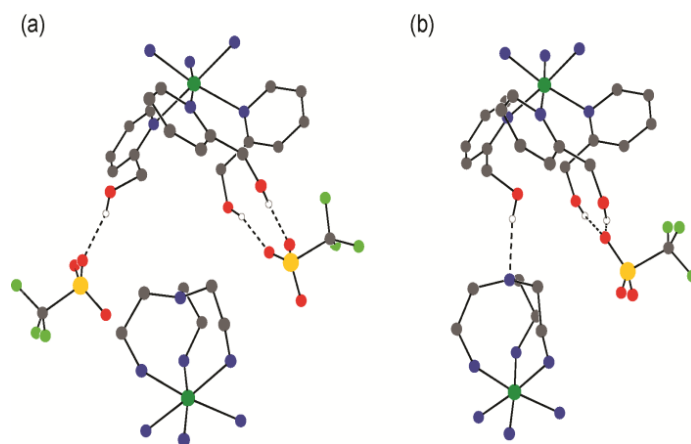


Figure 2.18. Comparison of key intermolecular interactions in **2.1·RT** (a) and **2.1·LT** (b). Dark green, blue, red, grey, yellow, and light green spheres represent Fe, N, O, C, S and F respectively. Disordered components, nonessential C atoms, non-hydroxyl H atoms, and the second triflate in (b) has been removed for clarity.

In the absence of a tether between the ligand arms, two iminopyridine-hydroxyl ligand arms coordinate in a meridonal tridentate fashion to produce **2.6**. The coordination environment of the iron(II) centre is different from the tethered ligand set, as oxygen and nitrogen atoms combine to give a N_4O_2 first coordination sphere. The Fe- N_{im} and Fe-O bond lengths (Table 2.2) are consistent with a HS species, in accordance with the magnetic susceptibility data. Interestingly, the Fe- N_{py} distances are actually more comparable to the LS podand structures; however, these shorter contacts are likely due to steric constraints imposed by the meridonal coordination mode, and is common for planar-terpyridine type ligands.³⁷ The “octahedral” coordination environment is highly strained as indicated by the large calculated Σ and θ values which are similar to values calculated for similar ligand environments.³³ A strong hydroxyl stretch at 3137 cm^{-1} is observed in the IR, signifying that the hydroxyl group is protonated. The presence of two triflate counteranions and C-O bond lengths typical for an sp^3 hybridized carbon,³⁸ indicate that the oxygens are not oxidized/deprotonated and metal is iron(II). There are hydrogen bonding interactions between the coordinated hydroxyl groups and the triflate counteranions, but no intermolecular interactions between cations are observed (Figure 2.19).

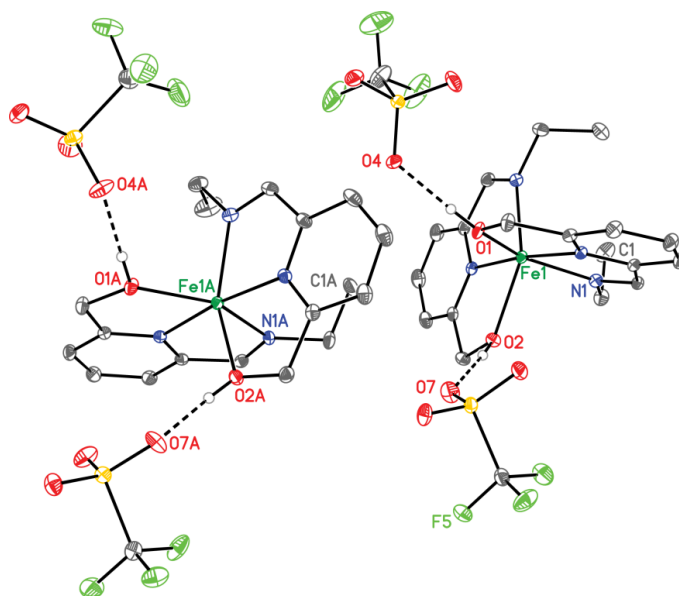


Figure 2.19. Cation-anion interactions for **2.6**. Fe, C, N, O, S and F atoms are colored dark green, dark gray, blue, red, yellow and light green respectively. Hydrogen atoms except those of the hydroxyls have been omitted for clarity.

2.4.4 Solution (magnetic) properties. Based on relatively low solid-state $T_{1/2}$ values, it is unlikely that SCO would be observed for the $[\text{FeL}^{6\text{-OH}}]^{2+}$ complex in solution within the limited temperature range available for most solvents; nevertheless solvent environments are sufficiently distinct from the crystal lattice that there are several examples of solid-state HS compounds which undergo spin equilibrium in solution.^{12,39} Even if $[\text{FeL}^{6\text{-OH}}]^{2+}$ were HS at all temperatures, establishing stability in polar solvents informs our efforts to corral labile ions in solution.

Crystals of **2.1**, **2.2**, or **2.4** dissolved in CD_3OD solution all show identical spectra, indicating that the anion has little effect on the solution characteristics of the cation at room temperature. The $[\text{FeL}^{6\text{-OH}}]^{2+}$ complex is HS, with paramagnetic shifting and broadening of proton resonances (Figure 2.21, bottom). There are four strong but broad resonances and several smaller peaks (–5 to 80 ppm) due to a combination of rapid ligand twisting and lability. Resonances assigned to a small amount of ligand dissociation and/or hydrolysis are observed, but these do not increase over time. In comparison to the tripodal complex, the ^1H NMR spectrum for $[\text{Fe}(\text{L}^2)_2]^{2+}$ contains 8 strong paramagnetically broadened and shifted peaks (–2 to 190 ppm, Figure A.1.8,

bottom). There is no indication of ligand hydrolysis upon dissolution in CD₃OD. Based on the solid state coordination environments for **2.1-2.5** and **2.6**, several coordination modes are possible for the tripodal complexes, including FeN₆ and FeN₄O₂. Switching between these two modes could account for the muddled ¹H NMR spectrum for [FeL^{6-OH}]²⁺, and dissociation of the third arm could make it susceptible to hydrolysis.

To test for SCO and possible anion dependence in solution, the magnetic susceptibilities of **2.1**, **2.2**, **2.4**, and **2.6** were studied in CD₃OD from 193-296 K using Evans' method (Figure 2.22). All three [FeL^{6-OH}]²⁺ salts and **2.6** remain HS down to 183 K. With cooling, the resonances for [FeL^{6-OH}]²⁺ sharpen and become more prolific (24 total), indicative of a low-symmetry species in solution (Figure 2.21). For comparison, the (non-hydroxylated) compound [Fe(6-Me-py)₃tren](PF₆)₂ is HS from room temperature to 185 K in acetone, due to the steric hindrance of the 6-position modification.¹⁷ Complex **2.6** demonstrates Curie behavior upon cooling down to 193 K in solution. The number of peaks observed remains constant indicating that the complex is symmetric at room temperature (Figure A.1.12).

The solution stabilities of **2.2** and **2.6** in CD₃OD were monitored by ¹H NMR over three days (Figures 2.20 and A.1.8). In both cases, small changes occur in the NMR spectra over time, indicative of a small amount of complex degradation/lability. No significant changes in $\chi_{\text{M}}T$ values (3.5 and 3.2 cm³ K mol⁻¹ for **2.2** and **2.6**, respectively) are seen, indicating that any lability imparts minimal effects on the solution magnetic properties. Through these stability studies, we can attribute any changes seen in $\chi_{\text{M}}T$ at variable temperatures to changes in the spin state and not due to complex degradation over the several hours required for the variable temperature experiment.

As a measure of each complex's stability in the presence of a strong field ligand, three equivalents of 2,2'-bipyridine (bpy) were added to solutions of **2.2** and **2.6**, respectively. Within 5

minutes, a decrease in χ_{MT} to $0.5 \text{ cm}^3 \cdot \text{K} \cdot \text{mol}^{-1}$ for **2.2** and $0.3 \text{ cm}^3 \cdot \text{K} \cdot \text{mol}^{-1}$ for **2.6** occurs, and signals corresponding to free ligands increase in intensity (Figures A.1.9–A.1.11), indicating the formation of LS $[\text{Fe}(\text{bpy})_3]\text{X}_2$ ($\text{X} = \text{Br}^-$ or OTf^-). The lability of the HS species allows bpy to easily substitute for the ligands and form LS complexes.

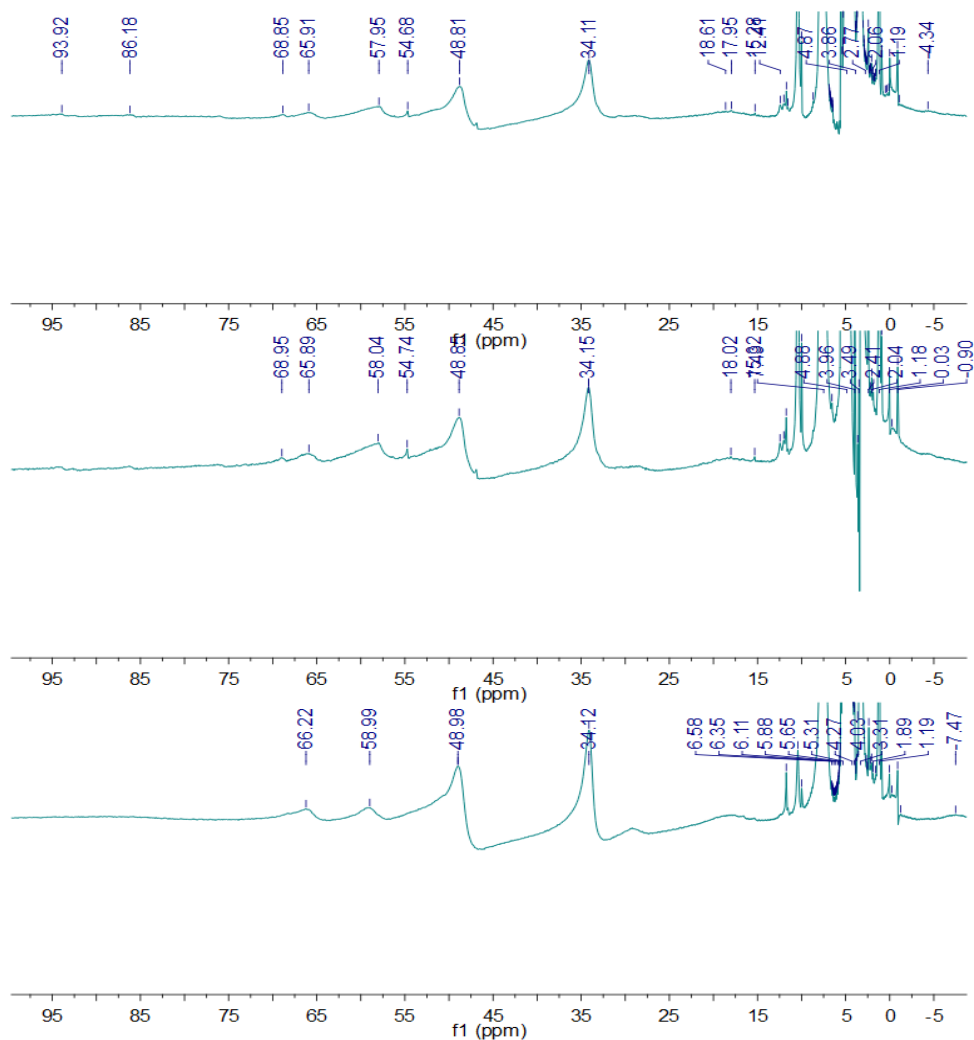


Figure 2.20. ^1H NMR spectra obtained at 295 K at 300 MHz with TMS as the reference of **2.2** at $t=10$ min. (bottom), $t=24$ hr (middle) and $t=3$ days (top). After 24 hours, additional peaks begin to appear at 54.7, 68.9, 86.2 and 93.9 ppm indicative of complex degradation.

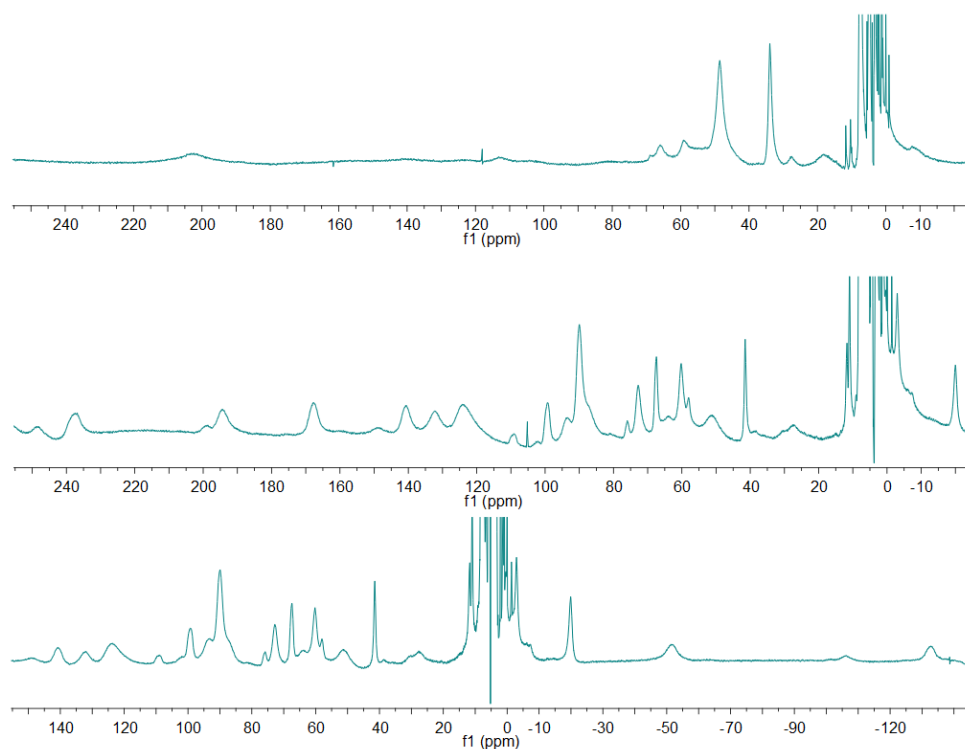
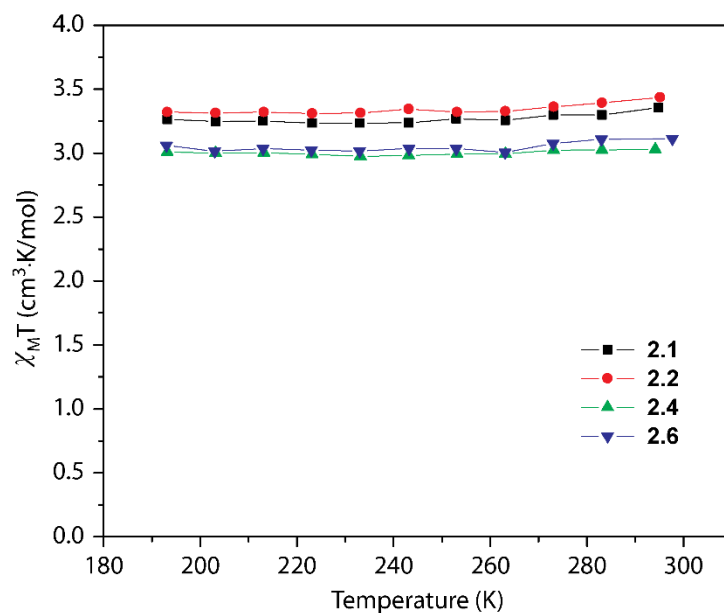


Figure 2.21. ^1H NMR spectra of **2.1** at 295 K (top) and 213 K (middle and bottom) obtained at 300 MHz with TMS as the reference. At room temperature, no peaks are observed below -20 ppm.



Figures 2.22. Variable temperature solution magnetic susceptibility of **2.1**, **2.2**, **2.4**, and **2.6** in CD_3OD using Evans method.

2.5 Conclusions.

We have prepared several salts of a new tripodal hexadentate $[\text{FeL}^{6\text{-OH}}]^{2+}$ complex and studied their temperature-dependent structural and magnetic properties. We observe that covalent linkage of iminopyridine-hydroxyl ligand arms is required to poise functional groups for anion binding: without it, the hydroxyl groups bind to the Fe(II) centre. Solid state SCO temperatures, completeness and cooperativity depend on several complex and interrelated factors, some of which are extracted from structural comparisons. We observe that larger anions capable of strong hydrogen bonding interactions appear to fit better with the hydroxyl-containing arms, and may also provide more flexibility for the complex to change shape upon HS \rightarrow LS conversion, while weakly interacting anions stabilize the HS state. Cation-cation and cation-solvent interactions impart somewhat capricious effects on SCO, but with the exception of **2.1** they appear to work against sharp transitions at higher temperatures. Subtle interactions are not easily controlled in the solid state; nevertheless the observation of anion dependence in SCO properties makes this complex promising for continued efforts in anion-triggered spin-state switching schemes.

In methanol solution, salts of $[\text{FeL}^{6\text{-OH}}]^{2+}$ remain HS down to 183 K, but show higher levels of stability are achieved than tris(bidentate) Fe(II) complexes with similar ligand fields. If the SCO temperature can be increased, then anion dependence in solution spin-state switching may be observed for tripodal Fe(II) complexes. In that vein, the structural analyses presented here suggest that only two arms are needed for anion chelation. Previous work by Steed and co-workers has shown that only two arms are necessary for strong anion binding in Ru(II) organometallic complexes.^{40,41} Using the third arm for electronic/steric tuning of the ligand field could drive SCO to higher temperatures in the solid-state and in solution. Efforts to incorporate such temperature tunability in heteroarm versions of $[\text{FeL}^{6\text{-OH}}]^{2+}$ are underway. This will allow us to address the

significance of anion chelation and/or “push-pull” interactions on the host:guest tuning of spin-state switching in solution.

2.6 Acknowledgments.

We thank the National Science Foundation (CHE-1058889) and Colorado State University for financial support.

REFERENCES

- (1) Gütlich, P.; Garcia, Y.; Goodwin, H. A. *Chem. Soc. Rev.* **2000**, 29, 419.
- (2) Gütlich, P.; Hauser, A. *Coord. Chem. Rev.* **1990**, 97, 1.
- (3) Real, J. A.; Gaspar, A. B.; Munoz, M. C. *Dalton Trans.* **2005**, 2062.
- (4) Halcrow, M. A. *Polyhedron* **2007**, 26, 3523.
- (5) Gütlich, P.; Goodwin, H. A. *Spin Crossover in Transition Metal Compounds I-III*; Springer: Berlin, 2004.
- (6) Bousseksou, A.; Molnar, G.; Matouzenko, G. *Eur. J. Inorg. Chem.* **2004**, 4353.
- (7) Halder, G. J.; Kepert, C. J.; Moubaraki, B.; Murray, K. S.; Cashion, J. D. *Science* **2002**, 298, 1762.
- (8) Neville, S. M.; Halder, G. J.; Chapman, K. W.; Duriska, M. B.; Moubaraki, B.; Murray, K. S.; Kepert, C. J. *J. Am. Chem. Soc.* **2009**, 131, 12106.
- (9) Gütlich, P.; Hauser, A.; Spiering, H. *Angew. Chem. Int. Ed.* **1994**, 33, 2024.
- (10) Lemerrier, G.; Bréfuel, N.; Shova, S.; Wolny, J. A.; Dahan, F.; Verelst, M.; Paulsen, H.; Trautwein, A. X.; Tuchagues, J.-P. *Chem. Eur. J.* **2006**, 12, 7421.
- (11) Ni, Z.; Shores, M. P. *J. Am. Chem. Soc.* **2008**, 131, 32.
- (12) Burnett, M. G.; McKee, V.; Nelson, S. M. *J. Chem. Soc., Dalton Trans.* **1981**, 1492.
- (13) Ni, Z.; Shores, M. P. *Inorg. Chem.* **2010**, 49, 10727.
- (14) Ni, Z.; McDaniel, A. M.; Shores, M. P. *Chem. Sci.* **2010**, 1, 615.
- (15) Ni, Z.; Fiedler, S. R.; Shores, M. P. *Dalton Trans.* **2011**, 40, 944.
- (16) Taube, H. *Chem. Rev.* **1952**, 50, 69.
- (17) Hoselton, M. A.; Wilson, L. J.; Drago, R. S. *J. Am. Chem. Soc.* **1975**, 97, 1722.
- (18) Kirchner, R. M.; Mealli, C.; Bailey, M.; Howe, N.; Torre, L. P.; Wilson, L. J.; Andrews, L. C.; Rose, N. J.; Lingafelter, E. C. *Coord. Chem. Rev.* **1987**, 77, 89.
- (19) Lazar, H. Z.; Forestier, T.; Barrett, S. A.; Kilner, C. A.; Letard, J. F.; Halcrow, M. A. *Dalton Trans.* **2007**, 4276.
- (20) Brewer, G.; Butcher, R. J.; Viragh, C.; White, G. *Dalton Trans.* **2007**, 4132.
- (21) Shavaleev, N. M.; Gumy, F.; Scopelliti, R.; Bünzli, J.-C. G. *Inorg. Chem.* **2009**, 48, 5611.
- (22) Hagen, K. S. *Inorg. Chem.* **2000**, 39, 5867.
- (23) *APEX 2*; Bruker Analytical X-Ray Systems, Inc.: Madison, WI., 2008.
- (24) Sheldrick, G. M. In *SHELXTL*; Version 6.14 ed.; Analytical X-Ray Systems: Madison, WI., 1999.
- (25) Kahn, O. *Molecular Magnetism*; VCH: New York, 1993.

- (26) Evans, D. F. *J. Chem. Soc.* **1959**, 2003.
- (27) Grant, D. H. *J. Chem. Educ.* **1995**, *72*, 39.
- (28) Ostfeld, D.; Cohen, I. A. *J. Chem. Educ.* **1972**, *49*, 829.
- (29) Haddad, M. S.; Federer, W. D.; Lynch, M. W.; Hendrickson, D. N. *J. Am. Chem. Soc.* **1980**, *102*, 1468.
- (30) Mueller, E. W.; Spiering, H.; Guetlich, P. *Inorg. Chem.* **1984**, *23*, 119.
- (31) Drew, M. G. B.; Harding, C. J.; McKee, V.; Morgan, G. G.; Nelson, J. *J. Chem. Soc., Chem. Commun.* **1995**, 1035.
- (32) Guionneau, P.; Marchivie, M.; Bravic, G.; Letard, J.-F.; Chasseau, D. *J. Mater. Chem.* **2002**, *12*, 2546.
- (33) Halcrow, M. A. *Chem. Soc. Rev.* **2011**, *40*, 4119.
- (34) Marchivie, M.; Guionneau, P.; Létard, J.-F.; Chasseau, D. *Acta Crystallogr. Sect. B: Struct. Sci.* **2005**, *61*, 25.
- (35) Sereidyuk, M.; Gaspar, A. B.; Kusz, J.; Bednarek, G.; Gütllich, P. *J. Appl. Crystallogr.* **2007**, *40*, 1135.
- (36) Brewer, C.; Brewer, G.; Patil, G.; Sun, Y.; Viragh, C.; Butcher, R. J. *Inorg. Chim. Acta* **2005**, *358*, 3441.
- (37) Cabort, A.; Michel, A.; Therrien, B.; Stoeckli-Evans, H.; Bernauer, K.; Suss-Fink, G.; Williams, A. F.; Stupka, G. *Inorg. Chim. Acta* **2003**, *350*, 193.
- (38) Mueller, P.; Herbst-Irmer, R.; Spek, A. L.; Schneider, T. R.; Sawaya, M. R. *Crystal Structure Refinement: A Crystallographer's Guide to SHELXL*; Oxford University Press: Oxford, 2006.
- (39) Weber, B.; Walker, F. A. *Inorg. Chem.* **2007**, *46*, 6794.
- (40) Dickson, S. J.; Biagini, S. C. G.; Steed, J. W. *Chem. Commun.* **2007**, 4955.
- (41) Dickson, S. J.; Paterson, M. J.; Willans, C. E.; Anderson, K. M.; Steed, J. W. *Chem. Eur. J.* **2008**, *14*, 7296.

CHAPTER 3. EFFORTS TOWARD SYNTHESIZING THE ASYMMETRIC TRIPODAL COMPLEX [FeL⁵⁵⁶]²⁺

3.1 Introduction.

Tripodal iminopyridine-based ligands based on tris(2-aminoethyl)amine (tren) are of interest owing to their electronic and steric tunability and increased stability over heteroleptic bidentate ligands due to the chelate effect. Initial reports employing this ligand type for spin-crossover purposes were first published in the 1970s,¹ and numerous studies have been published since.²⁻⁶ Usually, complexes using tren as a capping substituent to the ligand are devised as ‘homoarmed’ ligands (i.e. all the arms have the same functionalization) due to their straightforward syntheses. Many heterocycles have been employed to tune the ligand field^{6,7} as well as imparting steric bulk adjacent to the coordinating heteroatom.¹ Pyridine-based ligands without any steric bulk, when coordinated to any Fe(II) salt, produce low-spin, diamagnetic complexes, but by varying the amount of steric bulk imparted by the aromatic group, ligand field strength can be tuned, inducing spin crossover with varying temperature.¹ Previously described routes to synthesize ‘heteroarmed’ ligands incorporating steric bulk at the 6'-position relied on stoichiometric control to favor the synthesis of the desired product. One method employed selectively deprotonates tren·3 HCl using sodium methoxide (NaOMe) in methanol. Sequential Schiff base condensation reactions are then performed to introduce the pyridines to tren in the presence of the Fe(II) salt. Finally, an anion exchange from chloride to PF₆⁻ precipitates a reddish-purple solid.¹ Unfortunately, replication of this synthetic routes leads to mixtures of products (*vide infra*), which are difficult to separate.⁸

As seen in Chapter 2, steric hindrance adjacent to the coordination sphere of the metal center allows for anion-dependent spin crossover to occur, but at lower temperatures than desired.

It is seen through structural analysis of the various Fe(II) salts that one anion undergoes bifurcated hydrogen bonding interactions with two of the ligand arms. In our quest to tune the ligand field of these tripodal iminopyridine-based ligands, we attempted to synthesize $[\text{FeL}^{556}]^{2+}$ (Figure 3.1). Using two ligand arms functionalized with strong hydrogen-bond donating *tert*-butylamides should facilitate similar bifurcated guest binding observed for $[\text{FeL}^{6-\text{OH}}]^{2+}$ (highlighted in blue). This architecture has been used in Ru(II) complexes by incorporating bulky amide receptors onto the ligand, allowing for strong host:guest interactions in solution.^{9,10} The addition of steric bulk to only *one* arm should destabilize the low-spin state observed in the homoarmed derivative $[\text{FeL}^{5-\text{ONH}t\text{Bu}}]^{2+}$ (Figure 3.1, highlighted in red). This complex is known to show strong anion binding in polar solvents,¹¹ to induce anion-dependent spin state switching near room temperature.

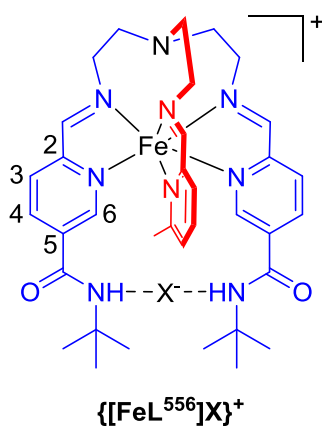


Figure 3.1. Depiction of the complex cation $[\text{FeL}^{556}]^{2+}$ highlighting the desired hydrogen bonding interactions (blue) and steric tuning (red).

3.2 Division of Labor.

Undergraduate student David R. Daley investigated reaction conditions to optimize the formation of the self-assembled species $[\text{FeL}^{556}]^{2+}$. All other syntheses and characterizations presented herein were performed by Christina M. Klug.

3.3 Experimental Section.

3.3.1 General Considerations. Manipulations of iron complexes were performed inside a dinitrogen-filled glovebox (MBRAUN Labmaster 130) or under air. Acetonitrile (MeCN), dichloromethane (DCM), and diethyl ether (Et₂O) used in the glovebox were sparged with dinitrogen, passed over molecular sieves, and subjected to three freeze-pump-thaw cycles prior to use. Tren·3 HCl,¹ 5-*tert*-butylamide-2-pyridinecarboxaldehyde¹¹, [Fe(MeCN)₂(OTf)₂]¹² were synthesized according to the literature. 6-methyl-2-pyridinecarboxaldehyde was sublimed prior to use. All other compounds and reagents were obtained commercially and used as received.

Synthesis of [FeL⁵⁵⁶] via Selective Deprotonation. A solution of sodium methoxide (NaOMe) (7.6 mg, 0.14 mmol) dissolved in 3 mL of methanol (MeOH) was added to tren·3 HCl (34.7 mg, 0.14 mmol). The solution was stirred for 20 minutes, then 6-methyl-2-pyridinecarboxaldehyde (16.6 mg, 0.14 mmol) was added. The solution was allowed to stir for another 20 minutes and then another portion of NaOMe (15.6 mg, 0.29 mmol) was added. After 20 minutes, 5-*tert*-butylamide-2-pyridinecarboxaldehyde (56.4 mg, 0.27 mmol) and 1.36 mL of water were added and the reaction was allowed to stir for an additional 20 minutes. Addition of FeCl₂·4 H₂O (27.8 mg, 0.14 mmol) immediately gave a bluish-purple solution. To this solution, an aqueous solution of KPF₆ (56.3 mg, 0.39 mmol, 3 mL) was added dropwise. After cooling to 0 °C overnight, the solution was filtered, and a small aliquot from the filtrate was removed for mass spectrometry in MeOH and analyzed immediately.

Nominal synthesis of *N,N*-Bis[2-(5-*tert*-butylamide-2-pyridyl)-3-aza-butenyl]-*N*-[2-(6-methyl-2-pyridyl)-3-aza-3-butenyl]amine (L⁵⁵⁶). To a solution of tren (86 mg, 0.77 mmol) in 5 mL of DCM, a solution of 5-*tert*-butylamide-2-pyridinecarboxaldehyde (345 mg, 1.7 mmol) in 5 mL of DCM was added and the resulting mixture was allowed to stir for 20 minutes. A solution of

6-methyl-2-pyridinecarboxaldehyde (92 mg, 0.76 mmol) in 4 mL of DCM and 3 Å molecular sieves (50 mg) were added to the reaction and the solution was allowed to stir for 2 hours. The light yellow solution was filtered and the solvent was removed in *vacuo*, resulting in a yellow oily solid (460 mg). The product was used without further purification. ESI-MS(+) (MeOH): m/z 733.3 [L⁵⁵⁵+Na]⁺, 648.3 [L⁵⁵⁶+Na]⁺, 563.3 [L⁵⁶⁶+Na]⁺, 478.2 [L⁶⁶⁶+Na]⁺. ¹H NMR in CD₃OD shows multiple products present. The spectrum was not interpreted for product distribution or coupling constants (Figure A.2.1).

General Reaction Procedure of [FeL⁵⁵⁶]²⁺ Using Presynthesized Ligand. Presynthesized L⁵⁵⁶ (50–100 mg) was dissolved in 3 mL MeOH, resulting in a light yellow solution. A solution of FeX₂ (10–60 mg) dissolved in 3 mL of MeOH was added to the ligand solution. The reaction mixture was allowed to stir until no visible discernable color changes occurred, usually 2 hours. A small aliquot was removed for mass spectrometry in MeOH and analyzed immediately.

General Reaction Procedure for *In Situ* Self-Assembly. The reaction starting materials FeX₂ (5–20 mg, X = Cl⁻, Br⁻, OTf⁻, BF₄⁻), tren (5–10 mg), 6-methyl-2-pyridinecarboxaldehyde (8–12 mg), and 5-*tert*-butylamide-2-pyridinecarboxaldehyde (20–50 mg) were massed and dissolved individually for a total combined volume of 5–10 mL of (MeOH) upon combination of reactants. The ligand starting materials were combined, resulting in a light yellow solution, and allowed to stir for 10 minutes. The solution of FeX₂ was added to the reaction and the solution was allowed to stir until no visible discernable color changes occurred. A small aliquot was removed for mass spectrometry in MeOH and analyzed immediately.

***N,N*-bis[(2-aminoethyl)]-*N*-(6-methylpyridyl)methylamino)ethyl]amine (tren(6-Me)(NH₂)₂).** A solution of 6-methyl-2-pyridinecarboxaldehyde (1.059 g, 8.74 mmol) dissolved in 40 mL of MeOH was added to a solution of tren (1.280 g, 8.75 mmol) in 12 mL of MeOH. The solution was allowed to stir for 1 hour at room temperature. NaBH₄ (2.558 g, 67.6 mmol) was slowly added to the stirring reaction, which was allowed to stir for 2 hours until effervescence had stopped. The reaction was quenched by addition of aqueous 1 M HCl solution to pH of 1 and 2 M NaOH was added until a pH of 12 was achieved. The product was extracted into CHCl₃ (3 × 125 mL) and the solvent removed under reduced pressure. The clear yellow oil was purified by column chromatography (SiO₂, 10:4:1 CHCl₃:MeOH:NH₄OH) resulting in a colorless oil (1.05 g, 48%). ¹H NMR (400 MHz, CD₃OD): 7.67 (1 H, t, J = 7.7 Hz), 7.21 (1 H, d, J = 7.7 Hz), 7.16 (1 H, d, J = 7.73 Hz), 3.83 (2 H, s), 2.68 (6 H, d, J = 6.14 Hz) 2.61 (2 H, d, J = 5.34 Hz), 2.52 (3 H, s), 2.50 (4 H, t, J = 5.89, 6.1 Hz) ppm. ¹³C NMR (CD₃OD): 159.5 (s), 159.4 (s), 139.0 (s), 123.5 (s), 121.3 (s), 58.2 (s), 55.2 (s), 55.1 (s), 47.7 (s), 40.3 (s), 24.2 (s) ppm.

[Fe(tren(6-Me)(NH₂)₂)Cl]Cl (3.1). To a solution of tren(6-Me)(NH₂)₂ (75 mg, 0.3 mmol) in 6 mL of MeCN, a suspension of FeCl₂ (35 mg, 0.28 mmol) in 6 mL of MeCN was added. The solution immediately turned bright yellow, and over two hours, a bright yellow precipitate formed. The reaction was allowed to stir for an additional 8 hours. The precipitate was isolated via vacuum filtration and washed with 5 mL of MeCN. X-ray quality crystals were obtained by slow Et₂O diffusion into a methanolic solution of the compound (95 mg, 91%). IR (ATR) ν_{NH} 3443 cm⁻¹, ν_{C=Npyridine} 1602 cm⁻¹. ESI-MS(+) (MeOH): *m/z* 342.2 [Fe(tren(6-Me)(NH₂)₂)+Cl]⁺, 306.2 [Fe(tren(6-Me)(NH₂)₂)-H]⁺. ¹H NMR (400 MHz, CD₃OD): δ 92.2, 65.3, 62.3, 56.2, 48.2, 43.9, 13.2, -13.7, -16.8 ppm.

***N,N*-bis[(5-*tert*-butylamide-pyridyl)-3-aza-3-butenyl]-*N*-(6-methyl-2-pyridyl)methylamino)ethyl]amine (**L**^{556-NH}). To a solution of **tren(6-Me)(NH₂)₂** (138.6 mg, 0.55 mmol) in 10 mL of MeCN, a solution of 5-*tert*-butylamide-2-pyridinecarboxaldehyde (263.7 mg, 1.3 mmol) in 10 mL of MeCN was added. The mixture was allowed to stir in the presence of 3 Å molecular sieves (50 mg) for 2 hours. The reaction was filtered to remove the sieves and the solvent was removed under reduced pressure. The resulting yellow solid (304 mg, 88 %) was used without further purification. IR (ATR) $\nu_{C=O}$ 1665 cm⁻¹, $\nu_{C=N}$ 1594, 1525 cm⁻¹. ¹H NMR (400 MHz, CD₃CN): 8.75 (2 H, s), 8.26 (2 H, s), 7.92 (2 H, d, *J* = 8.2 Hz), 7.82 (2 H, d, *J* = 8.2 Hz), 7.43 (1 H, t, *J* = 7.6 Hz), 7.0 (1 H, d, *J* = 7.7 Hz), 6.96 (1 H, d, *J* = 7.6 Hz), 6.82 (2 H, s), 3.67 (2 H, s), 2.85 (4 H, t, *J* = 5.84 Hz), 2.69 (2 H, d, *J* = 5.2 Hz), 2.64 (2 H, d, *J* = 5.2 Hz), 2.40 (4 H, s), 2.32 (4 H, b s), 1.45 (18 H, s) ppm.**

[FeL^{556-NH}]Cl₂ (Route 1) (3.2). The reactants, **L^{556-NH}** (74 mg, 0.12 mmol) dissolved in 1 mL of MeOH and FeCl₂ (16 mg, 0.13 mmol) dissolved in 3 mL of MeOH, were combined. The reaction instantly turned bluish-purple and was allowed to stir for an additional hour at room temperature. The solvent was concentrated to ¼ of the original volume under reduced pressure. The solution was slowly added to 20 mL of Et₂O and the precipitate was stirred until a dark purple free flowing solid was obtained. The solid was isolated by vacuum filtration and washed with 10 mL of Et₂O and used without further purification (80 mg, 90 %). IR (ATR) $\nu_{C=O}$ 1657, 1649 cm⁻¹, $\nu_{C=N}$ 1597, 1529 cm⁻¹. ¹H NMR (300 MHz, CD₃CN): 112.6, 86.5, 81.9, 76.7, 52.4, 40.2, 37.4, 31.9, 16.2, 8.3, 5.6, 2.9, 2.7, -4.7, -35.7 ppm. Absorption spectrum (MeCN): 376, 426 (sh), 544 (sh), 595 nm. ESI-MS(+) (MeOH): *m/z* 718.3 ([FeL^{556-NH}]+Cl)⁺, 341.7 [FeL^{556-NH}]²⁺.

[FeL^{556-NH}]Cl₂ (Route 2). A solution of 5-*tert*-butylamide-2-pyridinecarboxaldehyde (25 mg, 0.12 mmol) in 4 mL of MeCN was added to a suspension of **3.1** (19 mg, 0.05 mmol) in 6 mL

of MeCN. The reaction mixture was stirred for one hour during which the initially green solution became blue in color. The solution was concentrated under reduced pressure to 1/10 of the original volume and 15 mL of Et₂O was added to precipitate a purple solid. The mixture was stirred for one hour to produce a free-flowing solid which was isolated by vacuum filtration, washed with Et₂O (2 × 5 mL), and dried in *vacuo* to produce a dark purple solid (36 mg, 95%). The resulting solid was used without further purification. IR (ATR) $\nu_{C=O}$ 1662 cm⁻¹, $\nu_{C=N}$ 1595, 1535 cm⁻¹. ESI-MS(+) (MeOH): m/z 718.3 ([FeL^{556-NH}]₂Cl)⁺, 682.3 ([FeL^{556-NH}]-H)⁺, 341.7 [FeL^{556-NH}]₂⁺.

[FeL^{556-NH}](BF₄)₂ (3.3). To a solution of L^{556-NH} (56 mg, 0.089 mmol) dissolved in 1 mL of MeCN, Fe(BF₄)₂·6 H₂O (29 mg, 0.086 mmol) in 3 mL of MeCN was added. The reaction instantly turned purple and was allowed to stir for one hour. The solution was concentrated to ¼ of the original volume under reduced pressure and slowly added to 20 mL of Et₂O to form a purple precipitate. The suspension was stirred until a dark purple free flowing solid was obtained. The purple solid was isolated by vacuum filtration and washed with 10 mL of Et₂O (65 mg, 88%). The resulting solid was used without further purification. IR (ATR) $\nu_{C=O}$ 1659, 1649 cm⁻¹, $\nu_{C=N}$ 1602, 1535 cm⁻¹. ¹H NMR (500 MHz, CD₃CN): 133.4, 128.8, 118.4, 65.0, 48.6, 41.9, 36.2, 31.8, 26.4, 18.4, 16.7, 12.7, 9.8, 8.9, 8.4, 7.0, 2.4, 2.2 ppm. Absorption spectrum (MeCN): 364, 538 (sh), 582 nm. ESI-MS(+) (MeOH): m/z 718.3 ([FeL^{556-NH}]₂Cl)⁺, 702.3 ([FeL^{556-NH}]₂F)⁺, 682.33 ([FeL^{556-NH}]-H)⁺, 341.7 [FeL^{556-NH}]₂⁺.

3.3.2 Mass spectral analysis. Analyses of the mass spectra were performed as followed: (1) the relative abundances of the species were determined for the 1+ and 2+ peaks, (2) the abundance of the 1+ and 2+ peaks were summed, (3) the percentage of the species was determined by the summation of the relative abundance of the 1+ and 2+ peaks divided by the summation of

all species observed. Mass spectra were collected once per reaction after stirring for 2 hours. The values have been rounded to the nearest integer.

3.3.3 X-ray Structural Determination. All single crystals were coated in Paratone–N oil prior to removal from the glovebox. The crystals were supported on Cryoloops and mounted under a stream of cold dinitrogen. Data were collected using a Bruker Kappa Apex II CCD diffractometer with MoK α radiation and a graphite monochromator. Data were integrated and corrected for absorption effects with the Apex II software package.¹³ The SHELXTL software package was used for solving the structures by direct methods and for subsequent refinements.¹⁴ Unless otherwise noted, thermal parameters for all non-hydrogen atoms were refined anisotropically. Hydrogen atoms were added at the ideal positions and refined using a riding model where the thermal parameters were set at 1.2 times those of the attached carbon atom.

3.3.4 Other Physical Measurements. Infrared spectra were measured with a Nicolet 380 FT–IR using an ATR attachment with a ZnSe crystal. Electronic absorption spectra were obtained in air-free cuvettes with a Hewlett-Packard 8453 spectrophotometer. ¹H NMR spectra were recorded on a Varian instrument operating at either 300 or 500 MHz. Paramagnetic NMR spectra were collected using 1 second acquisition time, 0.1 second relaxation delay. Mass spectrometry were measured with a Finnigan LCQ Duo mass spectrometer equipped with an electrospray ion source and a quadrupole ion trap mass analyzer.

Table 3.1. Crystallographic data for compound **3.1**.

3.1	
Crystal code	msn368
Empirical formula	C ₁₂ H ₂₀ Cl ₂ FeN ₄ O
Formula weight, g·mol ⁻¹	363.07
Crystal color	Yellow
Habit	Block
<i>T</i> , K	120(2)
Space group	<i>P</i> $\bar{1}$
<i>Z</i>	2
<i>a</i> , Å	7.1836(2)
<i>b</i> , Å	8.7966(3)
<i>c</i> , Å	14.5595(5)
α , deg	85.320(2)
β , deg	76.716(2)
γ deg	76.480(2)
<i>V</i> , Å ³	870.22(5)
<i>d</i> _{calc} , g·cm ⁻³	1.386
GooF	1.137
<i>R</i> ₁ ^{<i>a</i>} (<i>wR</i> ₂) ^{<i>b</i>} %	5.19 (11.93)

^{*a*}*R*₁ = $\sum ||F_o| - |F_c|| / \sum |F_o|$; ^{*b*}*wR*₂ = $(\sum [w(F_o^2 - F_c^2)^2] / \sum [w(F_o^2)^2])^{1/2}$

3.4 Results and Discussion.

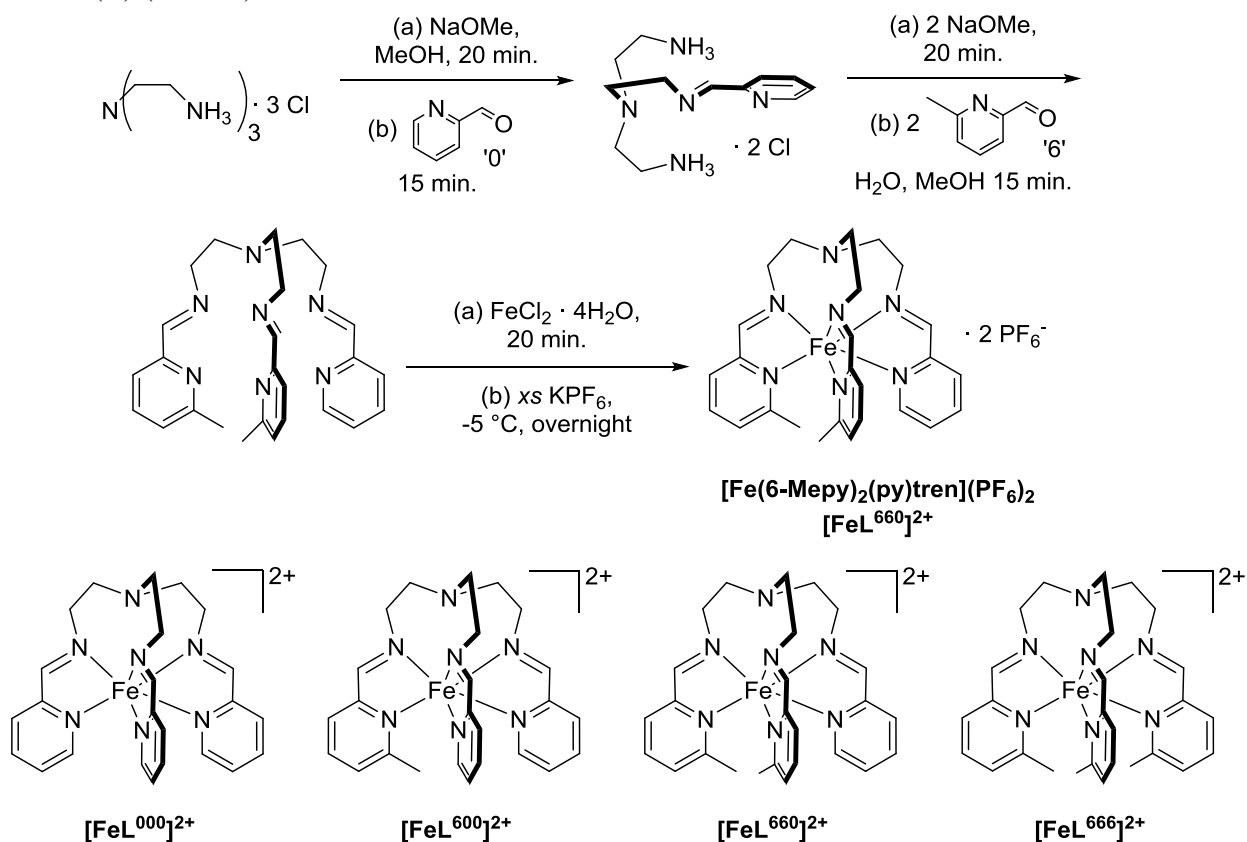
3.4.1 Syntheses via Self-assembly. In an effort to understand potential product distribution while synthesizing ‘heteroarmed’ tripodal ligands, replication of the synthetic scheme implemented to synthesize $[\text{Fe}(\text{6-Mepy})_2(\text{py})\text{tren}](\text{PF}_6)_2$ ($[\text{FeL}^{660}]^{2+}$; ‘6’ = 6-methyl-2-pyridine, ‘0’ = 2-pyridine) was attempted (Scheme 3.1).¹ Based on the reactants used, four potential products could be formed: $[\text{FeL}^{000}]^{2+}$, $[\text{FeL}^{600}]^{2+}$, $[\text{FeL}^{660}]^{2+}$, and $[\text{FeL}^{666}]^{2+}$. Due to the nature of the reactions and the certainty of obtaining mixtures of products, mass spectrometry was used for analysis of the reaction mixture, which were previously characterized using bulk characterization methods of ^1H NMR, IR and elemental analysis. From electrospray-ionization mass spectrometry (ESI-MS) in the positive mode, it was determined that replication of the synthetic procedure used by Drago and coworkers formed all of these potential products. The most abundant peak in the mass spectrum was assigned as the desired material, $[\text{FeL}^{660}]^{2+}$, but the other possible species were also apparent. These compounds were found in a 3%:17%:62%:18% of $[\text{FeL}^{000}]^{2+}$: $[\text{FeL}^{600}]^{2+}$: $[\text{FeL}^{660}]^{2+}$: $[\text{FeL}^{666}]^{2+}$, respectively. A statistical mixture based on the ratio of reactants (2:1:1:1 of ‘6’:‘0’:tren:FeX₂) should produce a distribution of 1:6:12:8 or 4%:22%:44%:30%, respectively. While the product distribution is skewed towards the formation of the desired product, the prevalence of other products is problematic as these species are difficult to separate due to similar molecular weights, sizes, and charges. A similar approach was undertaken by Brewer and Lockett while attempting to synthesize the asymmetric tripodal complexes $[\text{Fe}(\text{sal})_x(4\text{-CH}_3\text{Im})_y]$ (sal = salicylaldehyde, 4-CH₃ImH = 4-methyl-5-imidazole; x = 0 – 3, y = 3 – x).⁸ They also observed that a mixture of products was formed by ‘selectively’ deprotonating tren·3HCl to synthesize $[\text{FeL}^{600}]^{2+}$; from their mass spectral analysis, it was determined that the mixture of products were present in a 24%:48%:23%:5% ratio of

$[\text{FeL}^{000}]^{2+}$: $[\text{FeL}^{600}]^{2+}$: $[\text{FeL}^{660}]^{2+}$: $[\text{FeL}^{666}]^{2+}$. Again, while the most abundant peak in the mass spectrum is of the desired complex, the relative abundance of the other species in the mixture is significantly higher than desired.

This method of selectively deprotonating $\text{tren}\cdot 3\text{HCl}$ and sequential Schiff base condensations was initially employed for the synthesis of the desired functionalized heteroarmed species $[\text{FeL}^{556}]^{2+}$ ('5' = 5-*tert*-butylamide-2-pyridine, '6' = 6-methyl-2-pyridine). Based on the various complexes that could be formed with the addition of one equivalent of '6', tren , and FeX_2 with two equivalents of '5', a mixture of $[\text{FeL}^{555}]^{2+}$, $[\text{FeL}^{556}]^{2+}$, $[\text{FeL}^{566}]^{2+}$, and $[\text{FeL}^{666}]^{2+}$ would be expected (Scheme 3.2). In this case, a statistical mixture would produce a ratio of 8:12:6:1 or 30%:44%:22%:4%, respectively, of these species. With this issue in mind, we aimed to drive the synthesis towards the formation of $[\text{FeL}^{556}]^{2+}$. Unfortunately, this route also produced a mixture of species in a 48%:41%:9%:2% ratio, which deviates substantially from what is seen when '0' and '6' are used. We postulate that the addition of the amide groups appears to drive the formation of $[\text{FeL}^{555}]^{2+}$ as a result of the hydrogen-bonding ability of the amide. Presumably, the NH of the amides undergoes hydrogen-bonding interactions with either the anion or with other amides to promote the formation of $[\text{FeL}^{555}]^{2+}$ (*vide infra*).

Since the selective deprotonation route produced non-statistical distribution of products, two additional routes were attempted to drive the formation of the desired product. The first route, denoted "premade", attempted to synthesize the ligand, L^{556} , prior to metalation using one equivalent of tren , one equivalent of 6-methyl-2-pyridinecarboxaldehyde, and two equivalents of 5-*tert*-butylamide-2-pyridinecarboxaldehyde. A yellow solid was isolated and characterized by ^1H NMR and ESI-MS. As expected, the ^1H NMR spectrum shows the desired relative integrations of aromatic to aliphatic protons based on the stoichiometric ratio of reactants while ESI-MS of the

Scheme 3.1. Synthetic scheme employed for synthesis of $[\text{FeL}^{660}]^{2+}$ (top) and potential products formed from reactions of tren, 2-pyridinecarboxaldehyde, 6-methyl-2-pyridinecarboxaldehyde, and Fe(II) (bottom).



product indicated that a mixture of products was formed. The resulting solid was reacted with FeX₂ (X = Cl⁻, Br⁻, BF₄⁻, OTf⁻) in methanol. Mass spectral analyses of the product distribution are given in Table 3.2 (denoted by premade).

The second route attempted *in situ* ligand synthesis by combining the ligand reactants in methanol, then adding the Fe(II) salt. Characterization of these reactions by ¹H NMR showed a mixture of products as indicated by the presence of resonances in the normal proton window as well as paramagnetic broadening of the spectral window. Mass spectra of the resulting reaction mixtures show that a mixture of products are formed during the reaction which can be assigned to the various possible products. Depending on the Fe(II) salt used, the distribution of the four potential products is changed (*vide infra*).

3.4.2 Anion Dependence. Since we are trying to incorporate hydrogen-bonding functional groups to promote anion-dependent spin-state properties, efforts were placed on trying to promote the desired product formation by varying the anion. For analysis of the role various anions play on the product distribution, the reactions were performed in methanol to allow for direct comparison between reactions.

As apparent from the mass spectral analyses, mixtures of products are formed regardless of the synthetic route employed. In most cases, the amount of the desired $[\text{FeL}^{556}]^{2+}$ product formed was less than the amount expected from a purely statistical mixture (Table 3.2). One interesting trend of note is that when chloride is used as the anion, the formation of $[\text{FeL}^{555}]^{2+}$ becomes more prevalent. Presumably, this is due to the strong binding affinity of the amides towards chloride¹¹ which thus favors the formation of $[\text{FeL}^{555}]^{2+}$. It is expected that a similar effect is occurring during the synthesis using FeCl_2 , pushing the product formation towards $[\text{FeL}^{555}]^{2+}$ even in the presence of the protic solvent methanol. Another trend of note is the small amount of $[\text{FeL}^{666}]^{2+}$ produced. While this is to be expected based on the predicted statistical product distribution, the mass spectrum of the pre-synthesized L^{556} suggests an abundance of L^{666} was formed during synthesis. The substantial decrease in the appearance of $[\text{FeL}^{666}]^{2+}$ using the pre-synthesized ligand may be due to the steric hindrance of the 6-methyl group leading to more labile Fe(II) complexes. This would increase the propensity for the complex to undergo ‘arm scrambling’ to form a thermodynamically more stable moiety. Similar behavior has been observed with self-assembled $[\text{FeL}^{000}]^{2+}$ in aqueous solution.¹⁵ These data suggest that the formation of a species with substantial steric bulk adjacent to the coordination site of the metal is disfavored if aldehydes without this functionalization are present in the reaction mixture.

Scheme 3.2. General reaction scheme and potential products isolated with expected distribution based on stoichiometry.

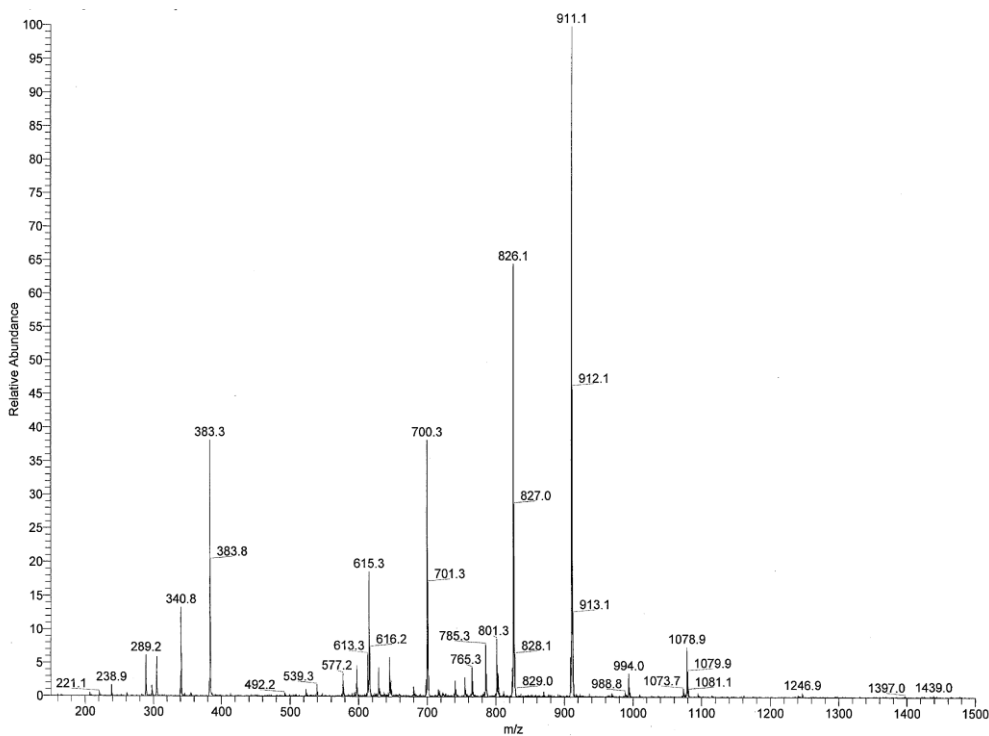
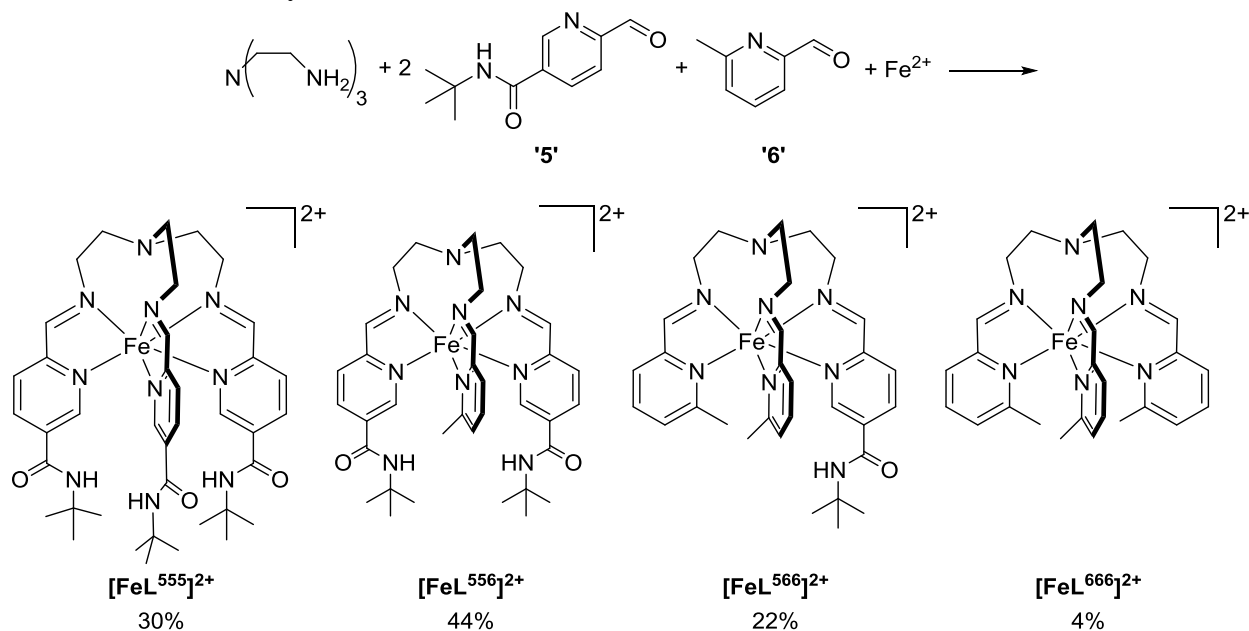


Figure 3.2. ESI-MS of $[FeL^{556}](PF_6)_2$ in positive mode. Peak assignments with relative abundances over 15% (m/z): 911.1 $\{[FeL^{555}]PF_6\}^+$, 826.1 $\{[FeL^{556}]PF_6\}^+$, 700.3 $\{[FeL^{556}]F\}^+$, 615.3 $\{[FeL^{566}]F\}^+$, 383.3 $[FeL^{555}]^{2+}$, 340.8 $[FeL^{556}]^{2+}$.

Table 3.2. Relative percentages of the sum of 1+ and 2+ species of complexes observed in mass spectra obtained on reaction mixtures.

	[FeL ⁵⁵⁵] ²⁺	[FeL ⁵⁵⁶] ²⁺	[FeL ⁵⁶⁶] ²⁺	[FeL ⁶⁶⁶] ²⁺
Statistical distribution	30%	44%	22%	4%
PF ₆ deprotonation	48%	41%	9%	2%
OTf premade	28%	34%	32%	6%
OTf templated	17%	38%	36%	10%
Br premade	50%	36%	10%	4%
Br templated	15%	56%	28%	1%
Cl·4H ₂ O premade	49%	40%	10%	1%
Cl·4H ₂ O templated	39%	40%	18%	3%
Cl templated	39%	35%	25%	4%
BF ₄ ·6H ₂ O premade	37%	47%	16%	0%
BF ₄ ·6H ₂ O templated	13%	36%	42%	10%

3.4.3 Solvent Dependence. In addition to exploring the anion dependence on product distribution, the dependence on solvent was also investigated. Based on these results, it appears that using ethanol or acetonitrile helps to skew the product distribution towards [FeL⁵⁵⁵]²⁺ and [FeL⁵⁵⁶]²⁺, regardless if BF₄⁻ or Cl⁻ are used as the anion, but still leads to the formation of several products (Table 3.2). From the results presented in Table 3.1 and 3.2, it appears that ethanol and acetonitrile are better solvents than methanol, but the distribution of products is still problematic.

3.4.4 Production Distribution Dependence on Stoichiometry and Order of Addition. An additional route for synthesis of the desired complex was attempted by adding a stoichiometric excess of the methylated pyridine to the reaction mixture. In this case, the ligand was synthesized *in situ* using a 1:2:2 tren to ‘5’ to ‘6’ ratio in methanol (Scheme 3.3b). Once FeCl₂·4 H₂O was added, the reaction became a reddish purple. By ESI-MS, the most abundant peak was determined to be [L⁵⁵⁶+Na]⁺ with the next most abundant peaks being assigned to [FeL⁵⁵⁶] as a 2+ ion and a

Table 3.2. Percentages of the sum of 1+ and 2+ species of complexes observed in mass spectra obtained of reaction mixtures in various solvents.

	[FeL ⁵⁵⁵] ²⁺	[FeL ⁵⁵⁶] ²⁺	[FeL ⁵⁶⁶] ²⁺	[FeL ⁶⁶⁶] ²⁺
Expected	30%	44%	22%	4%
Cl·4 H ₂ O MeOH	39%	40%	18%	3%
Cl·4 H ₂ O EtOH	39%	61%	0%	0%
Cl·4 H ₂ O MeCN	34%	60%	6%	0%
BF ₄ ·6 H ₂ O MeOH	13%	36%	42%	10%
BF ₄ ·6 H ₂ O EtOH	41%	58%	1%	0%
BF ₄ ·6 H ₂ O MeCN	57%	43%	0%	0%

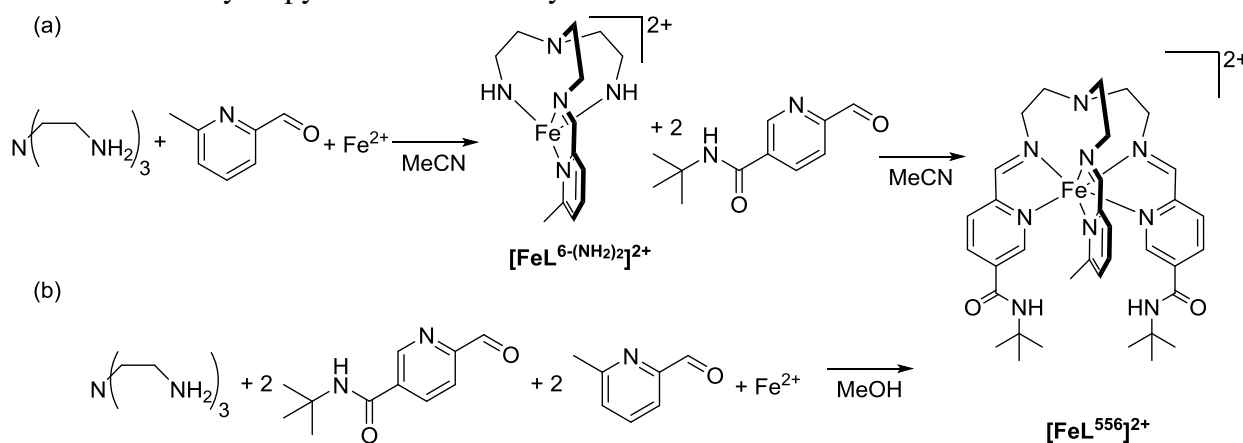
ion with chloride. While some [FeL⁵⁵⁵]²⁺ is apparent, in comparison to previous synthetic attempts, the relative abundance is decreased significantly (22% relative abundance of the Fe(II) containing products). Additionally, the production of [FeL⁵⁶⁶]²⁺ and [FeL⁶⁶⁶]²⁺ has been minimized and were not apparent in the mass spectrum. This provides a promising potential route for synthesizing the desired product relatively cleanly via the self-assembly method.

Further investigations performed by David Daley determined that the order of addition of the reactants has significant influence on the product distribution. Reactions of tren, '6', and [Fe(MeCN)₂(OTf)₂] in acetonitrile forms either [FeL⁶⁶⁶]²⁺ or the 'monoarmed' [FeL^{6-(NH₂)₂]²⁺, but not the 'diarmed' [FeL^{66-NH₂]²⁺ based on ESI-MS analysis (Scheme 3.3a). The addition of '5' to the reaction forms the desired product [FeL⁵⁵⁶]²⁺ in 63% relative abundance. This method presents a potentially viable method for compound synthesis, especially if the solubility of the desired product can be exploited (*vide infra*).}}

Attempts at crystallizing these complexes *via* diethyl ether diffusion to the reaction mixture were met with the formation of films or powders. It is presumed this occurs due to a couple reasons: (1) the differences in functionalities prevent viable crystallographic packing, (2) mixtures of products further prohibit purification by crystallization. Further methods of purification of the

Fe(II) complexes such as liquid chromatography (e.g. HPLC or ion-exchange chromatography) were not attempted, but could be viable methods of purification. Anion exchange of the resulting reaction mixtures with BPh_4^- or $\text{BAR}^{\text{F}-}$ is an additional potential method of purification. These anions, especially when a halide is bound within the trigonal pocket of $[\text{FeL}^{555}]^{2+}$, may have marked differences in solubility allowing for preferential precipitation of one compound over another. Additionally, these large anions may improve the packing ability of the cations and promote crystal formation.

Scheme 3.3. Reaction schemes controlling (a) order of addition and (b) stoichiometry by addition of excess 6-methyl-2-pyridinecarboxaldehyde.



3.4.5 Synthesis of $[\text{FeL}^{556-\text{NH}}]^{2+}$. An additional route to synthesize $[\text{FeL}^{556}]^{2+}$ *via* reductive amination and metal-assisted oxidative dehydrogenation was attempted. This scheme required the reductive amination of tren with 6-methyl-2-pyridinecarboxaldehyde in methanol using NaBH_4 as the reductant. The resulting product, **tren(6-Me)(NH₂)₂**, can be purified by column chromatography. Two different routes were attempted to synthesize the desired Fe(II) complexes: (1) ligand synthesis via Schiff base condensation of one equivalent **tren(6-Me)(NH₂)₂** with two equivalents of the aldehyde in acetonitrile, then subsequent reaction with the desired Fe(II) salt; or (2) complexation of **tren(6-Me)(NH₂)₂** with FeCl_2 in acetonitrile, then subsequent reaction with two equivalents of 5-*tert*-butylamide-2-pyridinecarboxaldehyde in methanol (Scheme 3.4).

Initially route 1 was employed with the hope that reaction with Fe(III) in the presence of dioxygen would promote oxidative dehydrogenation of the amine mediated by the Fe(III) center.^{16,17} If the metalation reaction is performed in air using presynthesized ligand, the conversion from amine to imine is low, as determined by mass spectrometry. We believe this is occurring because of the redox stability of the imines, which could stabilize both the Fe(II) and Fe(III) oxidation states. Additionally, chemical oxidation of the amine using IBX was also attempted. While this route is promising, the aqueous workup of the reaction resulted in recovery of the aldehyde due to the hydrolysis of the reformed imine. For chemical oxidation of the amine to be feasible, nonaqueous workups of the reactions are required to prevent the hydrolysis of the imine.

Reaction of **tren(6-Me)(NH₂)₂** in acetonitrile with FeCl₂ under inert conditions produces the yellow precipitate, **[Fe(tren(6-Me)(NH₂)₂)Cl]Cl (3.1)**. This species can be recrystallized from diethyl ether diffusion into a methanolic solution of the complex. The X-ray crystal structure shows a mononuclear complex with the coordination environment of the iron center composed of N₅Cl with coordination to the five nitrogens supplied by the ligand and one chloride ion (Figure 3.3). Based on the Fe–N bond lengths, the complex is high-spin, with average Fe–N bond lengths of 2.195(4) Å. The longest Fe–N distance occurs for the bridgehead nitrogen, which is 2.236(2) Å, while the shortest Fe–N distance is observed for the pyridine nitrogen (2.175(2) Å), which is *trans* to the bridgehead nitrogen. This compound can be further reacted with two equivalents of ‘5’ in methanol to form **[FeL^{556-NH}]Cl₂ (3.2)**.

More conventional routes of complex synthesis were also pursued by reacting **L^{556-NH}** with either Fe(BF₄)₂·6 H₂O (**3.3**) in acetonitrile or FeCl₂ in methanol (**3.2**) (Scheme 3.4). The resulting solid of the BF₄⁻ salt (**3.3**) isolated from this reaction is purple in color, which is markedly different than the blue solid that is isolated when chloride (**3.2**) is the counter anion (Figure 3.4). As seen

Scheme 3.4. Reaction scheme employed for the syntheses of **tren(6-Me)(NH₂)₂**, **L^{556-NH}**, **3.1**, **3.2** (Route 1 and 2), and **3.3**.

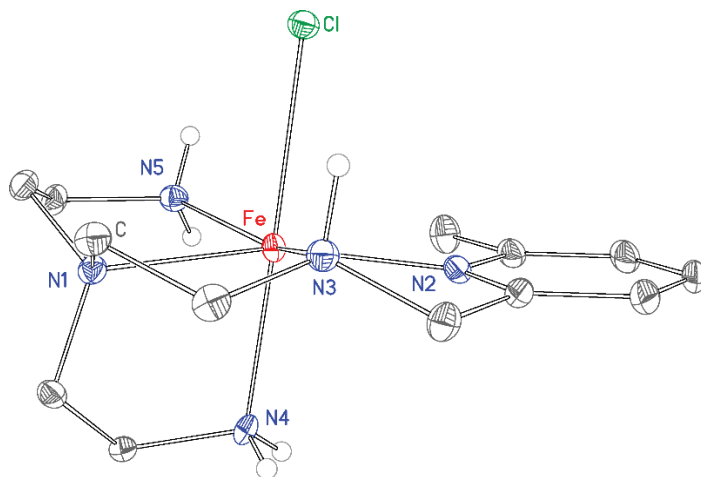
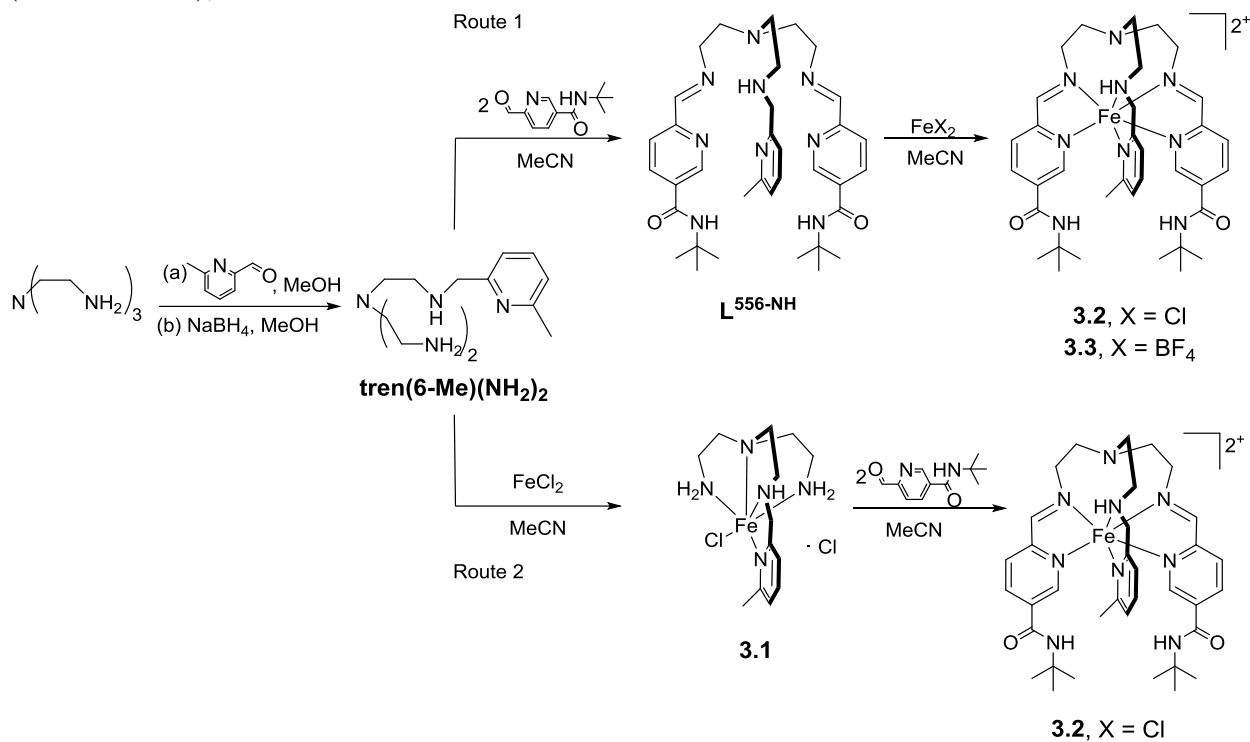


Figure 3.3. X-ray crystal structure of the cationic complex in compound **3.1**. Fe, C, N, and Cl atoms are represented by red, gray, blue, and green respectively. Thermal ellipsoids are rendered with 40% probability. Hydrogen atoms except those bound to the nitrogen atoms are omitted for clarity.

with the self-assembled species, numerous attempts at crystallizing the products resulted in powders. Comparison of the solution absorption spectrum in the visible region of **3.3** and **3.2** in acetonitrile shows that the chloride salt exhibits a red shift of the charge-transfer band centered around 580 nm for the BF_4^- salt and a blue shift of the absorbance centered around 375 nm. Presumably the color difference is due to the anion interaction with the secondary amine coordinated to the metal center.

Variable temperature solution magnetic susceptibility measurements of **3.2** and **3.3** were measured by Evans' method in d_3 -acetonitrile. At room temperature, **3.2** and **3.3** are high spin with $\chi_{\text{M}}T$ values of 3.0 and 3.2 $\text{emu}\cdot\text{K}\cdot\text{mol}^{-1}$, respectively. When the temperature is lowered, a decrease in the magnetic susceptibility is observed at temperatures less than 280 K for **3.2**, decreasing to 1.8 $\text{emu}\cdot\text{K}\cdot\text{mol}^{-1}$ at 232 K. In comparison, upon cooling a solution of **3.3** to 232 K, a less drastic decrease in the susceptibility is observed, falling to 2.7 $\text{emu}\cdot\text{K}\cdot\text{mol}^{-1}$ (Figure 3.5). Compared to the solution-state behavior of $[\text{FeL}^{600}]^{2+}$, the high-spin states of **3.2** and **3.3** are stabilized. This is expected as the substitution of the imine for an amine should weaken the ligand field.

There are several potential mechanisms through which the anion influences the spin-state behavior, highlighted in Scheme 3.5: (1) as previously mentioned, host:guest interactions with the coordinated secondary amine, (2) the hydrogen-bonding interaction of two of the ligand arms stabilizes the low-spin state by withdrawing electron density from the ligand, or (3) the ligand arms are forced into close proximity to one another to facilitate stronger hydrogen-bonding interactions, thus stabilizing shorter Fe–N bond lengths.

Scheme 3.5. Proposed binding modes possible for $[\text{FeL}^{556\text{-NH}}]^{2+}$.

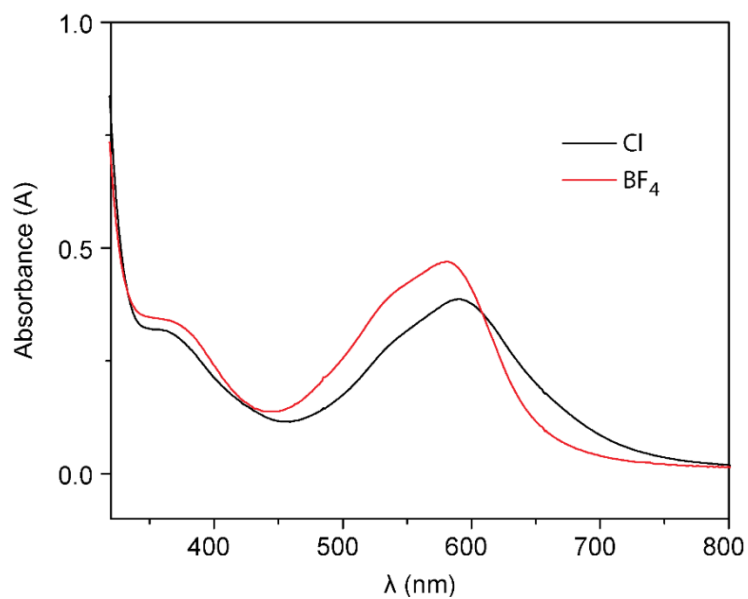
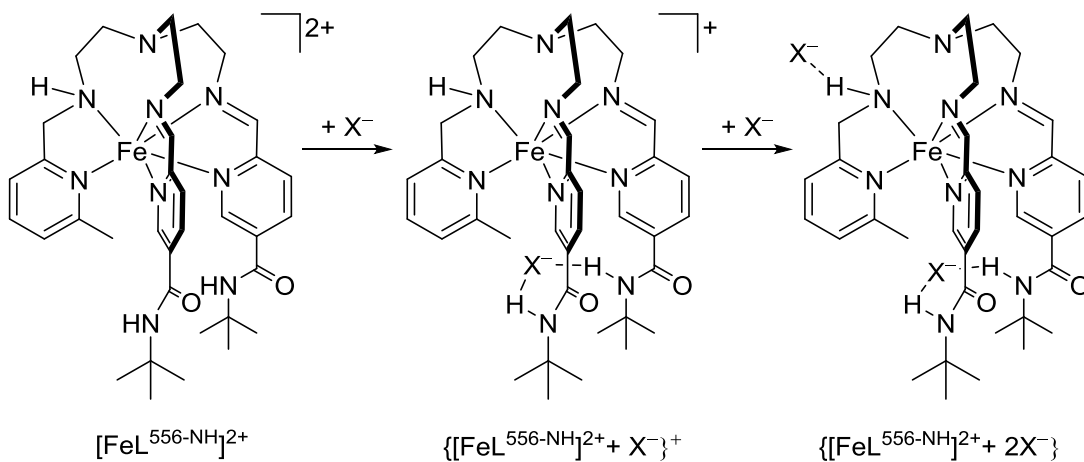


Figure 3.4. Qualitative UV-visible spectral comparison of **3.2** (black line) and **3.3** (red line) in acetonitrile between 325 and 800 nm.

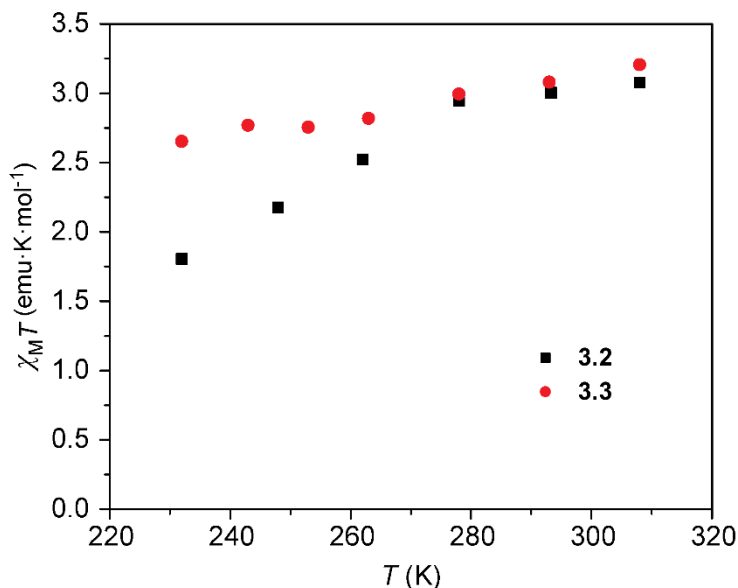


Figure 3.5. Variable temperature solution magnetic susceptibility measurement of **3.2** (black squares) and **3.3** (red circles) in *d*₃-acetonitrile.

3.5 Conclusions and Future Work.

The desired product $[\text{FeL}^{556}]^{2+}$ can be synthesized but with side product formation. The incorporation of H-bonding groups appears to drive the disproportionate formation of $[\text{FeL}^{555}]^{2+}$ compared to the predicted statistical distribution of species and the distribution seen with the synthesis of $[\text{Fe}(6\text{-Me})_2(\text{py})\text{tren}]^{2+}$. Halide salts seem to aid in formation of $[\text{FeL}^{555}]^{2+}$ and $[\text{FeL}^{556}]^{2+}$ in methanol. Furthermore, there appears to be a solvent dependence; if ethanol or acetonitrile are used, $[\text{FeL}^{555}]^{2+}$ and $[\text{FeL}^{556}]^{2+}$ are the major products formed. Future work for these species could focus on devising HPLC methods, size exclusion chromatography, or anion exchange to separate these species. Additionally, the order and speed of addition of the starting materials may be pivotal to encourage the formation of the desired product.

Additional routes were attempted to synthesize the ligand L^{556} by reductive amination then oxidative dehydrogenation promoted by Fe(III). Reactions attempted in oxygen to promote the oxidative dehydrogenation reaction with Fe(III) resulted in poor conversion to the imine as indicated by mass spectrometry. Reaction of **tren(6-Me)(NH₂)₂** with FeCl_2 in acetonitrile

produces $[\text{Fe}(\text{tren}(\mathbf{6}\text{-Me})(\text{NH}_2)_2)\text{Cl}]\text{Cl}$ (**3.1**), which can be crystallized and subsequently reacted with the desired aldehyde to make the Fe(II) complex. Interestingly, retention of the coordinating secondary amine to form $[\text{FeL}^{556\text{-NH}}]^{2+}$ produces material that is either purple as the BF_4^- salt or blue as the Cl^- salt in the solid state and in solution. Solution magnetic measurements of the chloride salt **3.2** show that the complex begins a spin state transition with decreasing temperature, while the BF_4^- salt **3.3** remains mostly high spin over the same temperature range.

Retention of the secondary amine allows for an interesting prospect for ligand synthesis and ligand tuning. This modification should weaken the ligand field, which could be used as an additional route to produce complexes that undergo spin crossover without extensive ligand synthesis. Furthermore, the secondary amine provides an additional location for hydrogen bonding interactions through which, additional anion-dependent behavior could be observed.

Further experimentation to determine the binding modes and spin-state behavior in the presence of one and two anions would help to elucidate which binding mode occurs first as well as the influence of these events individually on the spin state behavior. Additionally, comparison of the strength of the bifurcated anion-binding possible by the amides to the trifurcated anion-binding displayed by $[\text{FeL}^{5\text{-ONHtBu}}]^{2+}$.

3.6 Acknowledgments.

This work was supported by Colorado State University and NSF-CHE-1058889 and NSF-CHE-1363274.

REFERENCES

- (1) Hoselton, M. A.; Wilson, L. J.; Drago, R. S. *J. Am. Chem. Soc.* **1975**, *97*, 1722.
- (2) Brewer, C. T.; Brewer, G.; Butcher, R. J.; Carpenter, E. E.; Schmiedekamp, A. M.; Schmiedekamp, C.; Straka, A.; Viragh, C.; Yuzefpolskiy, Y.; Zavalij, P. *Dalton Trans.* **2011**, *40*, 181.
- (3) Brewer, C. T.; Brewer, G.; Butcher, R. J.; Carpenter, E. E.; Schmiedekamp, A. M.; Viragh, C. *Dalton Trans.* **2007**, 295.
- (4) Hagiwara, H.; Matsumoto, N.; Iijima, S.-I.; Kojima, M.-A. *Inorg. Chim. Acta* **2011**, *366*, 283.
- (5) Ikuta, Y.; Ooidemizu, M.; Yamahata, Y.; Yamada, M.; Osa, S.; Matsumoto, N.; Iijima, S.; Sunatsuki, Y.; Kojima, M.; Dahan, F.; Tuchagues, J.-P. *Inorg. Chem.* **2003**, *42*, 7001.
- (6) Lazar, H. Z.; Forestier, T.; Barrett, S. A.; Kilner, C. A.; Letard, J. F.; Halcrow, M. A. *Dalton Trans.* **2007**, 4276.
- (7) Halcrow, M. A. *Polyhedron* **2007**, *26*, 3523.
- (8) Brewer, G.; Luckett, C. *Inorg. Chim. Acta* **2005**, *358*, 239.
- (9) Beer, P. D.; Dent, S. W.; Wear, T. J. *J. Chem. Soc., Dalton Trans.* **1996**, 2341.
- (10) Dickson, S. J.; Biagini, S. C. G.; Steed, J. W. *Chem. Commun.* **2007**, 4955.
- (11) McDaniel, A. M.; Klug, C. M.; Shores, M. P. *Eur. J. Inorg. Chem.* **2013**, *2013*, 943.
- (12) Hagen, K. S. *Inorg. Chem.* **2000**, *39*, 5867.
- (13) In *APEX 2*; Bruker Analytical X-Ray Systems, Inc.: Madison, WI., 2008.
- (14) Sheldrick, G. M. In *SHELXTL*; Version 6.14 ed.; Analytical X-Ray Systems: Madison, WI., 1999.
- (15) Schultz, D.; Nitschke, J. R. *Angew. Chem., Int. Ed.* **2006**, *45*, 2453.
- (16) Duran, P. L.; Golobic, A.; Kozlevcar, B.; Gamez, P.; Kooijman, H.; Spek, A. L.; Reedijk, J. *Inorg. Chim. Acta* **2004**, *357*, 3697.
- (17) Arulsamy, N.; Hodgson, D. J. *Inorg. Chem.* **1994**, *33*, 4531.

CHAPTER 4. EFFECT OF IMINE REDUCTION ON THE SPIN STATE PROPERTIES OF
FE(II) COMPLEXES USING AMIDE-FUNCTIONALIZED TRIPODAL PYRIDINE-BASED
LIGANDS

4.1 Introduction.

Previous work with the tripodal iminopyridine-based ligand $L^{5\text{-ONH}t\text{Bu}}$ (Figure 4.1, right) shows that when coordinated to Fe(II), a diamagnetic complex is obtained.¹ Monitoring of the titration of the BF_4^- salt with Cl^- in d_3 -acetonitrile by ^1H NMR shows that strong anion binding occurs as indicated by significant downfield shift in the amide proton resonance due to the deshielding effect of the anion-binding event. As seen in the previous chapter, modification of tripodal ligands incorporating steric bulk and hydrogen-bonding functionalities does facilitate anion-dependent spin-state behavior, but it is not clear which modification, imine reduction or steric hindrance, has the greatest influence on the behavior.

As a method to tune the ligand field of tripodal iminopyridine-based ligands, we have synthesized a series of complexes with varying number of coordinating imines and amines (Figure 4.1). We postulate that by altering the π -accepting ability of the coordinating nitrogens, the ligand field can be tuned in an analogous manner to heteroleptic complexes, but with increased stability as a consequence of increased ligand denticity. To this end, three new tripodal ligands: tris{4-[(5-*tert*-butylamide-2-pyridyl]-3-amino-3-butenyl}amine ($L^{5(\text{NH})3}$), *N,N*-bis[2-(5-*tert*-butylamidepyridine-methylamine)ethyl]-*N*-[2-(5-*tert*-butylamidepyridine)-3-aza-3-butenyl]amine ($L^{5(\text{NH})2}$), and *N,N*-bis[2-(5-*tert*-butylamidepyridine)-3-aza-3-butenyl]-*N*-[2-(5-*tert*-butylamidepyridine-methylamine)ethyl]amine ($L^{5\text{-NH}}$) and their corresponding Fe(II) complexes: $[\text{Fe}L^{5(\text{NH})3}](\text{BF}_4)_2$ (**4.1**), $[\text{Fe}L^{5(\text{NH})2}](\text{BF}_4)_2$ (**4.2**), $[\text{Fe}L^{5\text{-NH}}](\text{BF}_4)_2$ (**4.3**) and $[\text{Fe}L^{5\text{-NH}}](\text{BPh}_4)_2$ (**4.4**) have been synthesized. Herein, we report the syntheses, structural, and magnetic

characterizations as well as studies towards understanding the anion dependence on the magnetic behavior of these compounds. Through these complexes we hope to understand: (1) what structural differences occur across the series of Fe(II) complexes, (2) how the spin state of each complex is affected by the change in conjugation of the ligand, (3) how the geometric changes of the ligand are translated to the trigonal binding pocket formed by the amides, and (4) how anion binding affects the spin state.

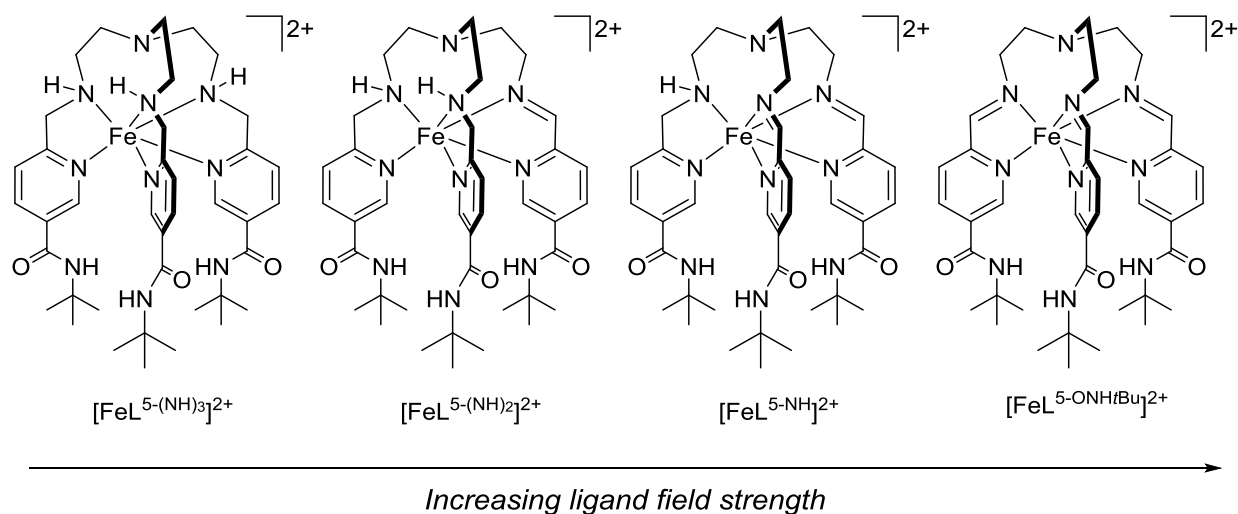


Figure 4.1. Schematic of the ligands and Fe(II) complexes with varying numbers of imines and amines.

4.2 Division of Labor.

The synthesis of L^{5-NH} was performed by Tarik Ozumerzifon. All other ligand and complex syntheses, characterizations and magnetic measurements were performed by Christina Klug.

4.3 Experimental Section

4.3.1 General considerations. Unless otherwise noted, all manipulations with Fe(II) were undertaken in a dinitrogen filled MBRAUN Labmaster 130 glovebox. The syntheses and characterizations of 5-*tert*-butylamide-2-pyridinecarboxaldehyde and $L^{5-ONHtBu}$,¹ *N,N*-Bis(2-aminoethyl)-*N*-[2-(*tert*-butylcarbamoyl)ethyl]amine (**monoBoc-tren**)² have been described previously. The precursor *N,N*-Bis(2-(*tert*-butylcarbamoyl)ethyl)-*N*-[2-aminoethyl]amine (**diBoc-**

tren) was isolated from the synthesis of *N,N*-Bis(2-aminoethyl)-*N*-[2-(*tert*-butylcarbamoyl)ethyl]amine, and used without further purification. For manipulations with Fe(II), acetonitrile (MeCN) and diethyl ether (Et₂O) were sparged with dinitrogen, passed over molecular sieves, and subjected to three freeze-pump-thaw cycles prior to use. All other reagents were obtained from commercial sources and used without further purification.

Tris{4-[(5-*tert*-butylamide-2-pyridyl]-3-amino-3-butenyl}amine (L^{5(NH)}₃). To a solution of L^{5-ONHtBu} (212 mg, 0.3 mmol) dissolved in 7 mL of methanol (MeOH), sodium borohydride (NaBH₄) (75 mg, 2 mmol) was slowly added in several portions over 20 minutes. After all the NaBH₄ was added, the reaction was allowed to stir for 4 hours. The solvent was removed under reduced pressure, resulting in a light yellow oil. Saturated Na₂CO_{3(aq)} (50 mL) was added to the residue and the product extracted into dichloromethane (DCM) (3 × 20 mL). The organic layer was dried over Na₂SO₄ and the solvent removed under reduced pressure resulting in a fluffy light yellow solid. The yellow solid was purified by column chromatography (SiO₂, 9:1:0.1 CHCl₃:MeOH:NH₄OH, *R*_f = 0.55). The desired fractions were combined and the solvent removed under reduced pressure to result in a light yellow solid (120 mg, 57 %). ¹H NMR (400 MHz, CDCl₃): 8.73 (3 H, s), 7.82 (3 H, dd, *J* = 2.3, 8.1 Hz), 7.23 (3 H, d, *J* = 8.2 Hz), 6.42 (3 H, s), 3.91 (6 H, s), 2.77 (6 H, t, *J* = 5.5 Hz), 2.67 (6 H, t, *J* = 5.4 Hz), 1.48 (27 H, s) ppm. ¹³C NMR (CDCl₃): 194.89, 165.48, 147.92, 135.43, 130.29, 121.99, 110.23, 54.38, 54.05, 52.26, 47.55, 29.06 ppm.

***N,N*-bis[2-(5-*tert*-butylamidepyridine-methylamino)ethyl]-*N*-[2-aminoethyl]amine (di-5-*tert*-butylamide-tren).** A solution of 5-*tert*-butylamide-2-pyridinecarboxaldehyde (1.578 g, 7.65 mmol) dissolved in 50 mL of MeOH was added to tris-(2-aminoethyl)amine (tren) (0.720 g, 4.9 mmol) in 8 mL of MeOH. The reaction mixture was allowed to stir for 5 hours, then slowly NaBH₄ (1.8 g, 47.6 mmol) was added in several portions to the reaction over 1 hour. The reaction

was allowed to stir for 16 additional hours. Upon completion, the reaction was quenched with water and the product extracted into DCM (3 × 30 mL). The organic layer was dried over MgSO₄ and the solvent removed under reduced pressure. The resulting yellow oil was purified by column chromatography (SiO₂, 10:1 CHCl₃:MeOH then 80:35:4 CHCl₃:MeOH:NH₄OH; R_f = 0.2, 10:1 CH₃:MeOH). A light yellow solid was isolated (1.40 g, 54 %). ¹H NMR (400 MHz, CDCl₃): 9.02 (2 H, s), 8.00 (2 H, dd, *J* = 2.12, 8.0 Hz), 7.24 (2 H, d, *J* = 8.1 Hz), 6.79 (2 H, s), 3.92 (4 H, s), 2.96 (2 H, t, *J* = 5.8 Hz), 2.71 (4 H, t, *J* = 5.0 Hz), 2.65 (4 H, t, *J* = 4.8 Hz), 2.57 (2 H, t, *J* = 5.9 Hz), 1.48 (18 H, s) ppm. ¹³C NMR (CDCl₃): 165.27, 161.65, 147.90, 136.46, 130.51, 122.09, 54.61, 54.47, 47.40, 38.57, 20.09 ppm.

***N,N*-bis[2-(5-*tert*-butylamidepyridine-methylamino)ethyl]-*N*-[2-(5-*tert*-butylamidepyridine)-3-aza-3-butyenyl]amine (L^{5-(NH)₂})**. The amine starting material **di-*tert*-butylamide-tren** (274 mg, 0.52 mmol) was dissolved in 4 mL of MeOH and combined with 5-*tert*-butylamide-2-pyridinecarboxaldehyde (118 mg, 0.57 mmol) dissolved in 4 mL of MeOH. The resulting solution was allowed to stir for two hours at room temperature. The solvent was removed under reduced pressure, resulting in a light yellow solid (350 mg, 94 %). The resulting solid was used without further purification. ¹H NMR (400 MHz, CD₃CN): 8.81 (1 H, s), 8.68 (2 H, s), 8.37 (1 H, s), 7.95 (2 H, dd, *J* = 2.2, 8.1 Hz), 7.85 (2 H, dd, *J* = 2.1, 8.1 Hz), 7.82 (1 H, d, *J* = 8.2 Hz), 7.24 (2 H, t, *J* = 8.1 Hz), 6.95 (1 H, s), 6.86 (2 H, s), 3.83 (4 H, s), 3.74 (2 H, t, *J* = 5.8 Hz), 2.94 (2 H, bs), 2.85 (4 H, t, *J* = 5.6 Hz) 2.71 (6 H, s), 1.45 (9 H, s), 1.43 (18 H, s) ppm.

***N,N*-bis[2-(4-nitro(phenylsulfonamido))ethyl]-*N*-[2-(*tert*-butylcarbamoylethyl)amine (dinosyl-monoBoc-tren)**. A solution of **monoBoc-tren** (0.753 g, 3.0 mmol) was mixed with 12 mL of DCM and freshly distilled triethylamine (1.04 mL, 7.4 mmol) was added and cooled to 0 °C. Solid 4-nitrobenzenesulfonyl chloride (1.65 g, 7.4 mmol) was slowly added to the stirring

reaction. The solution was allowed to stir at 0 °C for 2 hours, then allowed to warm to room temperature and stirred for an additional 12 hours. The solution was washed with water (20 mL) and the DCM removed under reduced pressure. The resulting yellow-orange solid was purified via column chromatography (SiO₂, 9:1:0.1 DCM:MeOH:NH₄OH, *R_f* = 0.45) to produce a light yellow solid (1.384 g, 74%). ¹H NMR (400 MHz, *d*₆-DMSO): 8.40 (4 H, d, *J* = 8.7 Hz), 8.04 (4 H, d, *J* = 8.7 Hz), 7.83 (2 H, br s), 6.63 (1 H, br s), 2.80 (6 H, m, *J* = 5.85 Hz), 2.37 (4 H, t, *J* = 5.5 Hz), 2.28 (2 H, t, *J* = 5.9 Hz), 1.33 (9 H, s) ppm. ¹³C (*d*₆-DMSO): 189.5, 149.5, 146.1, 127.9, 124.6, 110.1, 99.4, 77.6, 53.3, 40.6, 28.1 ppm.

***N,N*-bis[2-(4-nitro(phenylsulfonamido))ethyl]-*N*-[2-(amino)ethyl]amine (dinosyl-tren).** A solution of **dinosyl-monoBoc-tren** (830 mg, 1.35 mmol) dissolved in 7 mL of DCM was cooled to 0 °C under dinitrogen; trifluoroacetic acid (TFA) (1.24 mL, 1.84 g, 16.2 mmol) was slowly added dropwise over 10 minutes. After the addition was complete, the reaction was allowed to warm to room temperature and stirred for four days. Saturated NaHCO_{3(aq)} (20 mL) was added and the product extracted into DCM (3 × 30 mL). The organic layer was dried over MgSO₄ and the solvent removed under reduced pressure. The resulting yellow solid was purified by column chromatography (SiO₂, 9:1 DCM:MeOH then 9:1:0.2 DCM:MeOH:NH₄OH, *R_f* = 0.22 in 9:1:0.1 DCM:MeOH:NH₄OH). The fractions were combined and the solvent removed under reduced pressure resulting in a yellow solid (480 mg, 70 %). ¹H NMR (400 MHz, *d*₆-DMSO): 8.41 (4 H, d, *J* = 8.9 Hz), 8.04 (4 H, d, *J* = 9.0 Hz), 2.83 (4 H, t, *J* = 6.4 Hz), 2.64 (2 H, t, *J* = 5.8 Hz), 2.46 (2 H, t, *J* = 5.8 Hz), 2.42 (4 H, t, *J* = 6.4 Hz) ppm. ¹³C (*d*₆-DMSO): 159.0, 155.7, 137.4, 134.1, 88.6, 62.5, 49.9, 46.93 ppm.

***N,N*-bis[2-(4-nitro(phenylsulfonamido))ethyl]-*N*-[2-(5-*tert*-butylamidepyridine-methylamino)ethyl]amine (dinosyl-5-*tert*-butylamide-tren).** A solution of **dinosyl-tren** (411

mg, 0.80 mmol) and 5-*tert*-butylamide-2-pyridinecarboxaldehyde (181 mg, 0.88 mmol) were combined in 5 mL of MeOH and allowed to stir with 3 Å molecular sieves. After 4 hours, the solution was filtered and NaBH₄ (436 mg, 11.5 mmol) was added in several portions over 10 minutes and the reaction was allowed to continue stirring for 2 hours. The solvent was removed under reduced pressure and the resulting residue was extracted into DCM (3 × 75 mL). The organic layer was dried over MgSO₄ and the solvent removed. The resulting yellow solid was purified by column chromatography (SiO₂, 9:1 DCM:MeOH, R_f = 0.5) to isolate a yellow solid (525 mg, 80%). ¹H NMR (400 MHz, CDCl₃): 9.04 (1 H, s), 8.33 (4 H, d, *J* = 9.0 Hz), 8.11 (1 H, dd, *J* = 2.2, 8.0 Hz), 8.00 (4 H, d, *J* = 9.0 Hz), 7.37 (1 H, d, *J* = 7.6 Hz), 3.99 (2 H, s), 3.03 (4 H, t, *J* = 5.2 Hz), 2.73 (2 H, t, *J* = 5.0 Hz), 2.60 (4 H, t, *J* = 5.2 Hz), 2.55 (2 H, t, *J* = 4.9 Hz), 1.46 (9 H, s) ppm. ¹³C NMR (CDCl₃): 150.2, 148.2, 146.9, 146.2, 131.2, 128.5, 124.6, 123.0, 110.24, 54.5, 52.3, 41.1, 29.1, 28.9 ppm.

***N,N*-bis[2-(amino)ethyl]-*N*-[2-(5-*tert*-butylamidepyridine-methylamino)ethyl]amine (5-*tert*-butylamide-tren) (Route 1).** To a suspension of **dinosyl-5-*tert*-butylamide-tren** (525 mg, 0.74 mmol) in 5 mL of MeCN, K₂CO₃ (1.1 g, 7.9 mmol) and 1-dodecanethiol (1.8 mL, 7.5 mmol) were added. The reaction was allowed to stir at room temperature for 13 days. The product was extracted into H₂O (3 × 30 mL) using diethyl ether and the water was removed under reduced pressure. The resulting light yellow oil was purified by column chromatography (SiO₂, 80:35:4 CHCl₃:MeOH:NH₄OH then 10:4:1 CHCl₃:MeOH:NH₄OH). The desired fractions were combined and the solvent removed under reduced pressure, resulting in a light yellow oil (66 mg, 17%). ¹H NMR (400 MHz, CD₃OD): 9.04 (1 H, s), 8.33 (4 H, d, *J* = 9.0 Hz), 8.11 (1 H, dd, *J* = 2.2, 8.0 Hz), 8.00 (4 H, d, *J* = 9.0 Hz), 7.37 (1 H, d, *J* = 7.6 Hz), 3.99 (2 H, s), 3.03 (4 H, t, *J* = 5.2 Hz), 2.73 (2 H, t, *J* = 5.0 Hz), 2.60 (4 H, t, *J* = 5.2 Hz), 2.55 (2 H, t, *J* = 4.9 Hz), 1.46 (9 H, s) ppm.

***N,N*-bis[2-(*tert*-butylcarbamoylethyl)-*N*-[2-(5-*tert*-butylamidepyridine-methylamino)ethyl]amine (5-*tert*-butylamide-diboc-tren).** A solution of **diBoc-tren** (602 mg, 1.73 mmol) in 3 mL of MeOH was added to a solution of 5-*tert*-butylamide-2-pyridinecarboxaldehyde (401 mg, 1.94 mmol) in 3 mL of MeOH charged with 3 Å molecules sieves (50 mg); the resulting solution was allowed to stir at room temperature for 2 hours. The solution was filtered and NaBH₄ (940 mg, 24.8 mmol) was added in several portions to the reaction over 20 minutes; the solution was allowed to stir for 6 hours. The reaction was quenched with water (20 mL) and the product extracted into DCM (3 × 50 mL); the organic layer was dried over MgSO₄ and the solvent removed under reduced pressure. The resulting yellow solid was used without further characterization or purification.

***N,N*-bis[2-(amino)ethyl]-*N*-[2-(5-*tert*-butylamidepyridine-methylamino)ethyl]amine (5-*tert*-butylamide-tren) (Route 2).** A solution of **5-*tert*-butylamide-diBoc-tren** (819 mg) in 4 mL of DCM was cooled to 0 °C and TFA (2.33 mL, 13.7 mmol) was slowly added to the solution over 2 minutes. After all the TFA was added, the reaction was allowed to warm to room temperature. The reaction was allowed to stir for 4 hours. A solution of 2 M NaOH was added until a pH of 12 was achieved; the product was extracted with DCM into the aqueous layer (3 × 30 mL) and the water was removed under reduced pressure. The resulting light yellow oil was purified by column chromatography (SiO₂, 10:2 CHCl₃:MeOH to 80:35:4 to 10:4:1 CHCl₃:MeOH:NH₄OH). The desired fractions were combined and the solvent removed under reduced pressure, resulting in a light yellow oil (380 mg, 74%).

***N,N*-bis[2-(5-*tert*-butylamidepyridine)-3-aza-3-butyenyl]-*N*-[2-(5-*tert*-butylamidepyridine-methylamino)ethyl]amine (L^{5-NH}).** The ligand precursors **5-*tert*-butylamide-tren** (103 mg, 0.02 mmol) suspended in 3 mL of MeCN and 5-*tert*-butylamide-2-pyridinecarboxaldehyde (86 mg,

0.42 mmol) dissolved in 3 mL of MeCN were combined and 3 Å molecular sieves (0.25 g) were added to the solution. The reaction was allowed to stir for 2 hours. The yellow solution was filtered and the solvent removed in *vacuo*, resulting in a light yellow fluffy solid (130 mg, 100%). ¹H NMR (400 MHz, CD₃CN): 8.71 (2 H, d, *J* = 1.5 Hz), 8.65 (1 H, d, *J* = 1.6 Hz), 8.33 (2 H, s), 7.90 (2 H, dd, *J* = 2.2, 8.1 Hz), 7.89 (4 H, dd, *J* = 2.1, 8.1 Hz), 7.63 (2 H, d, *J* = 8.1 Hz), 7.30 (1 H, d, *J* = 8.2 Hz), 6.99 (2 H, bs), 6.85 (1 H, bs), 3.77 (4 H, t, *J* = 4.9 Hz), 3.20 (2 H, t, *J* = 5.6 Hz), 3.03 (2 H, t, *J* = 5.7 Hz), 3.01 (4 H, t, *J* = 5.5 Hz), 1.44 (18 H, s), 1.43 (9 H, s) ppm.

[FeL^{5-(NH)₃}](BF₄)₂ (4.1). To a yellow solution of L^{5-(NH)₃} (60 mg, 0.08 mmol) in 3 mL of MeCN, a solution of Fe(BF₄)₂·6 H₂O (30 mg, 0.09 mmol) in 3 mL of MeCN was added. The solution instantly turned greenish-yellow in color. The solution was allowed to stir for two hours then the volume concentrated by half. Yellow crystals suitable for X-ray analysis were obtained by slow diffusion of Et₂O into a MeCN solution of the compound (57 mg, 72%). IR (ATR): ν_{N-H} 3366, 3314 cm⁻¹. ESI-MS(+) (MeOH): *m/z* 807.3 ([FeL^{5-(NH)₃}+Cl]⁺, 771.4 ([FeL^{5-(NH)₃}-H]⁺, 346.1 [FeL^{5-(NH)₃}]²⁺. ¹H NMR (400 MHz, CD₃CN): 46.8, 41.3, 34.1, 31.9, 8.1, 6.0, 3.4, 2.4, 2.1 ppm. UV-vis (CH₃CN) λ_{max}/nm (ε_M/M⁻¹ cm⁻¹) 267 (12170), 393 (670), 606 (20).

[FeL^{5-(NH)₂}](BF₄)₂ (4.2). The ligand L^{5-(NH)₂} (55 mg, 0.08 mmol) was dissolved into 3 mL of MeOH, and a solution of Fe(BF₄)₂·6 H₂O (29 mg, 0.09 mmol) in 3 mL of MeOH was added. The solution instantly turned blue and was allowed to stir for 2 hours. The reaction was concentrated by ¼ *in vacuo*. Crystals suitable for X-ray diffraction were grown by slow Et₂O diffusion into a MeOH solution of the complex (60 mg, 82%). IR (ATR): ν_{N-H} 3375, 3351 cm⁻¹. ESI-MS(+) (MeOH): *m/z* 789.3 ([FeL^{5-(NH)₂}+F]⁺, 769.4 ([FeL^{5-(NH)₂}-H]⁺, 385.3 [FeL^{5-(NH)₂}]²⁺. ¹H NMR (400 MHz, CD₃CN): 33.9, 26.5, 24.7, 19.0, 15.1, 10.6, 7.8, 7.3, 2.4, 2.0, 1.8, 1.7, 0.9, -4.81, -12.3 ppm. UV-vis (CH₃CN) λ_{max}/nm (ε_M/M⁻¹·cm⁻¹) 268 (14870C), 290 (sh, 11610), 396 (1560),

569 (sh, 1560), 614 (2070). Anal. Calcd for C₃₉H₅₈B₂F₈Fe₂N₁₀O₃: C, 49.60; H, 6.19; N, 14.83. Found: C, 49.33; H, 6.25; N, 14.64.

[FeL^{5-NH}](BF₄)₂ (4.3). To a solution of L^{5-NH} (36 mg, 0.05 mmol) in 3 mL of MeOH, a solution of Fe(BF₄)₂·6 H₂O (14 mg, 0.04 mmol) in 3 mL of MeOH was added. The reaction instantly turned blue and was allowed to stir for 30 minutes. The solution was concentrated to 2 mL *in vacuo* and the compound was precipitated by the addition of 15 mL of Et₂O. The resulting suspension was allowed to stir for 1 hour. The blue solid was isolated by vacuum filtration and washed with 10 mL of Et₂O. The product was used without further purification. ESI-MS(+) (MeOH): *m/z* 855.3 ([FeL^{5-NH}]+BF₄)⁺, 803.4 ([FeL^{5-NH}]+Cl)⁺, 767.5 ([FeL^{5-NH}]-H)⁺, 384.3 [FeL^{5-NH}]²⁺.

[FeL^{5-NH}](BPh₄)₂·3 MeCN (4.4). A solution of 4.3 (81 mg, 0.086 mmol) in 2 mL of MeOH was added to a solution of NaBPh₄ (200 mg, 0.584 mmol) in 2 mL of MeOH to form immediately a purple precipitate; the mixture was stirred for one additional hour. The purple solid was isolated by filtration and washed with 10 mL of MeOH and 5 mL of Et₂O. The product was purified by recrystallization via slow diffusion of diethyl ether into an acetonitrile solution of the compound (40 mg, 33 % yield); X-ray quality crystals were selected from the product. IR (ATR): ν_{N-H} 3389, 3053 cm⁻¹. ESI-MS(+) (MeOH): *m/z* 1087.4 ([FeL^{5-NH}]+BPh₄)⁺, 768.4 ([FeL^{5-NH}])⁺, 384.3 ([FeL^{5-NH}])²⁺. ¹H NMR (400 MHz, CD₃CN): 68.2, 50.4, 43.9, 32.5, 26.9, 24.3, 19.2, 16.9, 9.5, 8.9, 8.0, 4.2, 2.4, 2.3, 2.2, 1.8, -15.7 ppm. UV-vis (CH₃CN) λ_{max}/nm (ε_M/M⁻¹·cm⁻¹) 235 (65300), 267 (22690), 275 (22720), 287 (21340), 366 (970), 550 (sh, 1850), 592 (2080).

4.3.2 X-ray Structure Determination. Structures were determined for the compounds listed in Table 4.1. All single crystals were coated in Paratone-N oil prior to removal from the glovebox. The crystals were supported on Cryoloops before being mounted on a Bruker Kappa

Apex II CCD diffractometer under a stream of cold dinitrogen. Data were collected with Mo K α radiation and a graphite monochromator. Initial lattice parameters were determined from reflections harvested from 36 frames, and data sets were collected targeting complete coverage and 4-fold redundancy. Data were integrated and corrected for absorption effects with the Apex II software package.³ Structures were solved by direct methods, unless otherwise noted, and refined with the SHELXTL software package.⁴ Unless otherwise noted, thermal parameters for all fully occupied, non-hydrogen atoms were refined anisotropically. Hydrogen atoms were added at the ideal positions and were refined using a riding model where the thermal parameters were set at 1.2 times those of the attached carbon atom (1.5 times that for methyl and amine protons).

The structure of **4.1** used a Patterson map to locate the heaviest atoms, difference maps were then used to determine the location of the other atoms. Disorder of the tetrafluoroborate anion in **4.2** was modelled into two components with partial occupancies and refined the thermal parameters were refined anisotropically. Free refinement of the site occupancy factor of the co-crystallized methanol for **4.2** resulted in 66% occupation and the thermal parameters were refined anisotropically. One *tert*-butyl group of the complex cation in complex **4.4** was disordered over two positions and modelled with partial occupancies; the thermal parameters were refined anisotropically. Free refinement of the disordered solvent for **4.4** resulted in two acetonitrile molecules with full occupation and one with 68% occupation; the thermal parameters were allowed to refine anisotropically.

4.3.3 Magnetic Measurements. Solid-state magnetic data were collected using a Quantum Design model MPMS-XL superconducting quantum interference device (SQUID) magnetometer. Measurements were collected using crystals of **4.1**, **4.2**, and **4.4** packed into the top of gelatin capsules and restrained with the bottom portion of the capsule. All samples were prepared under a

dinitrogen atmosphere and quickly loaded into the SQUID to minimize air exposure. The absence of ferromagnetic impurities was confirmed by observing the linearity of a plot of magnetization vs. field at 100 K. DC susceptibility measurements were collected from 5 K to 300 K under an applied DC field of 1000 Oe. Data were corrected for the magnetization of the sample holder by subtracting the susceptibility of an empty container and for diamagnetic contributions of the sample by using Pascal's constants.⁴ Solution-state samples were prepared under a dinitrogen atmosphere. Magnetic susceptibilities in solution were determined by Evans' method NMR using TMS as an internal reference.^{5,6}

4.3.4 Other Physical Methods. Infrared spectra were measured with a Nicolet 380 FT-IR under a dinitrogen flow using an ATR attachment. UV-visible electronic absorption spectra were obtained using an Agilent 8453 UV-visible spectrometer under air-free conditions using a quartz cuvette. Room temperature ¹H NMR spectra were recorded using a Varian 400MR instrument operating at 400 MHz. Variable temperature ¹H NMR spectra were recorded using a Agilent INOVA instrument operating at 500 MHz. Paramagnetic ¹H NMR spectra were acquired using an acquisition time of 1 second and 0.001 second relaxation delay. Mass spectra were obtained on a Finnigan LCQ Duo mass spectrometer equipped with an electrospray ion source and quadrupole ion trap mass analyzer in positive ion mode. Elemental analysis was performed by Robertson MicroLit Laboratories in Ledgewood, NJ.

Table 4.1. Crystallographic data for compounds [FeL^{5-(NH)₃}](BF₄)₂ (**4.1**), [FeL^{5-(NH)₂}](BF₄)₂ (**4.2**), and [FeL^{5-NH}](BPh₄)₂·3 MeCN (**4.4**)

	4.1	4.2	4.4
Crystal code	msn319	msn355	msn397
Empirical formula	C ₃₉ H ₆₀ B ₂ F ₈ FeN ₁₀ O ₃	C ₃₉ H ₅₈ B ₂ F ₈ FeN ₁₀ O ₃	C _{92.40} H _{104.05} B ₂ FeN _{12.70} O ₃
Formula wt., g·mol ⁻¹	946.44	944.42	1518.00
Crystal color	yellow	blue	purple
Habit	block	plate	block
<i>T</i> , K	120(2)	120(2)	120(2)
Space group	<i>P</i> 1	<i>P</i> $\bar{1}$	<i>P</i> 2 ₁
<i>Z</i>	1	2	2
<i>a</i> , Å	9.6362(4)	9.7563(9)	9.8781(4)
<i>b</i> , Å	9.9229(4)	10.0337(9)	26.0264(1)
<i>c</i> , Å	14.1865(6)	27.092(2)	16.9278(7)
α , deg	106.016(2)	90.078(4)	90
β , deg	94.891(2)	94.736(4)	102.111(2)
γ deg	118.071(2)	118.053(4)	90
<i>V</i> , Å ³	1112.85(8)	2330.0(4)	4255.1(3)
<i>d</i> _{calc} , g·cm ⁻³	1.412	1.346	1.185
GooF	0.652	1.200	1.019
<i>R</i> ₁ ^{<i>a</i>} (<i>wR</i> ₂) ^{<i>b</i>} %	5.49 (6.40)	8.66 (19.02)	5.93 (10.32)

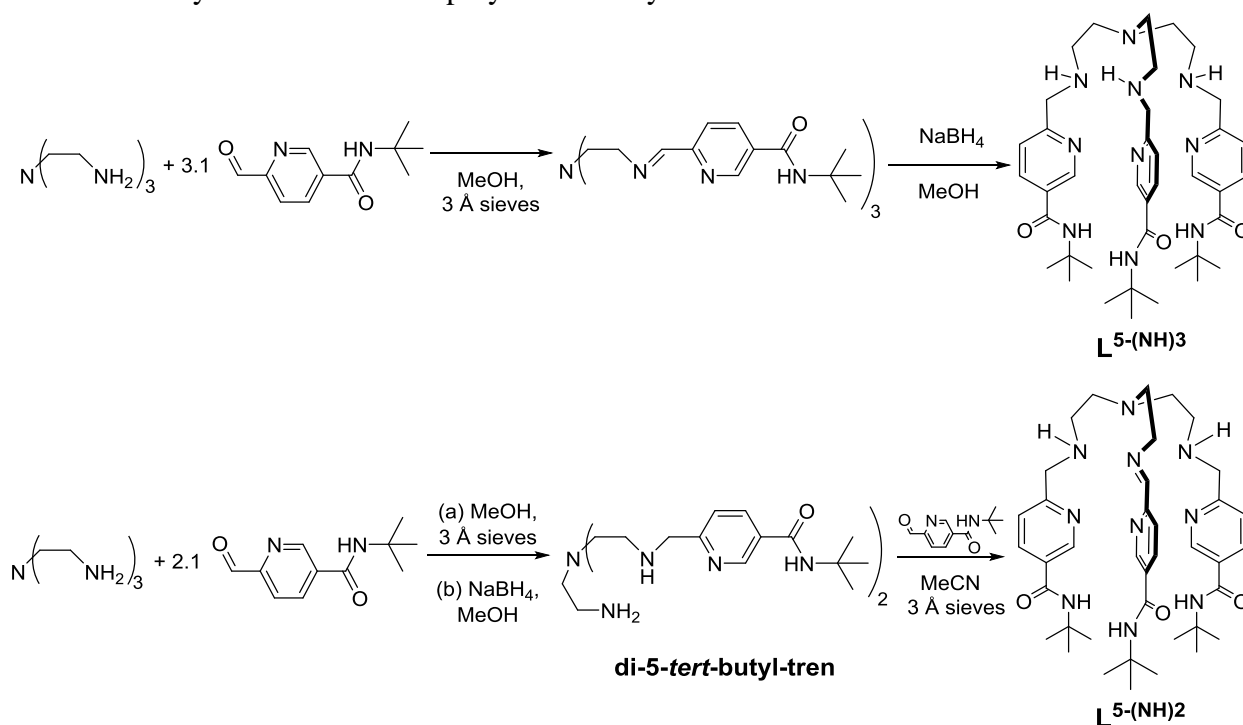
$$^a R_1 = \frac{\sum ||F_o| - |F_c||}{\sum |F_o|}; \quad ^b wR_2 = \left\{ \frac{\sum [w(F_o^2 - F_c^2)^2]}{\sum [w(F_o^2)^2]} \right\}^{1/2}$$

4.4 Results and Discussion.

4.4.1 Synthesis and Characterization. As shown in Scheme 4.1, $L^{5-(NH)3}$ and the pre-ligand **di-5-*tert*-butylamide-tren** of $L^{5-(NH)2}$ are synthesized by reductive amination *via* a Schiff-base condensation in methanol by adding 3.1 or 2.1 equivalents of 5-*tert*-butylamide-2-pyridinecarboxaldehyde, respectively, to one equivalent of tris(2-aminoethyl)amine (tren) then subsequent reduction of the imine using $NaBH_4$ (Scheme 4.1). The resulting products can be purified by column chromatography to isolate $L^{5-(NH)3}$ or the $L^{5-(NH)2}$ precursor **di-5-*tert*-butylamide-tren**. An additional Schiff-base condensation with **di-5-*tert*-butylamide-tren** and one equivalent of 5-*tert*-butylamide-2-pyridinecarboxaldehyde produces the desired ligand $L^{5-(NH)2}$. Numerous attempts to synthesize the pre-ligand for L^{5-NH} resulted in the formation of difunctionalized tren with little formation of the monofunctionalized tren. It is presumed that the introduction of the amide groups is forming hydrogen bonds between two or more amides after condensation with tren, leading to a higher prevalence of the difunctionalized tren product.

In order to synthesize L^{5-NH} , the protecting groups *tert*-butyloxycarbonyl (Boc) and 4-nitrobenzenesulfonyl chloride (nosyl) were used required (Scheme 4.2). Protection of one arm using Boc is achieved by slow addition of Boc_2O to tren in DCM at $-78\text{ }^\circ\text{C}$, which leads to the formation of a mixture of **monoBoc-tren** and **diBoc-tren**. In the first route attempted (route 1, Scheme 4.2) additional protection of the other two arms of **monoBoc-tren** using 4-nitrobenzenesulfonyl (nosyl) allows for selective cleavage of the Boc protecting group using trifluoroacetic acid (TFA) while preserving protection of the other two arms. Reductive amination of the free amine and 5-*tert*-butylamide-2-pyridinecarboxaldehyde then cleavage of the nosyl protecting groups using excess dodecanethiol and potassium carbonate in acetonitrile produces the

Scheme 4.1. Synthetic scheme employed for the syntheses of $L^{5-(NH)3}$ and $L^{5-(NH)2}$.



desired monofunctionalized tren. Lastly, Schiff-base condensation between the pre-ligand and 5-*tert*-butylamide-2-pyridinecarboxaldehyde in acetonitrile produces the ligand L^{5-NH} .

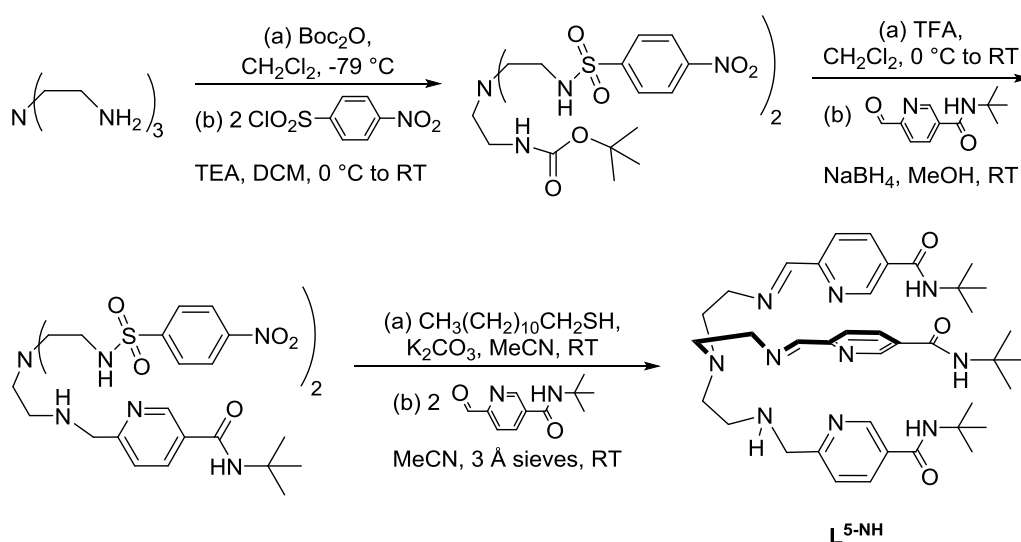
Another route employed (route 2, Scheme 4.2) used a diBoc-protected tren, a side product of the Boc protection of tren. Reductive amination of the free amine with 5-*tert*-butylamide-2-pyridinecarboxaldehyde and $NaBH_4$ then removal of the Boc protecting groups with TFA also produces the mono-armed tren, **5-*tert*-butylamide-tren**, in higher yields and less time. Regardless of the route used to synthesize **5-*tert*-butylamide-tren**, Schiff base condensation using two equivalents of 5-*tert*-butylamide-2-pyridinecarboxaldehyde with one equivalent of **5-*tert*-butylamide-tren** forms L^{5-NH} .

Once the ligands are synthesized, the preparation of the Fe(II) salts is straightforward. Addition of one equivalent $Fe(BF_4)_2 \cdot 6 H_2O$ in acetonitrile or methanol to one equivalent of either $L^{5-(NH)3}$, $L^{5-(NH)2}$, or L^{5-NH} results in the an immediate color change to the solution. An anion

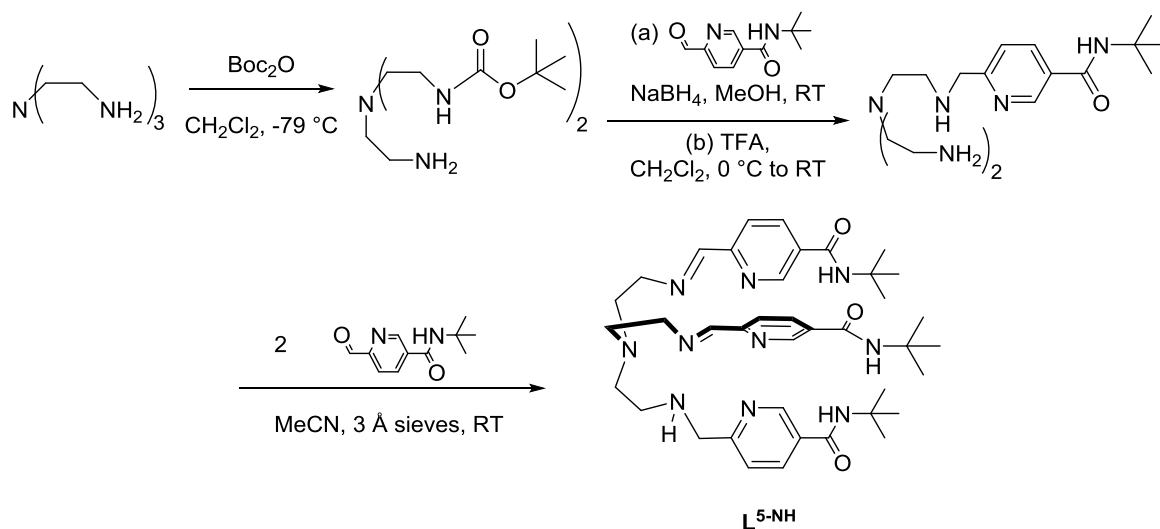
exchange from BF_4^- for $[\text{FeL}^{5\text{-NH}}]^{2+}$ to BPh_4^- was performed in methanol using excess NaBPh_4 to isolate **4.4**. Crystals of **4.1** and **4.4** were isolated by slow diethyl ether diffusion into acetonitrile solution, while crystals of **4.2** were isolated from slow diethyl ether diffusion into methanolic solutions of the compound.

Scheme 4.2. Synthetic scheme employed for the synthesis of **L^{5-NH}**.

Route 1



Route 2



The UV-visible absorption spectra of **4.1**, **4.2**, **4.4**, and $[\text{FeL}^{5\text{-ONHrBu}}](\text{BF}_4)_2$ were studied in acetonitrile (Figure 4.2). Strong absorbance in the UV region is observed ranging from 15,000–40,000 $\text{M}^{-1}\cdot\text{cm}^{-1}$ for **4.1**, **4.2**, and $[\text{FeL}^{5\text{-ONHrBu}}](\text{BF}_4)_2$ and 70,000 $\text{M}^{-1}\cdot\text{cm}^{-1}$ for **4.4** due to the tetraphenylborate anions. As more imines are added to the ligand, the molar absorptivities increase in the UV region of $\lambda < 330$ nm. This is most likely due to the increased conjugation the imines impart as these absorptions are assigned as ligand centered $\pi \rightarrow \pi^*$ transitions. Absorptions in the visible region of the spectrum have been previously assigned as metal-to-ligand charge transfer bands.⁷ Again, with increasing conjugation of the ligand for **4.2** and **4.4**, the molar absorptivities of the absorbances at $\lambda > 330$ nm increase. As a consequence of the HS nature at room temperature for **4.1**, **4.2**, and **4.4** (*vide infra*), the molar absorptivities of these complexes are substantially lower than those seen for $[\text{FeL}^{5\text{-ONHrBu}}](\text{BF}_4)_2$. The high spin nature of the Fe(II) complexes in solution at room temperature is supported by the paramagnetic shifting and broadening of the ^1H NMR as a consequence of the paramagnetic $S = 2$ state (Figure 4.3).

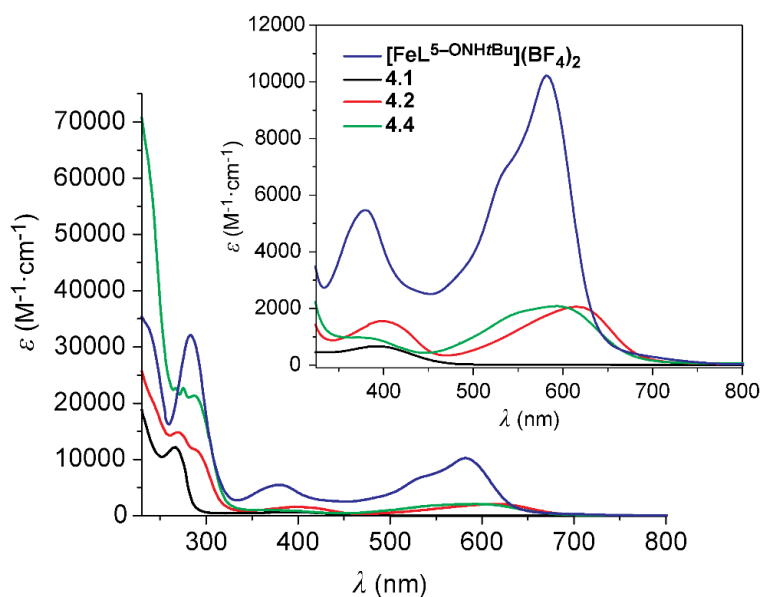


Figure 4.2. Electronic absorption spectra of **4.1**, **4.2**, **4.4**, and $[\text{FeL}^{5\text{-ONHrBu}}](\text{BF}_4)_2$ collected in acetonitrile from 230 to 800 nm. Inset: Visible range from 330 to 800 nm.

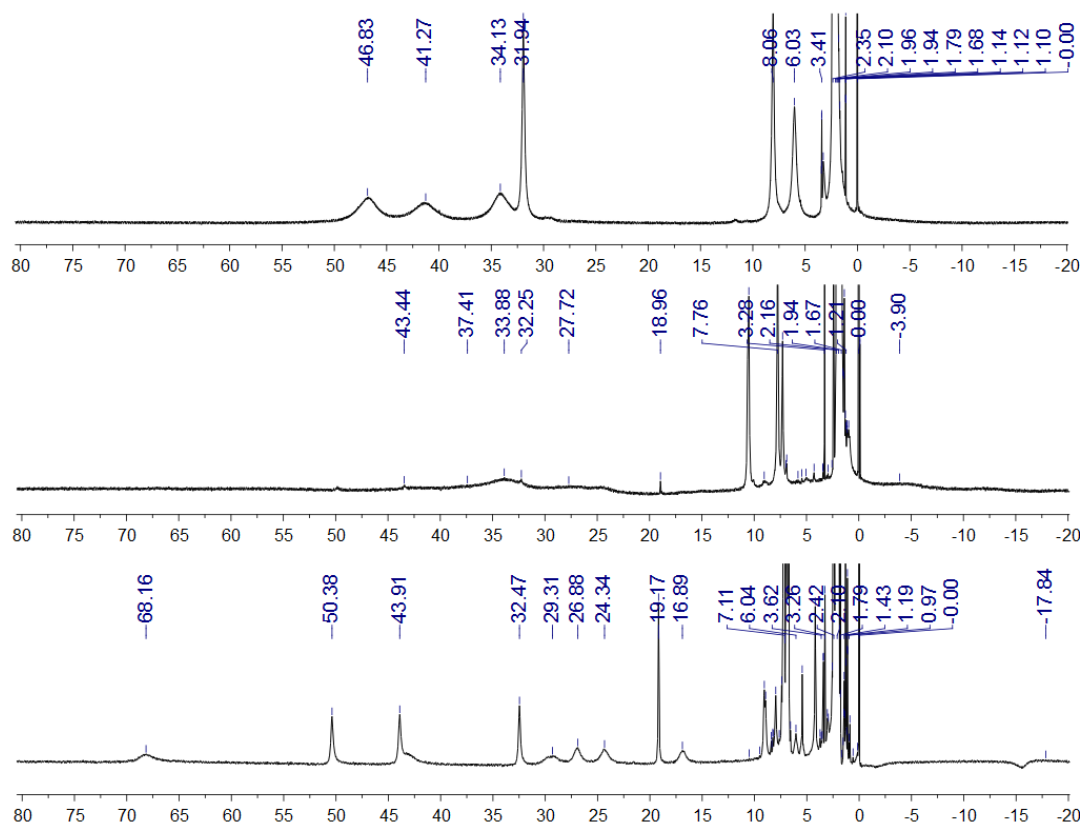


Figure 4.3. Paramagnetic ^1H NMR spectra of **4.1** (top), **4.2** (middle), and **4.4** (bottom) at 298 K in CD_3CN .

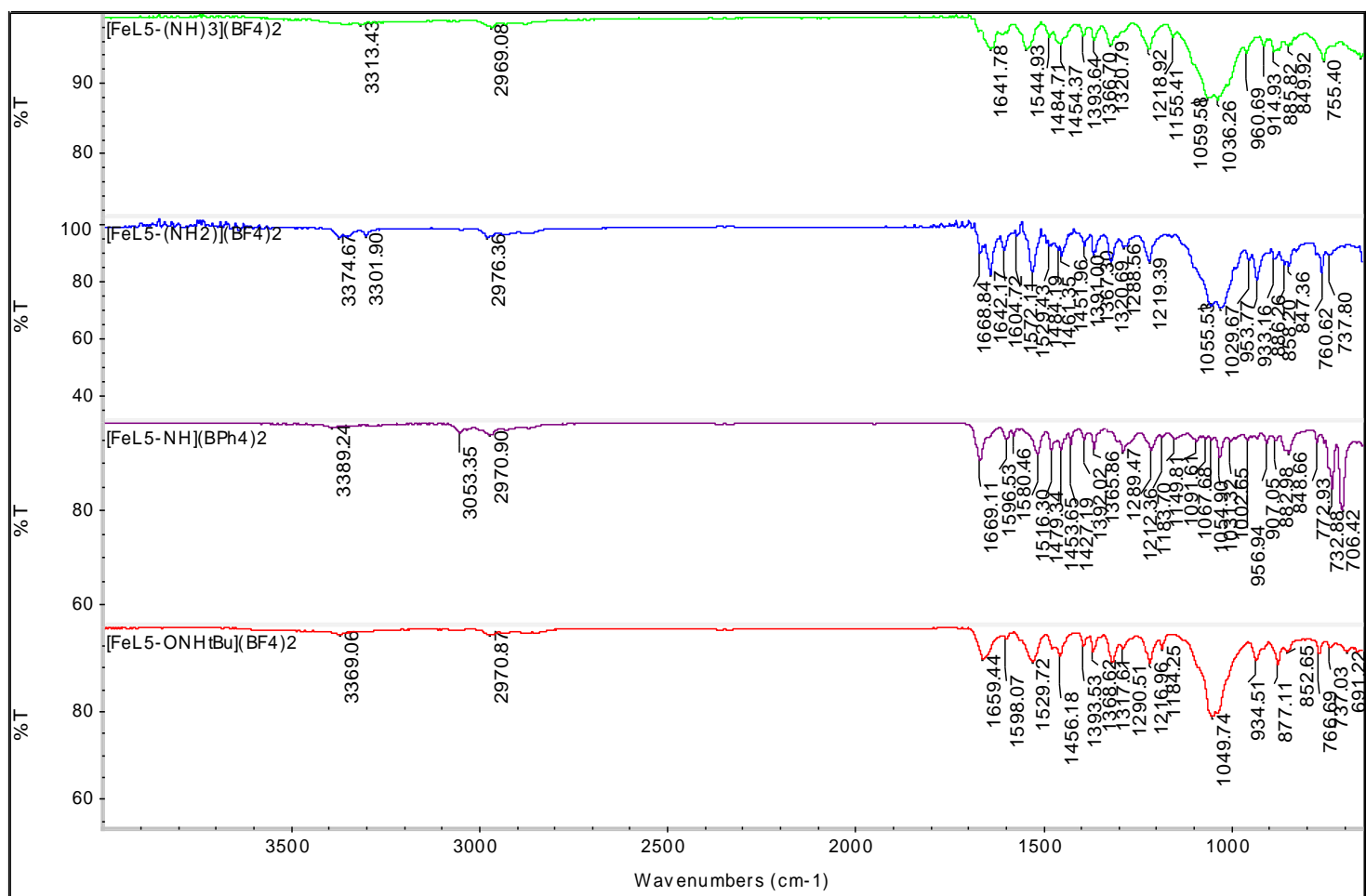


Figure 4.4a. FT-IR comparison of complexes **4.1**, **4.2**, **4.4** and $[\text{FeL}^5\text{-ONHtBu}](\text{BF}_4)_2$ performed by pressing crystalline samples onto a ZnSe ATR crystal.

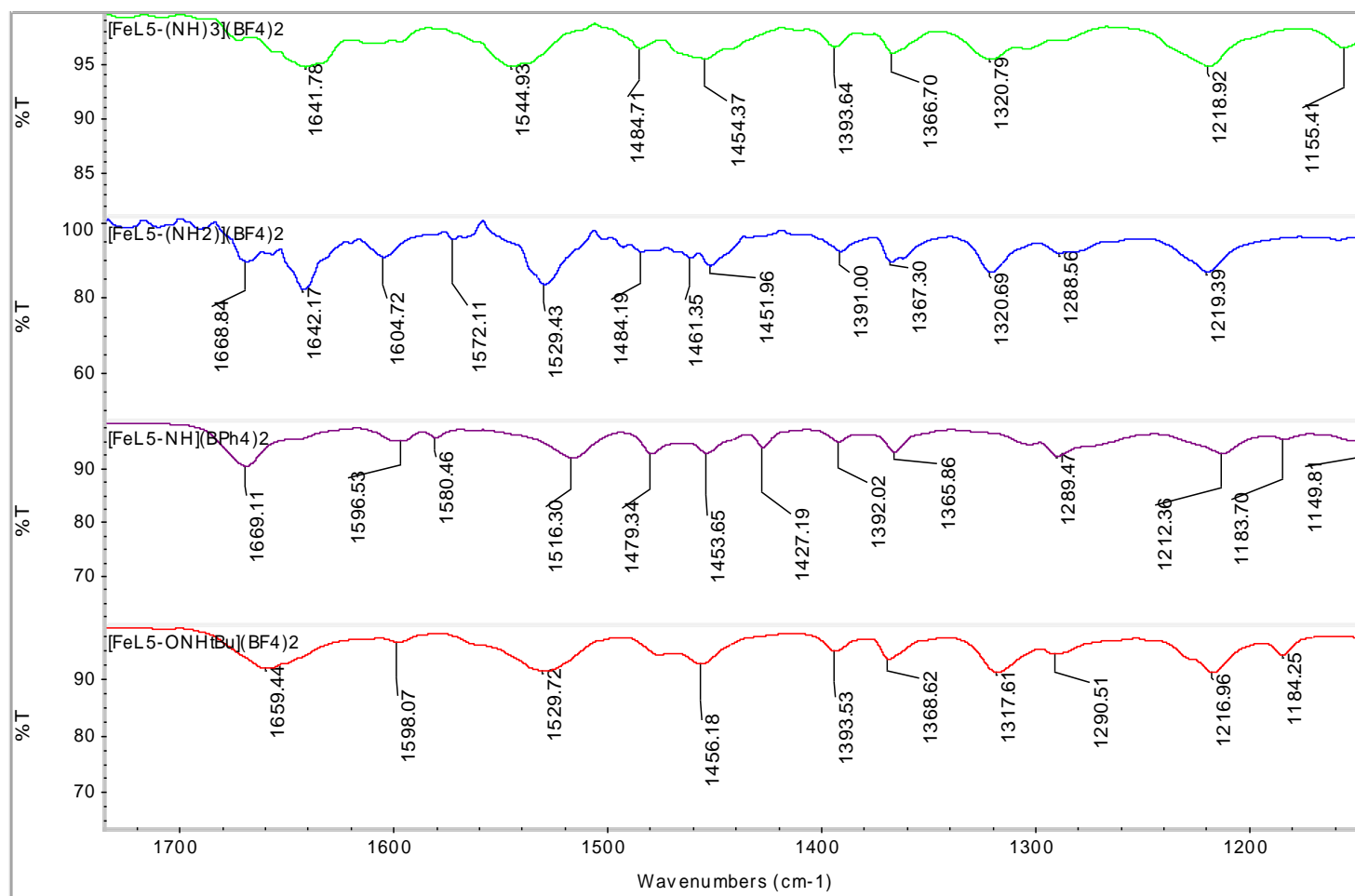


Figure 4.4b. FT-IR comparison of complexes **4.1**, **4.2**, **4.4** and $[\text{FeL}^5\text{-ONH}t\text{Bu}](\text{BF}_4)_2$ performed by pressing crystalline samples onto a ZnSe ATR crystal from 1750 to 1250 cm^{-1} .

4.4.2 X-ray Structural Analyses. To glean the influence of substituting amines for imines on the coordination environment of the Fe(II) center in the solid state, X-ray crystal structures of **4.1**, **4.2**, and **4.4** were collected at 120 K (Figure 4.5). The coordination environments around the Fe centers are octahedral in nature, with the first coordination sphere of the metal comprises six nitrogen atoms, three from the imines/amines and three from the pyridines. As is common with tripodal iminopyridine ligands,⁸ the Fe–N_{a/imine} bond lengths are shorter than the Fe–N_{pyridine} bond lengths. The average Fe–N bond lengths of 2.294(5) Å for **4.1**, 2.26(1) Å for **4.2**, and 2.23(1) Å for **4.4** are consistent with the complexes occupying the HS state at 120 K, and are substantially longer than those seen for the low spin {[FeL⁵-ONH_tBu]Cl}⁺ (Table 4.2). The Fe–N_{bridge} distances are substantially shorter for this set of complexes than the analogous distances seen for similar iminopyridine-based complexes regardless of the spin state; the shortest distance is observed for **4.1** at 2.459(2) Å and the longest distance occurring for **4.4** at 2.603(4) Å. Comparatively, the Fe–N_{bridge} distance for the known spin crossover complex, [FeL⁶-OH](OTf)₂, is 3.187(3) Å in the HS state, while in the LS state, this distance is 3.723(2) Å.⁹ Accounting for the close contact between the bridgehead nitrogen and the Fe center for this set of complexes, the coordination of the Fe center could be considered pseudo-heptacoordinate in nature. Moreover, the coordination environments are substantially distorted from perfect octahedral geometry as indicated by the structural distortion parameters Σ^{10-12} and Θ .^{11,13} For comparison, these structural distortion parameters for the tris-imine LS complex {[FeL⁵-ONH_tBu]Cl}⁺ are significantly closer to 0°,¹ the expected value for perfect octahedron, and are similar to other LS tripodal iminopyridine-based complexes.^{8,9} Measurement of the torsion angle (φ) for the three ligand arms shows that while the coordination environment is highly distorted, the geometry leans towards octahedral instead of trigonal prismatic.¹⁴

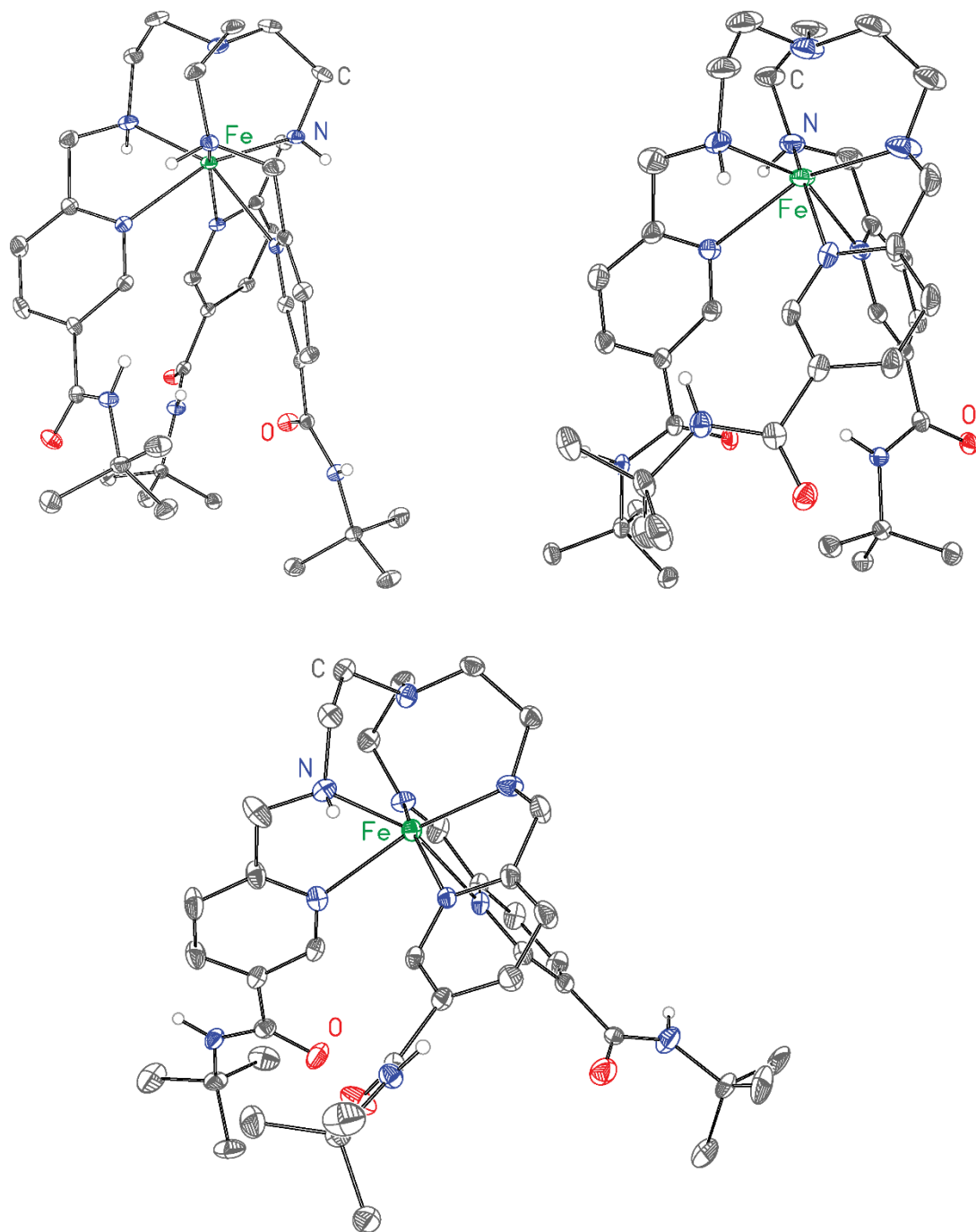


Figure 4.5. X-ray crystal structures of the complex cations of **4.1** (top, left), **4.2** (top, right), and **4.4** (bottom). Fe, C, H, N, O atoms are represented by green, dark gray, light gray, blue, and red respectively. Thermal ellipsoids are rendered with 40% probability. Hydrogen atoms except those of the nitrogens, anions, and solvent have been omitted for clarity.

Table 4.2. Selected bond lengths and angles for **4.1**, **4.2**, **4.4**, and $[\text{FeL}^{5\text{-ONHtBu}}]^{2+}$.

	4.1	4.2	4.4	$\{[\text{FeL}^{5\text{-ONHtBu}}]_2\text{Cl}\}^+$
Fe-N _{a/imine} (Å)	2.241(4) ^a	2.195(8)	2.161(8)	1.955(7)
Fe-N _{py} (Å)	2.346(3)	2.324(8)	2.309(8)	1.985(7)
Fe-N _{bridge} (Å)	2.459[2] ^b	2.521[4]	2.603[4]	3.480(5)
Σ (°)	155.3(3)	143.2(5)	130.7(6)	58.6(3)
Θ (°)	203.9	207.9	216.2	120.6
φ (°)	53.0	50.5	50.8	53.7
N _{a/imine} -N _{a/imine} (Å)	3.741(7)	3.63(1)	3.52(1)	2.90(1)
N _{py} -N _{py} (Å)	3.174(6)	3.134(3)	3.24(1)	2.893(9)
N _{a/imine} -C (Å)	1.460(8)	1.37(1)	1.31(1)	1.286(8)
C _{a/imine} -C _{pyr} (Å)	1.506(7)	1.49(1)	1.48(1)	1.445(9)
C _{pyr} -N _{pyr} (Å)	1.344(7)	1.346(9)	1.35(1)	1.362(8)
N _{amide} -N _{amide} (Å)	5.326(6)	5.382(8)	9.29(1)	5.51(1)
N _{amide} -O _{amide} (Å)	3.064[4]	3.056[4]	N/A	N/A
C ₆ -C ₆ (Å) ^c	3.437(8)	3.464(9)	4.00(1)	3.711(8)
$\Delta\text{C}_6\text{-C}_6$ (Å) ^d	0.196	0.273	0.354	0.180

^a The e.s.d determined as the square root of the sum of the e.s.d. of the averaged values.

^b Signifies the e.s.d. as determined by SHELXTL

^c Average distance defined as α -carbons of pyridine ring, see Figure 4.6.

^d Difference between the longest and shortest distances

Aside from differences in the coordination environment of the Fe center, significant differences are observed in the ligand. Some positional disorder of the imine and amine arms is noted by the elongated thermal parameters for the *a/imine* nitrogen and the adjacent carbons. This is most prominent for **4.2**. The average N_{a/imine}-C bond lengths shorten with increasing number of imines, decreasing from 1.460(8) Å for **4.1** to 1.31(1) Å for **4.4**. Furthermore, this also leads to a shortening of the bond length between the carbon atom adjacent to the *a/imine* and the 2'-position carbon of the pyridine ring, decreasing from 1.506(7) Å for **4.1** to 1.48(1) Å for **4.4**.

The deformation of the coordination environment of the metal center also leads to a distortion of the trigonal binding pocket formed by the amides. The weakly-interacting BF₄⁻ and BPh₄⁻ anions do not appear to participate in any hydrogen-bonding or π -O/NH interactions with the amides (Figures 4.6–8). The orientation of the amide nitrogens appears to be dictated by intermolecular hydrogen-bonding interaction between the amide nitrogen and the oxygen of an

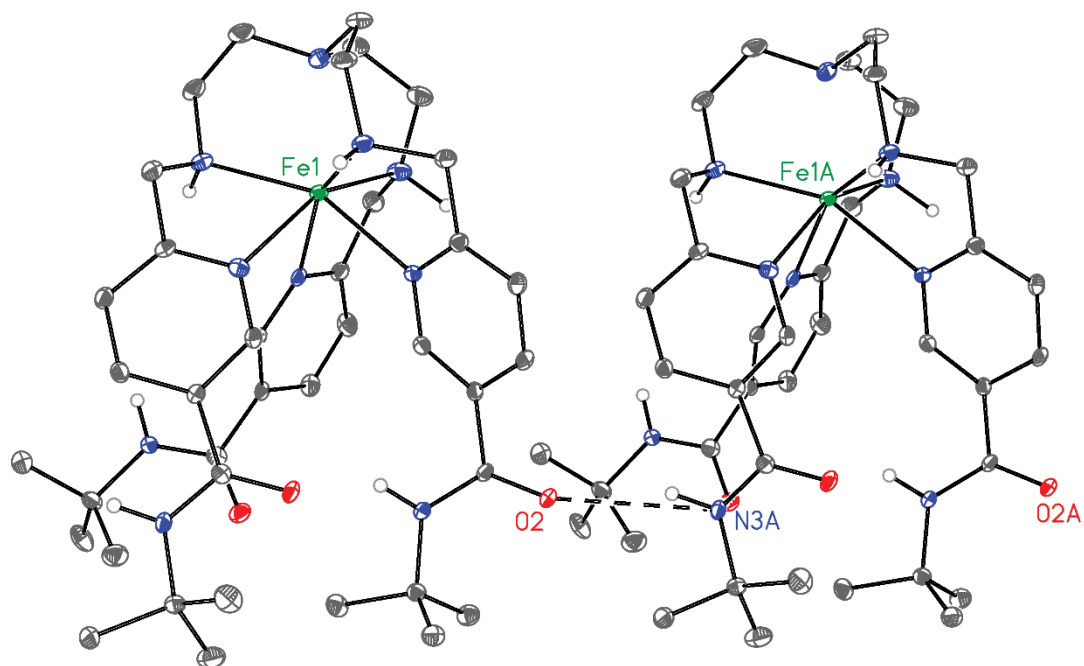


Figure 4.6. Cation-anion interactions for **4.1**. Fe, C, N, and O atoms are colored dark green, dark gray, blue, and red respectively. Hydrogen atoms except those of the amines and anions have been omitted for clarity.

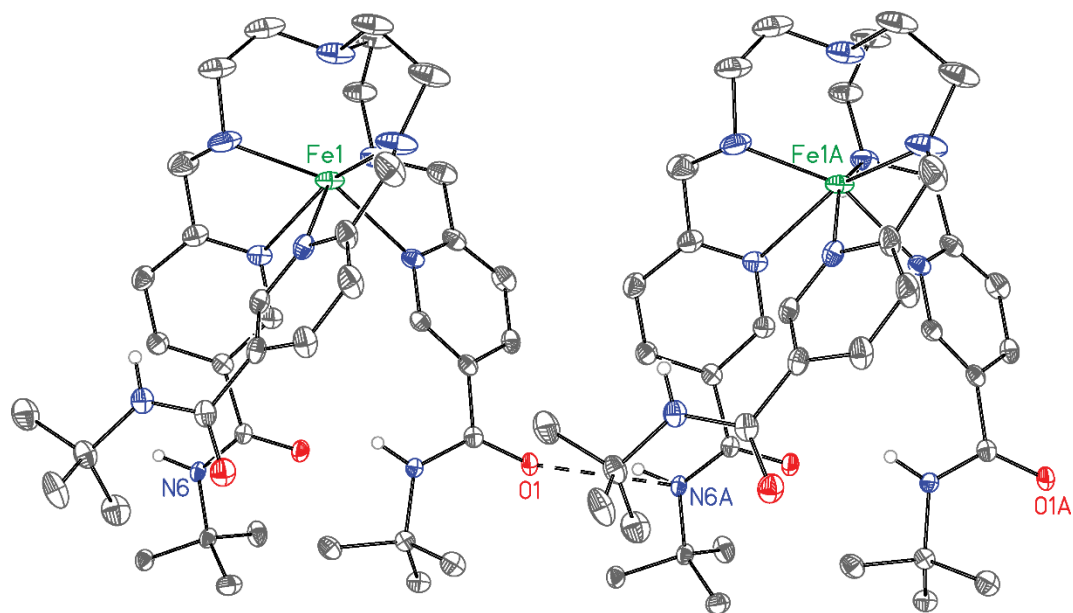


Figure 4.7. Cation-anion interactions for **4.2**. Fe, C, N, and O atoms are colored dark green, dark gray, blue, and red respectively. Hydrogen atoms except those of the amines, anions, and solvent have been omitted for clarity.

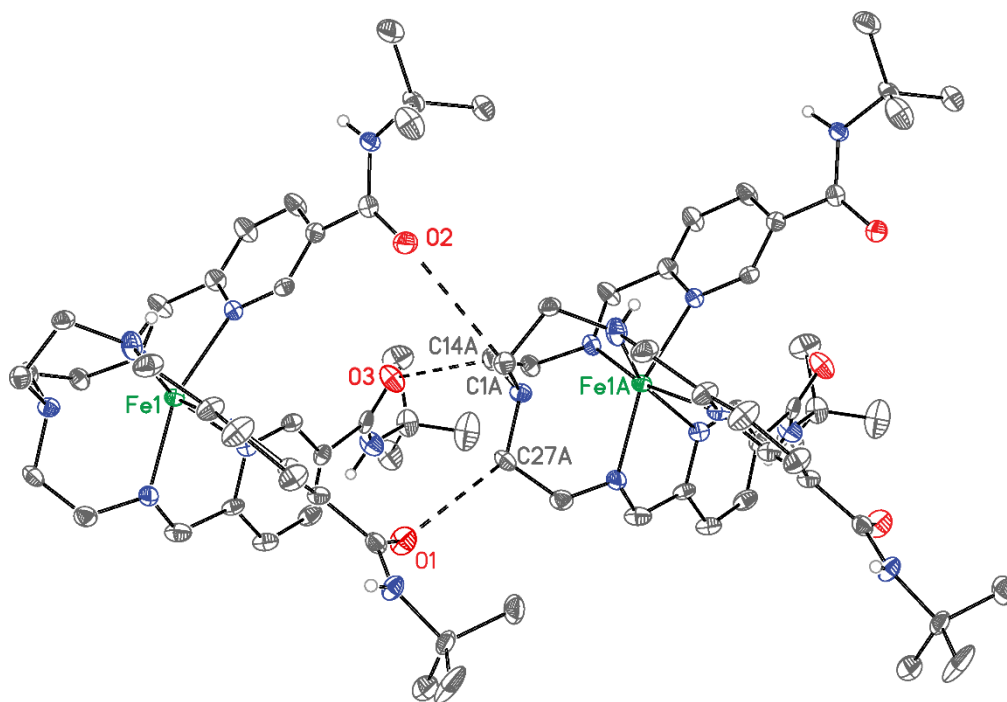


Figure 4.8. Cation-anion interactions for **4.4**. Fe, C, N, and O atoms are colored dark green, dark gray, blue, and red respectively. Hydrogen atoms except those of the amines, anions, and solvent have been omitted for clarity.

adjacent cation for complexes **4.1** and **4.2**. Similar interactions are not observed for **4.4**: the size of the BPh_4^- anions and the ‘head-to-toe’ packing of the cations precludes any formal intermolecular hydrogen-bonding interactions. Weak $\text{CH}\cdots\text{O}$ contacts between the ethylene backbone and the carbonyl of the amide are noted, forcing the amide groups to splay outward to accommodate the packing.

A secondary measure of the pocket distortion is the asymmetry of the triangle formed by the 6′-position carbons (Figure 4.9). From this analysis, the largest average distance between these carbon atoms occurs for **4.4** at 4.00(1) Å and shortest for **4.1** at 3.437(8) Å. Similarly, the largest difference between the longest and shortest distance between these atoms is also observed for **4.4** at 0.354 Å and therefore has the most asymmetric binding pocket. For comparison, the binding pocket of the tris-imine complex $\{[\text{FeL}^{5\text{-ONHtBu}}]\text{Cl}\}^+$ with a bound Cl^- is the most symmetric; the

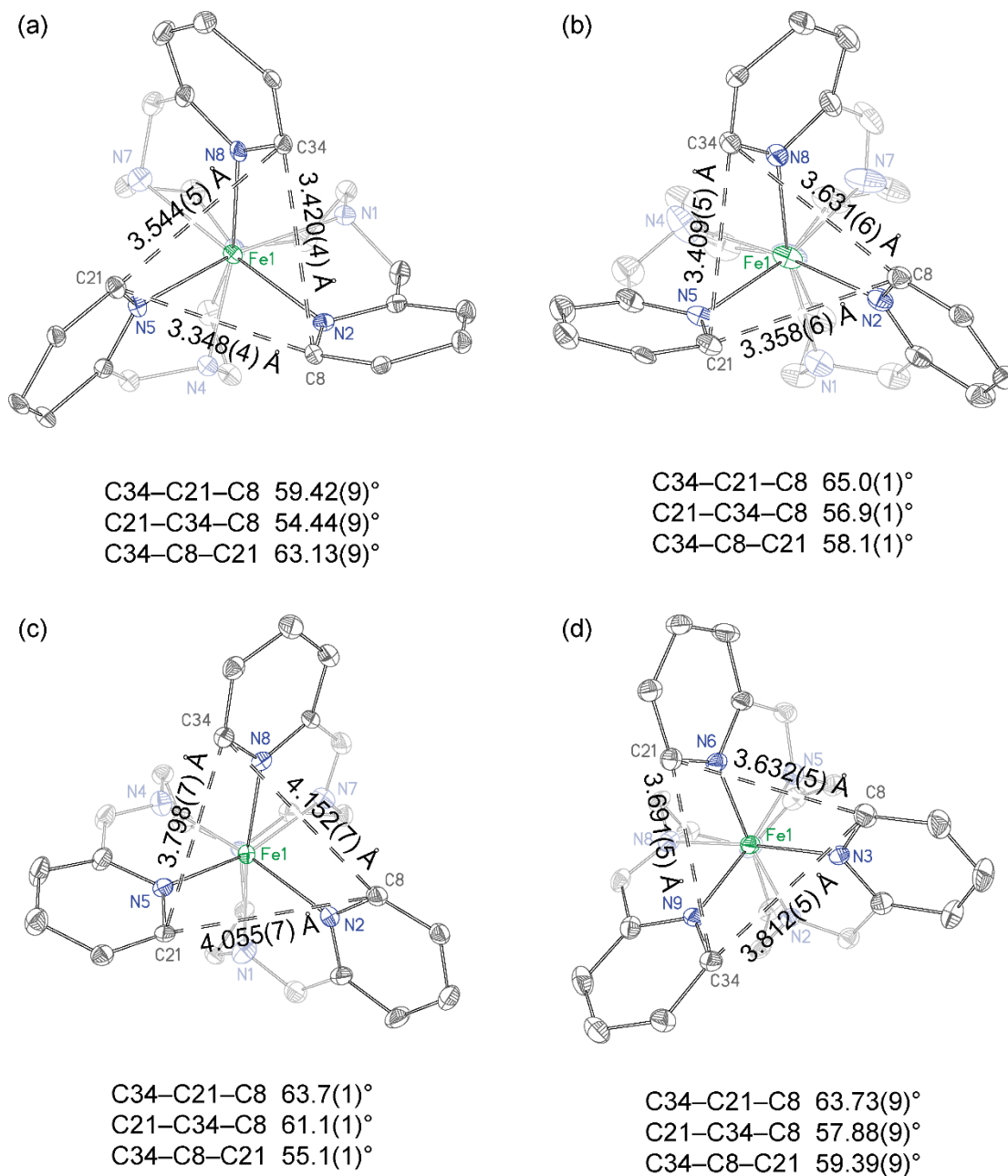


Figure 4.9. Trigonal pocket distortions as defined by 6'-position carbon atoms for **4.1** (a), **4.2** (b), **4.4** (c) and $\{[\text{FeL}^{5\text{-ONHtBu}}]\text{Cl}\}^+$. Fe, C, and N atoms are colored dark green, dark gray, and blue respectively. Hydrogen atoms, the amides, anions, and solvent have been omitted for clarity.

largest difference between C₆–C₆ is 0.18 Å. Unfortunately, a direct comparison in the absence/presence of host:guest interactions between the modified ligands and [FeL^{5-ONHtBu}]²⁺ of these structural parameters is not possible, as X-ray quality crystals of [FeL^{5-ONHtBu}](BF₄)₂ or halide salts of **4.1**, **4.2**, or **4.4** have not been isolated. Lastly, measurement of the angular distortion, defined as summation of the deviation from 60° of the three point of the triangle formed by the carbon atoms (Figure 4.9), range from 10.0° for **4.2** to 5.46° for {[FeL^{5-ONHtBu}]₂Cl}⁺ with **4.1** and **4.4** having similar angles of 9.3° and 9.7°, respectively.

4.4.3 Magnetic Properties. Measurements of the variable temperature magnetic susceptibility in solution and in the solid state were performed. At room temperature in the solid state, all the complexes are high spin with χ_{MT} values of 3.38, 3.47, and 3.58 cm³·K·mol⁻¹, for **4.1**, **4.2**, and **4.4**, respectively (Figure 4.10). These values are within the range expected for *S* = 2 complexes with *g* values greater 2 due to the deformation of the Fe(II) coordination environment. At low temperatures, the complexes all remain high spin down to 5 K, reaching minimums in χ_{MT} values at 5 K of 2.41 cm³·K·mol⁻¹ for **4.1**, 2.71 cm³·K·mol⁻¹ for **4.2**, and 2.36 cm³·K·mol⁻¹ for **4.4**. The decreases in the magnetic susceptibilities below 20 K are attributed to zero-field splitting due to the distorted octahedral coordination geometries of the Fe(II) centers. Presumably, along with the weak ligand fields for the three ligands, the coordination environments of the three complexes are too distorted in the solid state to make the significant structural change required to stabilize the low spin state, thus all three compounds remain HS at all temperatures.

To test for spin–state switching in solution, the temperature dependence magnetic susceptibility of **4.1**, **4.2**, and **4.4** were probed in (CD₃)₂CO using Evans' method^{5,6} (Figure 4.11). These results show that at room temperature, complexes **4.1** and **4.4** are fully HS with χ_{MT} values of 3.0 cm³·K·mol⁻¹ for both complexes, while **4.2** is mostly high spin at 298 K with a χ_{MT} value

of $2.5 \text{ cm}^3 \cdot \text{K} \cdot \text{mol}^{-1}$. Upon cooling, little change is seen in $\chi_{\text{M}}T$ for **4.1** and **4.4**, remaining consistently $3.0 \text{ cm}^3 \cdot \text{K} \cdot \text{mol}^{-1}$ between 298 K and 183 K. Interestingly, a marked difference in the magnetic behavior is observed for **4.2** upon cooling. With decreasing temperature, the $\chi_{\text{M}}T$ value decreases from $2.6 \text{ cm}^3 \cdot \text{K} \cdot \text{mol}^{-1}$ at 308 K to $1.0 \text{ cm}^3 \cdot \text{K} \cdot \text{mol}^{-1}$ at 183 K, a hallmark of spin-state switching.

While these results are unexpected, a potential mechanism can be proposed for the difference in behavior of **4.2**: the flexibility of the ligand arms of $\text{L}^{5\text{-NH}}$ allows for intramolecular hydrogen bonding between two of the amides. Two of the arms would be brought close together thus stabilizing the ligand field.¹⁵ This coupled with a sufficiently strong ligand field, which is not attained by **4.1**, may allow for stabilization of the LS state. While it is difficult to correlate solid-state and solution behavior due to the prevalence of intermolecular interactions, we propose that the increased rigidity of the additional imine arm for complex **4.4** prevents the stabilization of the low spin state. This forces the complex to remain high spin at all temperatures.

4.4.4 Anion-dependent Spin-state Behavior. Intrigued by the prospect of anion-dependent spin state behavior for these complexes, room temperature anion titrations of **4.2** and **4.4** and variable temperature magnetic susceptibility measurements of **4.1** and **4.2** were undertaken (Figure 4.12). The diamagnetic tris-imine complex $[\text{FeL}^{5\text{-ONHtBu}}]^{2+}$ is known to show strong host:guest interactions in CD_3CN through the amide moiety,¹ but similar detailed analyses of the proton chemical shift changes with anion binding are complicated by the paramagnetic broadening and shifting exhibited by these paramagnetic complexes and were not undertaken.

Monitoring of the magnetic susceptibility by Evans' method with the addition of Bu_4NCl to **4.2** and **4.4** at room temperature in CD_3CN shows complex **4.4** (Figure 4.12, green diamonds)

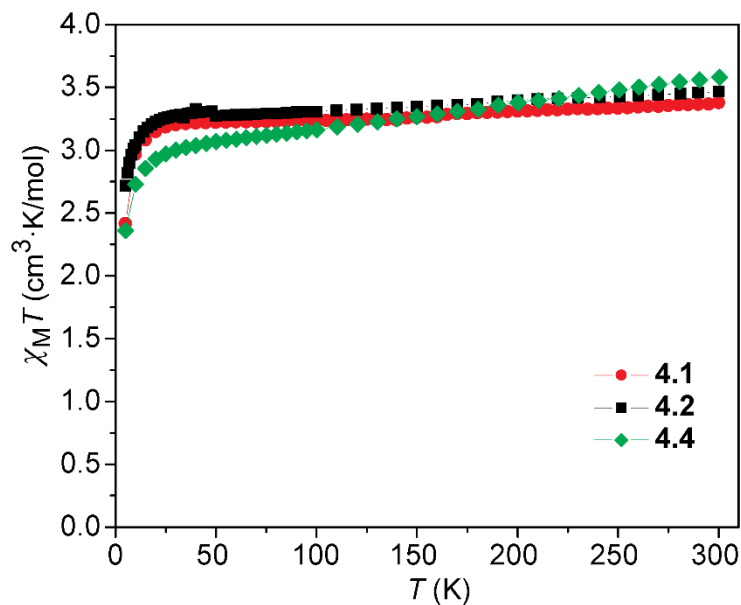


Figure 4.10. Solid-state magnetic susceptibility measurements of **4.1** (red squares), **4.2** (black squares), and **4.4** (green diamonds). $H_{dc} = 1000$ Oe. Lines are guides for the eye.

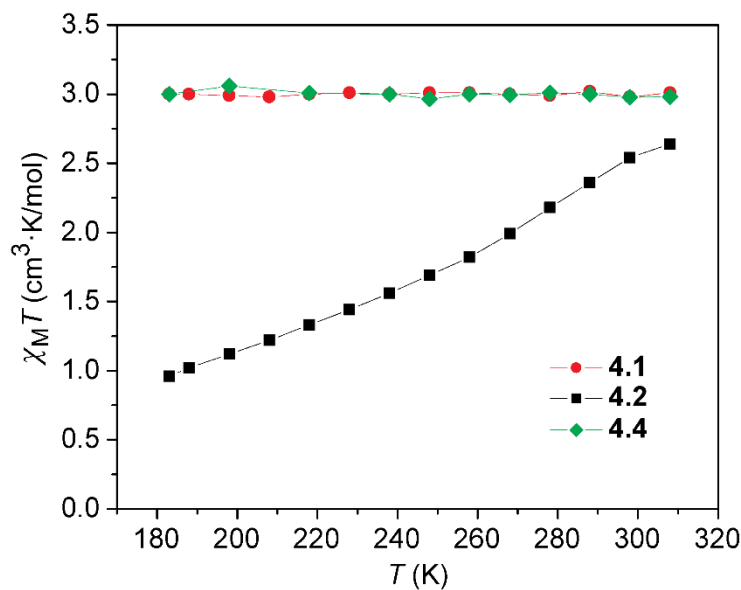


Figure 4.11. Solution variable temperature magnetic susceptibility for **4.1** (red circles), **4.2** (black squares), and **4.4** (green diamonds) collected between 308 and 183 K in d_6 -acetone. Lines are guides for the eye.

is high spin in the absence of Cl^- with a $\chi_{\text{M}}T$ value of $3.0 \text{ cm}^3 \cdot \text{K} \cdot \text{mol}^{-1}$ and remains consistently HS with the addition of up to 4 equivalents of Bu_4NCl .

A similar procedure was performed for complex **4.2** (Figure 4.12, black squares). With the addition of Bu_4NCl to **4.2**, a reproducible increase in the susceptibility is observed up to 1.0 equivalent, starting at $2.4 \text{ cm}^3 \cdot \text{K} \cdot \text{mol}^{-1}$ with zero equivalents of Cl^- and gradually increasing to $2.7 \text{ cm}^3 \cdot \text{K} \cdot \text{mol}^{-1}$ with 1.0 equivalent of Cl^- . Further addition of Cl^- up to two equivalents leads to a decrease in the susceptibility, dropping to $2.5 \text{ cm}^3 \cdot \text{K} \cdot \text{mol}^{-1}$, where the susceptibility plateaus up to the addition of five equivalents of Cl^- . Since there are two potential binding sites, the trigonal pocket formed by the amides and the coordinated secondary amines, it is hypothesized that the first equivalent of chloride would bind into the trigonal pocket formed by the amides (Figure 4.14). This binding would cause the trigonal pocket to expand, thus elongating the Fe-N bond lengths and promoting further population of the HS state. After the addition of one equivalent of Cl^- , additional hydrogen-bonding interactions could occur between the second Cl^- and the coordinated secondary amines. This second binding event is expected to influence the spin state in a similar fashion as H_2bip ; the interaction of the anion increases the σ -donating ability of the nitrogen atoms, thus increasing the ligand field strength.¹⁶

Addition of one equivalent of chloride to **4.1** in CD_3CN appears to have little influence on the spin state as determined between 295 and 232 K (Figure 4.14). The complex remains HS, maintaining a $\chi_{\text{M}}T$ value of $3.0 \text{ cm}^3 \cdot \text{K} \cdot \text{mol}^{-1}$ between these temperatures. Presumably, the ligand field is too weak to stabilize the low spin state even in the event of intramolecular hydrogen bonds or guest binding into the trigonal pocket formed by the amides, and therefore the species remains high spin within this temperature range.

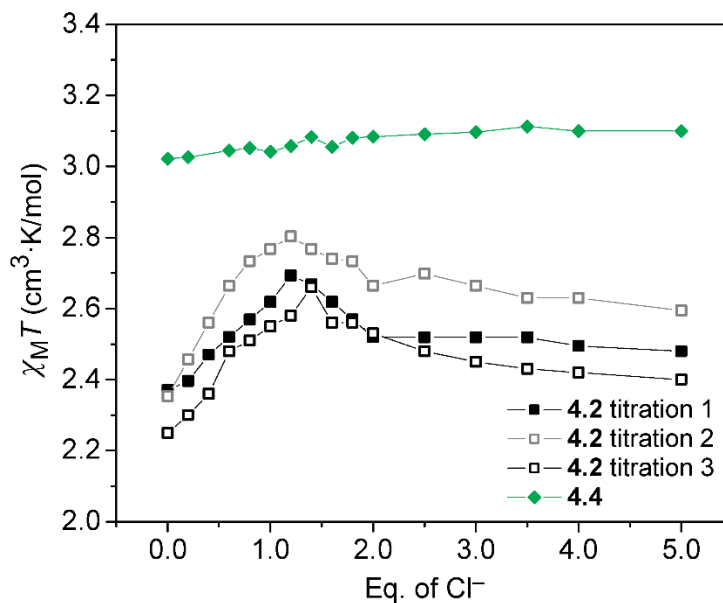


Figure 4.12. Changes in the solution room temperature χ_{MT} values upon addition of Bu_4NCl to **4.2** (black squares) and **4.4** (green diamonds) in CD_3CN . Open squares (gray and black) are replicate titrations of **4.2** to emphasize the range of χ_{MT} values between titrations. Lines are guides for the eye.

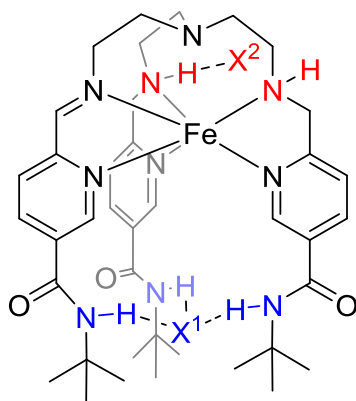


Figure 4.13. Proposed anion binding for **4.2** in the presence of a strongly interacting anion (X). Blue atoms indicate the first binding event with the first anion and red atoms the second binding event with the second anion.

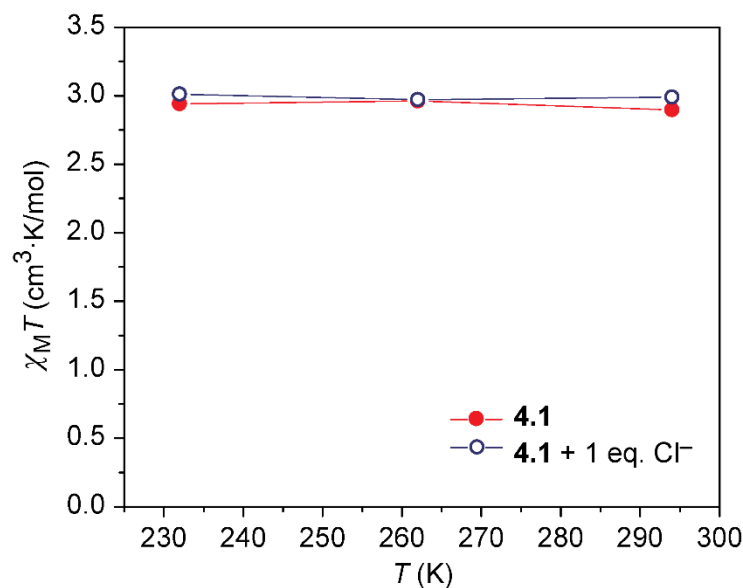


Figure 4.14 Variable temperature solution magnetic susceptibility measurements of **4.1** (red circle) and plus one equivalent of Bu₄NCl (open blue circles) collected between 294 and 232 K in CD₃CN. Lines are guides for the eye.

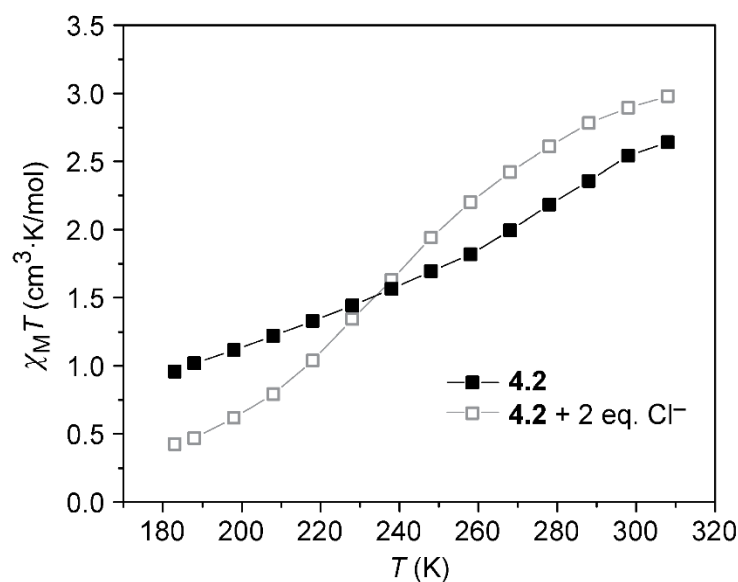


Figure 4.15. Variable temperature solution magnetic susceptibility measurements of **4.2** (black squares) and plus two equivalents of Bu₄NCl (open gray squares) collected between 308 and 183 K in *d*₆-acetone. Lines are guides for the eye.

In tune with the room temperature titration of **4.2** in CD₃CN, variable temperature magnetic susceptibility measurements in *d*₆-acetone with two equivalents of Bu₄NCl between 308 and 183 K show that the addition of two equivalents of Cl⁻ leads to an increase in the susceptibility from 2.6 cm³·K·mol⁻¹ to 3.0 cm³·K·mol⁻¹ at 308 K. The stabilization of the HS state is maintained upon cooling: the susceptibility of the chloride containing sample remains about 0.4 cm³·K·mol⁻¹ higher at temperatures between 308 and 258 K than when only BF₄⁻ is present. Below 228 K, it appears that the host:guest interactions stabilize the low spin state, ultimately the magnetic susceptibility decreases to 0.4 cm³·K·mol⁻¹ at 183 K, 0.5 cm³·K·mol⁻¹ lower than that determined for the BF₄⁻ salt.

4.5 Conclusions and Future Work.

A series of tripodal ligands using tren and 5-*tert*-butylamide-2-pyridinecarboxaldehyde have been synthesized. The three ligands differ in the ratio of coordinating imines to amines in attempt to tune the ligand field while maintaining the hydrogen-bonding ability of the *tert*-butylamide moiety. Structural analysis of Fe(II) complexes coordinated by these ligands as BF₄⁻ or BPh₄⁻ salts show that in the solid state, all of the complexes are high spin. Substantial distortion of the trigonal binding pocket formed by the amides is observed as a product of the ligand flexibility, which may have serious implications on anion-binding abilities. In the solid-state, all three species studied remain HS between 5 and 300 K. Variable temperature measurements in *d*₆-acetone show that complex **4.2** undergoes a gradual spin transition while complexes **4.1** and **4.4** remain high spin between 183 and 308 K. The anomalous behavior of **4.2** is exemplified by its anion-dependent behavior: room temperature titrations with Cl⁻ in CD₃CN monitored by Evans' method indicate that two binding events occur leading to first an increase in magnetic susceptibility with the first equivalent of Cl⁻ then a slight decrease with the second equivalent. Variable

temperature studies with two equivalents of Cl^- demonstrate the destabilization of the low spin state, as the magnetic susceptibility value trends higher in comparison to the weakly-interacting BF_4^- .

Ongoing studies will continue to focus on determining the anion dependence on the variable temperature solution data of **4.4** in d_6 -acetone as well as solid-state behavior of **4.1**, **4.2**, and **4.4**. Additionally, determination of the ligand field strength changes across the series by electronic absorption of Ni(II) analogues is imperative to fully understand the influence of the structural distortion and conjugation changes. To glean the influences of the various binding modes on the spin state, variable temperature solution-based measurements with one equivalent of anion will also be performed. Determination of binding constants by synthesizing diamagnetic analogues and subsequent anion titrations will allow us to understand how the deformation of the binding pocket alters anion binding. Other potential experiments of note include probing the influence of different anions (e.g. F^- , Br^- , I^- etc.) on the spin state behavior. Further studies could study the ligand field influences without the addition of any hydrogen-bonding functionalities. This would elucidate the influence the imines and amines have on the ligand field without the potential influence of the amide.

4.6 Acknowledgments.

This work was supported by Colorado State University and NSF-CHE-1058889 and NSF-CHE-1363274.

REFERENCES

- (1) McDaniel, A. M.; Klug, C. M.; Shores, M. P. *Eur. J. Inorg. Chem.* **2013**, 2013, 943.
- (2) Tecilla, P.; Tonellato, U.; Veronese, A.; Felluga, F.; Scrimin, P. *J. Org. Chem.* **1997**, 62, 7621.
- (3) *APEX 2*; Bruker Analytical X-Ray Systems, Inc: Madison, WI, 2008.
- (4) Bain, G. A.; Berry, J. F. *J. Chem. Educ.* **2008**, 85, 532.
- (5) Evans, D. F. *J. Chem. Soc.* **1959**, 2003.
- (6) Ostfeld, D.; Cohen, I. A. *J. Chem. Educ.* **1972**, 49, 829.
- (7) Monat, J. E.; McCusker, J. K. *J. Am. Chem. Soc.* **2000**, 122, 4092.
- (8) Seredyuk, M.; Gaspar, A. B.; Kusz, J.; Bednarek, G.; Guetlich, P. *J. Appl. Crystallogr.* **2007**, 40, 1135.
- (9) Klug, C. M.; McDaniel, A. M.; Fiedler, S. R.; Schulte, K. A.; Newell, B. S.; Shores, M. P. *Dalton Trans.* **2012**, 41, 12577.
- (10) Drew, M. G. B.; Harding, C. J.; McKee, V.; Morgan, G. G.; Nelson, J. *J. Chem. Soc., Chem. Commun.* **1995**, 1035.
- (11) Halcrow, M. A. *Chem. Soc. Rev.* **2011**, 40, 4119.
- (12) Guionneau, P.; Marchivie, M.; Bravic, G.; Letard, J.-F.; Chasseau, D. *J. Mater. Chem.* **2002**, 12, 2546.
- (13) Marchivie, M.; Guionneau, P.; Letard, J. F.; Chasseau, D. *Acta Crystallogr., Sect. B: Struct. Sci.* **2005**, B61, 25.
- (14) Larsen, E.; LaMar, G. N.; Wagner, B. E.; Parks, J. E.; Holm, R. H. *Inorg. Chem.* **1972**, 11, 2652.
- (15) Hauser, A. *Top. Curr. Chem.* **2004**, 233, 49.
- (16) Ni, Z.; Shores, M. P. *J. Am. Chem. Soc.* **2008**, 131, 32.

CHAPTER 5. TUNING THE MAGNETIC RELAXATION VIA OUT-OF-SPHERE
HYDROGEN-BONDING INTERACTIONS IN CO(II) TRIPODAL IMINOPYRIDINE
COMPLEXES

5.1 Introduction

Polynuclear metal complexes showing single-molecule magnet (SMM) properties have been known for the last few decades.¹ Recently, in addition to these polynuclear SMMs, focus has been placed in investigating mononuclear complexes containing lanthanides,^{2,3} actinides,⁴⁻⁷ and low-symmetry first-row transition metal complexes.⁸⁻¹² These mononuclear complexes allow for greater tunability of the coordination environment in the absence of significant intermolecular interactions, which is not always possible with self-assembled polynuclear complexes. In comparison to rare-earth metal complexes, the influence of ligand environment is significant to the magnetic properties of *3d* transition metal complexes, furthering the need for strategically designed ligands.

Among the mononuclear *3d* metal ions showing relaxation of magnetization high-spin cobalt(II) complexes are of interest. The $S = 3/2$ ion can display significant zero-field splitting and magnetic anisotropy due to the ion's intrinsic spin-orbit coupling.¹³ To date, numerous Co(II) complexes have been synthesized and have led to interesting three-,¹⁰ four-,¹⁴⁻²¹ five-,²² and six-coordinate^{23,24} complexes with significant magnetic anisotropy. Most of these mononuclear Co(II) complexes have been shown to possess *positive D* (axial anisotropy) values, yet with the application of applied field, show slow magnetic relaxation as a signature of SMM-like properties.^{16,18}

Several recent experimental examples²⁵⁻²⁹ and calculations³⁰ have explored the influence of subtle modifications of the metal center's coordination sphere on SMM-like properties. These

studies have shown that the ion's magnetic anisotropy and relaxation pathways are greatly affected by these alterations. In our continued pursuit of understanding how hydrogen-bonding interactions affect magnetic properties of first-row transition metals, we have synthesized and characterized a set of Co(II) complexes using the amide-functionalized tripodal ligand $L^{5\text{-OH}t\text{Bu}}$ (Figure 1.4).³¹ In this chapter, we aim to investigate how anion-binding modulates the coordination environment of the Co(II) center and influences the magnetic properties.

5.2 Division of Labor.

Sequences for magnetic measurements were developed in collaboration with Dr. Indrani Bhowmick. All complex syntheses, characterizations, and magnetic measurements were performed by Christina Klug.

5.3 Experimental Section

5.3.1 General Considerations. Unless otherwise noted, all manipulations were undertaken in a dinitrogen-filled MBRAUN Labmaster 130 glovebox. Acetonitrile (MeCN) and diethyl ether (Et₂O) were sparged with dinitrogen, passed over molecular sieves, and subjected to three freeze-pump-thaw cycles prior to use. The synthesis and characterization of $L^{5\text{-OH}t\text{Bu}}$ has been described elsewhere.³¹ All other reagents were obtained from commercial sources and used without further purification.

Caution! Perchlorate salts are potentially explosive and should be handled with care and in small quantities!

[CoL^{5-OH t Bu}] Cl_2 (5.1). To a suspension of CoCl₂ (18 mg, 0.14 mmol) in 4.5 mL of methanol, a solution of $L^{5\text{-OH}t\text{Bu}}$ (96 mg, 0.13 mmol) in 4.5 mL of methanol was added. The solution instantly turned orange and was allowed to stir for 16 hours until all the blue CoCl₂ had dissolved. The solution was concentrated to 2 mL in *vacuo* and crystals grown by ether diffusion

into the methanolic solution. Orange X-ray quality crystals were isolated by vacuum filtration and washed with diethyl ether (2×5 mL) to afford 96 mg of product (85% yield). ESI-MS (+) (MeOH): m/z 384.9 ($[\text{CoL}^{5\text{-ONHtBu}}]^{2+}$), 768.4 ($[\text{CoL}^{5\text{-ONHtBu-H}}]^+$), 804.3 ($[\text{CoL}^{5\text{-ONHtBu}}\text{Cl}]^+$). $^1\text{H NMR}$ (400 MHz, CD_3CN): 180, 135, 108, 53, 43, 13, -1.0 , -1.3 , -16 ppm. UV-vis (CH_3CN) $\lambda_{\text{max}}/\text{nm}$ ($\epsilon_{\text{M}}/\text{M}^{-1}\cdot\text{cm}^{-1}$) 234 (56400), 292, (43100), 373 (2800), 450 (sh, 650), 510 (sh, 240), 906 (10). Anal Calcd for $\text{C}_{40.8}\text{H}_{61.2}\text{Cl}_2\text{CoN}_{10}\text{O}_{4.8}$ (**5.1** \cdot 0.8 CH_3OH ; methanol is observed in the 1): C, 54.54; H, 6.87; N, 15.59. Found: C, 54.35; H, 6.77; N, 15.80.

$[\text{CoL}^{5\text{-ONHtBu}}]\text{Br}_2$ (5.2). A solution of $\text{CoBr}_2 \cdot x \text{H}_2\text{O}$ (12 mg, 0.054 mmol) in 3 mL of methanol was added to a solution of $\text{L}^{5\text{-ONHtBu}}$ (43 mg, 0.060 mmol) in 3 mL of methanol. The solution color instantly turned orange. The solution was stirred for 16 hours and then concentrated to 3 mL in *vacuo*. X-ray quality orange crystals were grown by ether diffusion into the methanolic solution. The crystals were isolated by vacuum filtration, washed with diethyl ether (2×5 mL) to afford 45 mg of product (88% yield). ESI-MS (+) (MeOH): m/z 384.8 ($[\text{CoL}^{5\text{-ONHtBu}}]^{2+}$), 848.3 ($[\text{CoL}^{5\text{-ONHtBu}}\text{Br}]^+$). $^1\text{H NMR}$ (400 MHz, CD_3CN): 181, 136, 109, 53, 43, 13, -0.6 , -0.8 , -15 ppm. UV-vis (CH_3CN) $\lambda_{\text{max}}/\text{nm}$ ($\epsilon_{\text{M}}/\text{M}^{-1}\cdot\text{cm}^{-1}$) 220 (sh, 45600), 240 (sh, 35000), 287 (24600), 369 (2900) 450 (sh, 675), 510 (sh, 250), 902 (10). Anal Calcd for $\text{C}_{40}\text{H}_{61.5}\text{Br}_2\text{CoN}_{10}\text{O}_{5.75}$ (**5.2** \cdot 1.75 $\text{H}_2\text{O}\cdot\text{MeOH}$; methanol and water are observed in the $^1\text{H NMR}$ spectrum): C, 48.36; H, 6.19; N, 14.11. Found: C, 48.37; H, 6.24; N, 14.10.

$[\text{CoL}^{5\text{-ONHtBu}}]\text{I}_2$ (5.3). A solution of CoI_2 (12 mg, 0.08 mmol) in 10 mL of methanol was added to a solution of $\text{L}^{5\text{-ONHtBu}}$ (54 mg, 0.08 mmol) in 3 mL of methanol. The solution color instantly turned orange. The solution was allowed to stir for 1 hour and concentrated to 3 mL in *vacuo*. X-ray quality orange crystals were grown by ether diffusion into the methanolic solution (73 mg, 94% yield). ESI-MS (+) (MeOH): m/z 384.8 ($[\text{CoL}^{5\text{-ONHtBu}}]^{2+}$), 769.5 ($[\text{CoL}^{5\text{-ONHtBu}}\text{H}]^+$),

896.3 ([CoL^{5-OH*t*Bu}]⁺). ¹H NMR (400 MHz, CD₃CN): 178, 148, 108, 52, 44, 13, 2.3, 0.0, -13 ppm. UV-vis (CH₃CN) λ_{max}/nm (ε_M/M⁻¹·cm⁻¹) 287 (35500), 370 (4000), 450 (sh, 900), 510 (sh, 360) 908 (10). Anal Calcd for C₄₀H₅₉I₂CoN₁₀O_{4.5} (**5.3**·1 CH₃OH·0.5 H₂O; methanol and water are observed in the ¹H NMR spectrum): C, 45.12; H, 5.59; N, 13.16. Found: C, 44.89; H, 5.44; N 13.24.

[CoL^{5-OH*t*Bu}](ClO₄)₂ (**5.4**). A solution of Co(ClO₄)₂ · 6 H₂O (81 mg, 0.22 mmol) in 4.5 mL of methanol was added to a solution of L^{5-OH*t*Bu} (150 mg, 0.21 mmol) in 10.5 mL of methanol. The reaction instantly turned orange. The solution was allowed to stir for 16 hours and then concentrated to 3 mL in *vacuo*. X-ray quality orange crystals were grown by ether diffusion into the methanolic solution (204 mg, 90% yield). ESI-MS (+) (MeOH): *m/z* 384.8 ([CoL^{5-OH*t*Bu}]²⁺), 868.4 ([CoL^{5-OH*t*Bu}](ClO₄)⁺). ¹H NMR (400 MHz, CD₃CN): 177, 160, 108, 51, 44, 13, 4, 0.2, 12 ppm. UV-vis (CH₃CN) λ_{max}/nm (ε_M/M⁻¹·cm⁻¹) 237 (31000), 287 (25400), 373 (3200), 450 (sh, 750), 510, (sh, 260), 900 (10). Anal Calcd for C₃₉H₅₄Cl₂CoN₁₀O₁₁: C, 48.35; H, 5.62; N, 14.46. Found: C, 48.49; H, 5.78; 14.46.

5.3.2 Magnetic Measurements. Magnetic data for **5.1**, **5.2** and **5.4** were collected using a Quantum Design model MPMS-XL superconducting quantum interference device (SQUID) magnetometer. Measurements were collected using crystals of **5.1**, **5.2**, and **5.4** packed into the top of gelatin capsules and restrained with the bottom portion of the capsule. All samples were prepared under a dinitrogen atmosphere and quickly loaded into the SQUID to minimize air exposure. Direct current (DC) susceptibility measurements of crystals of **5.3** were performed on a Quantum Design model PPMS Dynacool equipped with a VSM transport system. The sample was encased in a polypropylene powder holder prepared under a dinitrogen atmosphere and quickly loaded into the instrument to minimize air exposure. The absence of ferromagnetic impurities was

confirmed by observing the linearity of a plot of magnetization vs. field at 100 K. In all cases, DC susceptibility measurements were collected from 1.8 K to 300 K under an applied DC field of 1000 Oe. For magnetization experiments, crystals of **5.1**, **5.2**, and **5.4** were encased in six drops of solidified eicosane and crystals of **5.3** were pressed in a polypropylene powder holder and measured from 1.8 to 30 K under applied DC fields of 1, 2, 3, 4, and 5 T. Data were corrected for the magnetization of the sample holder by subtracting the susceptibility of an empty container and for diamagnetic contributions of the sample by using Pascal's constants.³² Theoretical fits of the susceptibility data were obtained using a relative error minimization routine (julX 1.41)³³ using a Hamiltonian of the form $\hat{H} = -2J\hat{S}_1 \cdot \hat{S}_2$. Fits of the magnetization data were obtained with the ANISOFIT2.0³⁴ program using a Hamiltonian of the form $\hat{H} = D\hat{S}_z^2 + E(\hat{S}_x^2 + \hat{S}_y^2) + g_{iso}\beta\vec{S} \cdot \vec{B}$. Alternating-current (AC) susceptibility was measured for **5.1–5.4** under a 4 Oe ac driving field at frequencies from 1 to 1488 Hz at 1.9 K under applied dc field from 0 to 5000 Oe. For variable temperature ac susceptibility of **5.1**, measurements were performed in the temperature range of 1.8 to 4.6 K under an applied dc field of 2500 Oe.

5.3.3 X-ray Structure Determinations. All single crystals were coated in Paratone–N oil prior to removal from the glovebox. Data collection was performed by mounting a single crystal on a Cryoloop under a stream of dinitrogen. Data sets were collected targeting complete coverage and fourfold redundancy. Integrations of the raw data were done using the Apex II software package and absorption corrections were applied using SADABS.³⁵ The structures were solved using direct methods and refined against F^2 using SHELXTL 6.14 software package.³⁶ Unless otherwise noted, thermal parameters for all non-hydrogen atoms were refined anisotropically. Hydrogen atoms were added at the ideal positions and refined using a riding model in which the

isotropic displacement parameters were set at 1.2 times those of the attached carbon atom (1.5 times for methyl carbons).

Due to the packing of the cations of **5.1**, **5.2**, and **5.3**, one of the charge-balancing anions appears to be highly disordered over several locations within an apparent void space. The addition of disordered solvent molecules further complicates modeling of the disordered anion. Several attempts to explicitly model the disorder in $P\bar{3}$ did not afford significant improvement to the agreement factors. Additional attempts to model the disorder in the lower symmetry space group $P\bar{1}$ gave similar problems with the disordered anion and solvent. Thus, SQUEEZE was employed to remove the residual electron density due to the second charge balancing anion. The residual electron density per unit cell for **5.1** was determined to be 70 electrons and 640 \AA^3 , which would account for two chloride anions and 2 methanol molecules per unit cell. For complex **5.2**, the void space within the crystal lattice was determined to be 650 \AA^3 and 114 electrons per unit cell. This equates to two bromide anions and 2.33 methanol molecules per unit cell. Lastly, the void space of complex **5.3** was determined to be 675 \AA^3 and 284 electrons per unit cell. This equates to two iodide anions and 9.8 methanol molecules per unit cell. The chemical formulas supplied in Table 5.1 do not account for the disordered components that were removed via SQUEEZE.

5.3.4 Other Physical Methods. Infrared spectra were measured with a Nicolet 380 FT-IR under a dinitrogen flow using an ATR attachment with a ZnSe crystal. Visible absorption spectra were obtained using an Agilent 8453 UV-visible spectrometer under air-free conditions using a quartz cuvette. ^1H NMR spectra were recorded using Varian INOVA instruments operating at 400 MHz. Paramagnetic spectra were acquired at room temperature collecting 512 scans in a spectral window from -22.5 to 200 ppm using an acquisition time of 1 second and a 1 ms relaxation delay. Mass spectra were obtained on a Finnigan LCQ Duo mass spectrometer equipped with an

electrospray ion source and quadrupole ion trap mass analyzer in positive ion mode. Elemental analysis was performed by Robertson Microlit Laboratories in Ledgewood, NJ.

Table 5.1. Crystallographic and structural refinement data for [CoL^{5-ONHtBu}]Cl₂ (**5.1**), [CoL^{5-ONHtBu}]Br₂ (**5.2**), [CoL^{5-ONHtBu}]I₂ (**5.3**), [CoL^{5-ONHtBu}](ClO₄)₂ (**5.4**).

	5.1	5.2	5.3	5.4
Empirical formula	C ₃₉ H ₅₄ ClCoN ₁₀ O ₃	C ₃₉ H ₅₄ BrCoN ₁₀ O ₃	C ₃₉ H ₅₄ ICoN ₁₀ O ₃	C ₃₉ H ₅₄ CoN ₁₀ Cl ₂ O ₁₁
Formula wt/g·mol ⁻¹	805.30	849.76	896.75	968.75
Crystal color	orange	orange	orange	yellow
Habit	parallelepiped	block	block	block
Temperature/K	120(2)	120(2)	120(2)	120(2)
Crystal system	Trigonal	Trigonal	Trigonal	Triclinic
Space group	<i>P</i> $\bar{3}$	<i>P</i> $\bar{3}$	<i>P</i> $\bar{3}$	<i>P</i> $\bar{1}$
Z	2	2	2	2
a/Å	15.23350(10)	15.5579(15)	15.8091(7)	12.7632(10)
b/Å	15.23350(10)	15.5579(15)	15.8091(7)	12.8064(10)
c/Å	12.5157(2)	12.1716(17)	12.0675(10)	14.9046(11)
α/°	90	90	90	75.900(4)
β/°	90	90	90	83.780(4)
γ/°	120	120	120	74.500(4)
Volume/Å ³	2515.27(5)	2551.4(6)	2611.9(3)	2274.4(3)
d _{calc} /g·cm ⁻³	1.063	1.106	1.140	1.415
GOF	1.073	1.157	1.086	1.023
R ₁ (wR ₂)/%	6.67 (20.82)	5.56 (19.65)	3.48 (9.84)	4.25 (8.41)

$$R_1 = \sum ||F_o| - |F_c|| / \sum |F_o|; wR_2 = \{ \sum [w(F_o^2 - F_c^2)^2] / \sum [w(F_o^2)^2] \}^{1/2}$$

5.4 Results

5.4.1 Synthesis and Characterization. The compounds $[\text{CoL}^{5\text{-ONHtBu}}]\text{X}_2$ ($\text{X} = \text{Cl}^-$ (**5.1**), Br^- (**5.2**), I^- (**5.3**) ClO_4^- (**5.4**)) were synthesized under a dinitrogen atmosphere by combining 1: 1 mixtures of CoX_2 and the tripodal ligand, $\text{L}^{5\text{-ONHtBu}}$, in methanol. The reaction is immediate as indicated by the instantaneous change in color of the solution, which persisted with time. Diffusion of diethyl ether into concentrated orange methanolic solutions readily afford orange crystals of the four salts. In solution and solid state, these species appear to be air-stable and remain orange upon exposure to air, but were treated as air-sensitive species to ensure complex stability and oxidation state of the metal.

All four salts were analyzed by ^1H NMR, IR, MS, and elemental analysis. In d_3 -acetonitrile at room temperature, the complexes are all high-spin, as indicated by the paramagnetic broadening of the NMR spectra (Figures 5.1). Depending on the charge-balancing anion, significant differences are observed in the chemical shifts of many of the protons, indicating that the hydrogen-bonding interactions imparted by the amide are maintained in a polar, aprotic solution. Similar behavior has been observed with salts of the analogous diamagnetic Fe(II) complex.³¹

Comparison of the IR spectra of the four salts indicates the influence of hydrogen-bonding on the complex. The broad N–H stretch of the amide functional group shifts from 3173 cm^{-1} for **5.1** to 3211 cm^{-1} for **5.2** to 3243 cm^{-1} for **5.3** while this stretch occurs for the perchlorate **5.4** at 3346 cm^{-1} (Figure 5.2). The carbonyl stretch also displays similar shifts to higher energy with increasing anion size, moving from 1647 cm^{-1} for **5.1** to 1661 cm^{-1} for **5.4**. Additionally, the IR stretch assigned as the $\text{C}=\text{N}_{\text{imine}}$ is centered around 1550 cm^{-1} with a 20 cm^{-1} difference between **5.1** (1550 cm^{-1}) and **5.4** (1530 cm^{-1}) (Figure 5.2b). Analogous to the ^1H NMR spectra of these

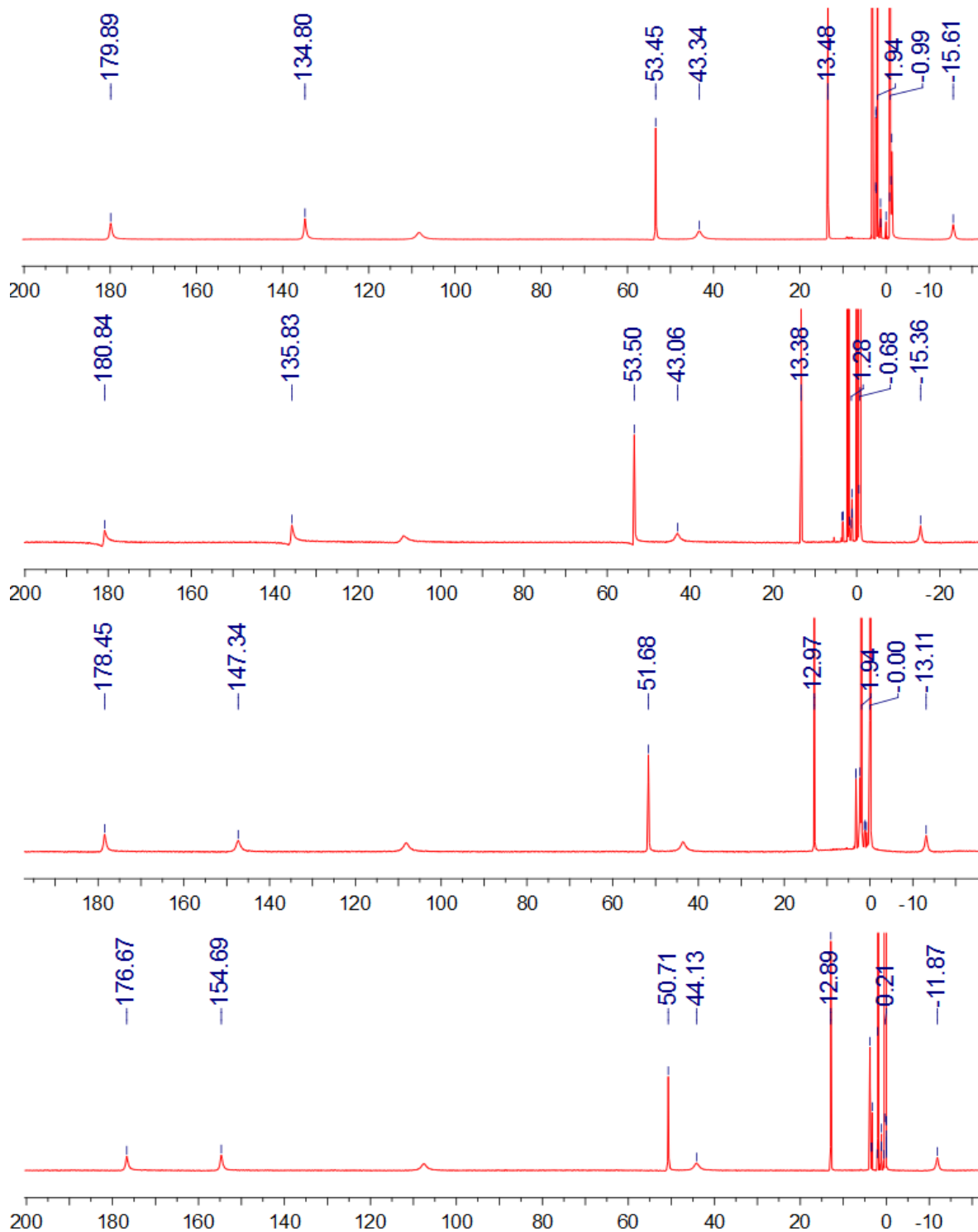


Figure 5.1. Paramagnetic NMR spectra of **5.1** (top), **5.2** (second from top), **5.3** (second from bottom), and **5.4** (bottom) obtained in CD_3CN at 296 K.

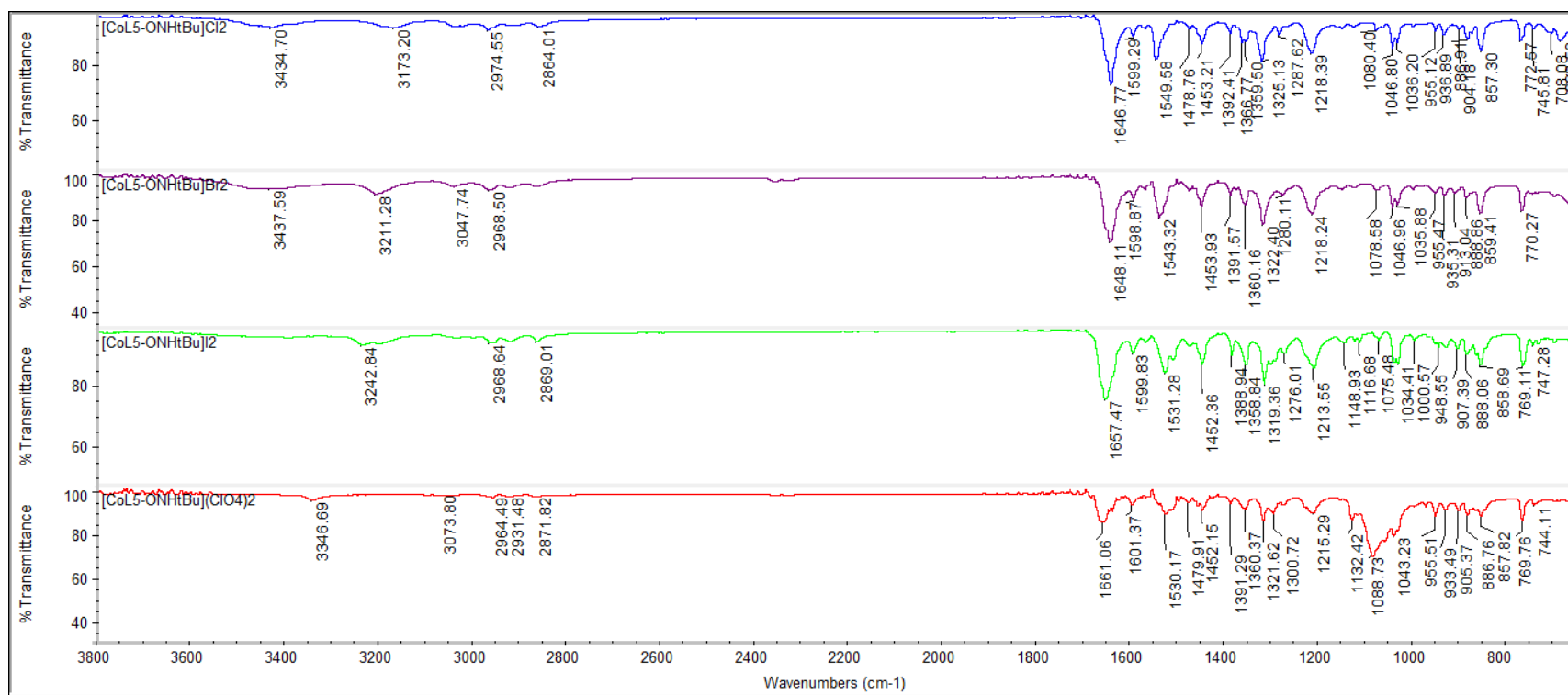


Figure 5.2. FT-IR comparison of complexes **5.1–5.4** performed by pressing crystalline samples onto a ZnSe ATR crystal.

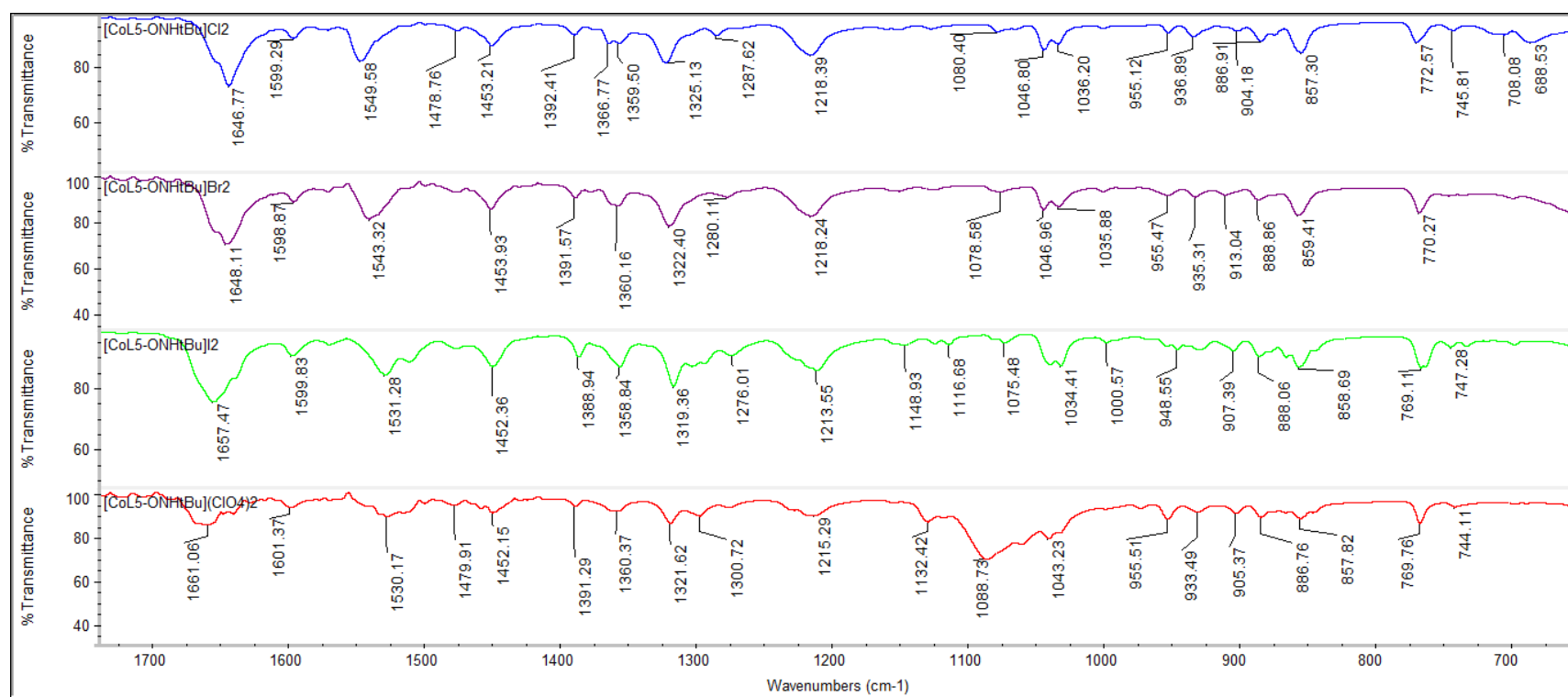


Figure 5.2b. FT-IR comparison of complexes **5.1–5.4** performed using by pressing crystalline samples onto a ZnSe ATR crystal from 1740 cm⁻¹ to 650 cm⁻¹.

salts, the hydrogen bonding interactions through the amides have an influence on the electronic structure of the ligand with more charge-dense anions having a greater influence than more charge-diffuse anions.

Mass spectrometry and elemental analysis of the halide salts, **5.1–5.3**, and the perchlorate salt, **5.4**, indicate that the desired products are formed. The mass-to-charge ratios observed in the spectra have the desired molecular weight for a 1+ species with one charge-balancing anion or the loss of a proton and a cobalt-containing species with a 2+ charge, which is consistent with a 2+ oxidation state of the metal. Cocrystallization of methanol is apparent for **5.1–5.3** by ^1H NMR, IR and EA. Based on the elemental analysis, complex **5.1** cocrystallizes with about two molecules per Co(II) center, **5.2** cocrystallizes with approximately 2.75 molecules, and **5.3** cocrystallizes with approximately 1.5 molecules per Co(II) center.

5.4.2 X-ray Structural Analyses. Single-crystal X-ray structures collected at 120 K show the halide salts **5.1–5.3** crystallize in the hexagonal space group $P\bar{3}$ and compound **5.4** crystallizes in $P\bar{1}$. The coordination environment of the metal center consists of the expected Co-N₆ coordination environment with bonds to three imine and three pyridine nitrogens in a distorted octahedron (Figure 5.3). The coordination environment for the cobalt centers show that the Co–N_{imine} bond lengths (2.091(3)–2.121(3) Å) are shorter than the Co–N_{pyridine} bond lengths (2.211(4)–2.264(4) Å) (Table 5.2). This is a trend seen in iminopyridine-based first-row transition metal complexes,^{37,38} and these bond lengths are typical for high-spin Co(II) in a N₆ coordination environment. The distortion parameters $\Sigma^{39,41}$ and $\Theta^{40,42}$ indicate that these structures are highly distorted from perfect octahedra as these values deviate substantially from 0°. Values of the trigonal distortion parameter ϕ^{43} range from 49.9° for **5.1** to 51.4° for **5.3**, indicating that while the

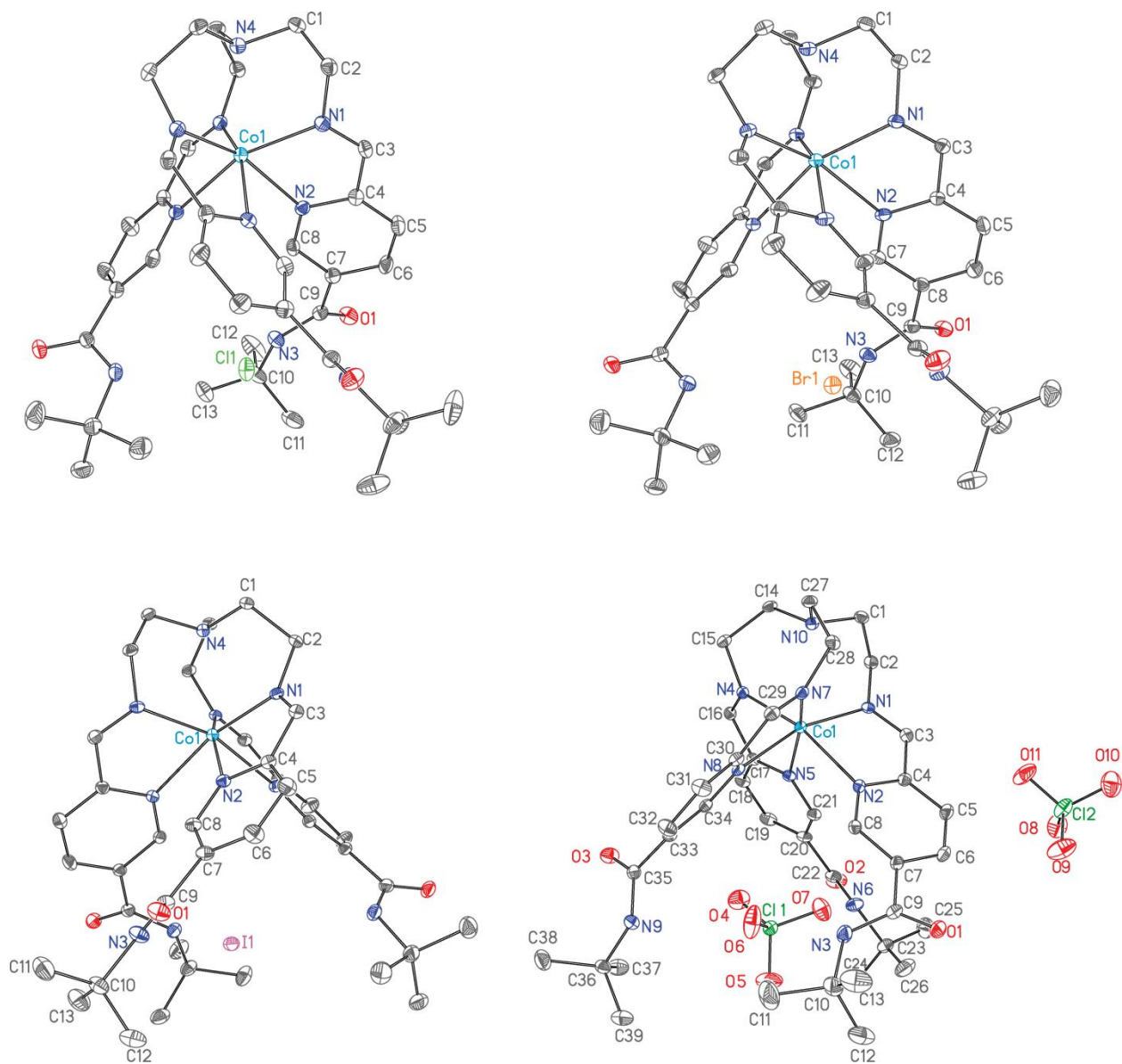


Figure 5.3. X-ray crystal structures of **5.1** (top, left), **5.2** (top, right), **5.3** (bottom, left), and **5.4** (bottom, right) depicted with 40% thermal ellipsoids. Co, N, C, O, Cl, Br, and I atoms are represented by teal, blue, gray, red, green, orange, and purple respectively. Hydrogen atoms and atoms labels for C_3 symmetric complexes have been omitted for clarity.

Table 5.2. Selected bond lengths and angles for **5.1–5.4**.

	5.1	5.2	5.3	5.4
Co–N _{imine} (Å)	2.121[3] ^a	2.106[3]	2.104[4]	2.100(3) ^b
Co–N _{pyridine} (Å)	2.262[3]	2.252[5]	2.259[4]	2.247(3)
Co–N _{bridge} (Å)	2.574[3]	2.595[4]	2.639[6]	2.706[2]
N _{imine} plane to N _{pyridine} plane (Å)	1.97[3]	2.09[4]	2.09[3]	2.04(1)
Co–N _{imine} plane (Å)	0.707	0.724	0.734	0.766
Co–N _{pyridine} plane (Å)	1.391	1.368	1.335	1.310
φ (°)	49.93[15]	50.7[2]	51.4[1]	51.3(8)
Σ (°)	125.9(3)	120.4(4)	116.9(5)	113.3(2)
Θ (°)	200	189	193	187
N–N _{imine} (Å)	3.463[5]	3.424[6]	3.415[6]	3.387(4)
N–N _{pyridine} (Å)	3.089[5]	3.099[6]	3.155[6]	3.162(4)
C=N _{imine} ^c (Å)	1.264[4]	1.281[5]	1.277[6]	1.266(4)
C–C _{imine} ^c (Å)	1.476[5]	1.461[6]	1.468[6]	1.467(5)
C=N _{pyridine} ^c (Å)	1.354[5]	1.365[5]	1.357[6]	1.354(5)
Amide torsion (°)	34.6	30.6	29.8	62.4
N _{amide} ···X	3.213[3]	3.424[4]	3.615[4]	3.026[2]
				2.918[3]
				3.370[3]
N _{amide} ···N _{amide}	5.557[5]	5.892[6]	6.209[3]	6.090[3]
				7.241[3]
				5.563[2]
Co···X	5.161[2]	5.238[1]	5.2116[6]	5.3027[7] ^d
Co···Co _{parallel} (Å)	12.5157[2]	12.172[2]	12.068[1]	12.763[1]
Co···Co _{anti-parallel} (Å)	9.2920[5]	9.392[1]	9.4798[9]	8.0030[8]
X···C _{ethylene}	4.569[4]	4.156[5]	4.062[2]	3.355[3] ^e
				3.208[3]
				3.316[3]

^a Signifies the e.s.d. as determined by SHELXTL

^b The e.s.d determined as the square root of the sum of the e.s.d. of the averaged values.

^c For definition, see Figure 5.4

^d Defined as Co···Cl distance

^e Defined as the O···C distance

coordination environments of the cations are highly distorted, the geometries are closer to octahedral (60°) than trigonal prismatic (0°).

For each metal salt studied, one anion is encapsulated within the trigonal pocket formed by the ligand. The three amide moieties of the ligand form hydrogen-bonding interactions with this

anion. Since the halide salts **5.1–5.3** assume three-fold rotational symmetry, these interactions are identical between the arms. In comparison, the asymmetry of the perchlorate structure of **5.4** makes these interactions uneven; one oxygen of the perchlorate partakes in a bifurcated hydrogen bond with two amides while the third arm engages in one hydrogen bond to an adjacent oxygen on the same anion. As expected, with increasing anion size, the distance between the anion's center and the NH of the amides increases in length (3.213[3] Å for **5.1** to 3.615[4] Å for **5.3**) and subsequently the size of the pocket, as measured by the N···N distances, also increases (Table 5.2).

Coincidentally, as the anion size increases from **5.1–5.4**, the Co–N bond lengths tend to shorten while the bridgehead nitrogen (N_{bridge}) to Co distance becomes longer. The coordination geometry of **5.1** could be considered more pseudo-heptadentate cobalt center then leads to more a more hexadentate coordination environment when larger anions in **5.2–5.4** are used. Additionally to the differences in the coordination environments between the salts, subtle differences in the bond lengths of the imines are also observed (Table 5.2 and Figure 5.4). Use of chloride as the charge-balancing anion in **5.1** produces the shortest C=N_{imine} (1.264[4] Å) and longest C–C_{imine} (1.476[5] Å) bond lengths observed for this series of complexes. Changing the anion to bromide in **5.2** promotes elongation of the C=N_{imine} bond (1.281[5] Å) and shortening of the C–C_{imine} bond (1.461[6] Å), which are the longest and shortest bonds observed for this series of salts, respectively. Recognizing that iminopyridines are known to be redox noninnocent,^{44,45} comparison of these bonds to other iminopyridine-based complexes indicate that these bonds are more reminiscent of neutral iminopyridines as opposed to ligand radicals. The iodide and perchlorate salts have bond lengths that lie within the range of the chloride and bromide salts.

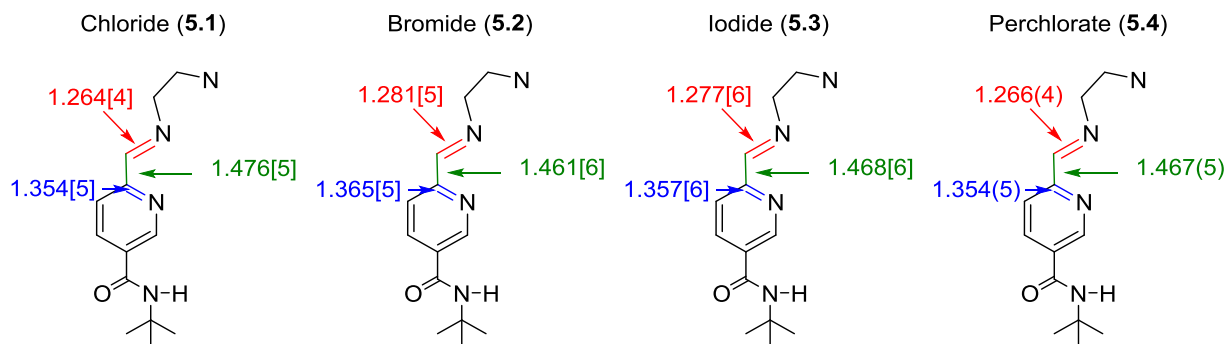


Figure 5.4. Comparison of the iminopyridine bond lengths (Å) for **5.1–5.4**. C=Nimine, C–Cimine, and C=Npyridine are represented in red, blue, and green, respectively.

The solid-state packing of complexes **5.1–5.3** results in the formation of channels within the structure, which contain cocrystallized solvent and the second charge-balancing anion (Figure 5.5). The shortest intermolecular Co \cdots Co distances range from (9.480[9] Å) for **5.3** to (8.003[8] Å) for **5.4**. For complexes **5.1–5.3**, these distances are sufficient to form well-isolated species, short intermolecular contacts are seen between the perchlorate packed within the ligand's trigonal pocket and the ethylene backbone of an adjacent cation (Figure 5.7). Analogous distances between the anion and ethylene backbone are substantially longer for the halide salts studied, indicating little communication between cations through these interactions.

5.4.3 Magnetic Susceptibility Measurements. The temperature dependent magnetic susceptibility ($\chi_M T$ vs T) collected under an applied dc field of 1000 Oe from 2 to 300 K indicate all species are high-spin ($S = 3/2$) at all temperatures (Figure 5.8). At room temperature, $\chi_M T$ for **5.1** is $2.82 \text{ cm}^3 \cdot \text{K} \cdot \text{mol}^{-1}$, **5.2** is $2.83 \text{ cm}^3 \cdot \text{K} \cdot \text{mol}^{-1}$, **5.3** is $3.02 \text{ cm}^3 \cdot \text{K} \cdot \text{mol}^{-1}$, and **5.4** is $2.91 \text{ cm}^3 \cdot \text{K} \cdot \text{mol}^{-1}$. These values are higher than the theoretical $\chi_M T$ value expected for a $S = 3/2$ spin system ($1.875 \text{ cm}^3 \cdot \text{K} \cdot \text{mol}^{-1}$) assuming $g = 2$, but are consistent with previously studied Co(II) complexes.^{22,46} The $\chi_M T$ values of all species remain relatively constant at temperatures above 50 K. Significant downturn in $\chi_M T$ is seen for **5.1** below 50 K, decreasing in value from $2.40 \text{ cm}^3 \cdot \text{K} \cdot \text{mol}^{-1}$ at 50 K to $1.52 \text{ cm}^3 \cdot \text{K} \cdot \text{mol}^{-1}$ at 2 K. At temperatures below 20 K, downturns in the

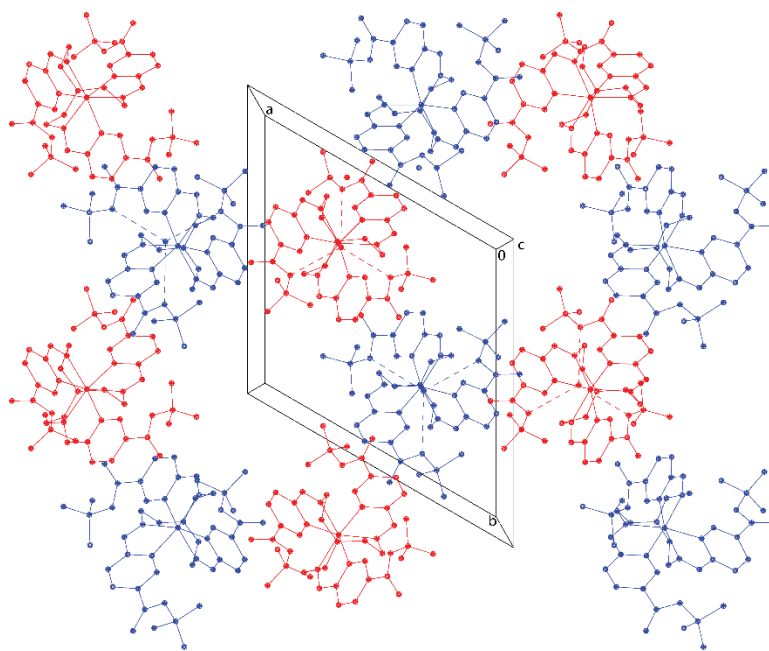


Figure 5.5. Packing plot of **5.1** down c axis. Complex cations depicted as either red or blue to differentiate the directionality of amide groups (red: out-of-plane of paper; blue: into plane of paper).

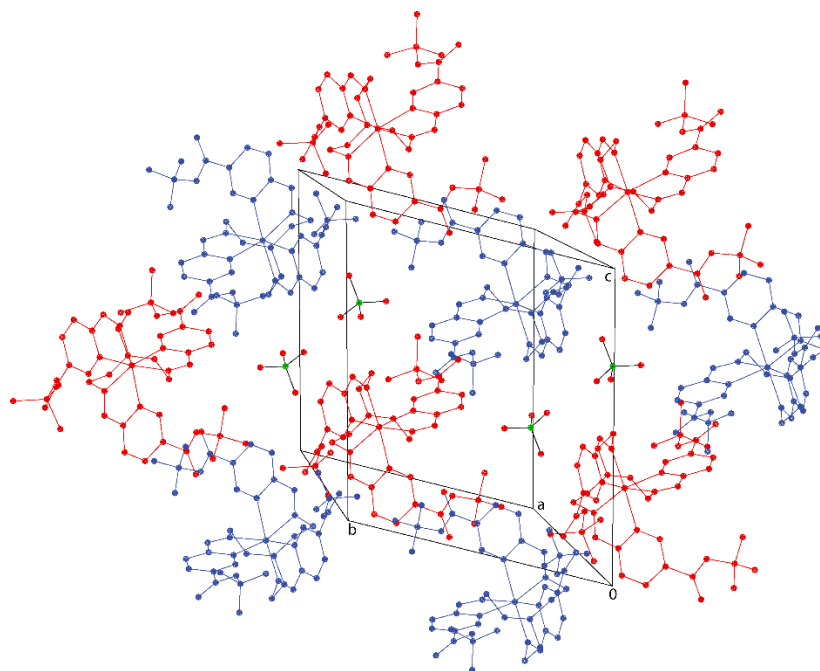


Figure 5.6. Packing plot of **5.4** down c axis. Complex cations depicted as either red or blue to differentiate the directionality of amide groups (red: out-of-plane of paper; blue: into plane of paper).

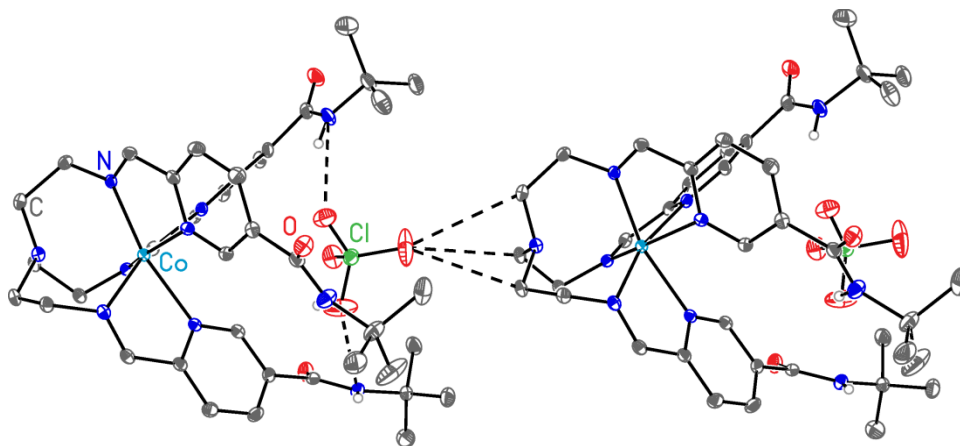


Figure 5.7. Intermolecular interactions for the structure of complex **5.4**. Atoms are rendered with 40% thermal ellipsoids. Co, N, C, O, and Cl atoms are represented by teal, blue, gray, red, and green respectively. Dashed lines indicate close intermolecular contacts. Hydrogen atoms, except those of the amides, are omitted for clarity.

magnetic susceptibility are also observed for **5.2** and **5.3**, decreasing from $2.47 \text{ cm}^3 \cdot \text{K} \cdot \text{mol}^{-1}$ at 20 K to $2.03 \text{ cm}^3 \cdot \text{K} \cdot \text{mol}^{-1}$ by 2 K for **5.2** and $2.27 \text{ cm}^3 \cdot \text{K} \cdot \text{mol}^{-1}$ at 20 K to $1.59 \text{ cm}^3 \cdot \text{K} \cdot \text{mol}^{-1}$ at 2 K for **5.3**. The significant downturn in $\chi_M T$ is attributed to the magnetic anisotropy of the Co(II) complex. In comparison, **5.4** displays a similar decrease in $\chi_M T$ at low temperatures, reaching a minimum at 34 K of $2.40 \text{ cm}^3 \cdot \text{K} \cdot \text{mol}^{-1}$, then displays a slight increase in $\chi_M T$, maximizing at $2.49 \text{ cm}^3 \cdot \text{K} \cdot \text{mol}^{-1}$ at 8 K and finally decreasing to $2.04 \text{ cm}^3 \cdot \text{K} \cdot \text{mol}^{-1}$ at 2 K. This increase displayed in $\chi_M T$ for **5.4** is tentatively attributed to weak ferromagnetic coupling between the metal centers through the perchlorate anion.

Fitting of the susceptibility data using julX^{33} for **5.1–5.3** with a spin Hamiltonian that incorporates a zero-field splitting parameter (D) were attempted of the data from 2 to 300 K (Table 5.3). The best fits of these data produced D values of 11.9, 2.4, and 3.6 cm^{-1} for **5.1–5.3**, respectively. There is also a significant amount of temperature-independent paramagnetism accounted for in the fitting, attributed to unquenched orbital angular momentum. Similarly, these fits also extracted $|E|/D$ values, which ranged from 0.045 cm^{-1} for **5.1** to 0.62 cm^{-1} for **5.3**. Since **5.4** displays apparent

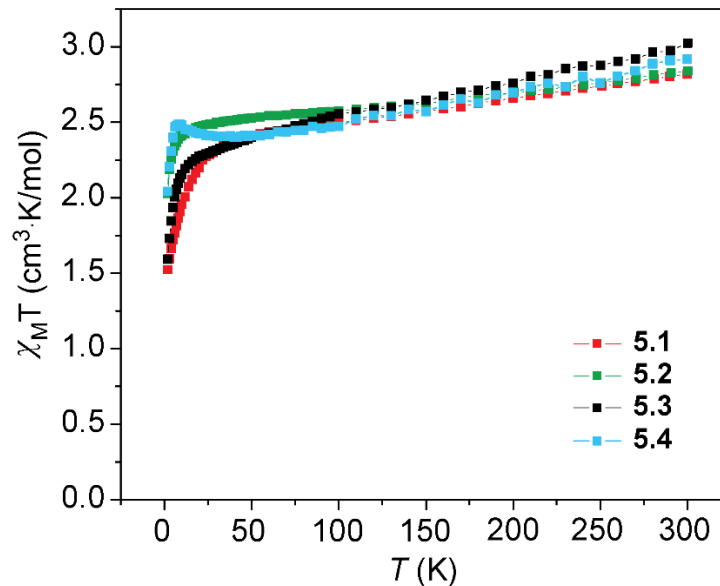


Figure 5.8. Variable temperature magnetic susceptibility measurements of **5.1–5.4**. The lines are guides for the eye. $H_{dc} = 1000$ Oe.

ferromagnetic coupling, attempts at modeling this data in a similar fashion was unsuccessful and supplied poor fits to the data.

Measurement of the magnetization was performed by sweeping temperature under various applied field up to 5 T (Figure 5.9). Saturation of the magnetization occurs around $2.5 \mu_B$ for **5.1**, **5.3**, and **5.4** with **5.2** saturating around $3 \mu_B$ at 5 T. This corroborates with the M (μ_B) values for three unpaired electrons, thus confirming a $S = 3/2$ ground state of these Co(II) complexes. Saturation values of less than $3 \mu_B$ are expected for $S = 3/2$ systems when g is greater than 2, which is an indication of magnetic anisotropy. The non-overlying isofield lines confirm that the downturn in $\chi_M T$ is due to the presence of magnetic anisotropy of the Co(II) center. Overall, the curve shapes are similar for all the salts, but the maximization of the magnetization for **5.2** is highest in comparison. This is consistent with lower anisotropy. Fitting of the reduced field data (M vs H/T) was performed using ANISOFIT 2.0,³⁴ (Table 5.3 and Tables 5.1–5.4). In cases where the fit from ANISOFIT 2.0 produced values $|E| \geq |1/3D|$, the principle values of the D -tensor were reassigned to fulfill the following relationship:⁴⁷

$$|D_{zz}| \geq |D_{yy}| \geq |D_{xx}| \quad (1)$$

The values of D_{zz} , D_{yy} , and D_{xx} were determined by the following equations, using the output D and E values obtained from ANISOFIT 2.0:

$$D_{zz} = 2/3D \quad (2a)$$

$$D_{yy} = 1/3D - E \quad (2b)$$

$$D_{xx} = 1/3D + E \quad (2c)$$

Cyclic permutations were performed in order to transform the largest value determined from the equations above to satisfy (1). Upon reorientation of the D -tensors the following equations are employed to calculate the new D and E values:

$$D = 3/2D_{zz} = -3/2(D_{xx} + D_{yy}) \quad (3)$$

$$E = 1/2(D_{xx} - D_{yy}) \quad (4)$$

Based on these fits, the chloride salt, **5.1**, exhibits the most anisotropic center with the largest D and smallest $|E|/D$ values, while **5.2** determined this species possess the smallest D value, but a moderate $|E|/D$ value. Comparison of these values with the values extracted from the fits of the variable-temperature magnetic susceptibility data give good qualitative agreement between the two methods. While the sign of D cannot be accurately determined using either of these methods, the agreement between these methods allows us to at least be confident in the magnitude of these values.

Table 5.3. Comparison of D and $|E|/D$ parameters obtained from fitting of susceptibility data using julX and magnetization data using ANISOFIT 2.0.

Compound	julX			ANISOFIT 2.0		
	g	D (cm ⁻¹)	$ E /D$ (cm ⁻¹)	g	D (cm ⁻¹)	$ E /D$ (cm ⁻¹)
5.1	2.24	11.87	0.045	2.32	9.49	0.004
5.2	2.29	2.42	0.13	2.30	2.53	0.058
5.3	2.20	3.59	0.62	2.17	4.22	0.335
5.4	N/D	N/D	N/D	2.22	4.63	0.060

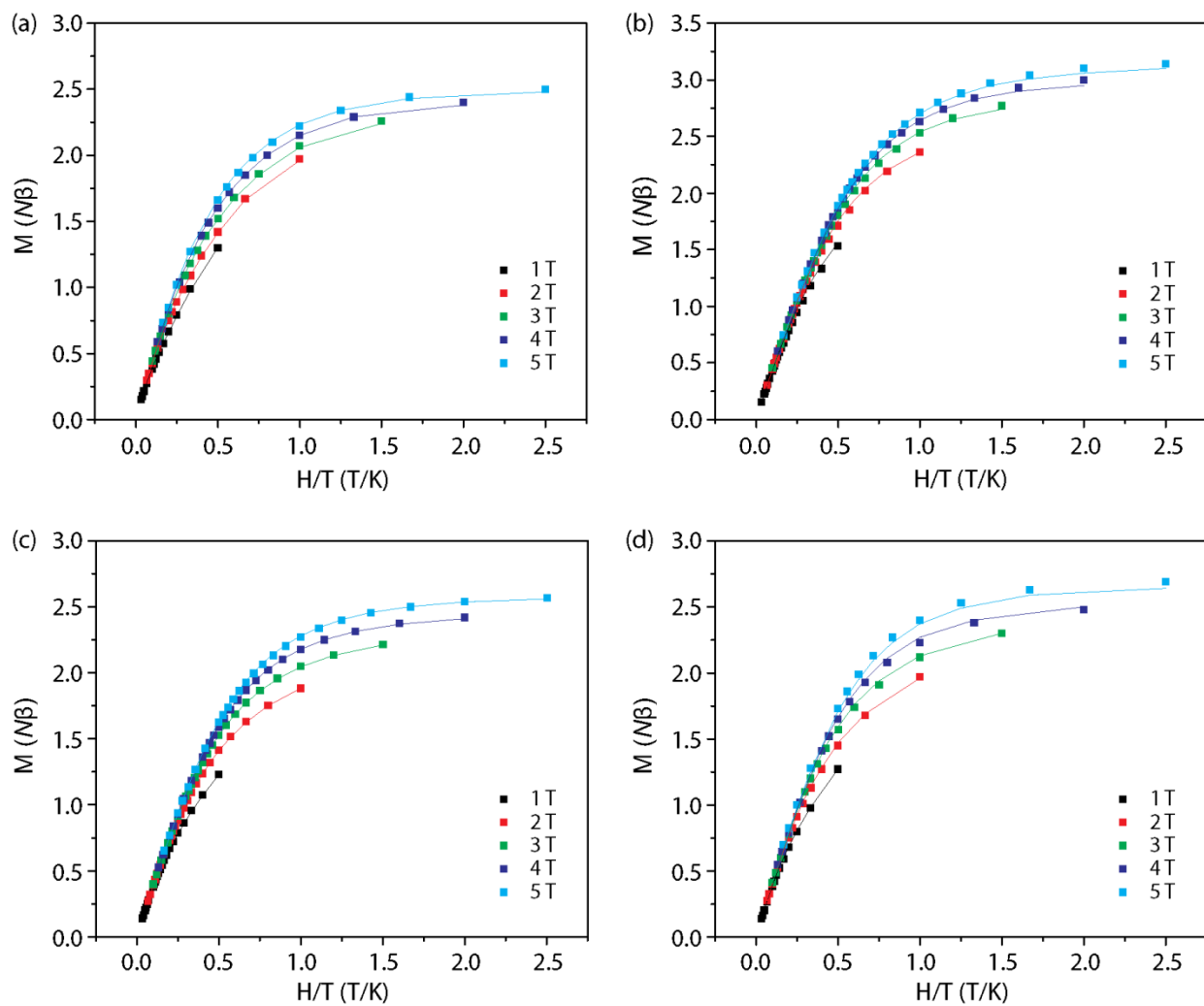


Figure 5.9. M vs H/T curves for **5.1** (a), **5.2** (b), **5.3** (c), and **5.4** (d). Lines are of best-fit determined by fitting in ANISOFIT 2.0

Table 5.4. Attempted fits using ANISOFIT 2.0 for **5.1.**

Entry	g_{initial}	g_{fit}	D_{initial} (cm^{-1})	D_{fit} (cm^{-1})	D_{fit} (cm^{-1})	E_{initial} (cm^{-1})	E_{fit} (cm^{-1})	E_{fit} (cm^{-1})	f sum
1	2.30	2.32	10	9.490	N/D	3	-0.039	N/D	0.005031
2	2	2.307	10	5.384	7.829	3	3.425	0.9792	0.02729
3	2.30	2.32	100	9.490	N/D	3	0.039	N/D	0.005031
4	2.30	2.307	100	5.384	7.829	3	3.425	0.9792	0.02729

Table 5.5. Attempted fits using ANISOFIT 2.0 for **5.2.**

Entry	g_{initial}	g_{fit}	D_{initial} (cm^{-1})	D_{fit} (cm^{-1})	D_{fit} (cm^{-1})	E_{initial} (cm^{-1})	E_{fit} (cm^{-1})	E_{fit} (cm^{-1})	f sum
1	2.20	2.30	5	2.530	N/D	0.100	0.146	N/D	0.034279
2	2.20	2.30	5	1.516	2.495	0.100	1.158	0.1793	0.023729
3	2.20	2.30	100	2.525	N/D	0.100	0.178	N/D	0.034326
4	2.20	2.30	100	1.517	2.495	0.100	1.158	0.1793	0.023729

Table 5.6. Attempted fits using ANISOFIT 2.0 for **5.3.**

Entry	g_{initial}	g_{fit}	D_{initial} (cm^{-1})	D_{fit} (cm^{-1})	D_{fit} (cm^{-1})	E_{initial} (cm^{-1})	E_{fit} (cm^{-1})	E_{fit} (cm^{-1})	f sum
1	2.20	2.30	10	4.502	N/D	3	1.3488	N/D	0.007271
2	2.20	2.17	10	3.770	4.218	3	1.571	1.414	0.004421
3	2.20	2.17	100	0.5015	4.248	3	2.665	1.082	0.003642
4	2.20	2.17	100	3.770	4.218	3	1.571	1.414	0.004421

Table 5.7. Attempted fits using ANISOFIT 2.0 for **5.4.**

Entry	g_{initial}	g_{fit}	D_{initial} (cm^{-1})	D_{fit} (cm^{-1})	D_{fit} (cm^{-1})	E_{initial} (cm^{-1})	E_{fit} (cm^{-1})	E_{fit} (cm^{-1})	f sum
1	2.30	2.22	10	2.226	4.628	3	2.349	0.053	0.02462
2	2.22	2.22	10	-2.226	4.628	3	2.349	0.053	0.02464
3	2.22	2.22	100	2.217	4.769	3	2.440	0.112	0.04126
4	2.22	2.22	100	2.217	4.769	3	2.440	0.112	0.04126
5	2.22	2.22	2.217	2.217	4.769	3	2.440	0.112	0.04126

5.4.4 Dynamic Magnetic Properties. In order to probe the dynamic magnetic behavior of these cobalt complexes, studies of the field- and frequency-dependence on the in-phase (χ') and out-of-phase (χ'') ac magnetic susceptibilities of **5.1–5.4** were performed. Under zero-applied dc field, no out-of-phase susceptibility was observed for any of the complexes, which is either due to quantum tunneling and/or intermolecular antiferromagnetic interactions induced by crystallographic packing.¹ Upon application of a 200 Oe static dc field to **5.1**, the species begins to display a non-zero out-of-phase magnetic susceptibility signal. This behavior is indicative of slow magnetic relaxation (Figure 5.10), a signature of SMM-like properties. Under an applied field of 2500 Oe (Figure 5.11), the χ'' value maximizes and the frequency minimizes, indicating the slowest dynamics occur at that field. Similar studies of the field-dependence of the out-of-phase susceptibility for **5.2** and **5.3** at 1.9 K display negligible out-of-phase response between 1 and 1500 Hz with the application of dc field up to 5000 Oe. Determination of the dynamic behavior under various applied fields of complex **5.4** at 1.9 K shows an increase in the out-of-phase response under 200 Oe dc field at high frequencies. This behavior becomes more apparent with the application of higher dc fields, reaching a maximum under 3500 Oe dc applied field. Similar to what is seen for **5.1**, above applied dc fields of 4000 Oe, the susceptibility value and frequency decrease with increasing applied dc fields. Interestingly, at lower frequencies, under applied fields greater than 4000 Oe, a small increase in χ'' also becomes apparent only for **5.4**.

The temperature and frequency dependence of the ac susceptibility was studied for **5.1** under an applied dc field of 2500 Oe in the temperature range of 1.8–4.6 K between 1 and 1500 Hz. Maxima in χ'' are observed between 1.8 and 3.0 K (Figure 5.12) and relaxation was not observed at temperatures above 3.6 K, as indicated by a plot of the temperature versus χ'' (Figure 5.13). The maxima in χ'' were used to build an Arrhenius plot ($\tau = \tau_0 \exp(U_{\text{eff}}/kT)$) to determine the

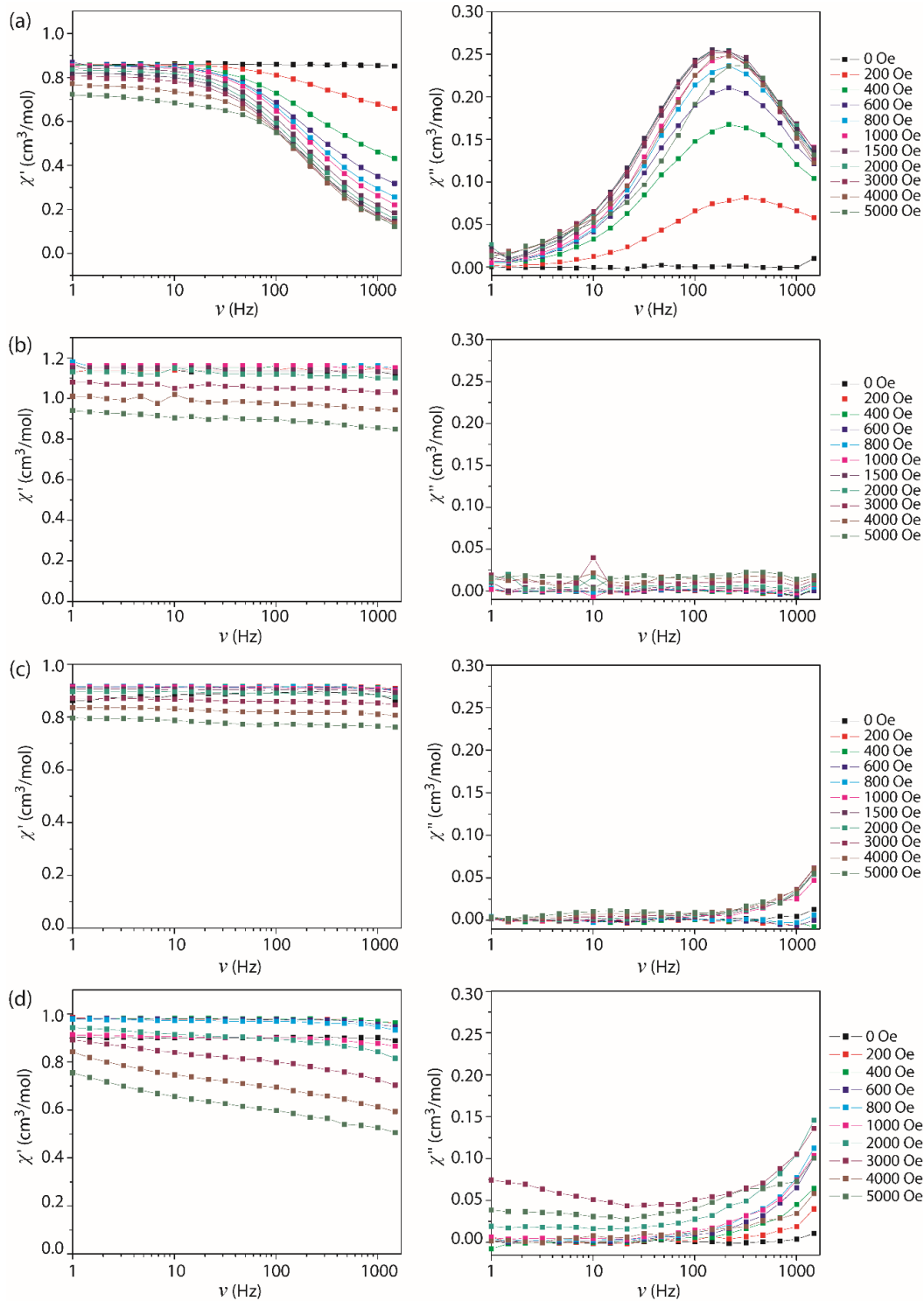


Figure 5.10. Variable-field in-phase (left) and out-of-phase (right) susceptibility data for **5.1** (a), **5.2** (b), **5.3** (c), and **5.4** (d). Data were collected at 1.9 K from 1 to 1500 Hz using a 4 Oe ac driving field.

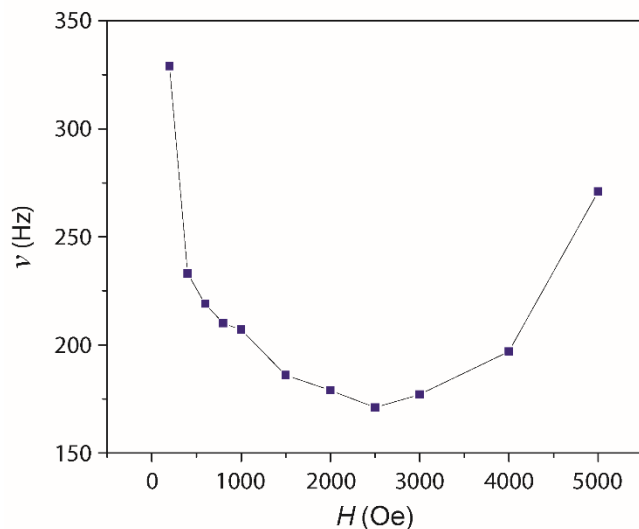


Figure 5.11. Frequency vs. field plot for **5.1**. The line is a guide for the eye.

activation barrier (U_{eff}) and temperature dependence of the relaxation time (where τ is the temperature dependent relaxation time and the τ_0 is pre-exponential constant) (Figure 5.14). From a linear fit of this plot, the anisotropic energy barrier was determined to be $U_{\text{eff}} = 9.9 \text{ cm}^{-1}$ ($\tau_0 = 8.97 \times 10^{-7} \text{ sec}$). Determination of the D value of **5.1** from the expression $U = (S^2 - 1/4)|D|$ from the ac susceptibility data leads to a value of 5 cm^{-1} . Using the D value extracted from the reduced magnetization data, the barrier height, U , was determined to be 19 cm^{-1} . While the value from the temperature-dependent out-of-phase magnetic data is lower than that determined by analysis of the reduced magnetization data, it is in qualitative agreement with these data.

5.6 Discussion.

In an effort to understand how the different anions influence the magnetic properties, several structural parameters were analyzed. Since complexes **5.1–5.3** pack in similar manners and thus have comparable intermolecular interactions, differing packing interaction imparted by the non-interacting anions and cocrystallizing solvent can be excluded. This implies this phenomenon is molecular in origin and somehow in response to the non-covalent second sphere interactions.

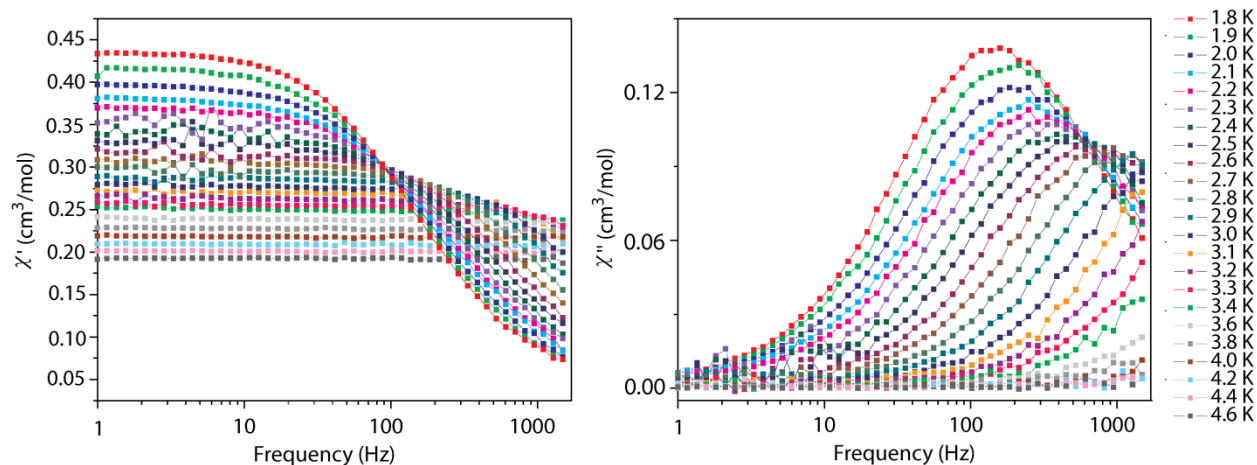


Figure 5.12. Dependence of temperature on the in-phase (left) and out-of-phase susceptibility (right) for complex **5.1** at various temperatures. The lines are guides for the eye. $H_{dc} = 2500$ Oe, $H_{ac} = 4$ Oe.

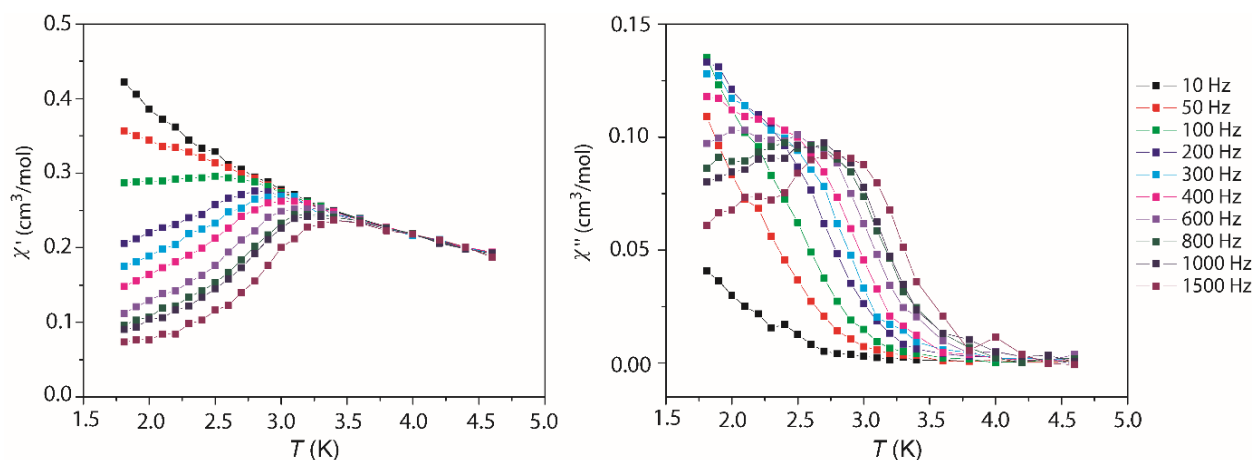


Figure 5.13. Temperature dependence on the in-phase (left) and out-of-phase (right) magnetic susceptibility of **5.1** at various frequencies. The lines are guides for the eyes. $H_{dc} = 2500$ Oe, $H_{ac} = 4$ Oe.

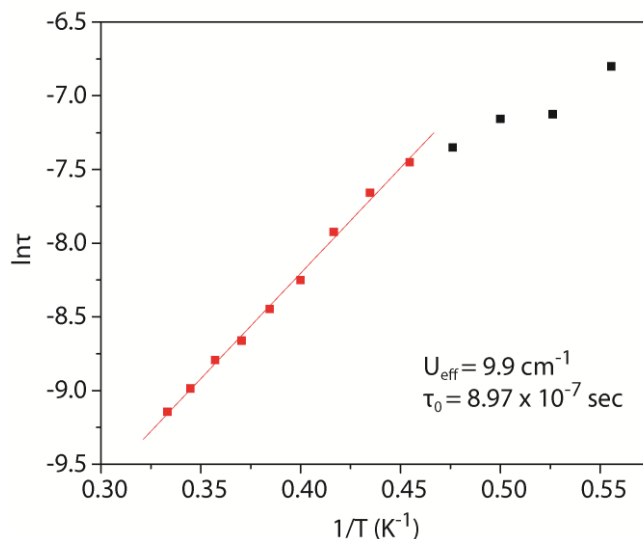


Figure 5.14. Arrhenius plot of **5.1** constructed from data collected under a dc field of 2500 Oe. The solid line represents the line of best fit for the linear portion of the data.

The exhibition of slow magnetic relaxation by the chloride salt, **5.1**, is concurrent with the maximum D and minimum $|E/D|$ values determined for the four species, as this species should possess the most axial magnetic anisotropy. These values are also similar to other Co(II) complexes that have displayed SMM-like behavior.^{16,18} From further comparison of the $|E/D|$ values presented in Table 5.3, it can be gleaned that with increasing halide size, the magnitude of $|E/D|$ increases, implying an increase in transverse anisotropy. While the D value is moderate for **5.3**, the significant transverse anisotropy presumably leads to the lack of magnetic relaxation even under the application of significant static DC fields. On the other hand, the perchlorate salt, **5.4**, and the iodide salt, **5.3**, display similar D values. While these D values may be sufficient to facilitate magnetic relaxation pathways, the larger $|E/D|$ component to the anisotropy for **5.2** suppresses the potential for slow magnetic relaxation by allowing for significant quantum tunneling.

One structural aspect that seems to mediate the magnetic properties is the Co–N_{bridge} distance. Comparison to other C_3 -symmetric Fe(II) and Co(II) species utilizing tripodal ligands capped by a nitrogen show that an increase in this distance also leads to a decrease in the magnitude of D . For example, in a series of Fe(II) complexes coordinated to functionalized ligands based on

tris(pyrrolyl- α -methyl)amine (tpa^{R}), a lengthening of the Fe–N_{bridge} distance from 2.144(1) Å to 2.196(2) Å is concurrent with a decrease in the D value obtained, ranging from -48 cm^{-1} for $[(\text{tpa}^{\text{t-Bu}})\text{Fe}]^-$ to -6.2 cm^{-1} for $[(\text{tpa}^{\text{DFP}})\text{Fe}]^-$ (Figure 5.15).⁸ Similarly, several Co(II) complexes based on Me₆tren with various axial ligands show differences in D values that coincide with a lengthening of the Co–N_{bridge} distance: for $[\text{Co}(\text{Me}_6\text{tren})\text{Cl}]^+$ the Co–N distance is 2.176(3) Å with D determined to be -6.2 cm^{-1} , while $[\text{Co}(\text{Me}_6\text{tren})\text{Br}]^+$ the Co–N distance is 2.215(4) Å and D was determined to be -2.5 cm^{-1} (Figure 5.15).⁴⁸ From these examples, it can be gleaned that subtle changes in the basicity either imparted by the ligand or by a coordinating anion influences the interaction of the d_z^2 orbital of the metal center with the lone pair of the apical nitrogen. This difference presumably aids in the formation of a magnetic axis, promoting larger D values and allowing for slow relaxation of the magnetization.

An additional structural parameter of interest is the displacement of the cobalt center from the planes of imine and pyridine nitrogens. The chloride salt, **5.1**, which displays slow magnetic relaxation, has the shortest distance between the plane of the imine nitrogen atoms and the Co center and the longest N_{pyridine}–Co distance. As the magnitude of D decreases, these distances

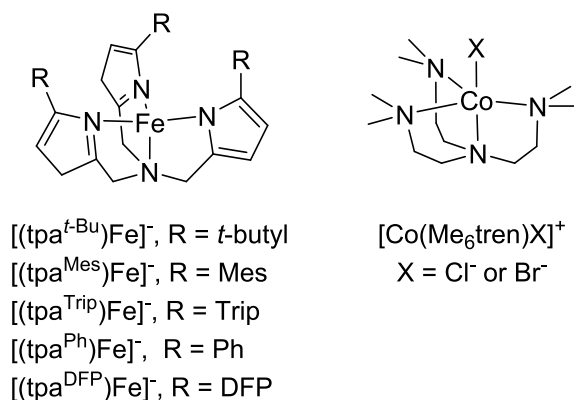


Figure 5.15. Depictions of $[(\text{tpa}^{\text{R}})\text{Fe}]^-$ and $[\text{Co}(\text{Me}_6\text{tren})\text{X}]^+$.

elongate and compress, respectively. Again evoking comparison to the C_3 -symmetric complexes of Fe(II) and Co(II), a correlation between the metal center displacement from the nitrogen plane can be seen. Maximization of this distance appears to maximize the magnetic anisotropy: for the Fe(II) complexes, displacement of 0.263 Å leads to the largest D value of -48 cm^{-1} seen for $[(\text{tpa}^{\text{t-Bu}})\text{Fe}]^-$, while a 0.233 Å displacement leads to a D value of -26 cm^{-1} for $[(\text{tpa}^{\text{Ph}})\text{Fe}]^-$.⁸ The Co(II) complexes of $[(\text{Me}_6\text{tren})\text{CoX}]^+$ also display analogous behavior: for the chloride salt, the Co center is displaced 0.327 Å from the plane of the amines and the bromide is slightly less displaced at 0.321 Å.⁴⁸ Similar structural distortions have been observed in several other complexes.^{22,25,29} This shows that even small structural distortions can modulate the magnetic anisotropy and relaxation processes of the metal centers.

5.7. Conclusions and Future Work.

While the synthesis of tripodal iminopyridine-based complexes of Co(II) has been previously undertaken, this is the first example of functionalization with the intent of incorporating hydrogen-bonding onto ligand in order to influence the magnetic anisotropy. In an effort to understand the influence of charge-balancing anions on the magnetic properties, we have synthesized four Co(II) salts: chloride, bromide, iodide, and perchlorate. The complexes, regardless of anion, are high-spin, indicating that the anion has little effect on the spin state of the metal. This is mainly due to the lack of the proper Jahn-Teller compression which is required to stabilize the low spin state.⁴⁹ Interestingly, there is a dependence of the magnetic anisotropy displayed by the metal center in response to the charge-balancing anion. This manifests as the ability for the cation to exhibit slow magnetic relaxation under applied field depending on the anion. These results add further evidence that suggest even small changes in the coordination environment can have drastic influences on magnetic properties. This appears to be the first

example of utilizing non-covalent hydrogen-bonding interactions to ‘turn-on’ single molecule magnet-like behavior.

Through theoretical calculations, more insight can be gleaned into the molecular origins of the magnetic anisotropy. Understanding how the subtle differences in coordination environment of the Co(II) center as well as the influence of the bridgehead nitrogen on the energy differences in the ligand field splitting of the *d* orbitals could allow us to devise other molecules to exploit this anion-dependence. Further studies could focus on using different capping ligands, such as tach (tach = *cis*-1,3,5-triaminocyclohexane), to force a more trigonal prismatic coordination environment on the metal. This has been shown to produce a Co(II) center than displays single-molecule magnet-like properties.⁵⁰ Coupling the trigonal prismatic coordination and anion-binding by using pyridines functionalized with hydrogen-bonding groups could amplify the importance of subtle modifications on the magnetic anisotropy of the metal center.

5.8 Acknowledgements.

This work was supported by Colorado State University and NSF-CHE-1058889 and NSF-CHE-1363274.

REFERENCES

- (1) Gatteschi, D. *Molecular nanomagnets*; Oxford University Press: Oxford; 2006.
- (2) Rinehart, J. D.; Long, J. R. *Chem. Sci.* **2011**, *2*, 2078.
- (3) Sessoli, R.; Powell, A. K. *Coord. Chem. Rev.* **2009**, *253*, 2328.
- (4) Coutinho, J. T.; Antunes, M. A.; Pereira, L. C. J.; Bolvin, H.; Marcalo, J.; Mazzanti, M.; Almeida, M. *Dalton Trans.* **2012**, *41*, 13568.
- (5) Rinehart, J. D.; Meihaus, K. R.; Long, J. R. *J. Am. Chem. Soc.* **2010**, *132*, 7572.
- (6) Rinehart, J. D.; Long, J. R. *J. Am. Chem. Soc.* **2009**, *131*, 12558.
- (7) Meihaus, K. R.; Long, J. R. *Dalton Trans.* **2015**, *44*, 2517.
- (8) Harman, W. H.; Harris, T. D.; Freedman, D. E.; Fong, H.; Chang, A.; Rinehart, J. D.; Ozarowski, A.; Sougrati, M. T.; Grandjean, F.; Long, G. J.; Long, J. R.; Chang, C. J. *J. Am. Chem. Soc.* **2010**, *132*, 18115.
- (9) Lin, P.-H.; Smythe, N. C.; Gorelsky, S. I.; Maguire, S.; Henson, N. J.; Korobkov, I.; Scott, B. L.; Gordon, J. C.; Baker, R. T.; Murugesu, M. *J. Am. Chem. Soc.* **2011**, *133*, 15806.
- (10) Eichhoefer, A.; Lan, Y.; Mereacre, V.; Bodenstern, T.; Weigend, F. *Inorg. Chem.* **2014**, *53*, 1962.
- (11) Zadrozny, J. M.; Atanasov, M.; Bryan, A. M.; Lin, C.-Y.; Rekker, B. D.; Power, P. P.; Neese, F.; Long, J. R. *Chem. Sci.* **2013**, *4*, 125.
- (12) Zadrozny, J. M.; Xiao, D. J.; Atanasov, M.; Long, G. J.; Grandjean, F.; Neese, F.; Long, J. R. *Nat. Chem.* **2013**, *5*, 577.
- (13) Kahn, O. *Molecular Magnetism*; VCH: New York, 1993.
- (14) Zadrozny, J. M.; Long, J. R. *J. Am. Chem. Soc.* **2011**, *133*, 20732.
- (15) Buchholz, A.; Eseola, A. O.; Plass, W. *C. R. Chim.* **2012**, *15*, 929.
- (16) Zadrozny, J. M.; Liu, J.; Piro, N. A.; Chang, C. J.; Hill, S.; Long, J. R. *Chem. Commun.* **2012**, *48*, 3927.
- (17) Cao, D.-K.; Feng, J.-Q.; Ren, M.; Gu, Y.-W.; Song, Y.; Ward, M. D. *Chem. Commun.* **2013**, *49*, 8863.
- (18) Huang, W.; Liu, T.; Wu, D.; Cheng, J.; Ouyang, Z. W.; Duan, C. *Dalton Trans.* **2013**, *42*, 15326.
- (19) Yang, F.; Zhou, Q.; Zhang, Y.; Zeng, G.; Li, G.; Shi, Z.; Wang, B.; Feng, S. *Chem. Commun.* **2013**, *49*, 5289.
- (20) Zadrozny, J. M.; Telser, J.; Long, J. R. *Polyhedron* **2013**, *64*, 209.
- (21) Boca, R.; Miklovic, J.; Titis, J. *Inorg. Chem.* **2014**, *53*, 2367.

- (22) Habib, F.; Luca, O. R.; Vieru, V.; Shiddiq, M.; Korobkov, I.; Gorelsky, S. I.; Takase, M. K.; Chibotaru, L. F.; Hill, S.; Crabtree, R. H.; Murugesu, M. *Angew. Chem. Int. Ed.* **2013**, *52*, 11290.
- (23) Vallejo, J.; Castro, I.; Ruiz-Garcia, R.; Cano, J.; Julve, M.; Lloret, F.; De Munno, G.; Wernsdorfer, W.; Pardo, E. *J. Am. Chem. Soc.* **2012**, *134*, 15704.
- (24) Herchel, R.; Vahovska, L.; Potocnak, I.; Travnicek, Z. *Inorg. Chem.* **2014**, *53*, 5896.
- (25) Habib, F.; Long, J.; Lin, P.-H.; Korobkov, I.; Ungur, L.; Wernsdorfer, W.; Chibotaru, L. F.; Murugesu, M. *Chem. Sci.* **2012**, *3*, 2158.
- (26) Campbell, V. E.; Bolvin, H.; Riviere, E.; Guillot, R.; Wernsdorfer, W.; Mallah, T. *Inorg. Chem.* **2014**, *53*, 2598.
- (27) Cucinotta, G.; Perfetti, M.; Luzon, J.; Etienne, M.; Car, P.-E.; Caneschi, A.; Calvez, G.; Bernot, K.; Sessoli, R. *Angew. Chem. Int. Ed.* **2012**, *51*, 1606.
- (28) Feng, X.; Mathonière, C.; Jeon, I.-R.; Rouzières, M.; Ozarowski, A.; Aubrey, M. L.; Gonzalez, M. I.; Clérac, R.; Long, J. R. *J. Am. Chem. Soc.* **2013**, *135*, 15880.
- (29) Jurca, T.; Farghal, A.; Lin, P.-H.; Korobkov, I.; Murugesu, M.; Richeson, D. S. *J. Am. Chem. Soc.* **2011**, *133*, 15814.
- (30) Gomez-Coca, S.; Cremades, E.; Aliaga-Alcalde, N.; Ruiz, E. *J. Am. Chem. Soc.* **2013**, *135*, 7010.
- (31) McDaniel, A. M.; Klug, C. M.; Shores, M. P. *Eur. J. Inorg. Chem.* **2013**, *2013*, 943.
- (32) Bain, G. A.; Berry, J. F. *J. Chem. Educ.* **2008**, *85*, 532.
- (33) Bill, E. julX; Version 1.41; Max Planck Institute for Bioinorganic Chemistry; Mulheim an der Ruhr, 2008.
- (34) Shores, M. P.; Sokol, J. J.; Long, J. R. *J. Am. Chem. Soc.* **2002**, *124*, 2279.
- (35) *APEX 2*; Bruker Analytical X-Ray Systems, Inc.: Madison, WI., 2008.
- (36) Sheldrick, G. M. *SHELXTL*; Version 6.14 ed.; Analytical X-Ray Systems: Madison, WI., 1999.
- (37) McDaniel, A. M.; Rappé, A. K.; Shores, M. P. *Inorg. Chem.* **2012**, *51*, 12493.
- (38) Hoselton, M. A.; Wilson, L. J.; Drago, R. S. *J. Am. Chem. Soc.* **1975**, *97*, 1722.
- (39) Guionneau, P.; Marchivie, M.; Bravic, G.; Letard, J.-F.; Chasseau, D. *J. Mater. Chem.* **2002**, *12*, 2546.
- (40) Halcrow, M. A. *Chem. Soc. Rev.* **2011**, *40*, 4119.
- (41) Drew, M. G. B.; Harding, C. J.; McKee, V.; Morgan, G. G.; Nelson, J. *J. Chem. Soc., Chem. Commun.* **1995**, 1035.
- (42) Marchivie, M.; Guionneau, P.; Létard, J.-F.; Chasseau, D. *Acta Crystallogr. Sect. B: Struct. Sci.* **2005**, *61*, 25.

- (43) Larsen, E.; LaMar, G. N.; Wagner, B. E.; Parks, J. E.; Holm, R. H. *Inorg. Chem.* **1972**, *11*, 2652.
- (44) van, G. M.; Lu, C. C.; Wieghardt, K.; Lubitz, W. *Inorg. Chem.* **2009**, *48*, 2626.
- (45) Lu, C. C.; Weyhermueller, T.; Bill, E.; Wieghardt, K. *Inorg. Chem.* **2009**, *48*, 6055.
- (46) Vallejo, J.; Castro, I.; Ruiz-Garcia, R.; Cano, J.; Julve, M.; Lloret, F.; De Munno, G.; Wernsdorfer, W.; Pardo, E. *J. Am. Chem. Soc.* **2012**, *134*, 15704.
- (47) Boča, R. *Theoretical foundations of molecular magnetism*; Elsevier: Amsterdam ;, 1999.
- (48) Ruamps, R.; Batchelor, L. J.; Guillot, R.; Zakhia, G.; Barra, A.-L.; Wernsdorfer, W.; Guihery, N.; Mallah, T. *Chem. Sci.* **2014**, *5*, 3418.
- (49) Goodwin, H. A. *Spin Crossover in Transition Metal Compounds II*; Springer Berlin Heidelberg: 2004; Vol. 234, p 23.
- (50) Gomez-Coca, S.; Cremades, E.; Aliaga-Alcalde, N.; Ruiz, E. *J. Am. Chem. Soc.* **2013**, *135*, 7010.

CHAPTER 6: MESITYLENE-BASED MOLECULES TOWARDS TOPOLOGICAL CONTROL OF FE(III)-ALKYNYL COMPLEXES

6.1 Introduction

Single-molecule magnets (SMMs) allow for external control of their magnetization for potential use in data storage or computation applications.¹ Many approaches are being investigated including the use of single ions of lanthanides,^{2,3} actinides,^{4,5} and first-row transition metals as well as the formation of large metal clusters.^{6,7} Efforts focused on polynuclear clusters seek to maximize the spin (S) and the zero-field splitting/magnetic anisotropy (D) of the species in order to maximize the barrier to spin reorientation (U). In complexes with significant exchange interactions, the exchange coupling (J) between the spin centers must also be maximized to isolate the high-spin ground state from low-lying, lower-spin excited states.⁸

Numerous examples of connecting metal centers using ethynylbenzenes to maximize communication between the metal centers are known.⁹⁻¹³ Some of the earliest research was performed by Field and Lapinte using diphosphine ligands such as 1,2-bis(dimethylphosphino)ethane (dmpe) and 1,2-bis(diphenylphosphino)ethane (dppe) and pentamethylcyclopentadiene (Cp*^{*}).¹⁴⁻¹⁷ An extension of this work from our lab used 1,3,5-triethynylbenzene (H₃TEB) as a bridging ligand between [(dmpe)₂FeCl]⁺ moieties to synthesize polynuclear complexes.¹⁸ While ferromagnetic coupling between the metal centers is apparent, the dmpe moieties are able to freely rotate around the Fe(III) centers. This prevents the optimum orbital overlap between the singly-occupied molecular orbital (SOMO) on the metal center, which was predicted to reside on a $d \pi$ -orbital located between the dmpe ligands, and the of the aryl π -system.

One method to improve coupling between the metal centers suggested by DFT calculations is to impart steric hindrance on the aryl ring. While it was predicted that the addition of the methyl

groups would only modestly increase the coupling between the metal centers due to the electronic differences, the steric bulk imparted by these methyl groups would force the dmpe ligands to maintain the desired orientation with respect to the π -system to facilitate better coupling between the metal centers.¹⁸ There are numerous examples of adding second- and third-row transition metals, mainly palladium, platinum and gold onto 1,3,5-triethynylmesitylene (H₃TEM). Most of these efforts are geared synthesizing dendimeric motifs,¹⁹⁻²⁵ with a few examples of these species being implemented for polymerization reactions,²⁶ but to this date, no examples of applying this ligand to bridging paramagnetic metal centers to study the magnetic exchange have been disseminated.

To this end, a new series of molecules have been synthesized and characterized using a mesitylene bridge between the Fe(III) centers. As an extension to work began by Dr. Stephanie Fiedler-Gleich, optimization of the synthesis of [(dmpe)₄Fe₂Cl₂(μ_2 -*m*-HTEM)] (**6.4**) and [(dmpe)₄Fe₂Cl₂(μ_2 -*m*-HTEM)] (**6.5**) were attempted. Additionally, to model the electronic contribution of the ligand to the magnetic properties, three novel mononuclear complexes [(dmpe)₂FeCl(CCTMS)](OTf) (**6.1**), [(dmpe)₂FeCl(MEM)] (**6.2**), and the ferric [(dmpe)₂FeCl(MEM)](OTf) (**6.3**) have been synthesized. Additionally, the ferrous and ferric dinuclear species, [(dmpe)₄Fe₂Cl₂(μ_2 -*m*-DEM)] (**6.6**) and [(dmpe)₄Fe₂Cl₂(μ_2 -*m*-DEM)](OTf) (**6.7**), respectively, have been synthesized to study the coupling of two metal centers in the absence of the third. The structural and magnetic properties of these species will be compared to the benzene-bridged species to determine if the inclusion of steric bulk within the aromatic ring promotes an increase in the ferromagnetic coupling between the metal centers.

6.2 Division of Labor.

Syntheses of **6.4** and **6.5**, X-ray crystal structure of **6.5** and optimization of synthesis and full complex characterization of $[(\text{dmpe})_6\text{Fe}_3\text{Cl}_3(\mu_3\text{-TEM})](\text{OTf})_3$ were performed by Dr. Stephanie Fiedler-Gleich.²⁷ Syntheses of complexes **6.1–6.3**, **6.6** and **6.7**, full complex characterizations of complexes presented herein, and magnetic measurements were performed by Christina Klug.

6.3 Experimental Section

6.3.1 Preparation of Compounds. Manipulations of iron complexes were performed inside a dinitrogen-filled glovebox (MBRAUN Labmaster 130) or on a Schlenk line under dinitrogen atmosphere. Acetonitrile (MeCN), dichloromethane (DCM), tetrahydrofuran (THF), diethyl ether (Et₂O) and toluene were sparged with dinitrogen, passed over molecular sieves, and subjected to three freeze-pump-thaw cycles prior to use. Pentane was distilled over sodium metal and subjected to three freeze-pump-thaw cycles prior to use. The ligands 1,3,5-triethynylmesitylene (H₃TEM)²⁸, monoethynylmesitylene (HMEM)²⁹, and diethynylmesitylene (H₂DEM)³⁰, the compounds $[\text{Fe}(\text{dmpe})_2\text{Cl}_2]$ ³¹ and $[(\text{dmpe})_6\text{Fe}_3\text{Cl}_3(\mu_3\text{-TEM})](\text{OTf})_3$ ²⁷ were synthesized according to the literature. Triethylamine (NEt₃) was freshly distilled and stored in the glovebox. All other compounds and reagents were obtained commercially and used as received.

$[(\text{dmpe})_2\text{FeCl}(\text{CCTMS})](\text{OTf})$ (6.1). A solution of AgOTf (146 mg, 0.57 mmol) in 4 mL of MeCN was added to an orange suspension of $[(\text{dmpe})_2\text{FeCl}(\text{CCTMS})]$ (168 mg, 0.34 mmol) in 6 mL of MeCN. The orange solution instantly turned teal in color and was allowed to stir for two hours. The reaction mixture was filtered and the filtrate solvent was removed under vacuum. The resulting solid was triturated with 20 mL of Et₂O to produce a free flowing teal powder. The solid was collected by vacuum filtration and recrystallized by Et₂O diffusion into a concentrated THF

solution of the compound. Overnight diffusion resulted in the formation of green X-ray quality crystals (128 mg, 58%). IR (KBr): $\nu_{\text{C}\equiv\text{C}}$ 1989 cm^{-1} . ESI-MS(+) (CH_2Cl_2): m/z 488.1 $[(\text{dmpe})_2\text{FeCl}(\text{CCTMS})]^+$. ^1H NMR (400 MHz, CD_2Cl_2): 9.1, -20.2, -20.4, -23.9, -24.4 ppm. UV-vis (CH_2Cl_2) $\lambda_{\text{max}}/\text{nm}$ ($\epsilon_{\text{M}}/\text{M}^{-1} \text{cm}^{-1}$): 295 (11240), 407 (470), 527 (sh, 270), 576 (sh, 1250), 635 (3290). Anal Calcd for $\text{C}_{18}\text{H}_{41}\text{ClF}_3\text{FeO}_3\text{P}_4\text{SSi}$: C, 33.89; H, 6.48. Found: C, 33.68; H, 6.26.

$[(\text{dmpe})_2\text{FeCl}(\text{MEM})]$ (6.2). A solution of HMEM (51 mg, 0.35 mmol) dissolved in 5 mL of methanol (MeOH) and $[(\text{dmpe})_2\text{FeCl}_2]$ (151 mg, 0.35 mmol) dissolved in 10 mL of MeOH, resulting in a forest green solution. Once all the reactants had dissolved, NEt_3 (400 μL , 2.8 mmol) was added. The solution immediately turned brown, and after stirring for 5 minutes, an orange precipitate began to form. The reaction was allowed to stir for one hour at room temperature, and then cooled to -40 $^\circ\text{C}$ for one hour to allow precipitation of additional product. The orange precipitate was isolated by vacuum filtration and washed with pentane (3×3 mL) and was used without further purification (113 mg, 60%). IR (KBr): $\nu_{\text{C}\equiv\text{C}}$ 2034 cm^{-1} . ESI-MS(+) (CH_2Cl_2): m/z 534.1 $[(\text{dmpe})_2\text{FeCl}(\text{MEM})]^+$, 499.2 $[(\text{dmpe})_2\text{Fe}(\text{MEM})]^+$ ^1H NMR (400 MHz, C_6D_6): 6.81 (s, 2 H, Ar-H), 2.42 (s, 6 H, Ar- CH_3), 2.19 (s, 3 H, Ar- CH_3), 1.73 (m, 8 H, P- CH_2), 1.36 (m, 24 H, P- CH_3) ppm. ^{13}C NMR was not obtained due to poor complex solubility. Elemental analysis was not determined; the compound was used as synthesized based on MS and ^1H NMR data.

$[(\text{dmpe})_2\text{FeCl}(\text{MEM})](\text{OTf})$ (6.3). A solution of AgOTf (101 mg, 0.39 mmol) dissolved in 4 mL of MeCN was added to a suspension of **6.2** (113 mg, 0.21 mmol) in 12 mL of MeCN. The reaction instantly turned green and was allowed to stir for one hour. The reaction was filtered to remove silver metal and the filtrate was concentrated to 2 mL. A green solid was obtained by precipitation with 20 mL of Et_2O and the resulting mixture was allowed to stir for one hour. The green solid was isolated by vacuum filtration and recrystallized by Et_2O diffusion into a

concentrated MeCN solution of the product (126 mg, 87%). IR (KBr): $\nu_{\text{C}\equiv\text{C}}$ 2005 cm^{-1} . ESI-MS(+) (CH_2Cl_2): m/z 534.1 ($[(\text{dmpe})_2\text{FeCl}(\text{MEM})]^+$). ^1H NMR (400 MHz, CD_2Cl_2): 81.1, 51.6, 30, -19.2, -19.9, -21.6, -22.1 ppm. UV-vis (CH_2Cl_2) $\lambda_{\text{max}}/\text{nm}$ ($\epsilon_{\text{M}}/\text{M}^{-1} \text{cm}^{-1}$): 298 (12800), 380 (4520), 427 (sh, 827), 598 (sh, 690), 690 (2700), 787 (11290). Anal Calcd for $\text{C}_{24}\text{H}_{43}\text{ClF}_3\text{FeO}_3\text{P}_4\text{S}_1$: C, 42.15; H, 6.34. Found: C, 42.07; H, 6.35.

$[(\text{dmpe})_{2x}\text{Fe}_x\text{Cl}_x(\mu\text{-}m\text{-}\text{H}_{3-x}\text{TEM})]$ (X = 1, 2) (6.4). Freshly sublimed H_3TEM (35.87 mg, 0.187 mmol) and $[(\text{dmpe})_2\text{FeCl}_2]$ (164 mg, 0.39 mmol) were dissolved in 24 mL of MeOH. Once all the reactants had dissolved, NEt_3 (420 μL , 3.0 mmol) was added. A tan precipitate formed immediately, and the mixture was allowed to stir for one hour. The resulting solid was isolated by vacuum filtration and the solid was washed with 12 mL of MeOH and 8 mL of pentane. A tan solid was isolated (90 mg, 49%) and used without further purification. IR (KBr): $\nu_{\text{C}\equiv\text{C-H}}$ 3305 cm^{-1} , $\nu_{\text{C}\equiv\text{C}}$ 2029 cm^{-1} . ESI-MS(+) (CH_2Cl_2): m/z 972.0 ($[(\text{dmpe})_4\text{Fe}_2\text{Cl}_2(\mu_2\text{-}m\text{-}\text{HTEM})]^+$, 582.1 ($[(\text{dmpe})_2\text{FeCl}(\text{HTEM})]^+$). ^1H NMR (400 MHz, C_6D_6): 3.10 (s, $\text{C}\equiv\text{C-H}$), 2.79 (s, Ar-CH_3), 2.70 (s, Ar-CH_3), 1.68 (m, P-CH_2), 1.34 (s, P-CH_3), 1.27 (s, P-CH_3) ppm. ^{13}C NMR was not obtained due to poor complex solubility. Elemental analysis was not determined; the compound was used as synthesized based on MS and ^1H NMR data.

$[(\text{dmpe})_{2x}\text{Fe}_x\text{Cl}_x(\mu\text{-}m\text{-}\text{H}_{3-x}\text{TEM})](\text{OTf})_x$ (X = 1, 2) (6.5). A solution of AgOTf (61 mg, 0.24 mmol) dissolved in 9 mL of MeCN was added to solid **6.4** (87 mg, 0.09 mmol based on dinuclear complex). The solution instantly turned green and was allowed to stir for one hour. The reaction was filtered to remove silver metal, and the solvent was removed from the filtrate in *vacuo*. The resulting green solid was triturated with Et_2O (20 mL) for one hour. A green free-flowing powder was isolated by vacuum filtration, washed with Et_2O (2×5 mL) and recrystallized by Et_2O diffusion into concentrated MeCN solution of the product. IR (KBr): $\nu_{\text{C}\equiv\text{C-H}}$ 3250 cm^{-1} , $\nu_{\text{C}\equiv\text{C}}$

2010 cm^{-1} . ESI-MS(+) (CH_2Cl_2): m/z 1120.9 $[(\text{dmpe})_4\text{Fe}_2\text{Cl}_2(\mu_2\text{-}m\text{-HTEM})](\text{OTf})^+$, 582.1 $[(\text{dmpe})_2\text{FeCl}(\text{HTEM})]^+$ 487.0 $[(\text{dmpe})_4\text{Fe}_2\text{Cl}_2(\mu_2\text{-}m\text{-TEM})]^{2+}$. ^1H NMR (400 MHz, CD_2Cl_2): 117.5, 97.5, 20.7, -20.6, -20.8, -23.4, -23.9 ppm. UV-vis (CH_2Cl_2) $\lambda_{\text{max}}/\text{nm}$: 299, 398, 440, 598, 670, 764. Anal Calcd for $\text{C}_{41}\text{H}_{74}\text{Cl}_2\text{F}_6\text{Fe}_2\text{O}_6\text{P}_8\text{S}_2$: C, 38.73; H, 5.87. Found: C, 41.55; H, 5.63. Note: elemental analysis suggests a mixture of mono- and dinuclear species in the bulk sample; calculated for 1:1 $[(\text{dmpe})_4\text{Fe}_2\text{Cl}_2(\mu_2\text{-}m\text{-HTEM})](\text{OTf})_2$: $[(\text{dmpe})_2\text{FeCl}(\text{H}_2\text{TEM})](\text{OTf})$: C, 41.37; H, 5.89.

$[(\text{dmpe})_4\text{Fe}_2\text{Cl}_2(\mu_2\text{-}m\text{-DEM})]$ (6.6). A solution of H_2DEM (28 mg, 0.17 mmol) dissolved in 5 mL of MeOH was added to a solution of $[(\text{dmpe})_2\text{FeCl}_2]$ (148 mg, 0.35 mmol) dissolved in 10 mL of MeOH, resulting in a forest green solution. Once all the reactants had dissolved, NEt_3 (300 μL , 2.1 mmol) was added. The solution immediately became brown and after stirring for 5 minutes, an orange precipitate developed. The mixture was allowed to stir at room temperature for 16 hours. The precipitate was isolated by vacuum filtration and washed with pentane (3×3 mL). A salmon-colored solid was isolated (128 mg, 81%) and used without further purification. IR (KBr): $\nu_{\text{C}=\text{C}}$ 2023 cm^{-1} . ESI-MS(+) (CH_2Cl_2): m/z 948.1 $[(\text{dmpe})_2\text{FeCl}(\text{DEM})]^+$. ^1H NMR (400 MHz, C_6D_6): 6.81 (s, 1 H, Ar- H), 2.70 (s, 3 H, Ar- CH_3), 2.39 (s, 6 H, Ar- CH_3), 1.75 (m, 16 H, P- CH_2), 1.39 (d, 48 H, P- CH_3) ppm. ^{13}C NMR was not obtained due to poor complex solubility. Elemental analysis was not determined; the compound was used as synthesized based on MS and ^1H NMR data.

$[(\text{dmpe})_4\text{Fe}_2\text{Cl}_2(\mu_2\text{-}m\text{-DEM})](\text{OTf})_2$ (6.7). A solution of AgOTf (101 mg, 0.39 mmol) dissolved in 5 mL of MeCN and added to a suspension of $[(\text{dmpe})_4\text{Fe}_2\text{Cl}_2(\mu_2\text{-}m\text{-DEM})]$ (100 mg, 0.10 mmol) in 12 mL of MeCN. The solution instantly turned green and was allowed to stir for one hour. A green solid was obtained after concentration in *vacuo* to 5 mL and subsequent

precipitation with Et₂O (20 mL). The suspension was allowed to stir for one hour. The green solid was isolated by vacuum filtration and washed with Et₂O (2 × 5 mL). X-ray quality crystals were obtained by Et₂O diffusion into a concentrated MeOH solution of the product (112 mg, 85%). IR (KBr): $\nu_{C=C}$ 2000 cm⁻¹. ESI-MS(+) (CH₂Cl₂): m/z 1097.1 ([*(dmpe)*₂FeCl(DEM)](OTf))⁺. ¹H NMR (400 MHz, CD₂Cl₂): 123.6, 102.6, 53.1, -20.5, -23.1, -23.5 ppm. UV-vis (CH₂Cl₂) λ_{max}/nm ($\epsilon_M/M^{-1} cm^{-1}$): 302 (27780), 386 (7110), 433 (sh, 1900), 595 (sh, 1820), 688 (5500), 781 (19300). Anal Calcd for C₃₉H₇₄Cl₂F₆Fe₂O₆P₈S₂: C, 37.55; H, 5.98. Found: C, 37.26; H, 5.92.

6.3.2 X-Ray Structure Determinations. Structures were determined for the compounds listed in Table 1. All single crystals were coated in Paratone–N oil prior to removal from the glovebox. The crystals were supported on Cryoloops before being mounted on a Bruker Kappa Apex II CCD diffractometer under a stream of cold dinitrogen. Data were collected with Mo K α radiation and a graphite monochromator. Initial lattice parameters were determined from reflections harvested from 36 frames, and data sets were collected targeting complete coverage and 4-fold redundancy. Refinement of the unit cell parameters was performed based on all data. Data were integrated and corrected for absorption effects with the Apex II software package.³² Structures were solved by direct methods, unless otherwise noted, and refined with the SHELXTL software package.³³ Unless otherwise noted, thermal parameters for all fully occupied, non-hydrogen atoms were refined anisotropically. Hydrogen atoms were added at the ideal positions and were refined using a riding model where the thermal parameters were set at 1.2 times those of the attached carbon atom (1.5 times that for methyl protons).

The structure for **6.1** is possibly twinned or cracked during data collection. CELL_NOW was implemented to remove the twinned component.³⁴ Integration was performed taking into account the multiple components. A Patterson map was used to determine the location of the

heaviest atoms, after which, difference maps were used to determine the positions of the other atoms. Attempts at refining all atoms anisotropically were unsuccessful as the thermal parameters of several atoms became non-positive definite with refinement. These atoms were allowed to refine isotropically. Disorder of one methyl of the trimethylsilane group was modeled into two components. Free refinement of a disordered THF molecule for **6.1** resulted in 75% occupation and the thermal parameters were refined isotropically.

The structure of **6.7** contained significant disorder of two of the dmpe moieties on the main residue. The disordered components were modelled with partial occupancies and the thermal parameters were refined isotropically due to the propensity for these atoms to become non-positive definite. Additional disorder was observed with the triflate anions, which were modeled in a similar fashion and refined anisotropically. Methanol molecules are also apparent in the structure with fixed occupancies of 50% (based on refinement as free variables) and thermal parameters were refined isotropically.

6.3.3 Magnetic Susceptibility Measurements. All samples were prepared under a dinitrogen atmosphere. Crystalline samples of **6.1**, **6.3**, and **6.7** were loaded into gelatin capsules and inserted into straws, which were sealed in a Schlenk tube prior to removal from the glovebox. Samples were quickly loaded (to minimize exposure to air) into a Quantum Design MPMS-XL SQUID magnetometer. The absence of ferromagnetic impurities was confirmed by observing the linearity of a plot of magnetization vs. field at 100 K. Magnetization experiments for (**6.7**) and $[(\text{dmpe})_6\text{Fe}_3\text{Cl}_3(\mu_3\text{-TEM})](\text{OTf})_3$ were performed by encasing the crystals in 6 drops of Eicosane and measuring between 2 and 30 K at applied DC fields of 1, 2, 3, 4, and 5 T. Data were corrected for the magnetization of the sample holder by subtracting the susceptibility of an empty gelcap and for diamagnetic contributions of the sample by using Pascal's constants.³⁵ Theoretical fits of the

susceptibility data for **6.7** were obtained using a relative error minimization routine (julX 1.41)³⁶ using a Hamiltonian of the form $\hat{H} = -2J\hat{S}_1 \cdot \hat{S}_2$. Fits of the magnetization data were obtained with the ANISOFIT 2.0³⁷ program using a Hamiltonian of the form $\hat{H} = D\hat{S}_z^2 + E(\hat{S}_x^2 + \hat{S}_y^2) + g_{iso}\beta\vec{S} \cdot \vec{B}$.

6.3.4 Other Physical Measurements. Infrared spectra were measured with a Nicolet 380 FT-IR using KBr pellets. Electronic absorption spectra were obtained in air-free cuvettes with a Hewlett-Packard 8453 spectrophotometer. ¹H NMR spectra were recorded on a Varian instrument operating at 400 MHz. Paramagnetic NMR spectra were collected using 0.1 second acquisition time and a 0.01 second relaxation delay. Cyclic voltammograms (CVs) were recorded with a CH Instruments potentiostat (model 1230A or 660C) using a Pt microelectrode working electrode, Ag/Ag⁺ reference electrode, and Pt wire auxiliary electrode at a scan rate of 0.1 V/s in 0.1 M solutions of (Bu₄N)PF₆ in CH₂Cl₂ solvent. Reported potentials are referenced to the [Cp₂Fe]⁺/[Cp₂Fe] (Fc⁺/Fc) redox couple and were determined by adding ferrocene as an internal standard at the conclusion of each electrochemical experiment. Mass spectrometry was measured with a Finnigan LCQ Duo mass spectrometer equipped with an electrospray ion source and a quadrupole ion trap mass analyzer. Electron paramagnetic resonance (EPR) spectra were measured using a continuous-wave X-band Bruker EMX 200U instrument equipped with a liquid nitrogen cryostat. To achieve a glass at low temperatures, the sample was dissolved in a 1:1 mixture of 1,2-dichloroethane and dichloromethane. Elemental analyses were performed by Robertson Microlit Laboratories Inc. in Madison, NJ.

Table 6.1. Crystallographic data for compounds [(dmpe)₂FeCl(CCTMS)](OTf) (**6.1**), [(dmpe)₂FeCl(MEM)](OTf) (**6.3**), and [(dmpe)₄Fe₂Cl₂(μ₂-*m*-DEM)](OTf)₂ (**6.7·1.5 MeOH**)

	6.1	6.3	6.7·1.5 MeOH
Crystal code	msn346	msn328	msn330
Empirical formula	C ₁₈ H ₃₇ ClF ₃ FeO ₃ P ₄ SiS	C ₂₄ H ₄₃ ClF ₃ FeO ₃ P ₄ S	C _{40.50} H ₇₉ Cl ₂ F ₆ Fe ₂ O _{7.50} P ₈ S ₂
Formula weight, g·mol ⁻¹	633.80	683.82	1294.51
Crystal color	blue	green	green
Habit	block	parellelpiped	block
<i>T</i> , K	120(2)	120(2)	120(2)
Space group	<i>P</i> 2 ₁ / <i>c</i>	<i>P</i> 2 ₁ 2 ₁ 2 ₁	<i>P</i> 2 ₁ / <i>n</i>
<i>Z</i>	10	4	4
<i>a</i> , Å	14(3)	12.5587(8)	12.9238(7)
<i>b</i> , Å	31.818	15.4730(9)	28.0962(16)
<i>c</i> , Å	14.434 15.9773(9)	17.6088(11)	
<i>α</i> , deg	90	90	90
<i>β</i> , deg	100.92	90	111.53
<i>γ</i> , deg	90	90	90
<i>V</i> , Å ³	6498.23	3104.7(3)	5947.8(6)
<i>d</i> _{calc} , g·cm ⁻³	1.695	1.463	1.446
GooF	1.107	1.035	1.059
<i>R</i> ₁ ^{<i>a</i>} (<i>wR</i> ₂) ^{<i>b</i>} , %	15.83 (36.09)	2.78 (5.42)	4.97 (15.52)

$${}^a R_1 = \sum ||F_o| - |F_c|| / \sum |F_o|; {}^b wR_2 = (\sum [w(F_o^2 - F_c^2)^2] / \sum [w(F_o^2)^2])^{1/2}$$

6.4 Results and Discussion

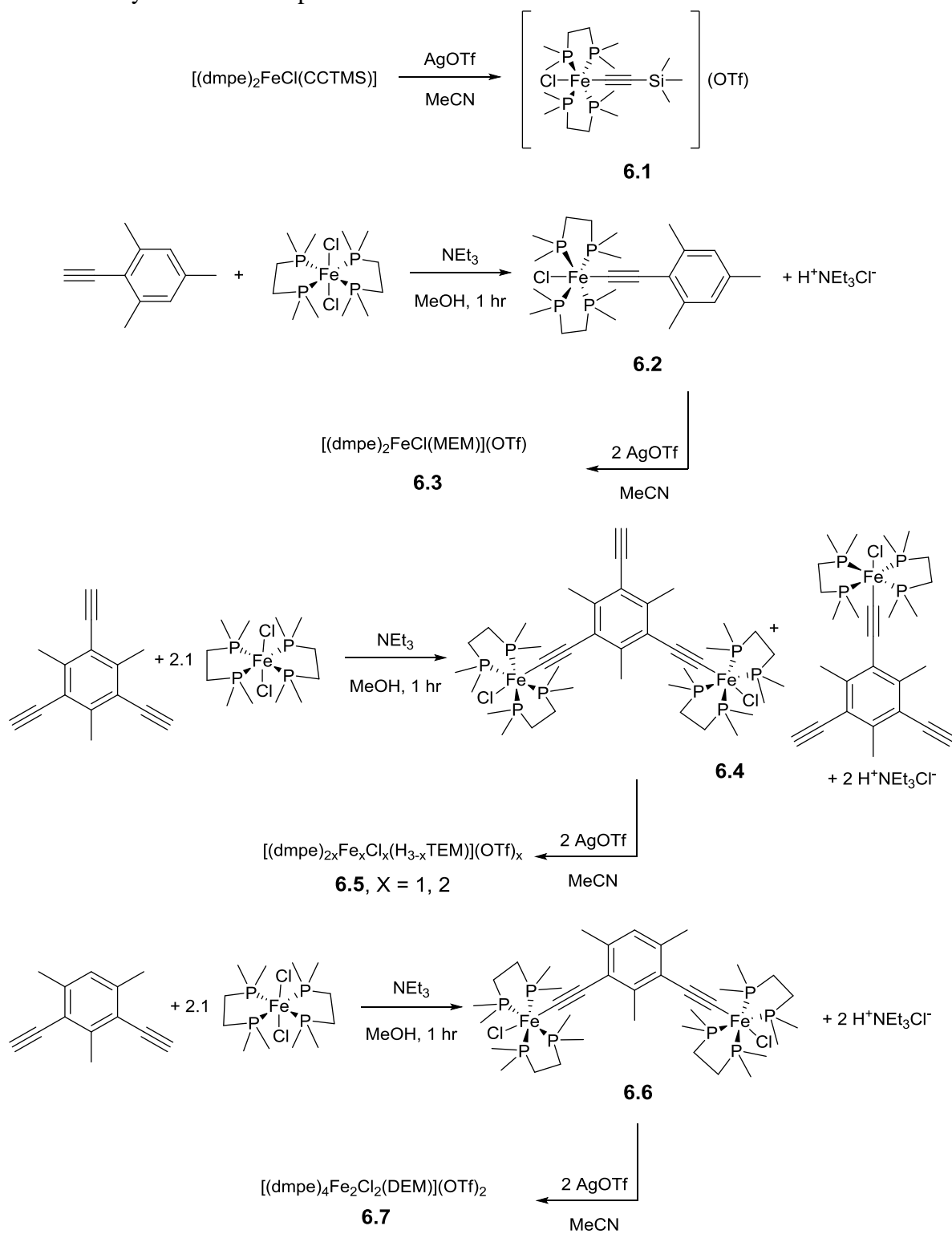
6.4.1 Syntheses and Characterizations. The preparations of the mono- and dinuclear species are outlined in Scheme 6.1. The synthesis of the ferrous complex **6.1**, $[(dmpe)_2FeCl(CCTMS)]$, was previously described by Berben;³⁸ the syntheses of the mononuclear complex, **6.1** $[(dmpe)_2FeCl(MEM)]$, and dinuclear complex **6.6**, $[(dmpe)_4Fe_2Cl_2(\mu_2-m-DEM)]$, were adapted from previously described syntheses of $[(dmpe)_2FeCl(C_2Ph)]$ ¹⁷ and $[(dmpe)_4Fe_2Cl_2(\mu_2-m-DEB)]$.³⁸ Complexes of the ferrous mono- and dinuclear complexes, **6.1** and **6.6**, precipitate cleanly from methanolic solutions of the reactants after approximately one hour. Attempts to synthesize the trinuclear $[(dmpe)_6Fe_3Cl_3(\mu_3-m-TEM)]$ complex with 3.1 equivalents of $[(dmpe)_2FeCl_2]$ to one equivalent of TEM at room temperature lead to the precipitation of $[(dmpe)_{2x}Fe_xCl_x(\mu_x-m-H_{3-x}TEM)]$ (**6.4**). From this precipitate, a mixture of a mono- and dinuclear TEM based complexes is formed. Oxidation with silver triflate in acetonitrile and purification *via* recrystallization by diethyl ether diffusion into an acetonitrile solution of the mixture afforded green crystals of $[(dmpe)_4Fe_2Cl_2H(\mu_2-m-HTEM)](OTf)_2$ **6.5**. A structure of the dinuclear species $[(dmpe)_4Fe_2Cl_2H(\mu_2-m-HTEM)](OTf)_2$ was obtained,²⁷ but bulk analysis of the crystals determined the persistence of the mononuclear impurity $[(dmpe)_2FeCl(H_2TEM)](OTf)$. While no attempts were made to purify the product, it appears that longer reaction times increase the prevalence of the mononuclear complex as indicated by ¹H NMR.

Purity of the ferrous species was determined by ¹H NMR, IR and mass spectrometry. Upon Fe(II) coordination, the IR resonance associated with the acetylene protons at 3300 cm⁻¹ disappeared in the cases of **6.2** and **6.6**, and the C≡C stretch moved to lower frequencies, from 2098 cm⁻¹ for free monoethynylmesitylene (HMEM) to 2029 cm⁻¹ with the formation of **6.2**. Additionally, the ¹H NMR resonances associated with acetylenic protons by disappeared and the

protons associated with the dmpe ligand persisted. In the case of **6.4**, the prevalence of the alkynyl proton stretch in the IR spectrum at 3305 cm^{-1} and ^1H NMR at 2.74 ppm indicate an incomplete reaction to the trinuclear species, and the formation of mono- and dinuclear complexes (Figure 6.2). The relative integrations of the methyl protons of the aromatic ring and the methyl and ethylene protons of the dmpe ligands via ^1H NMR add further evidence that a mixture of mono- and dinuclear products are formed when the reaction is run at room temperature in methanol even in the presence of excess $[(\text{dmpe})_2\text{FeCl}_2]$.

In order to determine if substituting benzene for mesitylene had any influence on the oxidation potential of the Fe(II) centers, cyclic voltammograms of complexes **6.2**, **6.3**, **6.6**, and **6.7** were performed. All complexes show two distinct redox processes: a $\text{Fe}^{\text{II}}/\text{Fe}^{\text{III}}$ couple and a $\text{Fe}^{\text{III}}/\text{Fe}^{\text{IV}}$ couple (Figures 6.3–6.4). Both of these are processes fully reversible with the $\text{Fe}^{\text{II}}/\text{Fe}^{\text{III}}$ couple centered at -0.6 V vs Fc^+/Fc and $\text{Fe}^{\text{III}}/\text{Fe}^{\text{IV}}$ couple centered on 0.65 V vs Fc^+/Fc . The values for the $\text{Fe}^{\text{II}}/\text{Fe}^{\text{III}}$ are similar to what has been previously observed for the benzene-bridged derivatives.¹⁷ The only difference between the behavior of the ferrous and ferric species is the voltage of the open circuit potential, which are consistent with the oxidation from Fe(II) to Fe(III). From these data, the ferric versions of **6.2** and **6.6** were synthesized by the addition of excess silver triflate in acetonitrile. For the dinuclear complexes, **6.6** and **6.7**, multiple redox processes are observed for the $\text{Fe}^{\text{II}}/\text{Fe}^{\text{III}}$ couple which is consistent with the formation of the mixed-valent monooxidized species $[\text{Fe}^{\text{II}}\text{Fe}^{\text{III}}]$ and the monovalent doubly oxidized $[\text{Fe}^{\text{III}}\text{Fe}^{\text{III}}]$. These fully reversible waves are centered at -0.56 and -0.67 V vs Fc^+/Fc ($\Delta E_{1/2} = 0.11\text{ V}$) with a peak-to-peak separation of 0.08 V for both events.

Scheme 6.1. Syntheses of complexes **6.1–6.7**.



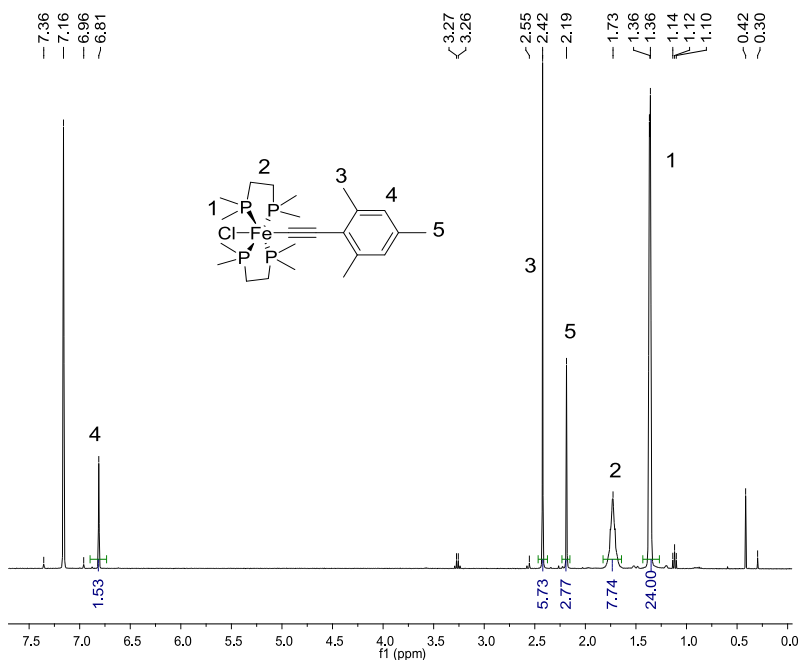


Figure 6.1. ^1H NMR of **6.2** in C_6D_6 . The resonances at 3.26 and 1.12 ppm are due to trace amounts of diethyl ether. The resonance at 0.42 ppm is due to trace amounts of water and 0.3 ppm is due to silicone grease.

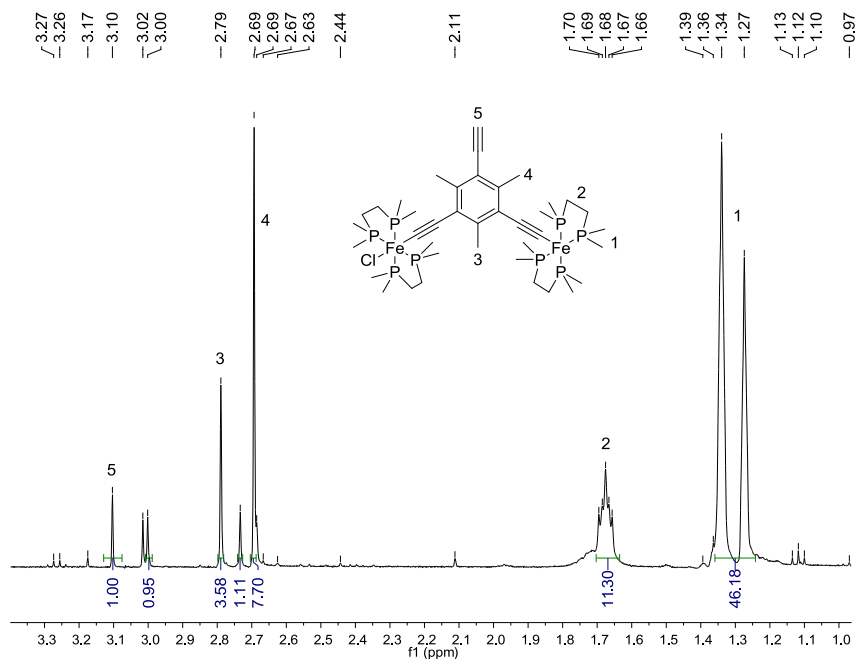


Figure 6.2. ^1H NMR of **6.4** in C_6D_6 . The resonances at 3.26 and 1.12 ppm are due to trace amounts of diethyl ether. The resonance at 3.02 ppm is due to trace amounts of methanol. Resonances at 3.00 and 2.74 ppm are presumed to be due to the mononuclear species.

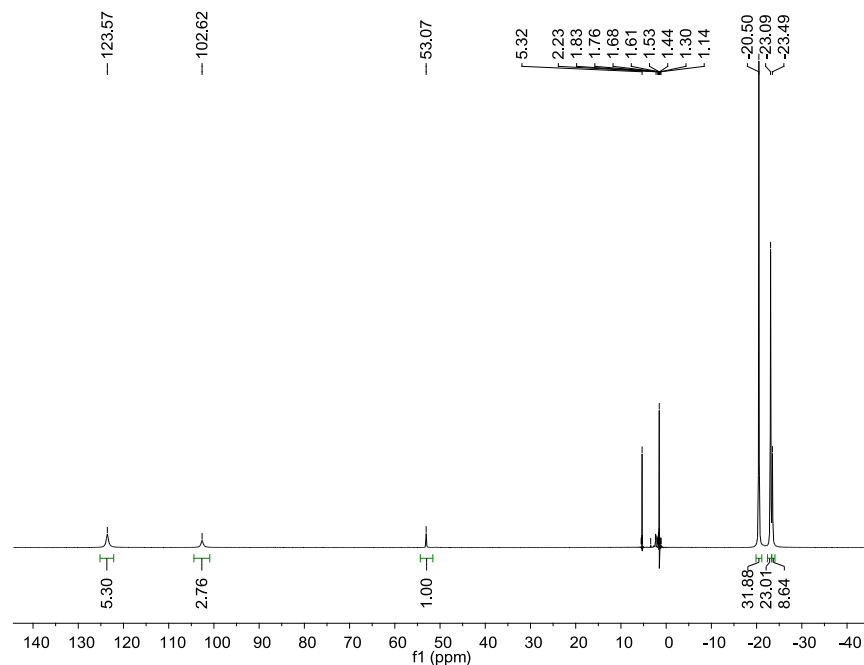


Figure 6.2. ^1H NMR of **6.7** in CD_2Cl_2 . The resonance at 1.53 ppm is due to trace water.

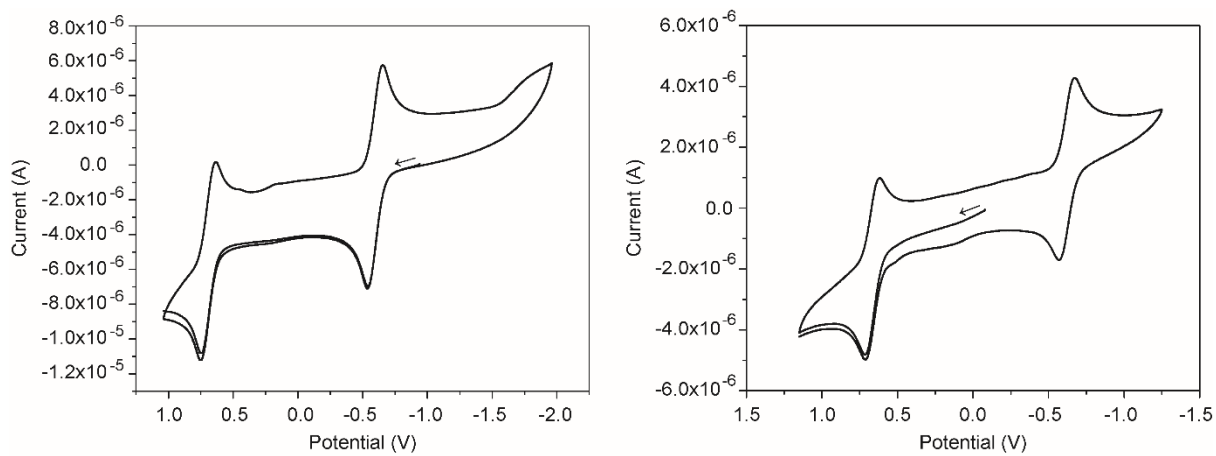


Figure 6.3. Cyclic voltammograms of **6.2** (left) and **6.3** (right) in 0.1 M $(\text{Bu}_4\text{N})\text{PF}_6$ in CH_2Cl_2 at a scan rate of 100 mV/s. Potentials are referenced versus Fc/Fc^+ . The arrows indicate scan direction.

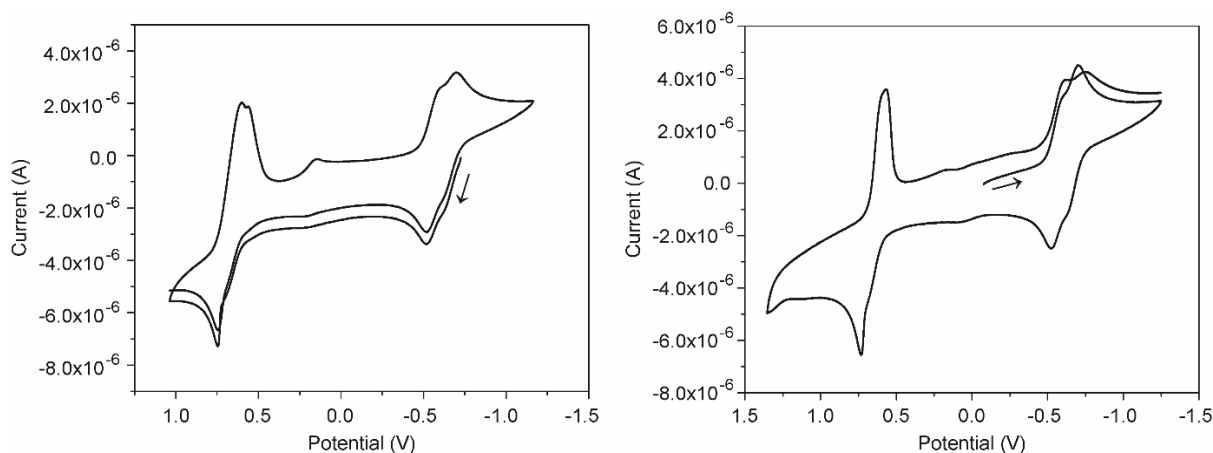


Figure 6.4. Cyclic voltammograms of **6.6** (left) and **6.7** (right) in 0.1 M (Bu₄N)PF₆ in CH₂Cl₂ at a scan rate of 100 mV/s. Potentials are referenced vs Fc/Fc⁺. The arrows indicate scan direction.

6.4.2 X-ray Structures. Structural analyses of the triflate salts of **6.1**, **6.3**, and **6.7** were performed at 120 K. All three complexes possess distorted octahedral coordination environments around the Fe center. The four equatorial positions are occupied by phosphorous atoms from the bidentate dmpe ligands while the axial positions are occupied by one chloride and the acetylide containing ligand (Figure 6.5).

The mononuclear mesitylene-based complex **6.3** crystallizes in *P*2₁2₁2₁, which is similar to the mononuclear benzene-based complex.^{18,39} The acetylide moiety is nearly linear with a C≡C–Fe angle of 175.5°. Comparison to the benzene derivative shows that inclusion of the methyl groups to the aromatic ring appears to elongate the ring–β carbon bond from 1.432[2] Å to 1.445[4] Å for **6.3** (Table 6.2). While the acetylide is similar lengths between the two, the C≡C–Fe distance is also elongated, 1.875[1] Å versus 1.891[3] Å for **6.3**. In addition, the torsion angle, φ , defined by a centroid between the phosphorous atoms of dmpe, the Fe center, and two carbon atoms of the aromatic ring, is 3.02°. This is significantly less twisted than what is observed for [(dmpe)₂FeCl(CCPh)](OTf) (12.39°). At least structurally, this supports the hypothesis that inclusion of the steric bulk imparted by the methyl groups on the aromatic ring should decrease the twist the dmpe moieties show with respect to the aromatic ring.

The structure of **6.7** shows the desired dinuclear species bridged through the diethynylmesitylene moiety. The intramolecular distance between the metal centers is 10.324(1) Å, which is comparable to what has been measured for the trinuclear TEM-based complex.²⁷ Similar to the mononuclear species, a slight bend is observed in the acetylide linkage with C–C–Fe angles of 177.8° for Fe1 and 174.6° for Fe2. The previously described torsion angle, φ , is close to 0°, 3.70° for Fe1 and 2.81° for Fe2, with no rotational disorder observed of the dmpe ligands. There is some disorder of the ethylene bridge of the dmpe ligands of Fe2, but this disorder appears to have little impact on the phosphorus atoms of the ligand.

The shortest *intermolecular* distances between complex cations is 9.4856(8) Å, which is significantly shorter than the *intramolecular* distance between the Fe centers. The cations pack such that the [(dmpe)₂FeCl]⁺ portion of the cation sits over the aromatic ring of an adjacent complex (Figure 6.6), which is similar to [(dmpe)₆Fe₃Cl₃(μ_3 -TEM)](OTf)₃.²⁷ The shortest distance between the aromatic ring and an adjacent complex cation (3.553(7) Å) occurs through the methyl group of the dmpe. Additionally, interactions between the methyl groups of the dmpe ligands and the SO₃ group of the triflate anions are noted along the *a* axis, with the shortest interaction of 3.32(3) Å. Comparison of similar interactions of the TEB-based complex shows that interactions between the dmpe ligand and the anion occurs through the ethylene bridge, as these ligand are twisted out of registry from the π -system of the bridging ligand. This adds further evidence that the addition of the methyl groups to the aryl ring imparts the proper steric bulk to stabilize the desired torsion of the dmpe ligands with respect to the aryl π -system.

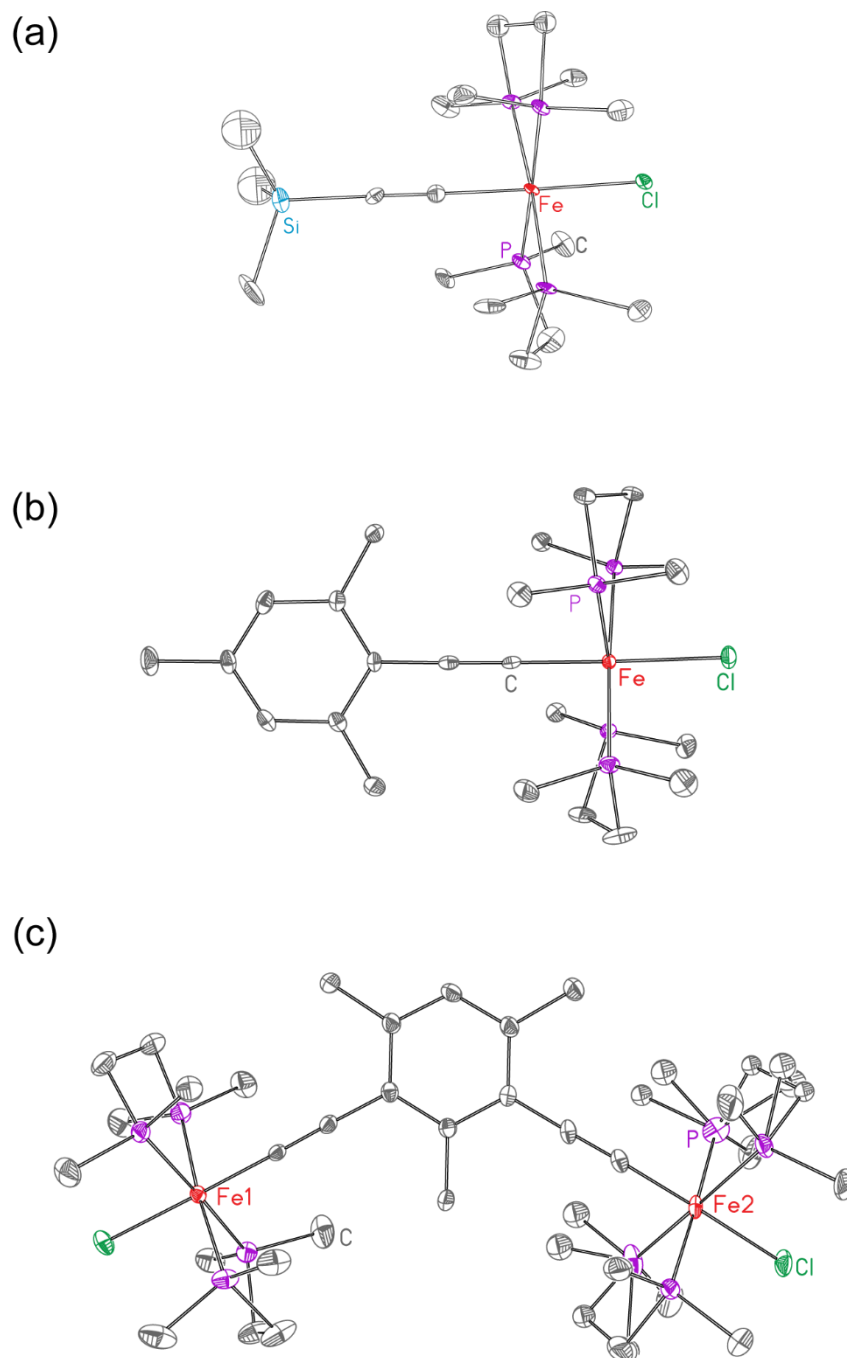


Figure 6.5. X-ray crystal structures of the complex cations of **6.1** (a), **6.3** (b), and **6.7** (c). Fe, C, P, and Cl atoms are represented by red, gray, purple, green respectively. Thermal ellipsoids are rendered at 40% probability. Hydrogen atoms were omitted for clarity.

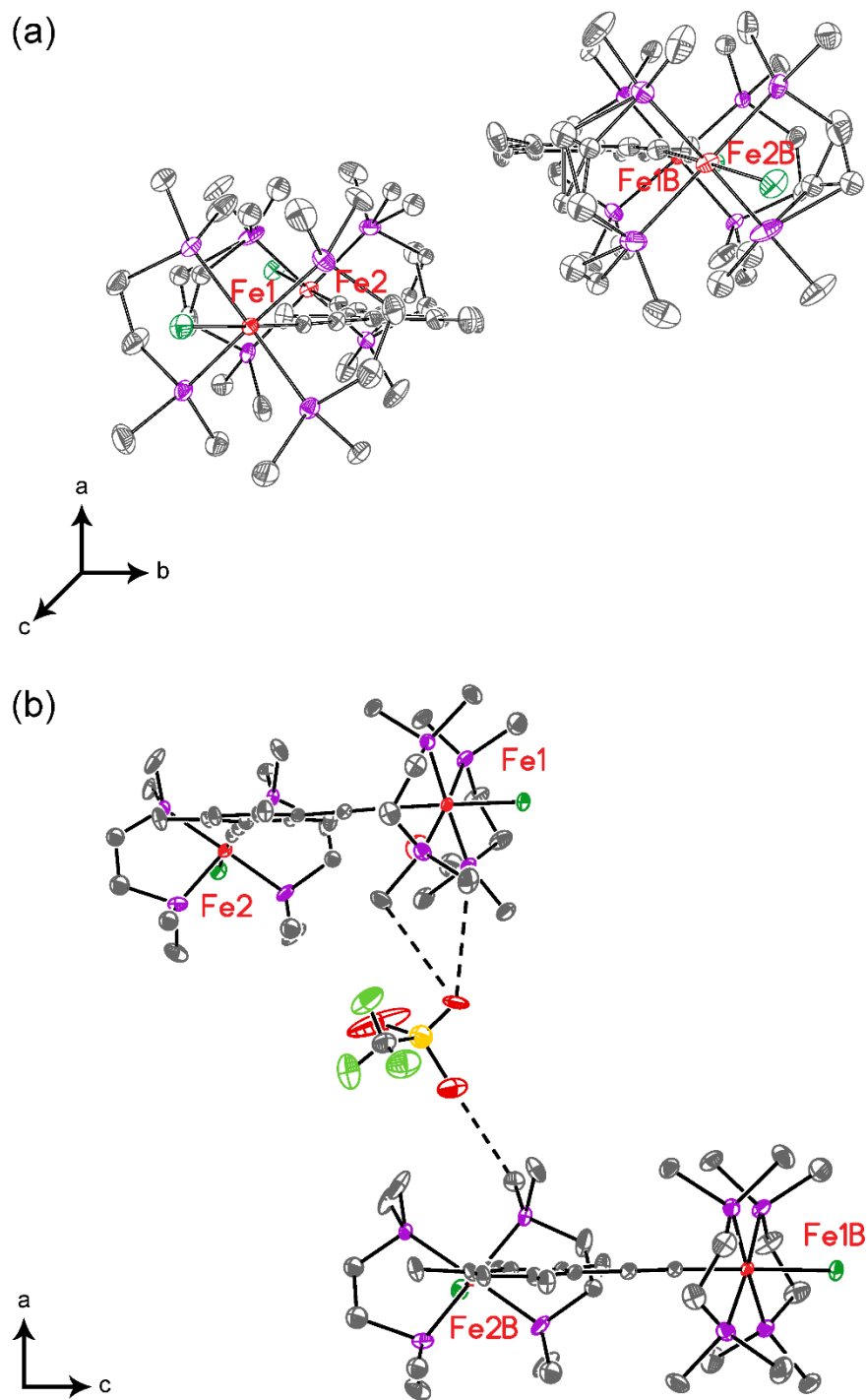


Figure 6.6. Packing diagrams for **6.7** viewed down the *c* axis (a), and viewed down the *b* axis (b). Fe, C, P, O, Cl, S, and F atoms are represented by red, gray, purple, red, dark green, orange, and light green, respectively. Dashed lines represent closest intermolecular contacts between the complex cations and triflate anion. Hydrogen atoms, atoms labels, and disordered components for (b) have been omitted for clarity.

Table 6.2. Comparison of structural components of [(dmpe)₂FeCl(MEM)](OTf) (**6.3**), [(dmpe)₂FeCl(CCPh)](OTf), [(dmpe)₄Fe₂Cl₂(μ₂-*m*-DEM)](OTf)₂ (**6.7**) and [(dmpe)₄Fe₂Cl₂(μ₂-*m*-DEB)](BAR^F)₂.

	6.3	[(dmpe) ₂ FeCl(CCPh)](OTf) ¹⁸	6.7	[(dmpe) ₄ Fe ₂ Cl ₂ (μ ₂ - <i>m</i> -DEB)](BAR ^F) ¹⁸
Fe–C(α) (Å)	1.891(3)	1.875(1)	1.886(4), 1.888(4)	1.95(2), 1.89(1)
C(α)≡C(β) (Å)	1.218(4)	1.219(2)	1.216(6), 1.218(6)	1.08(2), 1.20(2)
C(β)–C _{ring} (Å)	1.445(4)	1.432(2)	1.438(6), 1.441(6)	1.42(2), 1.42(2)
φ (°)	3.0	12.4	3.7, 2.8	~21, 86 ^a
Fe–C(α)–C(β) (°)	175.5	176.6	177.8, 174.6	172, 179
Fe1⋯Fe2 (Å)	N/A	N/A	10.324(1)	10.490(3)
Fe⋯Fe (Å) ^b	8.8158(8)		9.4856(8)	7.471(2)

^a Estimated from [(dmpe)₆Fe₃Cl₃(μ₃-TEB)](OTf)₃.

^b Shortest Fe⋯Fe distance observed.

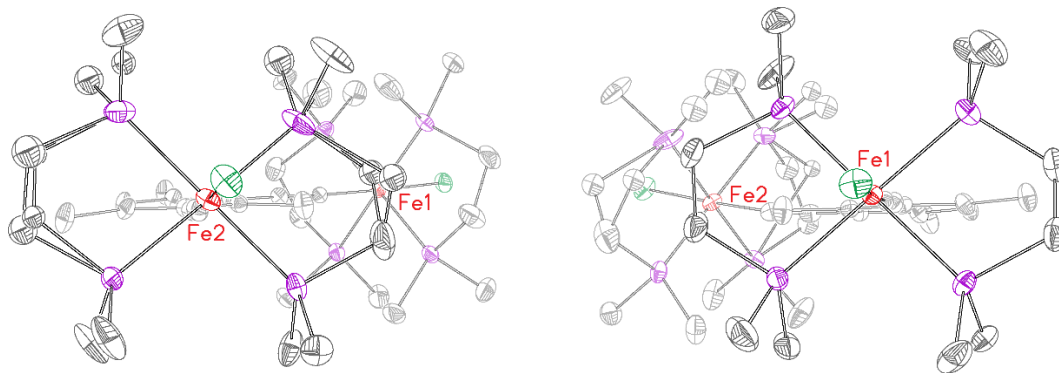


Figure 6.7. X-ray structure of the complex cation of **6.7** viewed down the Cl–Fe2–C axis (left) and down the Cl–Fe1–C axis (right). Fe, C, P, and Cl atoms are represented by red, gray, purple, green respectively. Thermal ellipsoids are rendered at 40% probability. Hydrogen atoms were omitted for clarity.

A structure for complex **6.1** was collected and sufficient to establish connectivity. Unfortunately, the quality of the data is poor (presumably due to twinning or cracking of the crystal during data collection). Accounting for the twinned component(s) using CELL_NOW³⁴ did improve the solution, but still prevents rigorous analysis of the relevant bond lengths and angles.

6.4.3 Magnetic Properties. Solid-state variable temperature magnetic susceptibility measurements were performed on the paramagnetic Fe(III) species **6.1**, **6.3**, and **6.7**. The data are shown in Figures 6.7–6.9. To test for the presence of ferromagnetic impurities, magnetization of the sample at 100 K was measured. In the case of a non-linear M vs H curve, the sample was tested under 5000 Oe applied dc field. This was done in an attempt to quench the influence of these impurities on the magnetic susceptibility of the sample, especially at high temperatures (> 100 K).

For the mononuclear complexes **6.1** and **6.3** (Figures 6.8 and 6.9, respectively), the $\chi_{\text{M}}T$ values at 300 K are similar, $0.73 \text{ cm}^3 \cdot \text{K} \cdot \text{mol}^{-1}$ and $0.69 \text{ cm}^3 \cdot \text{K} \cdot \text{mol}^{-1}$, respectively. With decreasing temperatures, the $\chi_{\text{M}}T$ values decrease almost linearly for both complexes down to 2 K, where these values reach their minimums of $0.45 \text{ cm}^3 \cdot \text{K} \cdot \text{mol}^{-1}$ and $0.44 \text{ cm}^3 \cdot \text{K} \cdot \text{mol}^{-1}$, respectively. These low temperature values are higher than is expected from a $S = 1/2$ system with $g = 2$, but are comparable to what has been reported for similar mononuclear $[(\text{dmpe})_2\text{FeCl}(\text{CC}-\text{X})]^+$ ($\text{X} = \text{Ph}, \text{TMS}$) complexes.^{18,38} The small downturn in susceptibility at low temperature is attributed to weak intermolecular antiferromagnetic coupling. Since the samples of **6.1** and **6.3** were measured under 5000 Oe field to saturate the magnetization of the ferromagnetic impurities, the linear increase in $\chi_{\text{M}}T$ and higher than expected values at room temperature are attributed to temperature independent paramagnetism (TIP). When the applied field is increased to 10,000 Oe, the high temperature data overlay with the data collected at 5000 Oe, indicating the increase in susceptibility is intrinsic to the compound.

Measurement of the solid-state magnetic susceptibility of **6.7** from 2 to 300 K produces a $\chi_{\text{M}}T$ value of $1.21 \text{ cm}^3 \cdot \text{K} \cdot \text{mol}^{-1}$ at 300 K (Figure 6.10). The $\chi_{\text{M}}T$ value at 300 K is greater than what is expected for two uncoupled $S = \frac{1}{2}$ centers with $g = 2$ (expect $0.75 \text{ cm}^3 \cdot \text{K} \cdot \text{mol}^{-1}$). With decreasing temperature, this value decreases, reaching a minimum of $1.09 \text{ cm}^3 \cdot \text{K} \cdot \text{mol}^{-1}$ at 90 K. A slight increase occurs at temperatures below 90 K, maximizing to a value of $1.16 \text{ cm}^3 \cdot \text{K} \cdot \text{mol}^{-1}$ at 7 K, then decreasing to $1.15 \text{ cm}^3 \cdot \text{K} \cdot \text{mol}^{-1}$ by 2 K. This increase at low temperatures is attributed to intramolecular ferromagnetic coupling between the metal centers. Similar to what is observed for the mononuclear complexes **6.1** and **6.3**, the higher than expected $\chi_{\text{M}}T$ values are attributed to unquenched orbital angular momentum. In this case, the M vs H plot collected at 100 K (inset, Figure 6.10) is linear and thus the amount of ferromagnetic impurities have been minimized.

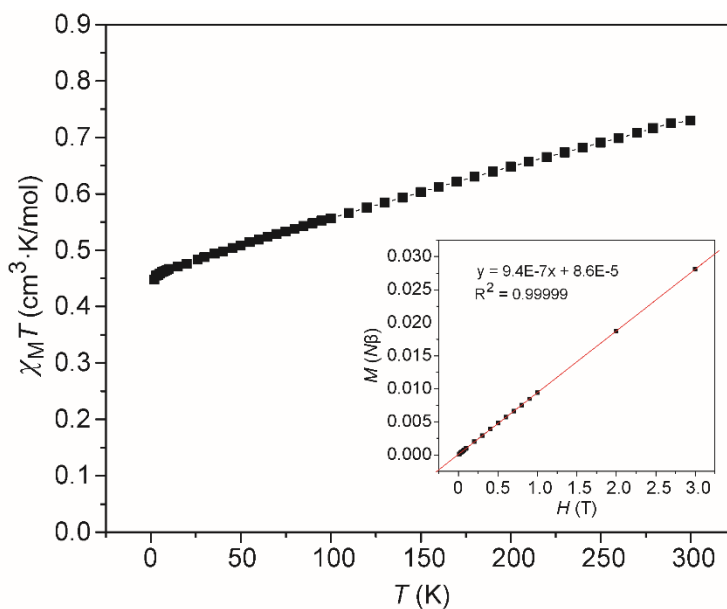
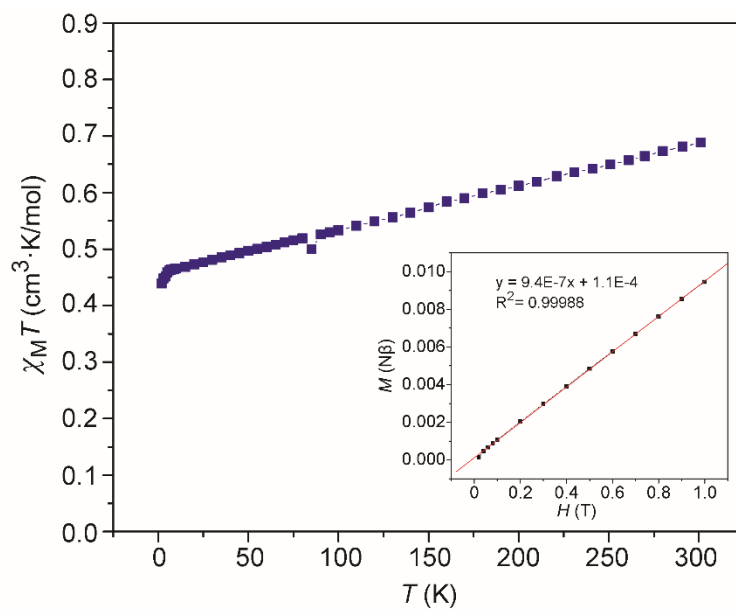


Figure 6.8. Temperature dependent magnetic susceptibility data for **6.1** collected at 5000 Oe. Inset: Magnetization data for **6.1** collected at 100 K.



Figures 6.9. Temperature dependent magnetic susceptibility data for **6.3** collected at 5000 Oe. Inset: Magnetization data for **6.3** collected at 100 K.

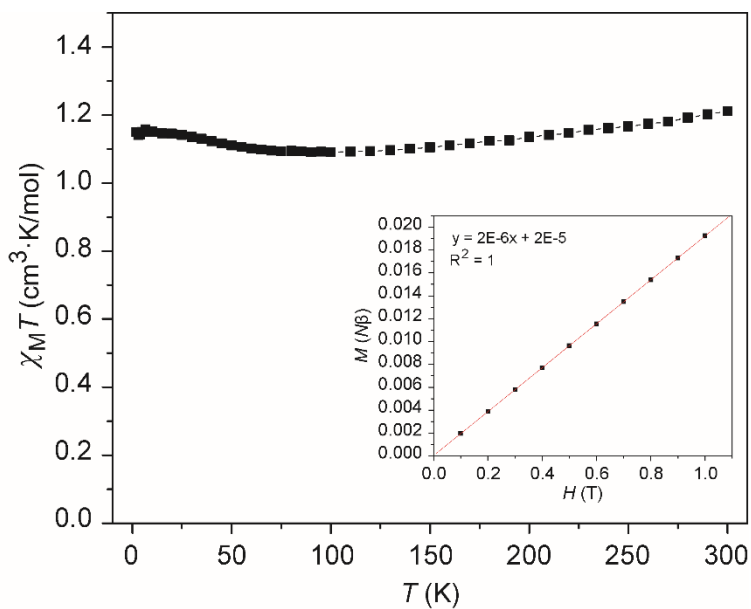


Figure 6.10. Temperature dependent magnetic susceptibility data for **6.7** collected at 1000 Oe. Inset: Magnetization data for **6.7** collected at 100 K.

Electron paramagnetic resonance (EPR) spectra were obtained for **6.1**, **6.3**, **6.7**, and $[(\text{dmpe})_6\text{Fe}_3\text{Cl}_3(\mu_3\text{-TEM})](\text{OTf})_3$ (Figures 6.11–6.14). The Fe(III) salts were chosen, as the low spin diamagnetic Fe(II) species are EPR silent. In order to make a direct comparison to the benzene derivatives, the data were collected as frozen glasses in 1:1 dichloromethane:dichloroethane at 100 K. In all cases, the spectra show a similar shape: a half field transition centered at 1500 G corresponds to the $\Delta m = 1$ transition⁴⁰ and a broad rhombic signal centered around 3300 G corresponds to a g value of approximately 2. The spectra for **6.7** and $[(\text{dmpe})_6\text{Fe}_3\text{Cl}_3(\mu_3\text{-TEM})](\text{OTf})_3$ are complicated by exchange interactions. Extraction of the g values for the mononuclear complexes **6.1** and **6.3** give g_{iso} values of 2.16 ($g_1 = 1.83$, $g_2 = 1.95$, and $g_3 = 2.70$) (Figure 6.11) and 2.16 ($g_1 = 1.89$, $g_2 = 2.00$, $g_3 = 2.58$) (Figure 6.12), respectively.

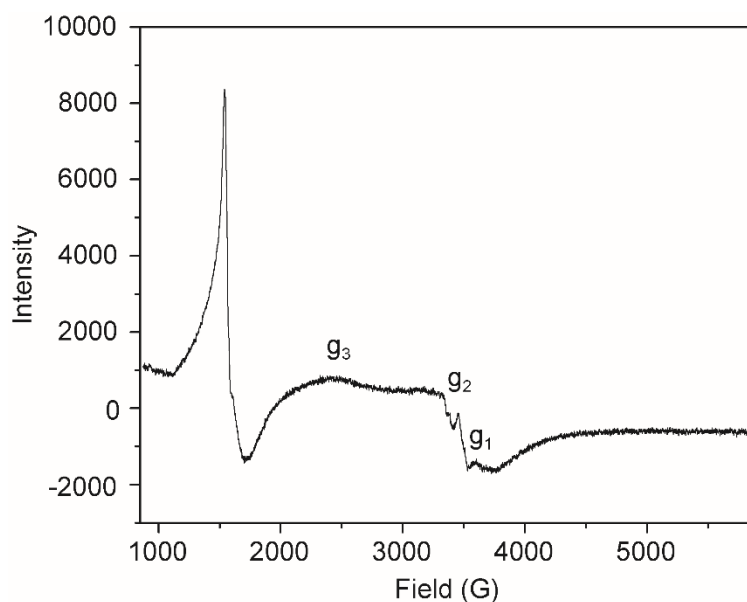


Figure 6.11. X-band EPR spectrum of **6.1** in a dichloromethane:dichloroethane glass at 100 K.

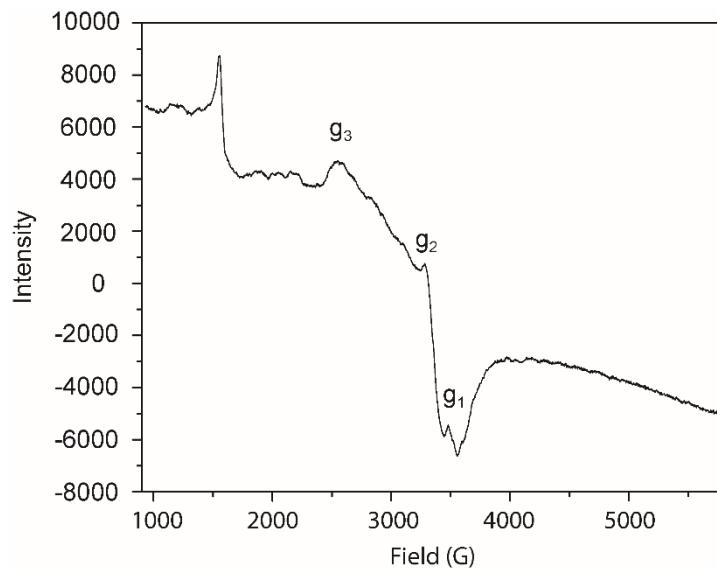


Figure 6.12. X-band EPR spectrum of **6.3** in a dichloromethane:dichloroethane glass at 100 K.

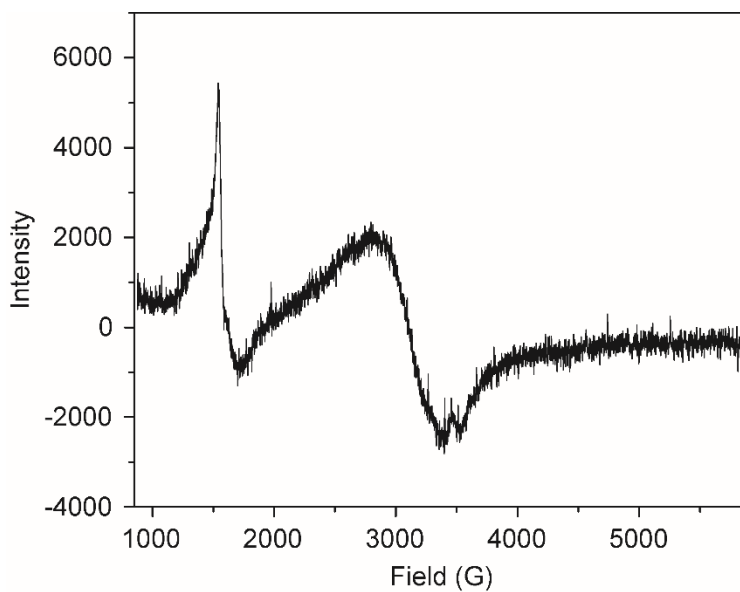


Figure 6.13. X-band EPR spectrum of **6.7** in a dichloromethane:dichloroethane glass at 100 K.

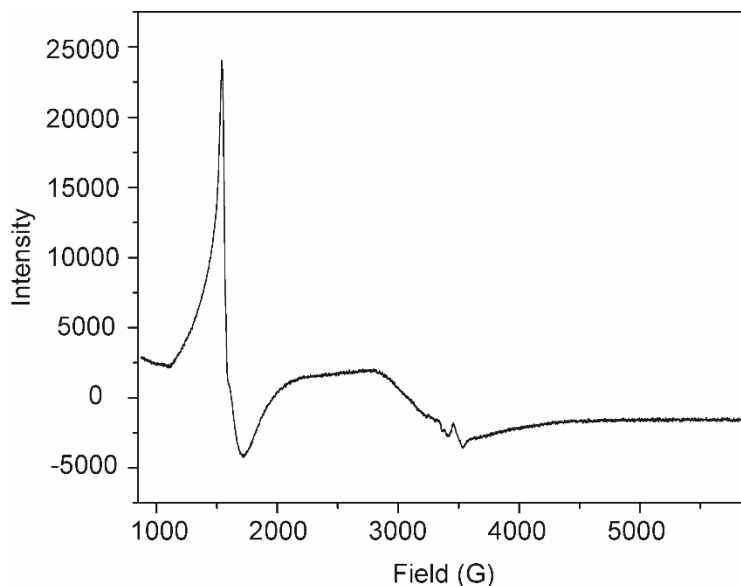


Figure 6.14. X-band EPR spectrum of $[(\text{dmpe})_6\text{Fe}_3\text{Cl}_3(\mu_3\text{-TEM})](\text{OTf})_3$ in a dichloromethane:dichloroethane glass at 100 K.

6.5.3 Fitting of Magnetic Data. Fittings of the solid-state variable temperature magnetic susceptibilities for the mononuclear complexes, **6.1** and **6.3**, for g , TIP, and mean-field correction for weak intermolecular coupling (θ) were performed (Figures 6.15 and 6.16). From these analyses, lines of best fit for these data provided g values of 2.22 and 2.21 for **6.1** and **6.3**, respectively. This value is an average for all temperatures and thus is presumably high due to the large susceptibility values determined at high temperature. Significant temperature independent paramagnetism has been extracted from the fits of these complexes, with values of 9.262×10^{-4} and 7.652×10^{-4} emu for **6.1** and **6.3**, respectively. Removal of the TIP component to the magnetic susceptibility significantly reduces the $\chi_{\text{M}}T$ values determined for the mononuclear complexes at 300 K down to $0.46 \text{ cm}^3 \cdot \text{K} \cdot \text{mol}^{-1}$ for both **6.1** and **6.3**. Additionally, the application of a mean-field approximation to these data provides θ values of -0.066 K for **6.1** and -0.057 K for **6.3**, indicative of weak intermolecular antiferromagnetic coupling.

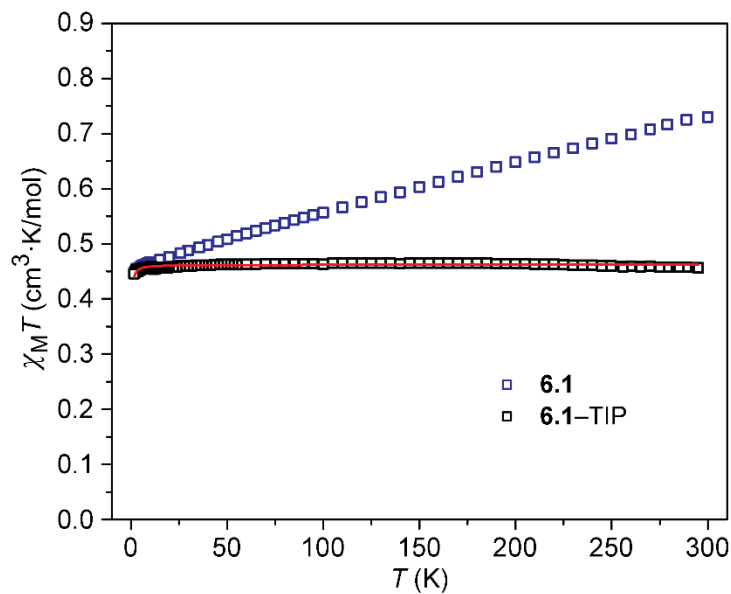


Figure 6.15. Raw (blue squares) and TIP-corrected (black squares) magnetic susceptibility data for **6.1**. Red line is best fit.

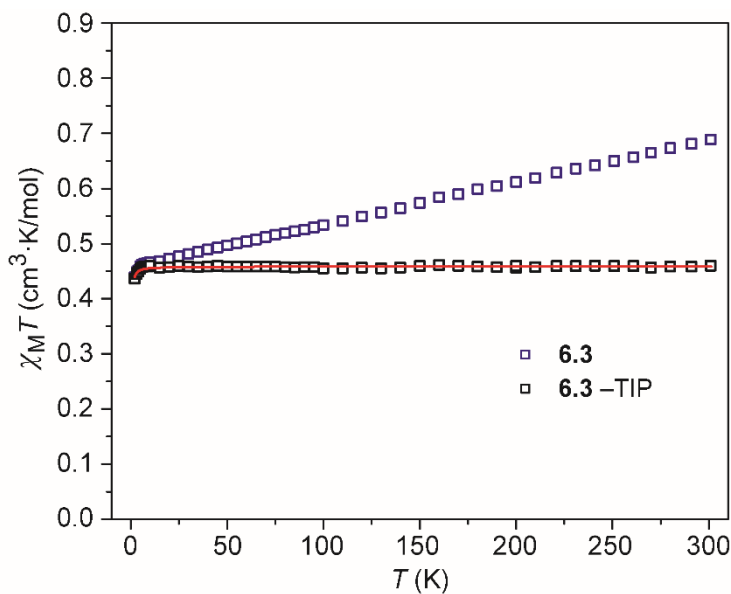


Figure 6.16. Raw (blue squares) and TIP-corrected (black squares) magnetic susceptibility data for **6.3**. Red line is best fit.

Multiple methods of data interpretation of the magnetic data for **6.7** have been employed. The first method (Model 1) attempted to fit the magnetic data as is using julX.³⁶ From this fit, taking into account potential TIP contributions to the magnetic properties at high temperatures and constraining $g = 2.15$, values of $J = 23 \text{ cm}^{-1}$, $\text{TIP} = 9.88 \times 10^{-4} \text{ emu}$ ($f_{\text{sum}} = 0.00769$) were determined (Figure 6.17). The coupling constant value lies between the values determined for the PF_6^- and BArF_4^- salts of $[(\text{dmpe})_4\text{Fe}_2\text{Cl}_2(\mu\text{-}m\text{-DEB})]^{2+}$ of 11^{38} and 41 cm^{-1} , respectively, and is in good agreement with the DFT-calculated exchange coupling value.¹⁸ The TIP contribution is in line with the TIP value determined from the mononuclear complexes.

A second fitting scheme (Model 2) was attempted in order to separate the exchange contributions to the magnetic properties from TIP and unquenched orbital angular momentum, which was previously employed for the benzene-based complexes. This analysis was performed by removing the orbital contribution of the Fe(III) centers by: subtracting two equivalents for the susceptibility of **6.1** maintaining the TIP contribution, then adding the ligand contribution (difference between the susceptibility values of **6.1** and **6.3**) and spin-only value for two $S = \frac{1}{2}$ with $g = 2.17$. From this subtraction, a new room temperature magnetic susceptibility value was determined to be $0.68 \text{ cm}^3 \cdot \text{K} \cdot \text{mol}^{-1}$ (Figure 6.18). This value is similar to what is reported by Berben after a comparable subtraction scheme was applied to the dinuclear benzene derivative $[(\text{dmpe})_4\text{Fe}_2\text{Cl}_2(\text{DEB})](\text{PF}_6)_2$,³⁸ but substantially lower than what is observed when this subtraction scheme is applied by Hoffert with $[(\text{dmpe})_4\text{Fe}_2\text{Cl}_2(\text{DEB})](\text{OTf})_2$.¹⁸ Attempts to fit these data produced poor fits if TIP was not included. When TIP was included into the fit and g constrained to 2.15, a J value of 16 cm^{-1} was determined with a TIP contribution of $-1.52 \times 10^3 \text{ emu}$ ($f_{\text{sum}} = 0.00182$) (Figure 6.18).

Fitting the linear portion at high temperature of the χ^{-1} vs T plot without the subtraction for TIP or the orbital contribution for the dinuclear complex **6.7** with a mean-field approximation from 150 – 300 K provides a θ value of -34 cm^{-1} or -24 K (Figure 6.19). This value is complicated by potential intermolecular antiferromagnetic coupling as well as the significant orbital contribution to the magnetic susceptibility. When a similar fit is applied to $[(\text{dmpe})_4\text{Fe}_2\text{Cl}(\mu_2\text{-}m\text{-DEB})](\text{OTf})_2$, a θ value of -100 K is determined. Possible reasons for these differences between the DEB and DEM are: (1) the electron-donating nature of the methyl groups is altering the electronic structure of the bridging ligand or (2) ferromagnetic impurities present in the DEB and TEB samples lead to higher than anticipated $\chi_{\text{M}}T$ values at room temperature.

Table 6.3. Attempted fitting scenarios for **6.7**. “TW temp” is a mean-field correction for weak intermolecular magnetic exchange. “ f_{sum} ” value is the sum of the point-by-point squared errors.

	g	J (cm^{-1})	TIP ($1 \times 10^{-6} \text{ cm}^3$)	TW temp (K)	D (cm^{-1})	E/D (cm^{-1})	f_{sum}
1	2.15 ^a	23.261	988.8	N/A	N/A		0.00769
2	2.15 ^a	23.603	986.8	-0.063	N/A		0.004956
3	2.15 ^a	23.599	987.0	-0.063	-1.601, -1.803	0.002, 0.002	0.004956
4	2.15 ^a	23.599	987.0	-0.063	-118.57, -135.57	35.675, 44.478	0.004956
5	2.113, 2.154	26.850	1013.7	0.014			0.003669
6	2.13 ^a	28.583	998.0 ^a	N/A	11.594, 10.602	0.282, 0.164	0.005104
7	2.13 ^a	28.583	998.0 ^a	N/A	1.159, 1.060	0.282, 0.164	0.005104
8	2.13 ^a	27.760	998.0 ^a	N/A	10.00 ^a	0.330 ^a	0.005559
9	2.13 ^a	28.583	998.0 ^a	N/A	-115.94, -106.02	0.282, 0.164	0.005104
10	2.130, 2.137	26.873	1014.0	0.014	-109.82, -131.733	0.245, 0.256	0.00367

^a Parameter constrained

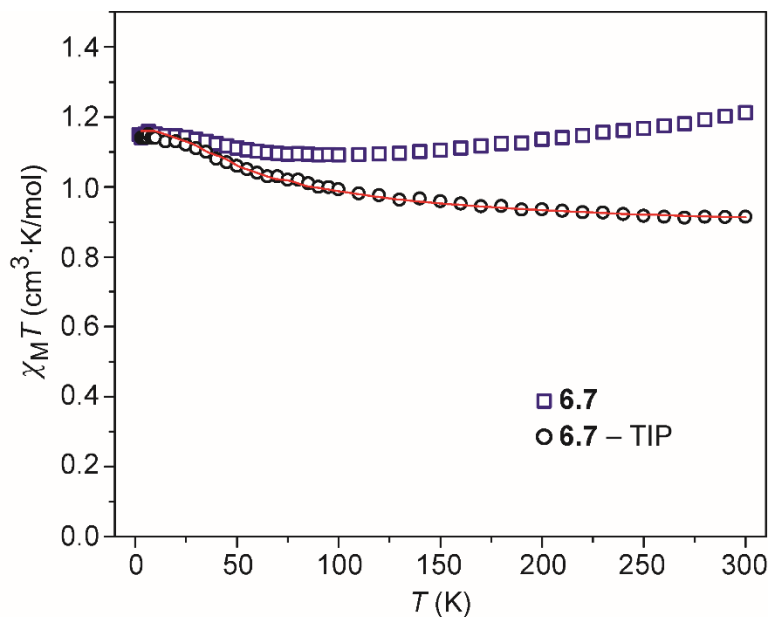


Figure 6.17. Raw (blue squares) and TIP-corrected (black circles) magnetic susceptibility data for **6.7** with best fit from J model (model 1). Red line is best fit.

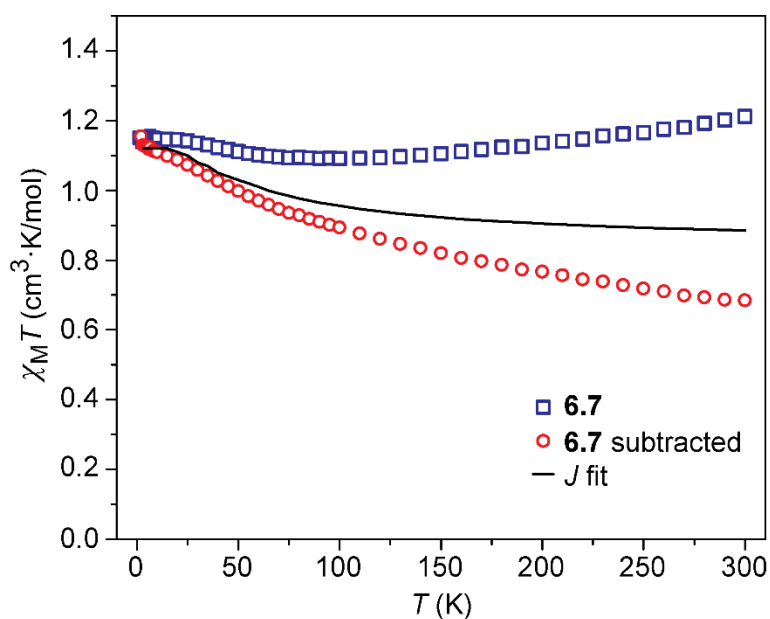


Figure 6.18. Raw (blue squares) and subtracted (red circles) magnetic susceptibility data for **6.7** with best fit from J model (model 2). Black line is best fit of data.

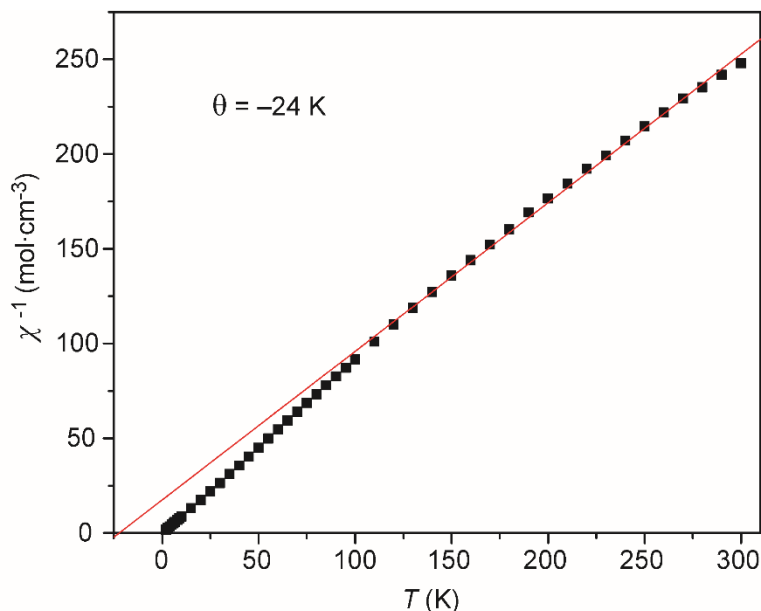


Figure 6.19. Weiss plot of **6.7**. Linear regression was calculated from data between 100 and 300 K. The Curie constant was determined to be $1.3 \text{ cm}^3 \cdot \text{K} \cdot \text{mol}^{-1}$.

Low temperature magnetization data under dc fields up to 5 T were collected for **6.7** and $[(\text{dmpe})_6\text{Fe}_3\text{Cl}_3(\mu_3\text{-TEM})](\text{OTf})_3$. These data support the assignment of an $S = 1$ ground state for **6.7**, as the magnetization saturates at approximately $2 \mu_B$ (Figure 6.20). Similarly, for $[(\text{dmpe})_6\text{Fe}_3\text{Cl}_3(\mu_3\text{-TEM})](\text{OTf})_3$, the assignment of an $S = 3/2$ ground state is supported by the saturation of the magnetization at approximately $3 \mu_B$ (Figure 6.21). The overlaying isofield lines from the magnetization data indicate that these systems possess little magnetic anisotropy. Attempts were made to fit these data using ANISOFIT 2.0 to extract D and $|E|/D$ values for both species. The best fit of the data provided D and $|E|/D$ values of -1.35 cm^{-1} and $1.8 \times 10^{-4} \text{ cm}^{-1}$, respectively for **6.7**. A similar fitting procedure was performed for $[(\text{dmpe})_6\text{Fe}_3\text{Cl}_3(\mu_3\text{-TEM})](\text{OTf})_3$ and cyclic permutations of the D and E components as described in Chapter 5 produced a value of -0.96 cm^{-1} for D and 0.17 cm^{-1} for $|E|/D$ values. Attempts to fit the variable temperature susceptibility data of **6.7** for D and $|E|/D$ using various starting parameters did improve the fit, but in some cases gave unreasonably large D values (Table 6.3).

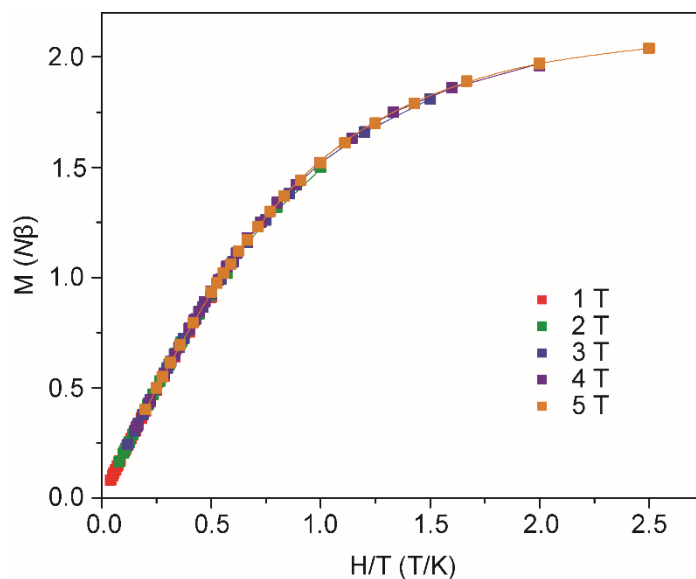


Figure 6.20. Magnetization versus reduced field data for **6.7**. The lines are of best fit obtained from fitting using ANISOFIT 2.0.

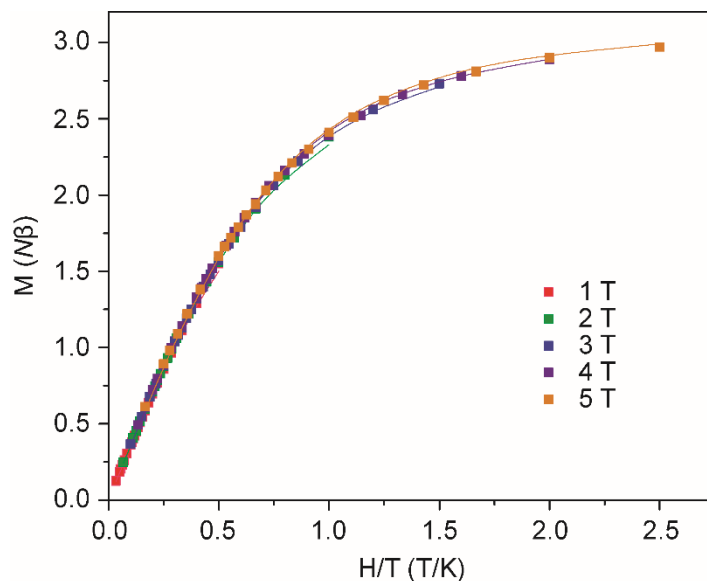


Figure 6.21. Magnetization versus reduced field data for $[(dmpe)_6Fe_3Cl_3(\mu_3-TEM)](OTf)_3$. The lines are of best fit obtained from fitting using ANISOFIT 2.0.

6.6 Conclusions.

A series of $[(\text{dmpe})_2\text{FeCl}]^+$ complexes bridged by ethynylmesitylene-containing ligands has been synthesized and characterized. Mononuclear complexes of $[(\text{dmpe})_2\text{FeCl}(\text{CCTMS})](\text{OTf})$ (**6.1**) and $[(\text{dmpe})_2\text{FeCl}(\text{MEM})](\text{OTf})$ (**6.3**) have been synthesized to model the orbital contribution of the ligand to the magnetic susceptibility. Variable temperature magnetic measurements of the mononuclear complexes display an $S = 1/2$ spin state with temperature independent paramagnetism at high temperatures. The dinuclear complex, $[(\text{dmpe})_4\text{Fe}_2\text{Cl}(\mu_2\text{-}m\text{-DEM})](\text{OTf})_2$ (**6.7**), displays magnetic properties consistent with an isotropic $S = 1$ species at low temperature. Modeling of the variable temperature magnetic susceptibility data of **6.7** with and without subtraction indicate an increase in the exchange coupling between the metal centers: with subtraction, $J = 16 \text{ cm}^{-1}$, and without $J = 23 \text{ cm}^{-1}$. These values agree with the values determined by DFT calculations performed for a dinuclear meta-bridged complex with minimization of the dmpe torsion angle. Structural comparison of the benzene-bridged and mesitylene-bridged complexes indicate that the addition of the methyl groups to the aryl ring promotes the desired orientation of the dmpe with respect to the aryl π -system. This allows for better orbital overlap with the π -system of the aryl ring, promoting improved magnetic coupling between the metal centers.

6.7 Acknowledgements.

This work was supported by Colorado State University and NSF-CHE-1058889. The author would also like to thank Dr. Wesley Hoffert and Ethan Hill for preliminary work.

REFERENCES

- (1) Gatteschi, D. *Molecular nanomagnets*; Oxford University Press: Oxford; 2006.
- (2) Rinehart, J. D.; Long, J. R. *Chem. Sci.* **2011**, *2*, 2078.
- (3) Sessoli, R.; Powell, A. K. *Coord. Chem. Rev.* **2009**, *253*, 2328.
- (4) Meihaus, K. R.; Long, J. R. *Dalton Trans.* **2015**, *44*, 2517.
- (5) Rinehart, J. D.; Harris, T. D.; Kozimor, S. A.; Bartlett, B. M.; Long, J. R. *Inorg. Chem.* **2009**, *48*, 3382.
- (6) Aromi, G.; Brechin, E. K. *Struct. Bonding* **2006**, *122*, 1.
- (7) Glaser, T. *Chem. Commun.* **2011**, *47*, 116.
- (8) Curély, J.; Barbara, B. *Single-Molecule Magnets and Related Phenomena*; Winpenny, R., Ed.; Springer Berlin Heidelberg: 2006; Vol. 122.
- (9) De Montigny, F.; Argouarch, G.; Costuas, K.; Halet, J.-F.; Roisnel, T.; Toupet, L.; Lapinte, C. *Organometallics* **2005**, *24*, 4558.
- (10) Long, N. J.; Williams, C. K. *Angew. Chem. Int. Ed.* **2003**, *42*, 2586.
- (11) Low, P. J. *Coord. Chem. Rev.* **2013**, *257*, 1507.
- (12) McDonagh, A. M.; Humphrey, M. G.; Samoc, M.; Luther-Davies, B. *Organometallics* **1999**, *18*, 5195.
- (13) Packheiser, R.; Lohan, M.; Braeuer, B.; Justaud, F.; Lapinte, C.; Lang, H. *J. Organomet. Chem.* **2008**, *693*, 2898.
- (14) Le Narvor, N.; Lapinte, C. *Organometallics* **1995**, *14*, 634.
- (15) Weyland, T.; Lapinte, C.; Frapper, G.; Calhorda, M. J.; Halet, J.-F.; Toupet, L. *Organometallics* **1997**, *16*, 2024.
- (16) Weyland, T.; Costuas, K.; Mari, A.; Halet, J.-F.; Lapinte, C. *Organometallics* **1998**, *17*, 5569.
- (17) Field, L. D.; George, A. V.; Laschi, F.; Malouf, E. Y.; Zanello, P. *J. Organomet. Chem.* **1992**, *435*, 347.
- (18) Hoffert, W. A.; Rappe, A. K.; Shores, M. P. *J. Am. Chem. Soc.* **2011**, *133*, 20823.
- (19) Chow, H.-F.; Leung, C.-F.; Xi, L.; Lau, L. W. M. *Macromolecules* **2004**, *37*, 3595.
- (20) Vicente, J.; Chicote, M.-T.; Alvarez-Falcon, M. M.; Jones, P. G. *Organometallics* **2005**, *24*, 2764.
- (21) Onitsuka, K.; Yabe, K.-I.; Ohshiro, N.; Shimizu, A.; Okumura, R.; Takei, F.; Takahashi, S. *Macromolecules* **2004**, *37*, 8204.
- (22) Ohshiro, N.; Takei, F.; Onitsuka, K.; Takahashi, S. *J. Organomet. Chem.* **1998**, *569*, 195.
- (23) Ohshiro, N.; Takei, F.; Onitsuka, K.; Takahashi, S. *Chem. Lett.* **1996**, 871.

- (24) Onitsuka, K.; Fujimoto, M.; Ohshiro, N.; Takahashi, S. *Angew. Chem., Int. Ed.* **1999**, *38*, 689.
- (25) Onitsuka, K.; Fujimoto, M.; Kitajima, H.; Ohshiro, N.; Takei, F.; Takahashi, S. *Chem. - Eur. J.* **2004**, *10*, 6433.
- (26) Ohshiro, N.; Shimizu, A.; Okumura, R.; Takei, F.; Onitsuka, K.; Takahashi, S. *Chem. Lett.* **2000**, 786.
- (27) Fiedler, S. R., A study of magnetostructural parameters related to spin crossover and single-molecule magnetism. Ph.D., Colorado State University. Libraries, 2013.
- (28) Ohshiro, N.; Takei, F.; Onitsuka, K.; Takahashi, S. *J. Organomet. Chem.* **1998**, *569*, 195.
- (29) Ishihara, K.; Kobayashi, J.; Nakano, K.; Ishibashi, H.; Yamamoto, H. *Chirality* **2003**, *15*, 135.
- (30) Vicente, J.; Chicote, M. a. T.; Alvarez-Falcón, M. M.; Abrisqueta, M. a.-D.; Hernández, F. J.; Jones, P. G. *Inorg. Chim. Acta* **2003**, *347*, 67.
- (31) Girolami, G. S.; Wilkinson, G.; Galas, A. M. R.; Thorntonpett, M.; Hursthouse, M. B. *J. Chem. Soc., Dalton Trans.* **1985**, 1339.
- (32) *APEX 2*; Bruker Analytical X-Ray Systems, Inc: Madison, WI, 2008.
- (33) Sheldrick, G. M. *SHELXTL, Version 6.14*; Bruker Analytical X-Ray Systems, Inc.: Madison, WI, 1999.
- (34) Sheldrick, G. M. *CELL_NOW* University of Goettingen, 2003.
- (35) Bain, G. A.; Berry, J. F. *J. Chem. Educ.* **2008**, *85*, 532.
- (36) Bill, E. *julX*, 1.41; Max Planck Institute for Bioinorganic Chemistry: Mulheim an der Ruhr, 2008 (http://ewww.mpi-muelheim.mpg.de/bac/logins/bill/julX_en.php).
- (37) Shores, M. P.; Sokol, J. J.; Long, J. R. *J. Am. Chem. Soc.* **2002**, *124*, 2279.
- (38) Berben, L. A., Toward acetylido- and N-heterocycle-bridged materials with strong electronic and magnetic coupling. Ph.D., University of California, Berkeley, 2005.
- (39) Field, L. D.; George, A. V.; Hambley, T. W. *Inorg. Chem.* **1990**, *29*, 4565.
- (40) Abragam, A. *Electron paramagnetic resonance of transition ions*; Oxford University Press: Oxford, 2012.

APPENDIX 1. SUPPORTING INFORMATION FOR CHAPTER 2.

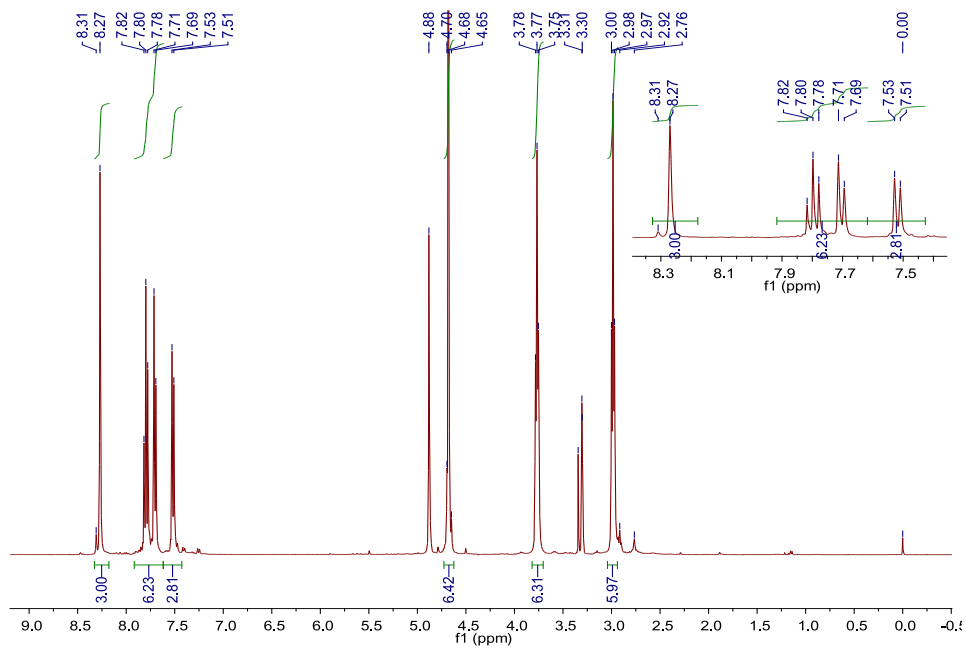


Figure A.1.1. ^1H NMR spectrum of $\text{L}^{6\text{-OH}}$ in CD_3OD at 400 MHz using TMS as the reference.

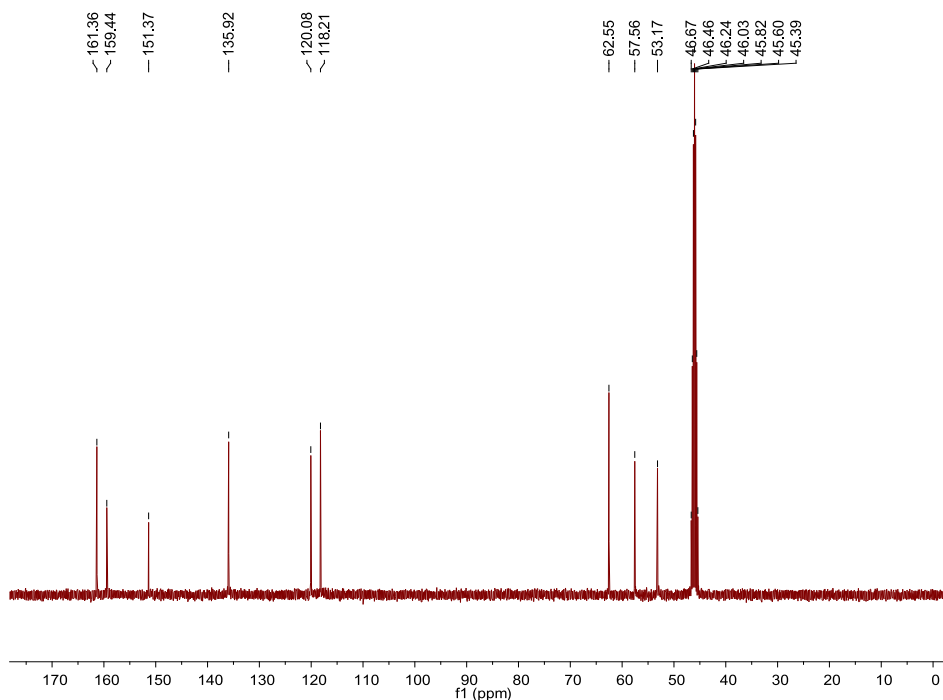


Figure A.1.2. ^{13}C NMR spectrum of $\text{L}^{6\text{-OH}}$ in CD_3OD , obtained on a 400 MHz NMR. Multiplet at 46 ppm is CD_3OD .

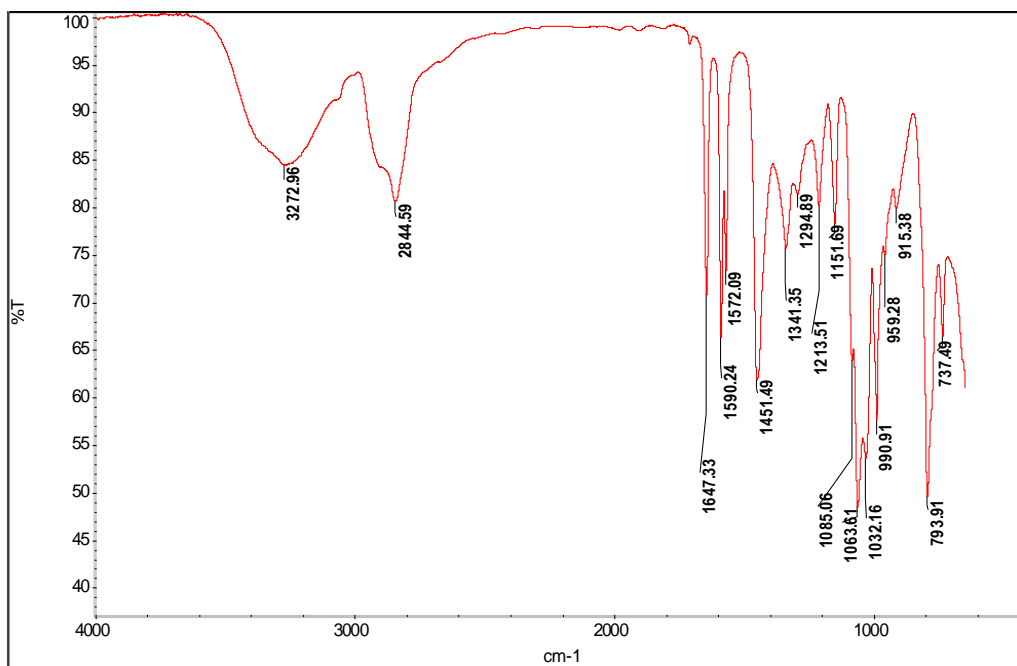


Figure A.1.3. FT-IR spectrum of L^{6-OH} obtained by pressing a solid sample on a ZnSe ATR crystal.

$[FeL^{6-OH}](BPh_4)_{1.75}Br_{0.25} \cdot MeCN$ (A.1.1). Carried out in a manner similar to the preparation of **2.4**, anion exchange of **2.2** (0.073 g, 0.102 mmol) into 6 mL of methanol with $NaBPh_4$ (0.140 g, 0.409 mmol) produced a light pink precipitate. The mixture was stirred for an additional 30 minutes, and then the solid was isolated by filtration. The resulting residue was triturated with methanol (2×6 mL) and 6 mL of Et_2O to produce a brick red, free flowing powder. Crystals were obtained by Et_2O diffusion into a concentrated acetonitrile solution (0.069 g, 58 % yield); X-ray quality crystals were not obtained by this method. IR (ATR) ν_{OH} 3509 cm^{-1} . λ_{max} (MeCN)/nm 489 ($1340\text{ M}^{-1}\cdot\text{cm}^{-1}$). 1H NMR (CD_3CN): 75.3, 56.9, 47.9, 40.7 32.3, 10.4, 8.9 ppm. $\chi_M T$ (SQUID, 296 K) = $3.62\text{ cm}^3\text{ K mol}^{-1}$ ($\mu_{eff} = 5.38\ \mu_B$). Anal. Calcd for $C_{71}H_{71} N_8O_3Fe B_{1.75}Br_{0.25}$: C, 72.3; H, 6.1 N, 9.5. Found: C, 72.3; H, 6.0; N, 9.1.

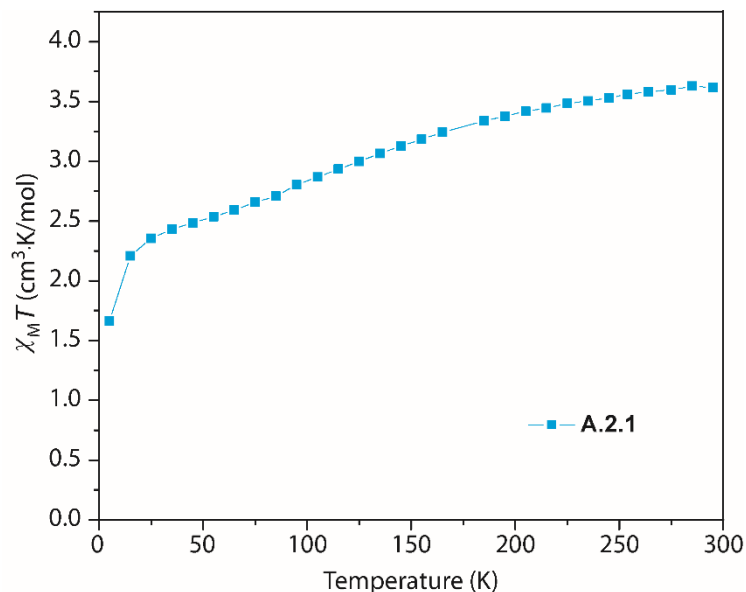


Figure A.1.4. Temperature dependence of $\chi_M T$ for **A.1.1**. Lines connecting data points are guides to the eye. $H_{dc} = 1000$ Oe.

The magnetic behavior of the mixed anion salt **A.1.1** (Figure A.1.4) is distinct from what one might expect from a mixture of **2.2** and “[FeL^{6-OH}](BPh₄)₂” in that no distinct SCO is observed at ca. 100 K. Instead $\chi_M T$ for **2.6** is 3.62 cm³ K mol⁻¹ at 295 K, and slowly decreases to 2.21 cm³ K mol⁻¹ by 15 K. The sharp downturn in $\chi_M T$ to 1.66 cm³ K mol⁻¹ at 5 K is ascribed to zero-field splitting in the residual HS fraction. The microscopic origins of the unique spin-state behavior for this compound are unknown, as structural analysis has not been performed on this compound.

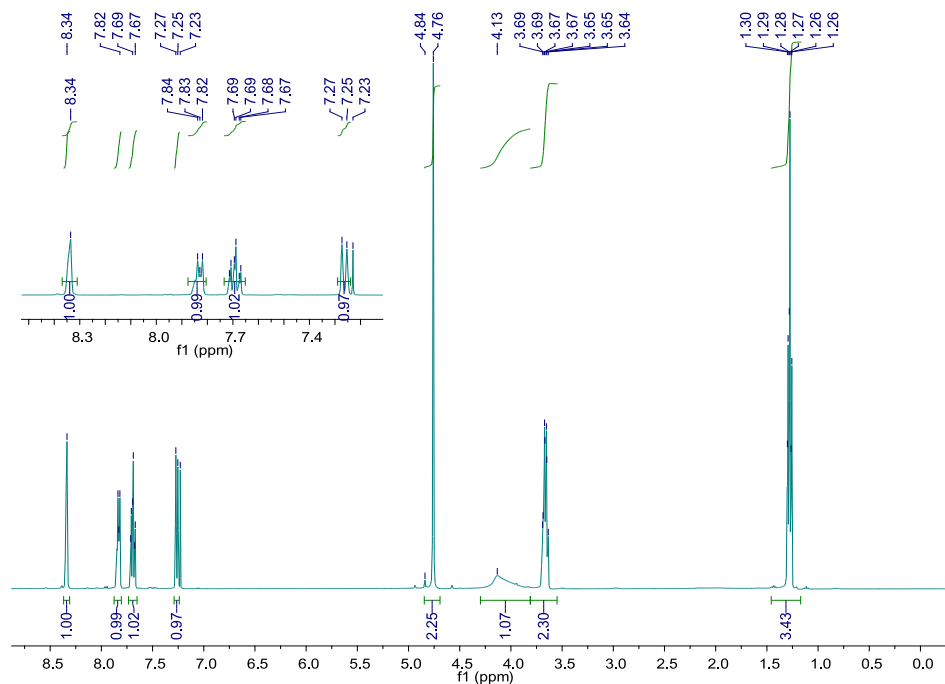


Figure A.1.5. ^1H NMR spectrum of L^2 in CDCl_3 at 400 MHz using CDCl_3 as the reference.

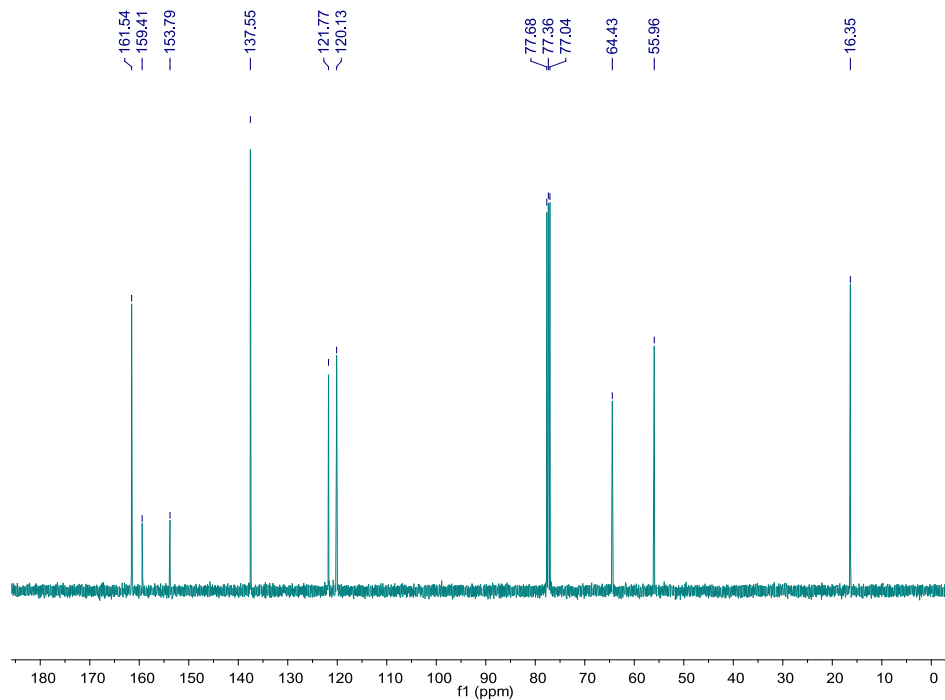


Figure A.1.6. ^{13}C NMR spectrum of L^2 in CDCl_3 , obtained on a 400 MHz NMR. Multiplet at 77 ppm is CDCl_3 .

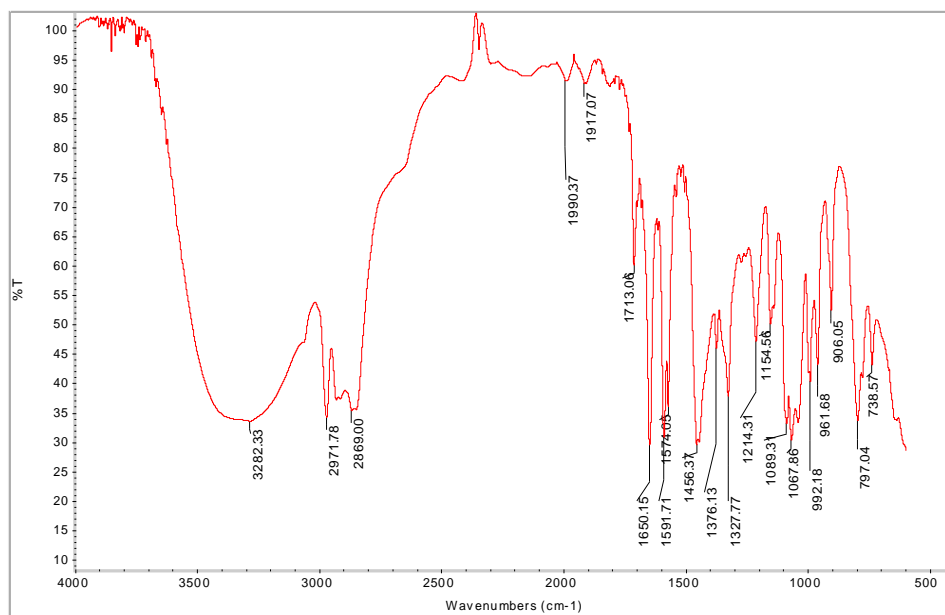


Figure A.1.7. FT-IR spectrum of L² obtained by pressing a solid sample using KBr salt plates.

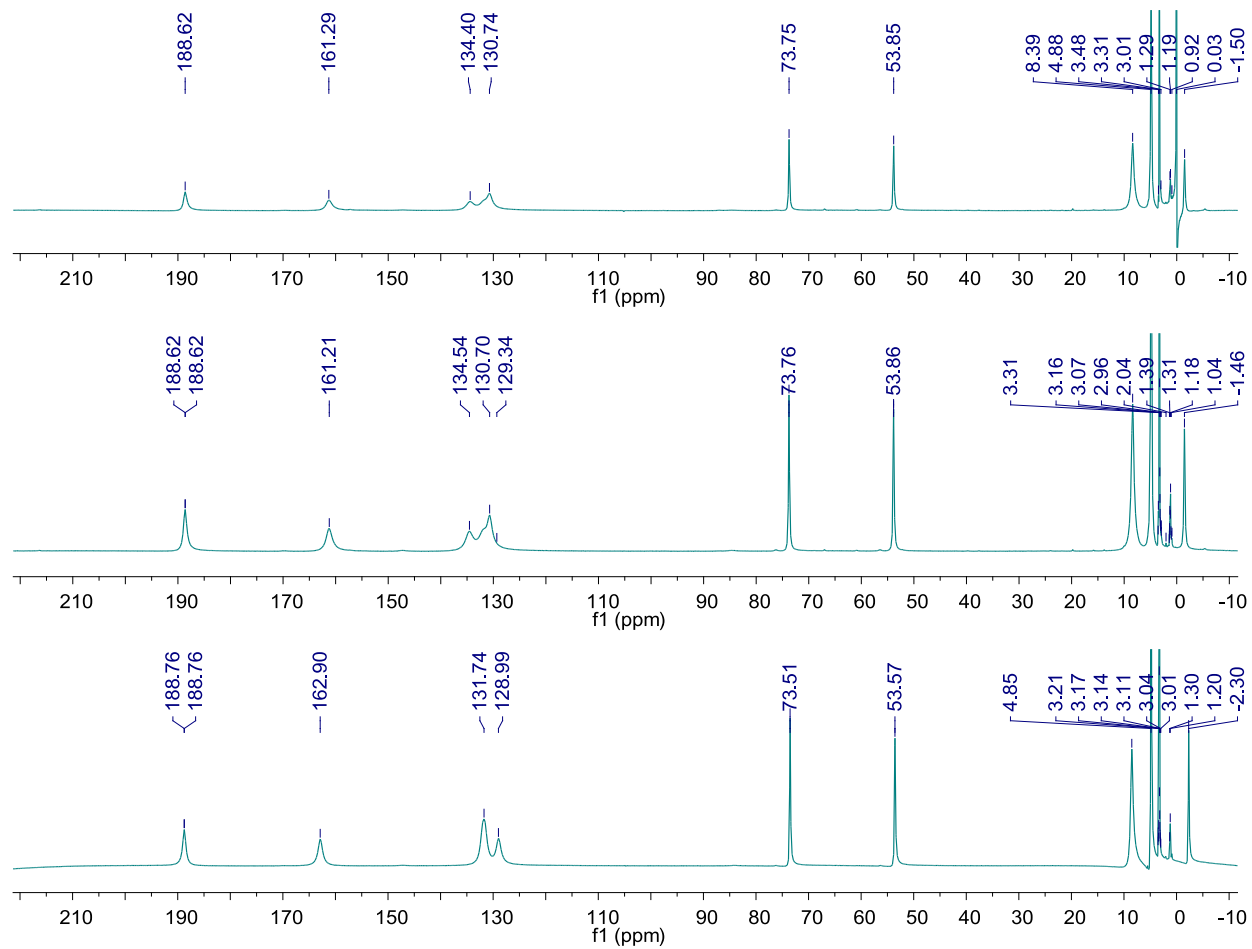


Figure A.1.8. ^1H NMR spectra obtained at 295 K at 300 MHz with CD_3OD as the reference of **2.6** at $t=10$ min. (bottom), $t=1$ day (middle) and $t=3$ days (top). Shifts in some peaks and the growth of small resonances are seen over time.

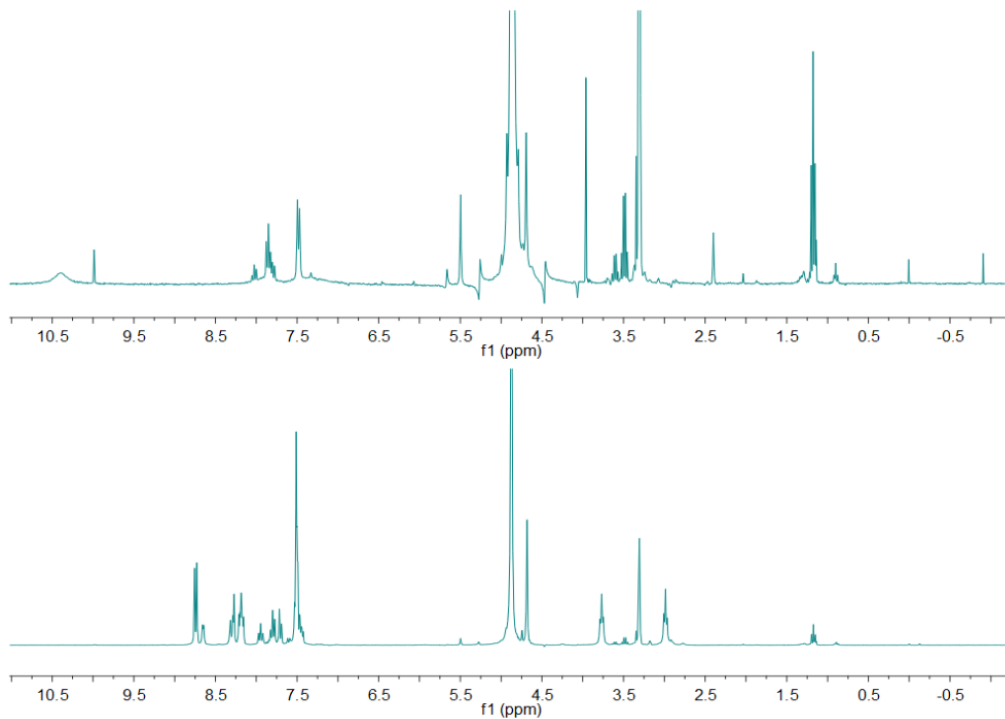


Figure A.1.9. ^1H NMR spectra of **2.2** (normal/diamagnetic window) before (top) and after (bottom) addition of 3 equivalents of 2,2'-bipyridine. NMR spectra obtained at 295 K at 300 MHz with TMS reference.

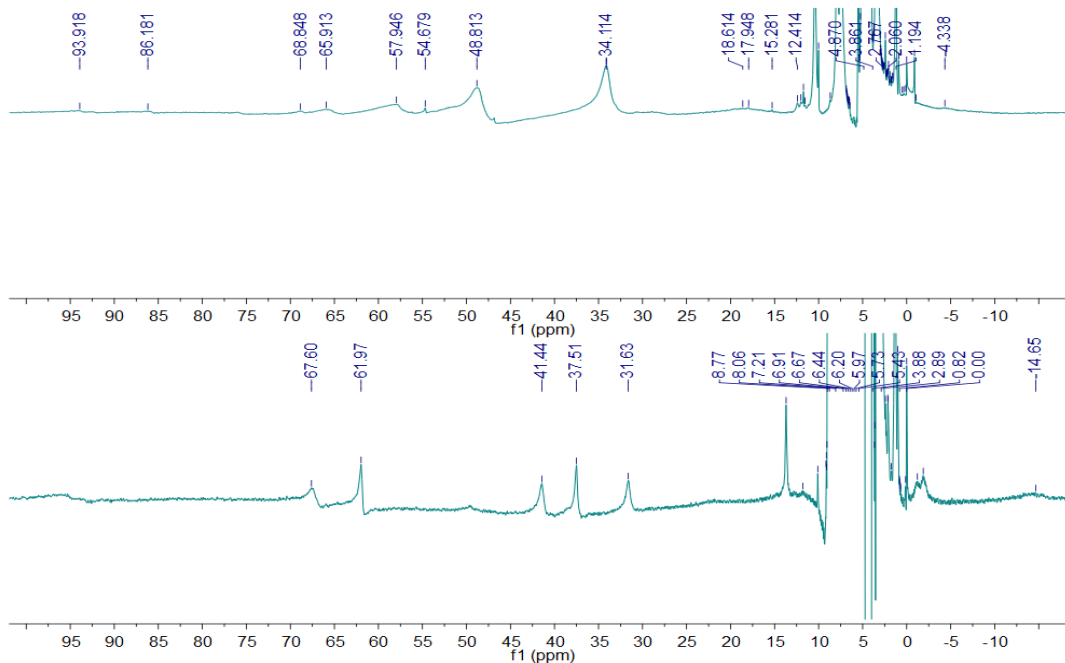


Figure A.1.10. ^1H NMR spectra of **2.2** (wider window) before (top) and after (bottom) addition of 3 equivalents of 2,2'-bipyridine. NMR spectra obtained at 295 K at 300 MHz with TMS as the reference.

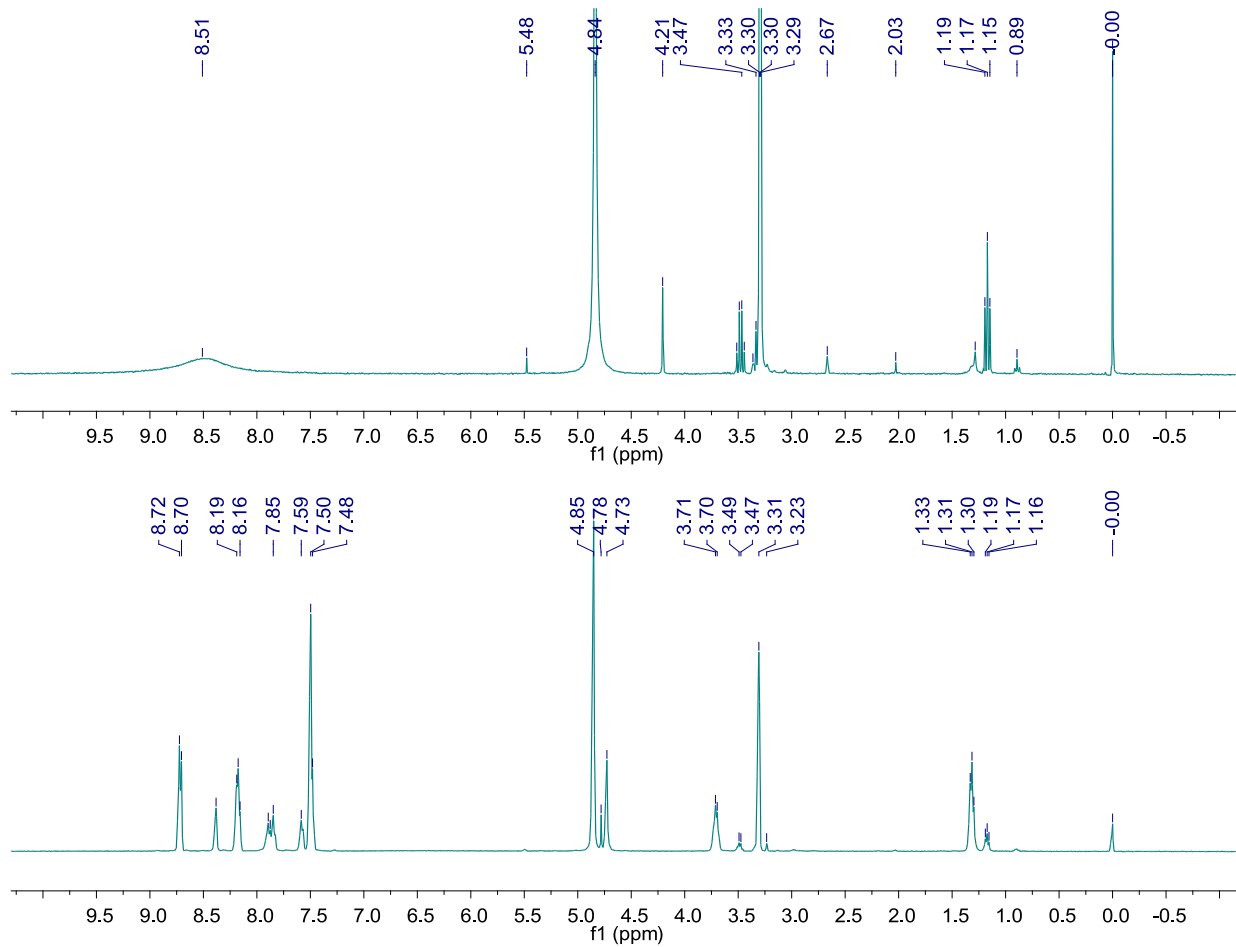


Figure A.1.11. ^1H NMR spectra of **2.6** (normal/diamagnetic window) before (top) and after (bottom) addition of 3 equivalents of 2,2'-bipyridine. NMR spectra obtained at 295 K at 300 MHz with TMS reference.

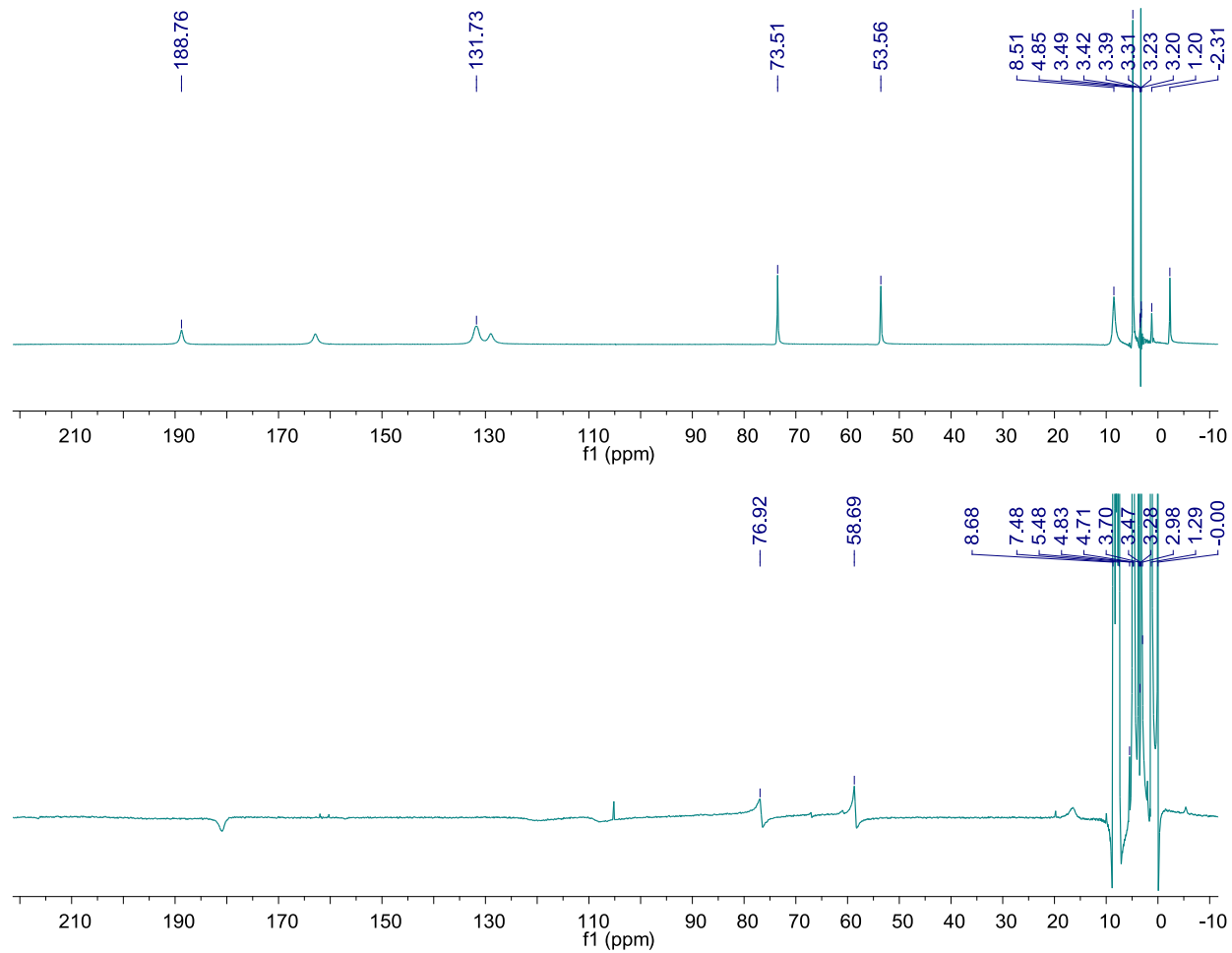


Figure A.1.12. ^1H NMR spectra of **2.6** (wider window) before (top) and after (bottom) addition of 3 equivalents of 2,2'-bipyridine. NMR spectra obtained at 295 K at 300 MHz with TMS reference.

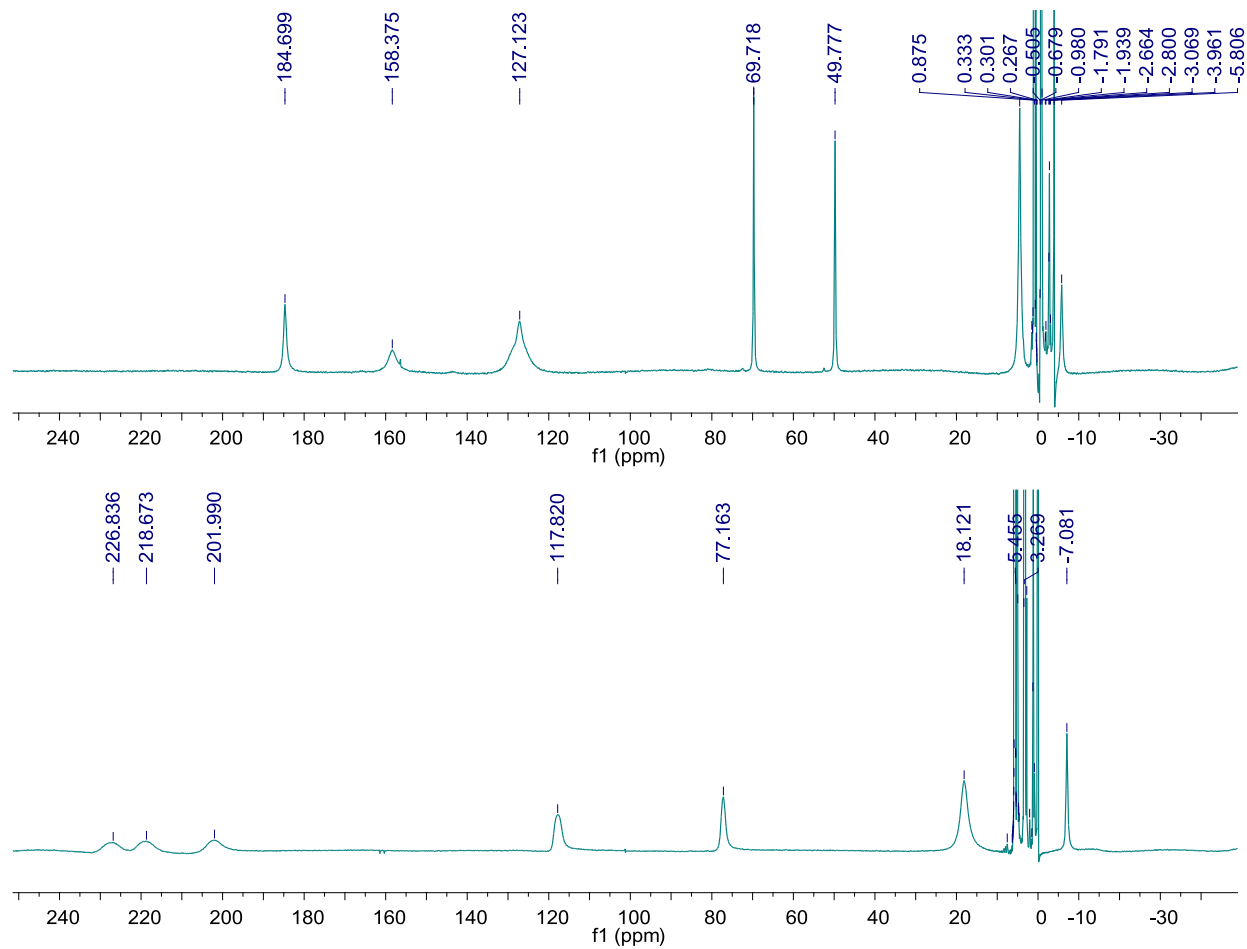


Figure A.1.13. ^1H NMR spectra of **2.6** at 298 K (top) and 193 K (bottom) obtained at 300 MHz with TMS as the reference. The peak at 127.123 ppm has a small shoulder due to peak coalescence at 298 K.

APPENDIX 2. SUPPORTING INFORMATION FOR CHAPTER 3.

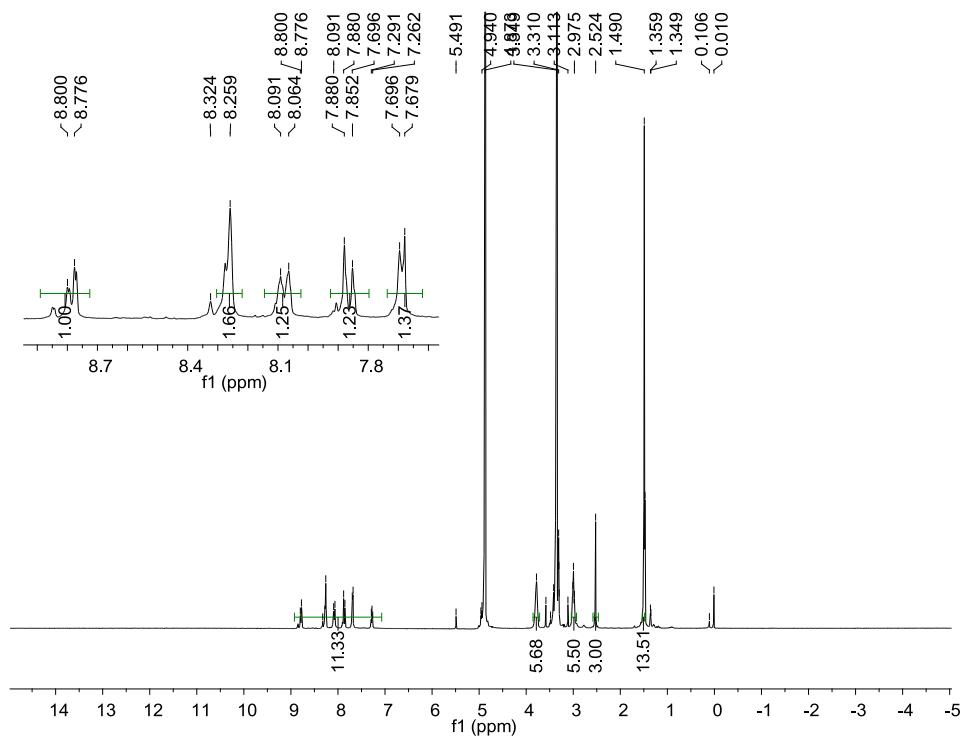


Figure A.2.1. ^1H NMR spectrum of L^{556} in CD_3OD , obtained on a 300 MHz NMR. Singlet at 4.87 ppm is due to trace water and 3.33 ppm is methanol. Inset: Zoomed in on aromatic region.

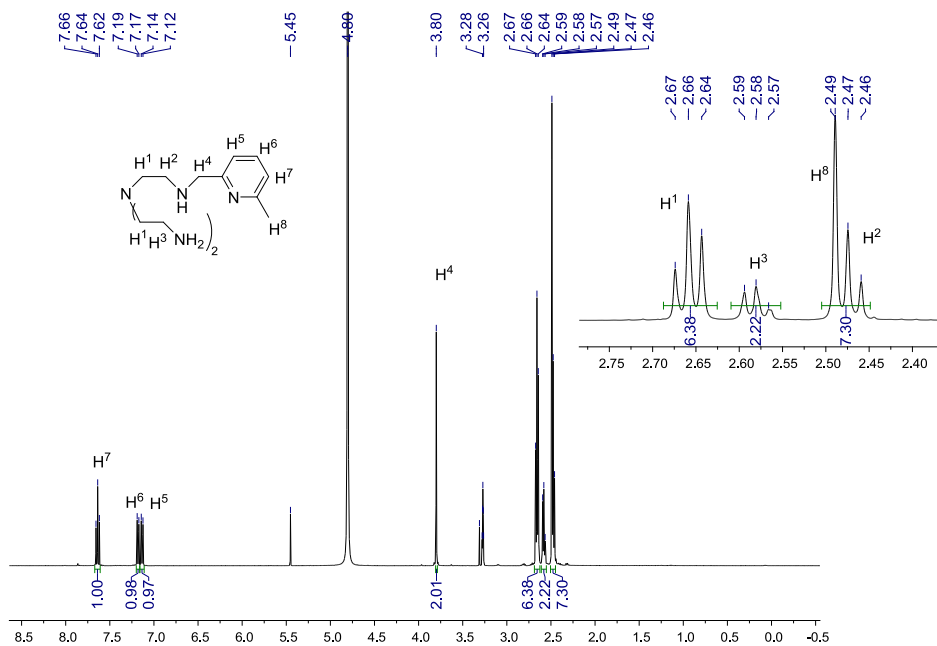


Figure A.2.2. ^1H NMR spectrum of $\text{tren}(6\text{-Mepy})(\text{NH}_2)_2$ in CD_3OD at 400 MHz NMR.

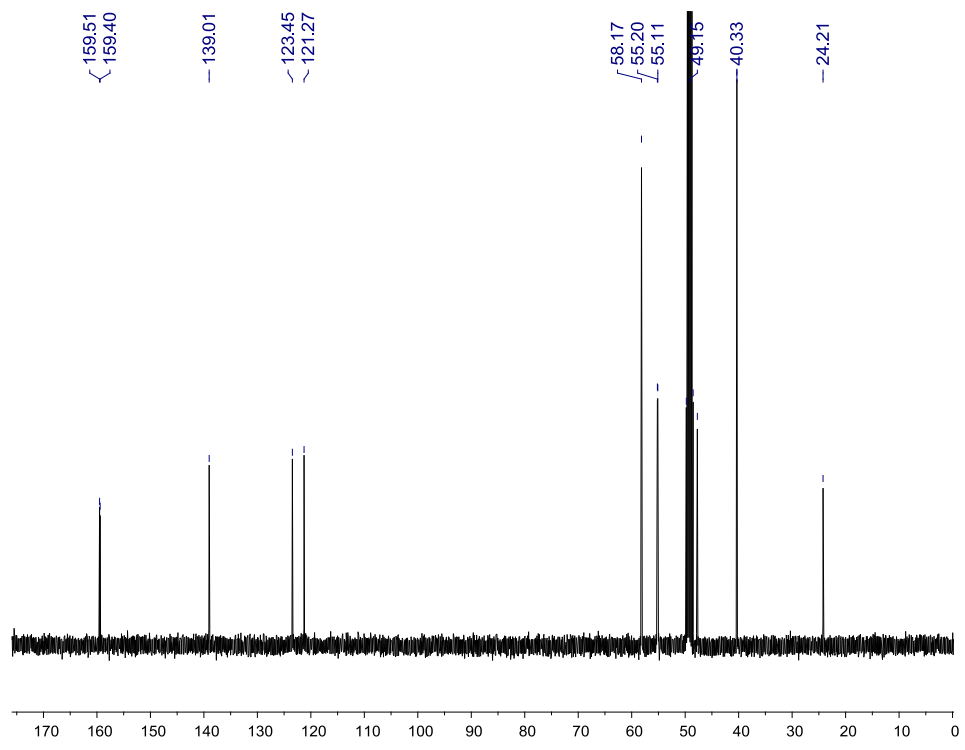


Figure A.2.3. ^{13}C NMR spectrum of $\text{tren(6-Mepy)(NH}_2)_2$ in CD_3OD . Multiplet at 49 ppm is due methanol.

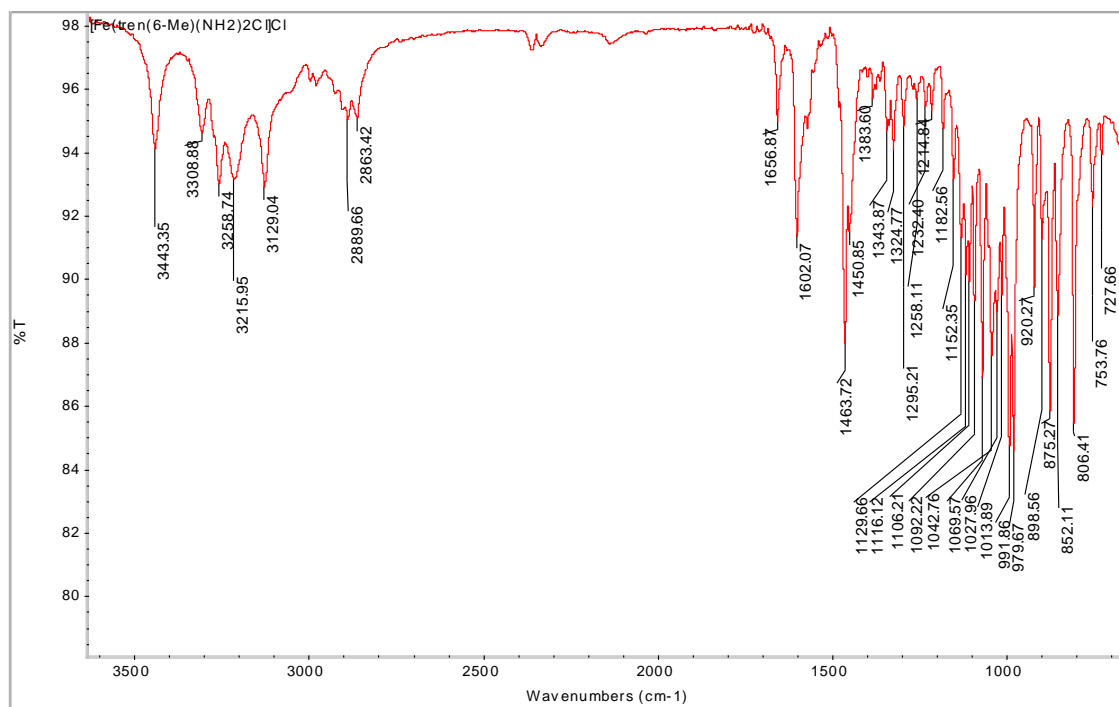


Figure A.2.4. FT-IR spectrum of **3.1** obtained by pressing crystals on to ZnSe ATR crystal.

APPENDIX 3. SUPPORTING INFORMATION FOR CHAPTER 4.

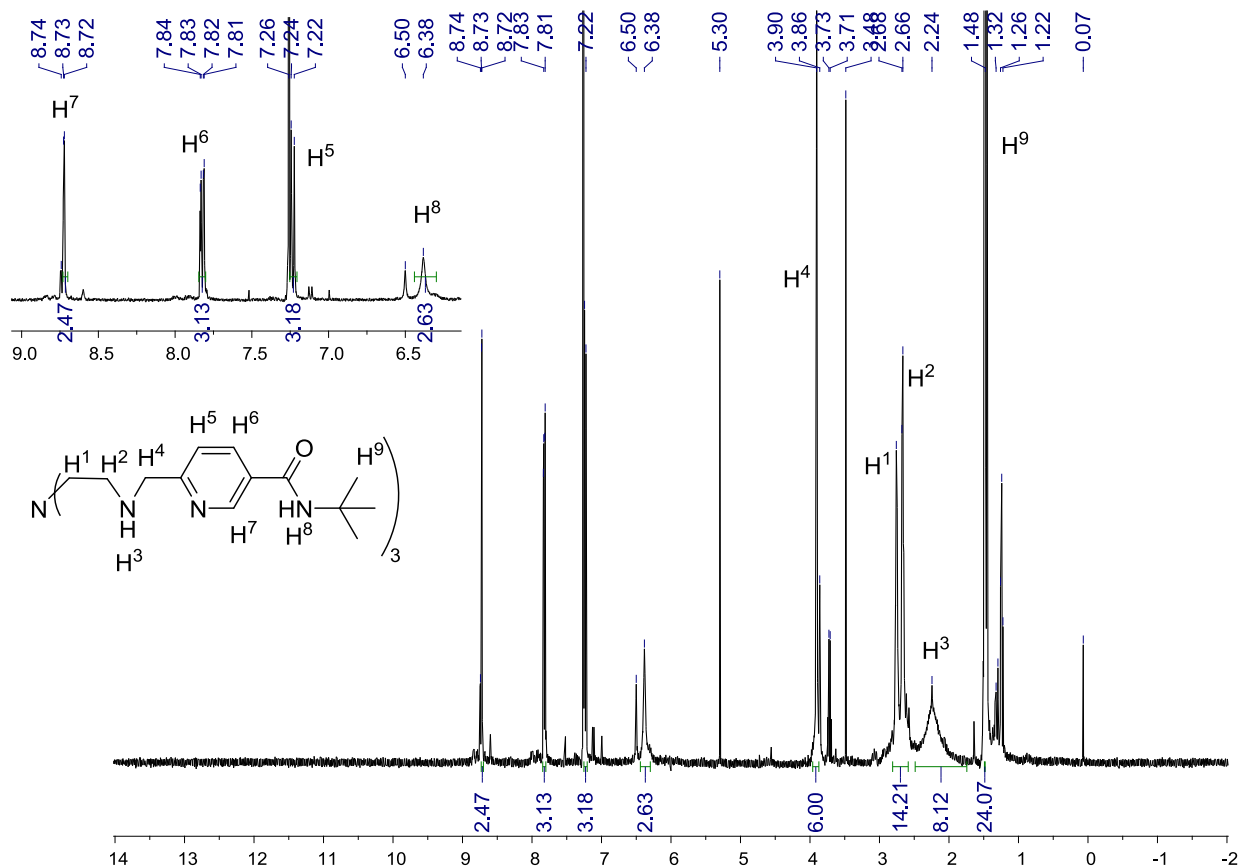


Figure A.3.1. ¹H NMR spectrum of **L**^{5-(NH)}₃ obtained in CDCl₃ on a 400 MHz NMR. Resonance at 5.30 ppm is due to residual DCM, 3.48 and 1.21 ppm are due to Et₂O, and 0.07 ppm due to silicone grease.

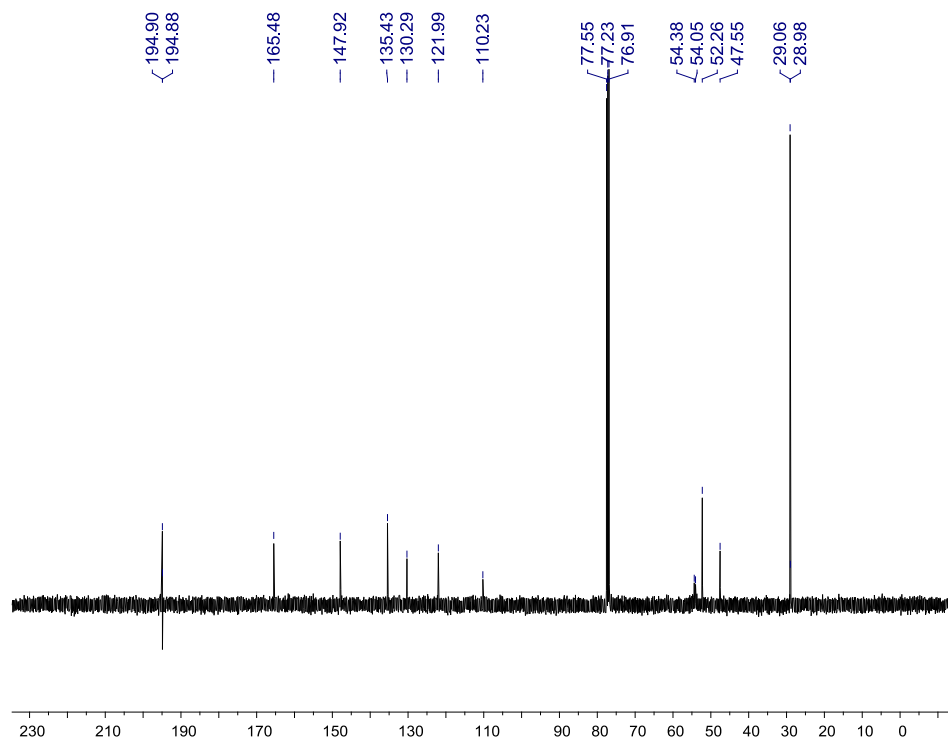


Figure A.3.2. ^{13}C NMR spectrum of $\text{L}^{5-(\text{NH})3}$ obtained in CDCl_3 . Triplet at 77 ppm is CDCl_3 .

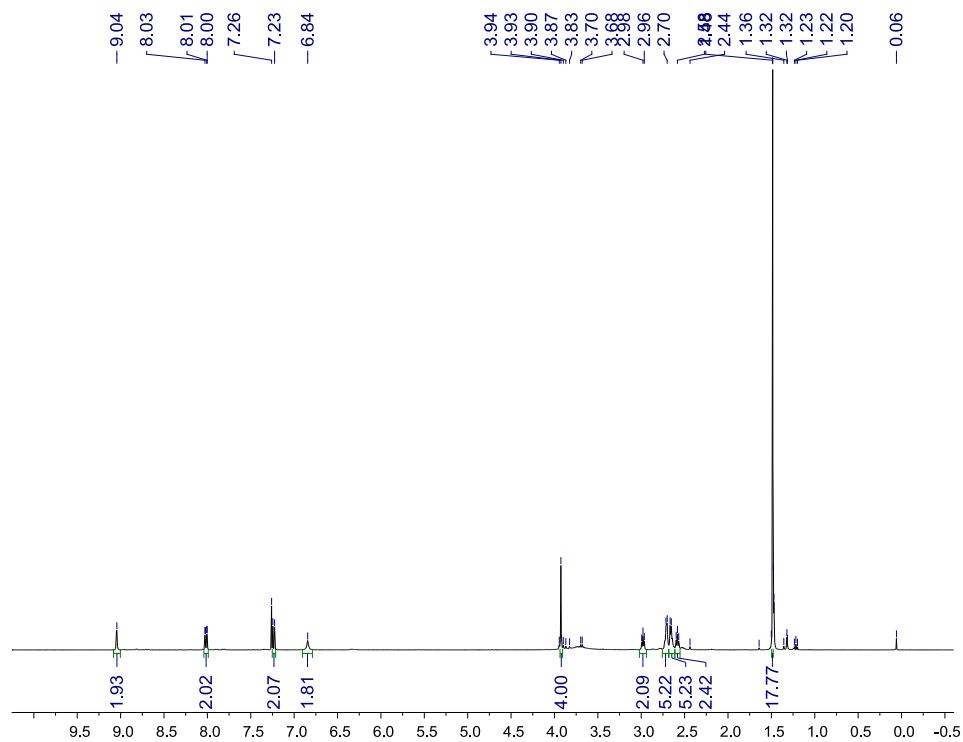


Figure A.3.3. ^1H NMR spectrum of **di-5-tert-butylamide-tren** obtained in CDCl_3 . Resonance at 7.26 ppm is CHCl_3 .

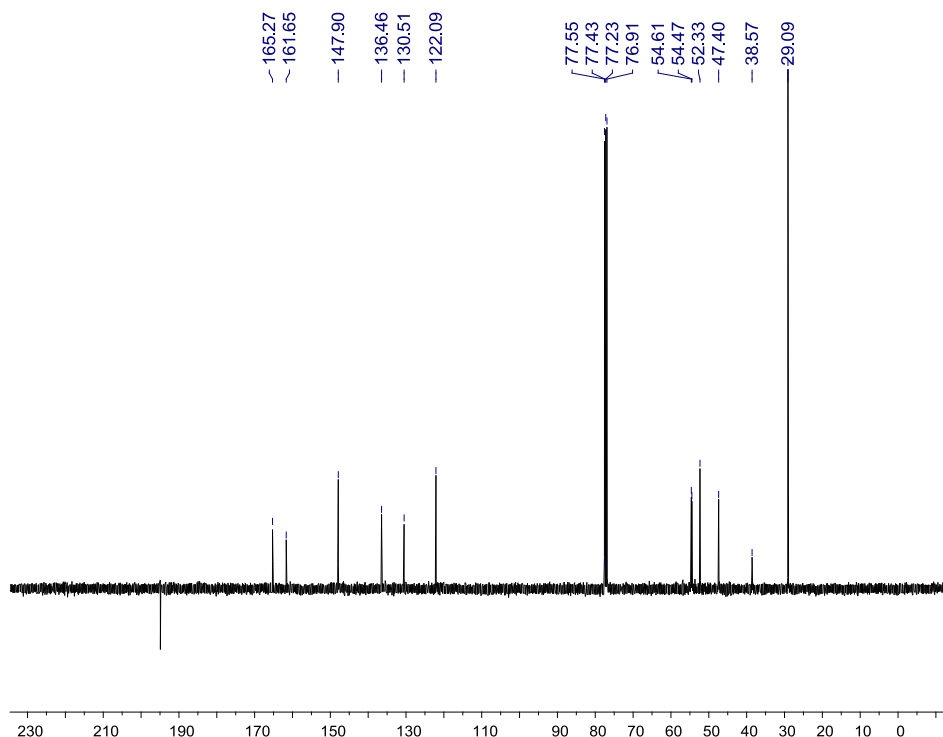


Figure A.3.4. ^{13}C NMR spectrum of **di-5-tert-butylamide-tren** obtained in CDCl_3 . Triplet at 77 ppm is CDCl_3 .

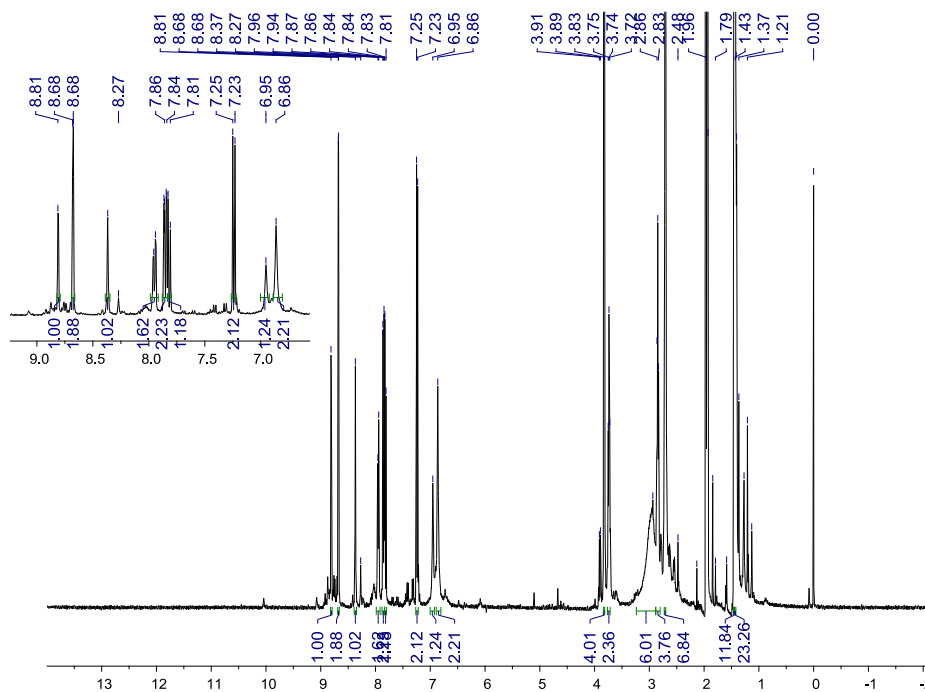


Figure A.3.5. ^1H NMR spectrum of **L^{5-(NH)₂}** obtained in CD_3CN on a 400 MHz NMR. Inset: Zoomed in on the aromatic region.

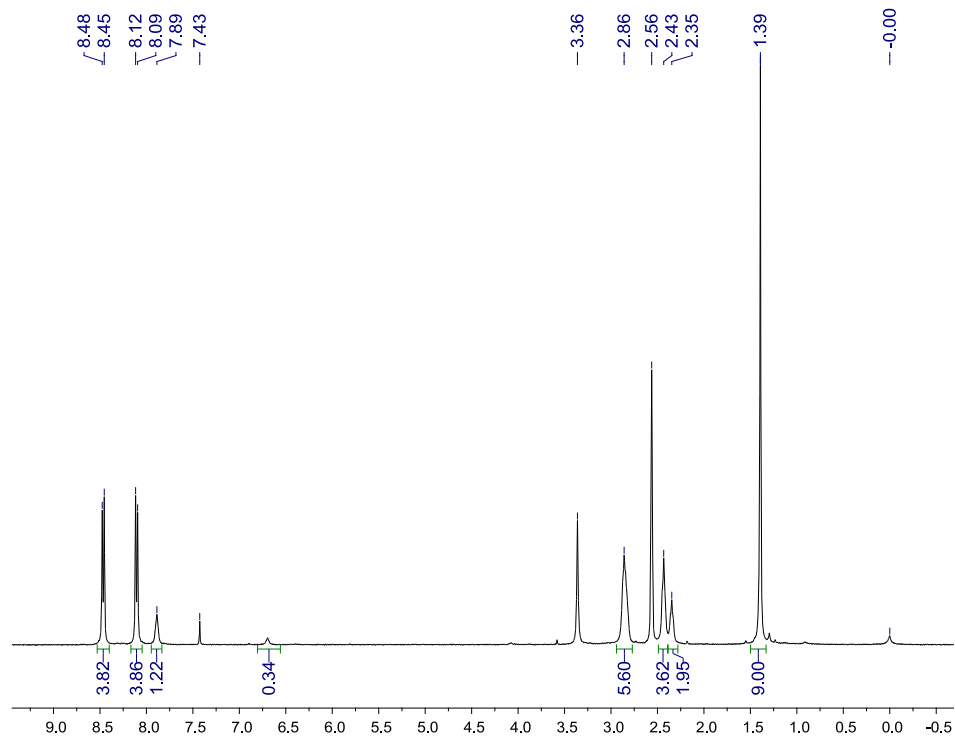


Figure A.3.6. ^1H NMR spectrum of **dinosyl-monoBoc-tren** obtained in d_6 -DMSO at 400 MHz NMR.

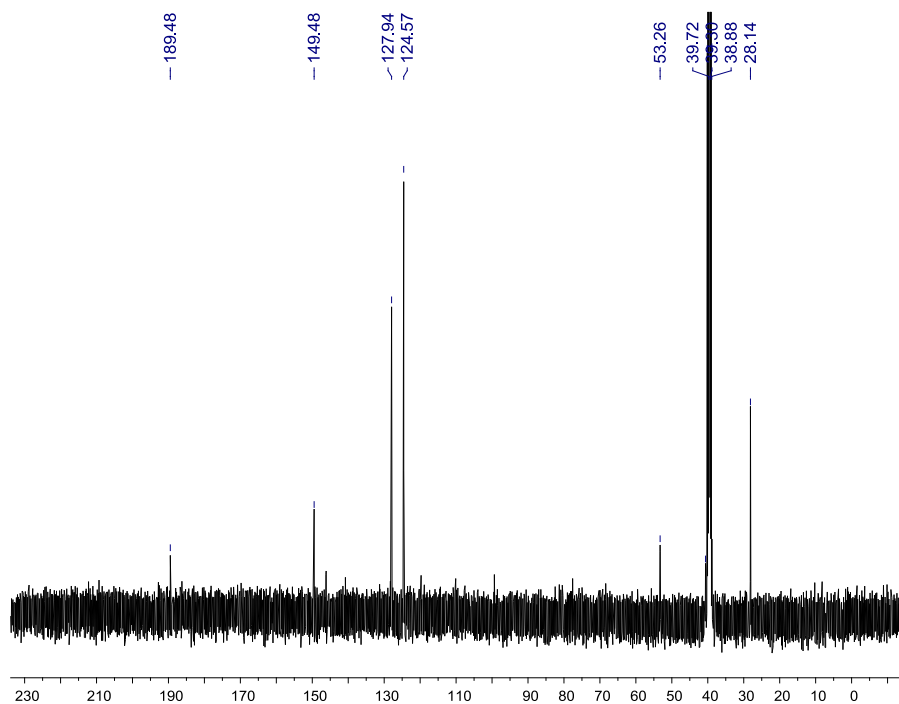


Figure A.3.7. ^{13}C NMR spectrum of **dinosyl-monoBoc-tren** obtained in d_6 -DMSO. Multiplet at 39 ppm is d_6 -DMSO.

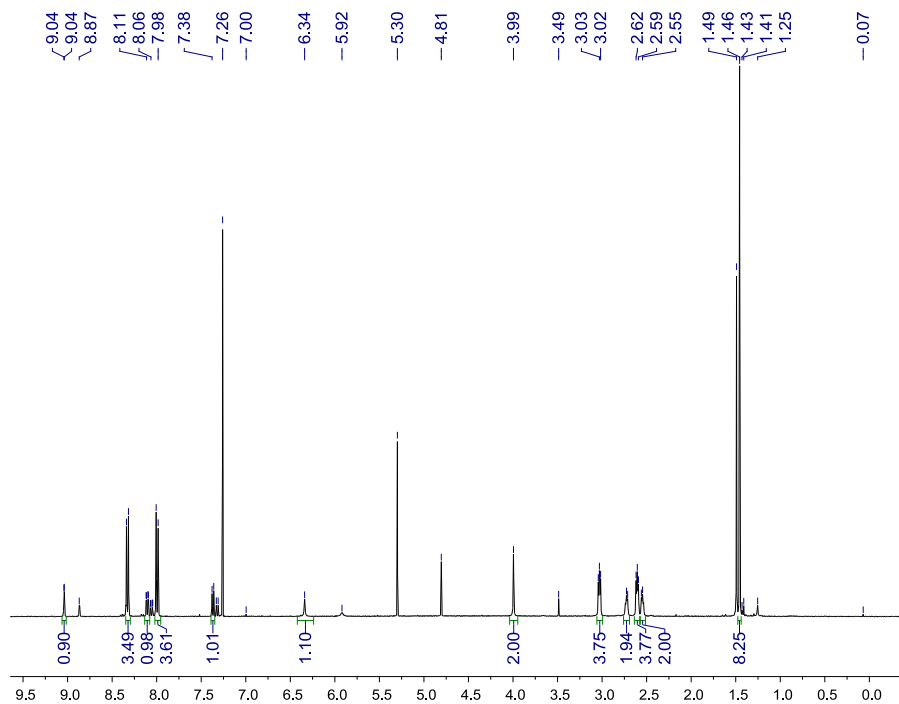


Figure A.3.8. ^1H NMR spectrum of **dinosyl-5-*tert*-butylamide-tren** obtained in CDCl_3 on a 400 MHz NMR. Resonances at 8.87, 7.33, 3.99, and 1.49 ppm are attributed to 5-*tert*-butylamide-2-pyridinemethanol. The resonance at 5.30 is due to residual DCM.

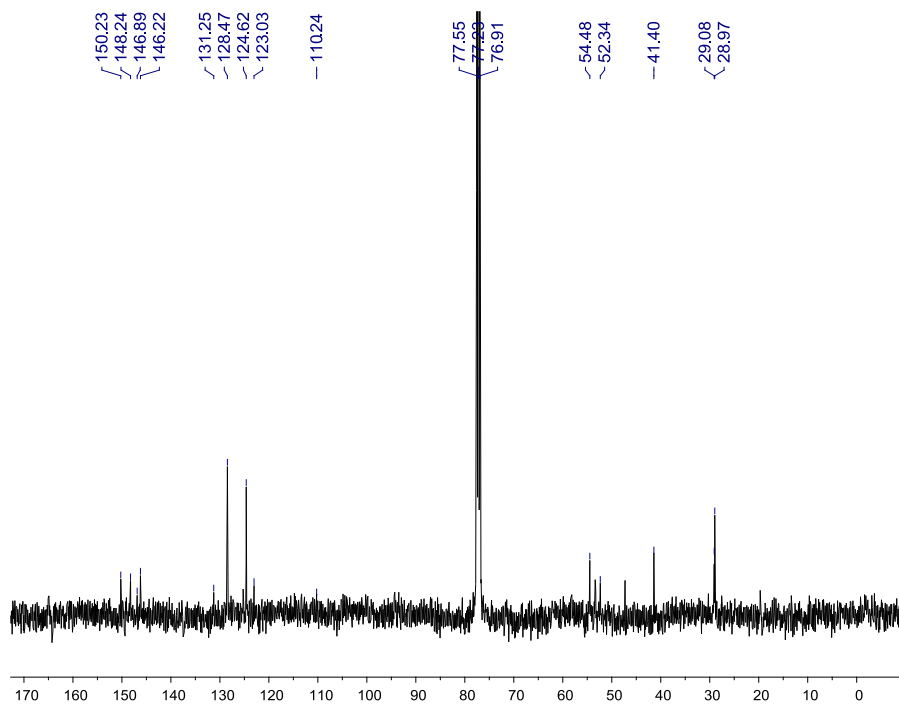


Figure A.3.9. ^{13}C NMR spectrum of **dinosyl-5-*tert*-butylamide-tren** obtained in CDCl_3 . Multiplet at 77 ppm is CDCl_3 .

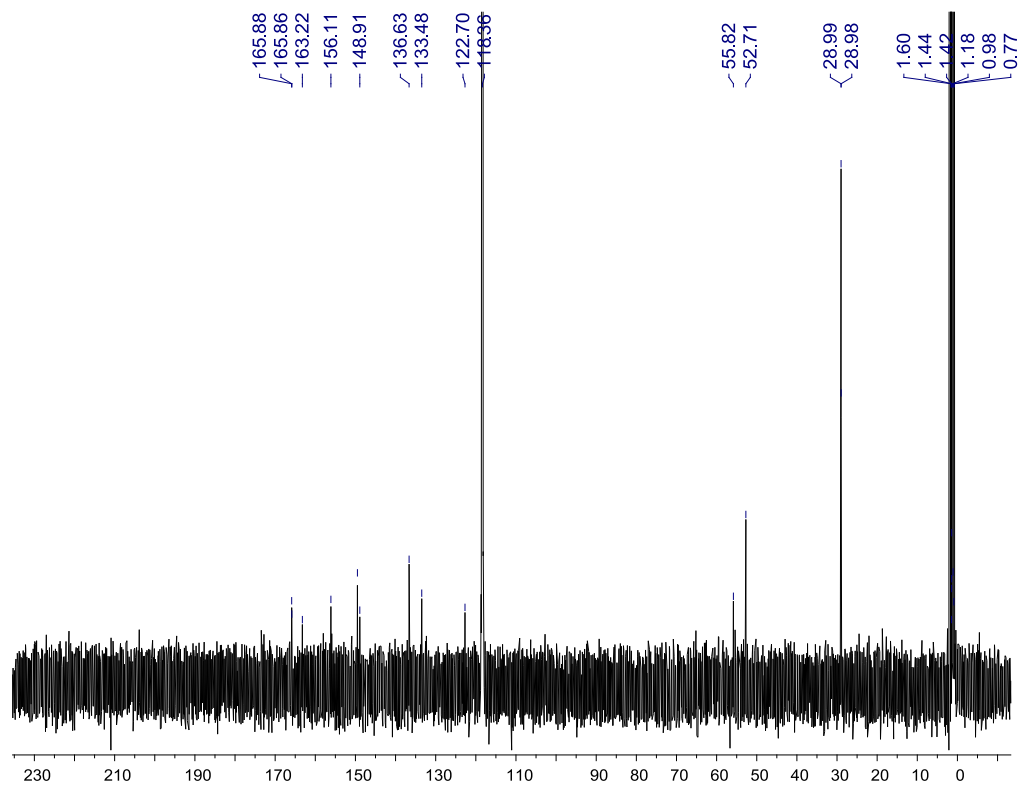


Figure A.3.12. ^{13}C NMR spectrum of $\text{L}^{5\text{-NH}}$ obtained in CD_3CN . Singlet at 118 ppm and multiplet at 1.32 ppm is CD_3CN .

APPENDIX 4. SUPPORTING INFORMATION FOR CHAPTER 5.

In addition to the complexes presented in Chapter 5, Co(II) species using a non-tethered version of $L^{5\text{-ONHtBu}}$ were synthesized and characterized.

A.4.1 Preparation of Compounds. Unless otherwise noted, all manipulations were undertaken in a dinitrogen-filled MBRAUN Labmaster 130 glovebox. Acetonitrile (MeCN) and diethyl ether (Et₂O) were sparged with dinitrogen, passed over molecular sieves, and subjected to three freeze-pump-thaw cycles prior to use. The synthesis and characterization of 5-*tert*-butylamide-2-pyridinecarboxaldehyde has been described elsewhere.¹ All other reagents were obtained from commercial sources and used without further purification.

Caution! Perchlorate salts are potentially explosive and should be handled with care and in small quantities!

(*E*)-*N*-(*tert*-butyl)-6-((ethylimino)methyl)nicotinamide ($L^{\text{ethyl-5-ONHtBu}}$). To a solution of 5-*tert*-butylamide-2-pyridinecarboxaldehyde (357 mg, 1.7 mmol) in 10 mL methanol, 70% ethylamine in H₂O (178 mg, 3.95 mmol) and 2 grams of 3 Å molecular sieves were added. The reaction was allowed to stir for 4 hours and the resulting yellow solution was filtered. The solvent was removed under reduced pressure. The product was dried under vacuum overnight to result in a light yellow solid (294 mg, 73%). ¹H NMR (300 MHz, CDCl₃) δ ppm 8.94 (1 H, s), 8.42 (1 H, s), 8.06 (2 H, d), 5.92 (1 H, bs), 3.75 (2 H, q), 1.50 (9 H, s), 1.34 (3 H, t).

[Co($L^{\text{ethyl-5-ONHtBu}}$)₃]Cl₂ (A.4.1). A solution of $L^{\text{ethyl-5-ONHtBu}}$ (58 mg, 0.25 mmol) in 6 mL dry acetonitrile was added to a suspension of CoCl₂ (10 mg, 0.08 mmol) in 3 mL acetonitrile. The solution was allowed to stir for 16 hours after which all the CoCl₂ appeared to dissolve and an orange precipitate formed. The resulting solid was isolated by vacuum filtration and washed with 10 mL acetonitrile and 10 mL diethyl ether. Crystallization was performed by diethyl ether

diffusion into a concentrated methanolic solution of the compound (56 mg, 87%). $^1\text{H NMR}$ (400 MHz, CD_3CN) δ ppm 94.5, 91.1, 85.7, 82.2, 78.2, 75.8, 72.3, 72.2, 69.4, 67.3, 66.2, 64.6, 62.4, 53.9, 17.7, 14.7, 13.5, -1.4, -4.1, -21.7, -30.0. ESI-MS(+) (MeOH): m/z 560.2 $\{[\text{Co}(\text{L}^{\text{ethyl-5-ONHtBu}})_2]\text{Cl}\}^+$, 262.7 $[\text{Co}(\text{L}^{\text{ethyl-5-ONHtBu}})_2]^{2+}$.

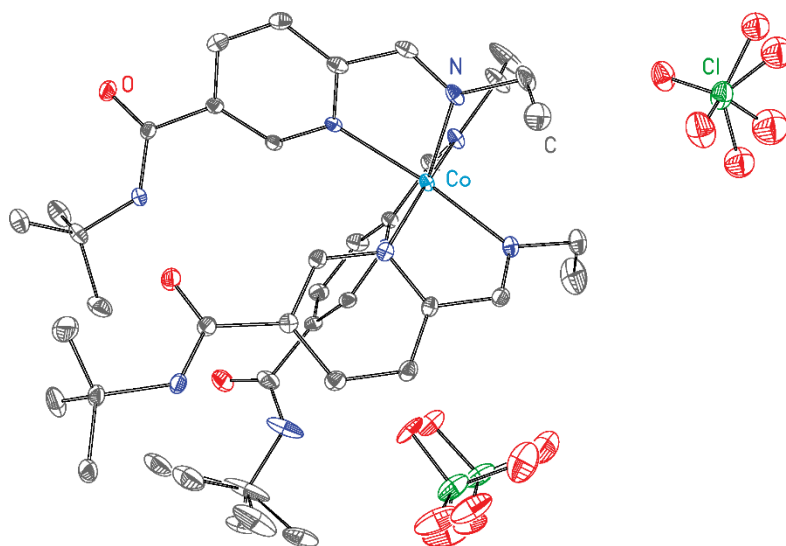
$[\text{Co}(\text{L}^{\text{ethyl-5-ONHtBu}})_3](\text{ClO}_4)_2$ (A.4.2). A solution of $\text{L}^{\text{ethyl-5-ONHtBu}}$ (103 mg, 0.44 mmol) in 6 mL dry acetonitrile was added to a solution of $\text{Co}(\text{ClO}_4)_2 \cdot 6 \text{H}_2\text{O}$ (51 mg, 0.14 mmol) in 4.5 mL acetonitrile. The solution was allowed to stir for 16 hours. The solvent was removed under vacuum. X-ray quality crystals were isolated from diethyl ether diffusion into a concentrated methanolic solution of the compound (120 mg, 90%). $^1\text{H NMR}$ (400 MHz, CD_3CN) δ ppm 98.3, 92.6, 89.9, 87.6, 83.5, 81.9, 78.4, 76.7, 68.7, 68.2, 67.7, 63.7, 63.3, 62.8, 58.5, 18.8, 16.4, 16.3, 15.8, 15, -0.6, -0.8, -1.3, -1.4, -1.6, -2.6, -3.9, -4.3, -8.3, -10.3, -16.6. ESI-MS(+) (MeOH): m/z 624.1 $\{[\text{Co}(\text{L}^{\text{ethyl-5-ONHtBu}})_2]\text{ClO}_4\}^+$, 262.7 $[\text{Co}(\text{L}^{\text{ethyl-5-ONHtBu}})_2]^{2+}$.

Table A.4.1. Crystallographic data for $[\text{Co}(\text{L}^{\text{ethyl-5-OHrBu}})_3](\text{ClO}_4)_2$ (A.4.2) .

	A.4.2
Crystal code	msn341
Empirical formula	$\text{C}_{39}\text{H}_{57}\text{Cl}_2\text{CoN}_9\text{O}_3$
Formula weight, $\text{g}\cdot\text{mol}^{-1}$	829.76
Color	Orange
Habit	Block
T , K	120(2)
Space group	$P\bar{1}$
Z	2
a , Å	9.9131(6)
b , Å	10.0815(6)
c , Å	26.2117(16)
α , deg	98.197(4)
β , deg	91.443(4)
γ deg	118.366(3)
V , Å ³	2268.5(2)
d_{calc} , $\text{g}\cdot\text{cm}^{-3}$	1.215
Goof	1.035
R_1^a (wR_2) ^b %	7.76 (13.28)

$$^a R_1 = \frac{\sum ||F_o| - |F_c||}{\sum |F_o|};$$

$$^b wR_2 = \left\{ \frac{\sum [w(F_o^2 - F_c^2)^2]}{\sum [w(F_o^2)^2]} \right\}^{1/2}$$

**Figure A.4.1.** X-ray crystal structure of A.4.2. Co, C, N, O, and Cl atoms are represented by teal, gray, blue, red, and green respectively. Thermal ellipsoids are rendered with 40% probability. Hydrogen atoms have been omitted for clarity.

A.4.2. Additional Structural Comparison. In order to understand the influence of the amides on the ligand, comparisons between these complexes and previously synthesized tripodal iminopyridine-based ligands were made. These Co(II) tripodal iminopyridine-based ligands either bear no functionalization² or incorporate methylesters³ at the 5'-position. These species show that the addition of the amide moiety to the ligand promotes an elongation of the Co–N_{imine} and Co–N_{pyridine} bond lengths regardless of the anion. This is not unexpected as an anion is not interned within the trigonal pocket formed when the ligand is not functionalized or modified with a methylester functionalization. The iminopyridine bonds of interest are influenced by the addition of the amide group. In this case, C=N_{imine} bond lengths of 1.267 Å and 1.266 Å for [Cotren(py)₃]²⁺ and [CoL^{5-OOMe}]²⁺, respectively, are longer than **5.1**, shorter for **5.2** and **5.3** and comparable for **5.4**. Changing the bridging ligand to tach (tach = *cis*-1,3,5-triaminocyclohexane) leads to a more trigonal prismatic geometry around the Co center.⁴ With this change, a lengthening of the Co–N_{imine} and shortening of Co–N_{pyridine} bond lengths are seen in comparison to any of the [CoL^{5-ONH*t*Bu}]²⁺ salts.

The other major structural component of interest, the Co–N_{bridge} distance, was determined for [Cotren(py)₃]²⁺ and [CoL^{5-OOMe}]²⁺. The addition of the esters at the 5'-position of the pyridine rings also leads to a decrease in this distance over the nonfunctionalized [Cotren(py)₃]²⁺ complex; this distance is 2.626 Å for [CoL^{5-OOMe}]²⁺ and 2.87 Å for [Cotren(py)₃]²⁺.

REFERENCES

- (1) McDaniel, A. M.; Klug, C. M.; Shores, M. P. *Eur. J. Inorg. Chem.* **2013**, 2013, 943.
- (2) Kirchner, R. M.; Mealli, C.; Bailey, M.; Howe, N.; Torre, L. P.; Wilson, L. J.; Andrews, L. C.; Rose, N. J.; Lingafelter, E. C. *Coord. Chem. Rev.* **1987**, 77, 89.
- (3) McDaniel, A. M.; Rappé, A. K.; Shores, M. P. *Inorg. Chem.* **2012**, 51, 12493.
- (4) Wentworth, R. A. D.; Dahl, P. S.; Huffman, C. J.; Gillum, W. O.; Streib, W. E.; Huffman, J. C. *Inorg. Chem.* **1982**, 21, 3060.

APPENDIX 5. NOTEBOOK CROSS-REFERENCES AND CRYSTAL STRUCTURE DATA SETS FOR RELEVANT COMPOUNDS. NOTEBOOK IDS FROM NOTEBOOKS BELONGING TO KELSEY SCHULTE (KAS) AND CHRISTINA KLUG (CMK).

Compound	Dissertation ID	Relevant Notebook ID	Crystal ID
L^{6-OH}	N/A	CMK 1-118 CMK 2-26	N/A
$[FeL^{6-OH}](OTf)_2$	2.1·RT	CMK 1-136	msn300
$[FeL^{6-OH}](OTf)_2$	2.1·LT		msn306
$[FeL^{6-OH}]Br_2$	2.2	CMK 1-152 CMK 2-11	msn254
$[FeL^{6-OH}]Br_2 \cdot solv$	2.3	CMK 2-13	msn168
$[FeL^{6-OH}]I_2$	2.4·RT	CMK 1-66	msn260
$[FeL^{6-OH}]I_2$	2.4·LT	CMK 1-136 CMK 2-85	msn240
$[FeL^{6-OH}](BPh_4)_2$	2.5	CMK 2-15	msn308
L^2	N/A	KAS 1-72 KAS 1-97	N/A
$[Fe(L^2)_2](OTf)_2$	2.7	KAS 1-74 KAS 1-100 KAS 1-106	msn309
L^{556}	N/A	CMK 3-90 CMK 3-128	N/A
tren(6-Me)(NH ₂) ₂	N/A	CMK 7-143	N/A
$[Fe(tren(6-Me)(NH_2)_2Cl)Cl]$	3.1	CMK 7-146 CMK 7-148	msn368
$[FeL^{556-NH}]Cl_2$	3.2a/b	CMK 9-117	N/A
$[FeL^{556-NH}](BF_4)_2$	3.3	CMK 9-118	N/A
$L^{5-(NH)3}$	N/A	CMK 5-65 CMK 9-91	N/A
di-5- <i>tert</i> -butylamide-tren	N/A	CMK 8-55	N/A
$L^{5-(NH)2}$	N/A	CMK 9-57	N/A
Dinosyl-monoboc-tren	N/A	CMK 9-97 CMK 9-107	N/A
Dinosyl-tren	N/A	CMK 9-99 CMK 9-105	N/A
Dinosyl-5- <i>tert</i> -butylamide-tren	N/A	CMK 9-100	N/A
Diboc-5- <i>tert</i> -butylamide-tren	N/A	CMK 9-145	
5- <i>tert</i> -butylamide-tren	N/A	CMK 9-111 CMK 9-147	N/A
L^{5-NH}	N/A	CMK 10-9	N/A

$[\text{FeL}^{5-(\text{NH})_3}](\text{BF}_4)_2$	4.1	CMK 8-22 CMK 9-94	msn319
$[\text{FeL}^{5-(\text{NH})_2}](\text{BF}_4)_2$	4.2	CMK 8-64 CMK 9-60	msn355
$[\text{FeL}^{5-\text{NH}}](\text{BF}_4)_2$	4.3	CMK 9-153	N/A
$[\text{FeL}^{5-\text{NH}}](\text{BPh}_4)_2$	4.4	CMK 9-154	msn397
$[\text{CoL}^{5-\text{ONH}t\text{Bu}}]\text{Cl}_2$	5.1	CMK 6-78 CMK 8-79	msn335
$[\text{CoL}^{5-\text{ONH}t\text{Bu}}]\text{Br}_2$	5.2	CMK 8-114	msn357
$[\text{CoL}^{5-\text{ONH}t\text{Bu}}]\text{I}_2$	5.3	CMK 8-115	msn369
$[\text{CoL}^{5-\text{ONH}t\text{Bu}}](\text{ClO}_4)_2$	5.4	CMK 6-77	msn340
$[(\text{dmpe})_2\text{FeCl}(\text{CCTMS})](\text{OTf})$	6.1	CMK 7-138	msn346
$[(\text{dmpe})_2\text{FeCl}(\text{MEM})]$	6.2	CMK 5-145 CMK 6-103	N/A
$[(\text{dmpe})_2\text{FeCl}(\text{MEM})](\text{OTf})_2$	6.3	CMK 5-147 CMK 6-105	msn328
$[(\text{dmpe})_4\text{Fe}_2\text{Cl}_2\text{H}(\mu_2\text{-}m\text{-HTEM})]$	6.4	CMK 5-25 CMK 5-47 CMK 5-49	N/A
$[(\text{dmpe})_4\text{Fe}_2\text{Cl}_2\text{H}(\mu_2\text{-}m\text{-HTEM})](\text{OTf})_2$	6.5	CMK 5-27 CMK 5-51 CMK 5-53	msn302
$[(\text{dmpe})_4\text{Fe}_2\text{Cl}_2(\mu_2\text{-}m\text{-DEM})]$	6.6	CMK 6-47 CMK 6-55 CMK 6-122	N/A
$[(\text{dmpe})_4\text{Fe}_2\text{Cl}_2(\mu_2\text{-}m\text{-DEM})](\text{OTf})_2$	6.7	CMK 6-50 CMK 6-58 CMK 6-123	msn330
$\text{L}^{\text{ethyl-5-ONH}t\text{Bu}}$	N/A	CMK 6-114	N/A
$[\text{Co L}^{\text{ethyl-5-ONH}t\text{Bu}}]\text{Cl}_2$	A.4.1	CMK 7-19	N/A
$[\text{Co L}^{\text{ethyl-5-ONH}t\text{Bu}}](\text{ClO}_4)_2$	A.4.2	CMK 7-21	msn341